Spring 5-15-2018

Fundamental studies of solid-fuel combustion using a two-stage flat-flame burner

Adewale Ayodeji Adeosun
Washington University in St. Louis

WASHINGTON UNIVERSITY IN ST. LOUIS

School of Engineering & Applied Science

Department of Energy, Environmental, and Chemical Engineering

Dissertation Examination Committee:

Richard L. Axelbaum, Chair
Ramesh Agarwal
Pratim Biswas
Rajan Chakrabarty
Benjamin M. Kumfer
Patricia Weisensee

Fundamental studies of solid-fuel combustion using a two-stage flat-flame burner

By

Adewale Ayodeji Adeosun

A dissertation presented to
The Graduate School
of Washington University in
partial fulfillment of the
requirements for the degree
of Doctor of Philosophy

May, 2018
St. Louis, Missouri

Table of Contents

List of Figures

List of Tables

Acknowledgments

My sincere gratitude goes to my advisor, Professor Richard L. Axelbaum. His ability to use science for practical engineering applications is unparalleled. His passion for clean coal utilization is evident in every conversation. Thanks for the guidance over the course of my PhD studies. I also want to thank Professor Pratim Biswas for his leadership and incredible energy to spur me into action. The encouraging words and mentorship from Professor Rajan Chakrabarty and Professor Benjamin Kumfer have been really helpful. I remember telling Professor Kumfer about my plan to study coal ignition some years ago. He said: “just do it”. I am glad you said that. I deeply appreciate Professor Ramesh Agarwal and Professor Patricia Weisensee for serving on my dissertation committee.

Dr. Fei Xia was my first point of contact at the Laboratory for Advanced Combustion and Energy Research. He is a great mentor. He also introduced me to computational fluid dynamics (CFD) simulations. Special thanks go to Dr. Zhiwei Yang. I have immensely gained from his expertise in combustion and CFD simulations. To my former colleague Dr. Akshay Gopan, I am grateful for every advice. Professor Xuebin Wang’s energy and passion for science are inspirational, and I am glad our paths crossed. I am deeply indebted to Professor Tianxiang Li. I have on many occasions called upon his technical skills and his expertise in combustion. He deeply cares for me. Thank you. I sat in the same office with Zhenghang Xiao, who was on a six-month exchange program from Tsinghua University. Knowing him was one of the greatest delights of my PhD period. We are friends with a lot in common and I learnt a lot from him. To all my colleagues in the Laboratory for Advanced Combustion and Energy Research, including Dr. Wendong Wu, Dr. Mike Shen, Jose Madero, Dishant Khatri, Piyush Verma, and Pan Du, I say thank you from

the depth of my heart. It has been a pleasure working with you all. Special thanks also to all 2013 PhD entrants, especially Shalinee Kavadiya, Michael Walker, Ahmed Abokifa, Chris Bowen, Kelsey Haddad, and Begum Karakocak. They are amazing people I have come to know over the last five years. It is a great honor to have you all as friends

I acknowledge the funding agencies for my work, including the Consortium for Clean Coal Utilization at Washington University in St Louis, the U.S.-China Clean Energy Research Center, and the Department of Energy. My PhD study would have been impossible without these supports.

I received two handwritten letters during my PhD study. Dr. Manan Pathak lives in Seattle, and Dr. Aravind Muthiah, a friend I schooled with during my Master's degree, lives in Singapore. Both had the same message: "When things go wrong, as they sometimes will. When the road you are trudging seems all uphill, and you want to smile but you must sigh. Rest if you must friend but don't you quit!". I will forever cherish these words.

To my dad (Morolayo), my mum (Felicia), my brother (Ayotunde) and my sister (Ayooluwa), I am honored to be a part of you. The strength to endure and the courage to overcome obstacles that you all have taught me saw me through it all. I look forward to seeing you all soon.

And last but not least, my wife, Elizabeth, I am incredibly grateful for your sacrifices and endurance. Your belief in me, your hope for my future, and your thoughts on the father that I should be and will be to my son, Obaloluwa, and my daughter, Obafisayo, scare the hell out of me every day. I hope to surpass your expectations. I truly believe your words that all will be well with hard work and prayer. Thank you all!

Adewale Ayodeji Adeosun

Washington University in St. Louis

May 2018

This work is dedicated to

Almighty God, the Giver of Life and the Author of Faith

My wife, Elizabeth, for her sacrifices, dedication, and love for me and the kids

My kids (Obaloluwa & Obafisayo).

Abstract of the dissertation

Fundamental studies of solid-fuel combustion using a two-stage flat-flame burner

by

Adewale Ayodeji Adeosun

Doctor of Philosophy in Energy, Environmental, and Chemical Engineering

Washington University in St. Louis, 2018

Professor Richard L. Axelbaum, Chair

Innovative coal technologies are essential for addressing concerns about air pollution and global climate change. A key pathway to advancing these technologies is through developing a thorough understanding of the fundamental physical and chemical processes that occur during coal combustion. Ignition influences many aspects of coal combustion, including flame stability, submicron aerosol evolution, and char burnout. As important as ignition and these associated processes are, they are challenging to study because they depend on many factors, such as the combustion environment, particle size, and particle-particle interactions.

While there have been many studies of coal ignition, none have studied the process in a way that simulates the coal particles going from a reducing to an oxidizing environment, which is characteristic of what coal particles experience in the near-burner region of pulverized coal furnaces. Fundamental studies of the impacts of this "reducing-to-oxidizing" environment on ignition as a function of residence time, gas temperature, and particle size can provide valuable insights for optimizing advanced burner design.

In addition to ignition, ultrafine aerosols are mainly formed in the near-burner region of pulverized coal furnaces where temperature is high, and a better understanding of the formation mechanisms in the reducing-to-oxidizing environment can aid the development of in-flame control

of particulate formation. Thus, in this dissertation, a new experimental platform, called a two-stage Hencken flat-flame reactor, is designed and fabricated for evaluating coal ignition and aerosol formation in conditions relevant to pulverized coal furnaces with respect to timescales, gas temperatures, and combustion environments.

With this new reactor, particles first experience a reducing environment and then transition to an oxidizing environment, in a residence time characteristic of typical coal furnaces. Using this unique experimental apparatus, single particle ignition and coal stream ignition data are obtained under a wide range of conditions. The methods to obtain these data include high-speed videography, image-processing technique (particle tracking and intensity extraction), and scanning electron microscopy. Together with computational model predictions, characteristics of single particle ignition and coal stream ignition are obtained which include ignition mechanisms, ignition delay times and induction times.

First, a proof-of-concept study is performed to evaluate the influence of the "reducing-to-oxidizing" environment (R-O) on single particle ignition. The proof-of-concept study is repeated for single particles experiencing an oxidizing environment only (O). The results show that the R-O affects single particle ignition significantly. Specifically, at a high gas temperature of 1800 K, a hetero-homogeneous mechanism is promoted in the R-O while a homogeneous-to-heterogeneous mechanism prevails in the oxidizing environment. For 1300 K gas temperature environment, it is found that volatiles are released mainly after the particle has transitioned to the oxidizing environment, thus promoting homogeneous ignition. Due to the R-O, average ignition delay times for single particles in nominal 1300 K and 1800 K gas temperatures increase over those of O by 20% and 40% respectively.

Next, the role of different particle sizes on single particle ignition is studied. Unique to the R-O, ignition delay times for particles above 106 μm size are found to be similar in 1800 K gas temperature. The similarity is due to high volatile fluxes from such large particles. Hence, homogeneous ignition occurs as soon as such a particle with its volatile transitions to the oxidizing environment from the reducing environment. In a 1300 K gas temperature environment (lower heating rate), the ignition delay times in O and R-O are similar for the same particle size range because significant volatile release occurs after the reducing zone. For the various particle sizes studied, gas temperature in O has a first order effect on single particle ignition, reducing ignition times in an 1800 K environment by a factor up to 5 times over those in 1300 K environment.

The next study on single particle ignition involves statistical ignition analysis aimed at investigating the ignition behavior of coal particles over a wide particle size range. Typically, coal particles are classified into narrow size ranges before single particle experiments. The ignition behavior of the narrow particle size range is then based on data from a few sampled particles, usually with no knowledge of what particle sizes in the size range are sampled. To address this limitation and eliminate the need for particle classification, single particle ignition experiments are conducted using 75-149 μm particles, and a new algorithm is developed that allows for simultaneous determination of particle size before ignition and ignition delay time from the experimental data. Using the new algorithm, statistical ignition data from these experiments are compared to the experimental results from ignition studies using four different narrow particle size ranges. The results show that the use of narrow size ranges in evaluating ignition behavior of coal compares well on average to the statistical ignition data. As expected, the results using the four narrow size ranges do not capture the variations in ignition delay times.

Apart from the single particle ignition experiments, the effects of particle size and the reducing-to-oxidizing environment on pulverized coal stream ignition are also studied. The results show that ignition delay time is independent of particle size at 1800 K gas temperatures in either the oxidizing or the reducing-to-oxidizing environment condition, but depends significantly on particle size at 1300 K. This finding indicates that ignition delay time is determined by the amount of volatiles released (depending on particle size), by the gas temperature, and by the local oxygen concentration. For all particle size ranges considered, homogeneous-to-heterogeneous ignition is observed. The reducing-to-oxidizing environment increases ignition delay times by 100% on average over those of oxidizing conditions at 1800 K gas temperature. In the reducing-to-oxidizing environment, longer ignition delay times are due to the oxidation of volatiles released before the particles exit the volatile flame front at the flame front. Hence, for homogeneous ignition to occur, more volatiles must be generated downstream of the reducing-to-oxidizing environment zone. On the other hand, at a 1300 K nominal gas temperature, ignition delay times and modes strongly depend on particle size in the stream. Interestingly though, there exists a crossover at which the ignition delay times in the reducing-to-oxidizing environment are less than those of the oxidizing environment for large particles (i.e., 90-124 μm and 125-149 μm) at 1300 K.

The experimental observations are consistent with model predictions. With both experimental and computational modeling tools, this dissertation offers new fundamental understanding of coal ignition as an early-stage process of coal combustion.

Chapter 1

Introduction

1.1 Background and motivation

1.1.1 Fossil fuels: Meeting present and future global energy needs

According to the International Energy Agency and the British Petroleum Statistical Review of World Energy, the world's total energy consumption in 2015 was 575 quadrillion British thermal units, and about 81% of this consumption came from fossils fuels.[1] Even with a considerable and unprecedented effort to develop renewable energy sources, fossil fuels will account for about 80% of the projected primary energy needs in 2040.[2, 3] Based on the statistical projections shown in Figure 1-1, petroleum and other liquids will be the world's primary energy sources, fulfilling a third of the needs primarily for transportation and feedstock for chemical industries. Natural gas production will also increase, meeting 25% of all demands.[4] Coal currently provides about a third of global energy needs but the total share of coal in the world's energy consumption will decline to about 22% in 2040.[2, 3, 5] However, while there is a decline in the percentage contribution of coal to the total energy demand, Figure 1-1 shows that global coal consumption will remain flat, at about 9 billion short tons every year through the projected period.[2] Therefore, the use of natural gas, petroleum, and coal will be central to sustaining future technological development and industrialization, with coal still dominant in electricity generation across the globe.[5, 6]

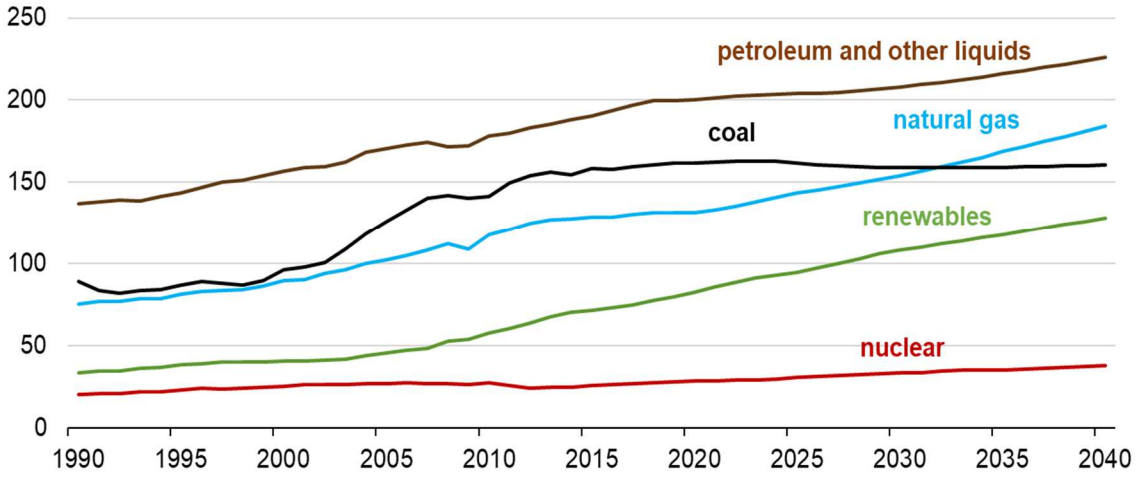

Figure 1-1. World energy consumption in quadrillion BTU by energy source. Source: www.eia.gov/ieo

1.1.2 The path to sustainable coal utilization and the role of fundamental studies

Electricity is the world's fastest growing form of end-use energy consumption.[7] Coal has been the main fossil fuel source for electricity and heat generation globally.[2, 4, 5] While the United States will see a decrease in its use of coal and an increase in the use of natural gas for electricity generation, many of the developing nations including India, China, and countries in Asia and Africa, will continue to rely on coal combustion for electricity generation because it is reliable, readily available, and cheap. Coal is a difficult fuel to consume efficiently and cleanly because its combustion involves complex multiphase reactions.[8, 9] Concerns are mounting about coal utilization as the largest contributor of greenhouse gases, sulphur oxides, and nitrogen oxides to the atmosphere[10-12] as well as about the environmental and health consequences of combustion-generated aerosols.[13-15]

According to a recent publication by the World Coal Association[16], India has grown its renewables sector, especially solar, by 81% in the most recent years. However, putting that growth in perspective, solar energy sources still provide only 1% of the electricity generated in India, a country with abundant solar energy. In an extreme case scenario, even if India's annual growth rates of all renewables are maintained above 10%, they are unlikely to constitute 10% of the primary energy mix before 2040.[5, 16] So, despite extensive investment in renewable alternative energy sources such as wind and solar, coal continues to be a key contributor to the primary energy mix. Thus, the reality is that we need to focus on addressing the key challenges of coal utilization by developing technologies for sustainable coal utilization. This approach will afford the world the use of its abundant coal resources without compromising the environment and with minimal impact of carbon dioxide (CO_2) emissions on global climate.[17, 18]

The key pathway to addressing these challenges, including greenhouse gas emission control, electricity generation efficiency improvement, and control of pollutants such as aerosols, nitrogen oxides, and sulphur oxides, is through a thorough understanding of the fundamental physical and chemical processes that occur during coal combustion.[8] Coal particle reactions are at the core of efficient combustion and are also the key rate-limiting steps controlling the formation of particulate matter, nitrogen- and sulphur-containing species. As part of the reactions in a furnace, particles undergo processes typically referred to as the early-stage processes of coal combustion. These processes, including particle heating, devolatilization, ignition, and mineral matter vaporization occur within the first few tens of milliseconds (less than 200 ms [19-21]). These processes are known to dictate char burnout, combustion efficiency, aerosol formation, and heat transfer.[22-26] Thus, fundamental studies on early-stage processes can lead to efficient designs of burners, improved heat transfer characteristics, and in-flame control of particulate formation.

1.2 Fundamental studies of the early-stage processes of coal combustion

There are three main characteristics of the near-burner regions of conventional pulverized coal boilers where the early-stage processes of coal combustion occur [27-30]: high particle concentrations, high gas temperatures, and an environment that transitions from reducing to oxidizing (herein termed reducing-to-oxidizing environment). Coal particles are fed into the boiler through the pulverizer, with a stoichiometric ratio significantly lower than one. The amount of air is limited for safety.[31] The coal particles are heated as they are fed into the boiler, with the moisture in the particles vaporizing as the particle temperature rises. Once sufficiently heated, coal particles are pyrolyzed. The released volatiles, because of group devolatilization, consume the oxygen in the near-burner region and create a reducing environment (described as very fuel rich zone in Fig. 1.2). Further downstream, the particles transition to an oxidizing environment.

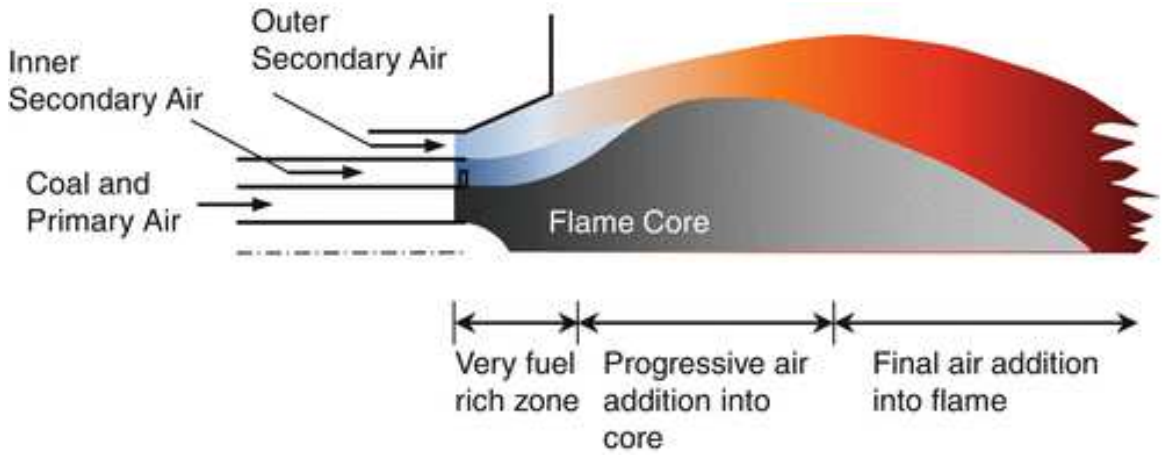

Figure 1-2. Near-burner region of a conventional pulverized coal boiler showing the fuel-rich zone through which particles must transition to oxidizing environments

Depending on the temperature and particle concentration, pyrolysis can consume as much as 80% of the total particle weight and can take place within a few milliseconds.[8, 32] The transition from a reducing zone to an oxidizing zone, coupled with a volatile concentration that may be beyond the flammability limits, can lead to delayed ignition. Since coal particles have a very short residence time in the boiler (about 2 to 3 seconds depending on the design of the boiler and coal quality [33]), an increase in the ignition delay time, even a few milliseconds, will negatively impact char burnout and combustion efficiency. Previously, it has been shown that the mechanism of ignition can also change depending on coal ranks, particle size, and gas temperature.[34-36] Since the reducing-to-oxidizing environment will affect where the coal particles ignite, it is expected to also influence the ignition mechanisms and delay times. Knowing the ignition behavior of coal particles (i.e., the prevailing mechanism of ignition and the characteristic delay time) is both important for efficient pulverized coal combustion in existing plants and for designing new burners for technologies such as Staged-Pressurized Oxy-Combustion (SPOC)[37], high-temperature air combustion (HiTAC) or moderate and intense low- oxygen dilution (MILD) [35], and high-temperature agent gasifier (HiTAG).[38, 39] In a conventional burner, no ignition delay is desired once the coal particles enter the boiler, leading to a preference for swirl burners where internal recirculation is strong. Thus, coal particles are well mixed with oxidizer streams in the high-temperature near-burner region, minimizing ignition delay time. For other technologies, such as HiTAC [40, 41], a long ignition delay time or no ignition at certain regions is desired, with the objective of creating flameless combustion. Here at Washington University in St Louis, the non-swirl (Type 0, axial-flow) burners for SPOC are designed to obtain a very short ignition delay time and self-sustained coal flames at elevated pressures. In summary, for any coal furnace technology, an understanding of the ignition behavior of the coal particles is quite important.

In addition to ignition, the reducing-to-oxidizing environment will affect the formation of submicron aerosols. Redox (reduction-oxidation) reactions can be significantly promoted in a reducing-to-oxidizing environment. As reported [27-29], if coal particles have enough residence time in a reducing zone at high-temperature conditions, refractory oxides in the mineral content of coal particles are reduced and can melt or form volatile suboxides. Once the suboxides interact subsequently with an oxidizing environment, they oxidize, become supersaturated, and then form particles by nucleation, followed by growth by condensation and coagulation. The activation of submicron particle formation through the suboxide pathway can significantly affect aerosol concentration and size distribution.[27] Thus, in addition to the gas-to-particle pathway from coal inorganic volatiles such as sodium and potassium, consideration for the redox reaction pathway may provide a more accurate description of submicron particle evolution.[29, 42] Hence, fundamental studies on aerosol formation as an early-stage process of coal combustion are also important for improving our understanding and designing new aerosol control methods.

1.3 Platforms for fundamental coal studies

Coal combustion in boilers is a chemically reacting flow in turbulent conditions. Thus, in addition to the phase change associated with coal combustion, there is a coupling between chemistry and eddies at various scales of turbulence. However, in a laminar environment with its characteristic smooth velocity, temperature, and concentration profiles, the degree of complexity can be greatly reduced, and fundamental insights into coal combustion can be inferred. As a result, many investigators over the years have preferentially studied ignition in laminar systems such as a drop tube furnace (DTF) [43-46], thermogravimetric analyzer (TGA) [47], laser-induced ignition apparatus [48], McKenna burner [49], and Hencken flat-flame burner.[35, 50-59] The results of these studies are quite different due to different heating rates, reactor types, and experimental conditions.[60]

Among the various setups, the Hencken flat-flame burner stands out as a particularly useful reactor for fundamental studies of ignition and submicron particle evolution.[20, 59-62] First, it is a reactor that can reach very high heating rates, similar to those in practical coal furnaces. Second, it provides a platform for considering the effect of residence time on early-stage processes of coal combustion; thus, ignition can be studied as a transient process in an active gas environment, as found in practical furnaces. Compared to other burners, such as the McKenna burner, the flat flames in a Hencken burner consist of surface-mixing diffusion flamelets. As a result, a wider range of downstream stoichiometries and temperatures can be obtained, and the Hencken burner does not suffer from sintering of the burner surface.[61, 63]

1.4 A novel two-stage Hencken burner

This dissertation presents a new Hencken flat-flame burner that is designed in a way to simulate coal particles going from a reducing environment to an oxidizing environment, which is characteristic of what coal particles experience in the near-burner region of pulverized coal boilers. The new two-stage Hencken burner is used to study coal ignition and aerosol formation. Evolution of submicron particles during the early-stage of coal combustion initiates ash deposition, which can severely reduce heat transfer to boiler tubes.[64, 65] The evolution of these aerosols depends on the particle composition and ignition behavior of coal particles, since ignition controls the release of both mineral and organic matter, which are the precursors for the submicron aerosols.

Extensive work has been done to improve our understanding of coal particle ignition, either in single particle ignition studies [33, 35, 45, 50-56, 66-68] or particle stream ignition studies.[57, 58, 69-72] But, to date, there are no studies that consider the effects of the reducing-to-oxidizing environment on ignition. Thus, using the two-stage Hencken burner, the effect of the reducing-to-oxidizing environment on coal particle ignition can be studied systematically. The typical condition for

fundamental ignition studies, as extensively reported in the literature, is a post-flame oxygen composition of a 20 mole% basis.[36, 44, 45, 73-77] In this dissertation, results of ignition in reducing-to-oxidizing atmospheres are compared to oxidizing atmospheres (i.e., 20-mole% oxygen), at two nominal gas temperatures of 1300 K and 1800 K. The gas temperatures are chosen to span the range typical of studies on early-stage coal combustion processes.

1.5 Dissertation outline

The dissertation can be broadly divided into two parts: ignition studies and aerosol formation studies. For ignition studies, results from single particle ignition experiments, single particle modeling, and coal stream ignition experiments are presented. For aerosol formation studies, the contribution of the organic volatiles vs. the inorganic volatiles (i.e., mineral sources) to the submicron particle evolution during early-stage of coal combustion is presented. Experiments on aerosol formation from biomass combustion using the Hencken flat-flame burner are rare. In an attempt to fill this research gap, early-stage processes of ignition and aerosol formation during wheat straw biomass combustion are investigated. The effects of water-washing of wheat straw biomass, and the early-stage release of potassium, on ignition and aerosol formation are specifically studied. The findings from this work on submicron particle formation will provide insights that will guide more comprehensive studies on the formation, composition, and characteristics of ash. The dissertation is divided into seven tasks:

1. Design and characterize a new two-stage Hencken burner with a reducing-to-oxidizing environment. Chapter 2 presents the process involved in the design of the burner and provides information on the instrumentation and results of characterization.
2. Evaluate the effect of the reducing-to-oxidizing environment in different nominal gas temperatures on single particle ignition. As a proof-of-concept study and under various

conditions, Chapter 3 presents the findings on single particle ignition using a 125-149 μm particle size range.

3. Study the effect of particle size and the importance of classifying coal particles into narrow size ranges in single particle ignition investigations. (See Chapter 4).
4. Study the significance of particle size and the reducing-to-oxidizing environment on pulverized coal stream ignition at different gas temperatures (Details in Chapter 5).
5. Computationally model single particle ignition to compare the ignition behavior of a coal particle in an oxidizing environment to that in an environment with a reducing-to-oxidizing environment. (See Chapter 6).
6. Perform a study on submicron particle formation during the early-stage of pulverized coal combustion, using the two-stage Hencken burner. The results are presented in Chapter 7.
7. Evaluate the effects of water-washing on ignition and submicron particle emission during biomass combustion, with specific focus on the role of early-stage release of potassium on ignition delay and the mineral composition of particulates (See Chapter 8).

Key conclusions and recommendations for future work are itemized and explained in Chapter 9. Appendix A contains MATLAB codes written for the various tasks in this dissertation, including codes for 1) single-particle emission intensity extraction, 2) simultaneous determination of particle size and ignition delay time, 3) group particle emission intensity extraction, and 4) single particle combustion modeling.

Chapter 2

Design and characterization of a novel two-stage Hencken burner

2.1 Introduction

As mentioned in Chapter 1, in pulverized coal (pc) burners, coal particles usually transition from a locally reducing environment to an oxidizing environment. Such a "reducing-to-oxidizing" environment can influence combustion processes such as ignition, particulate formation, and char burnout. To understand these processes at a fundamental level, a system is desired that mimics such a transition from a locally reducing environment to an oxidizing environment. Hence, a new two-stage Hencken burner is developed that allows coal particles to experience a reducing environment followed by a transition to an oxidizing environment. This work presents the design as well as the characterization of this new two-stage Hencken burner and its new coal feeder.

2.2 Burner design and characterization

2.2.1 Two-stage Hencken flat-flame burner description

A Hencken flat-flame burner is a multi-element non-premixed laminar burner with a heating rate similar to that of conventional pc burners[56, 60, 78] and wide global "lean" and "rich" flammability limits. This design provides for more operational flexibility with respect to the hot gas environment, without the need to cool the tubes that make up the burner.[78] A typical Hencken burner used in coal studies has a central tube for injection of coal, surrounded by many flamelets

that can yield the desired post-combustion temperatures and compositions.[20, 52, 59] Conventionally, Hencken burners are designed so that fuel flows through hypodermic tubes that are arranged into a stainless-steel honeycomb, and the oxidizer flows through the honeycomb channels that are not occupied. Figure 2-1 shows a view of this arrangement.[79] The result provides rapid mixing of the fuel and oxidizer streams downstream of the burner surface, yielding a planar reaction zone and producing a steady stream of equilibrium products above the reaction zone.[79] Operation of the Hencken burners usually results in a slight lifting of the reaction zone from the burner, creating a nearly adiabatic condition.[80] Another important benefit of the Hencken design in this configuration is that the small passageways and low volumetric flow rates promote laminar and uniform flow over the entire area (i.e., a low Reynolds number).[80] Also, since the flames produced by the burner are short, no special effort is needed for flame stabilization. Given these characteristics, the Hencken burner is a suitable platform for fundamental studies of coal combustion.

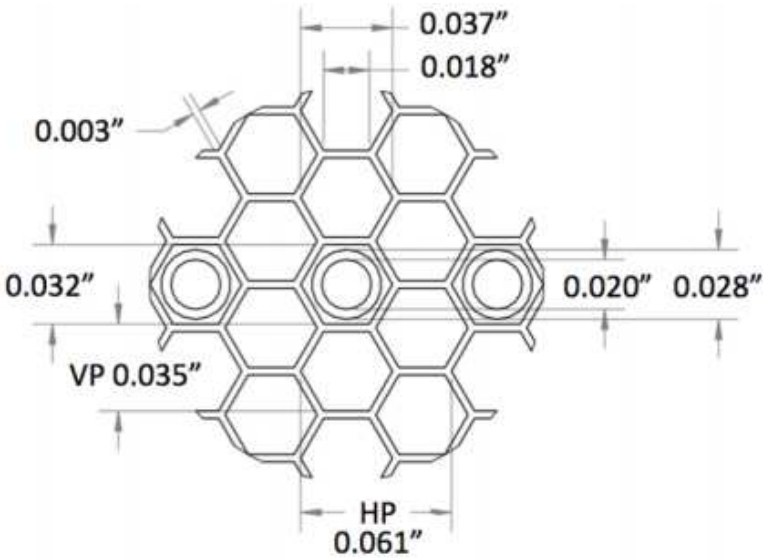

Figure 2-1. A view of the honeycomb mesh with small fuel tubes inserted. VP stands for vertical pattern and HP stands for horizontal pattern.

Different from other flat-flame burners, the new burner has two flat-flame configurations (inner and outer); hence the name two-stage Hencken flat-flame burner (Figure 2-2). A central 14-mm ID stainless steel tube separates the inner flame zone from the outer flame zone. The up-fired burner, used in this research, is designed with a circular cross section to ensure symmetry in temperature and gas composition. The circular cross section is another key improvement of the Hencken burner design over others in the literature which are typically square in cross section. The burner pieces, the fuel tubes, and the honeycomb are made of stainless steel because of its chemical integrity and high melting point.

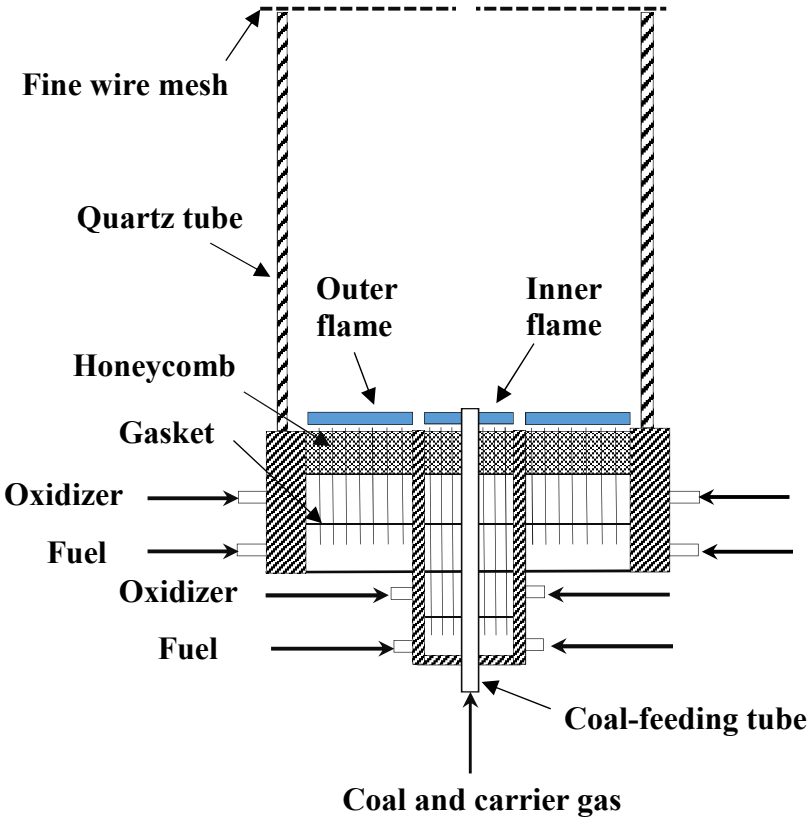

Figure 2-2. A cross-section of the two-stage Hencken flat-flame burner, showing the inner and outer flames

The burner, with an 80-mm diameter, is composed of 570 hypodermic tubes creating an equivalent number of non-premixed flamelets. The hypodermic tubes all have internal diameters of 1.2 mm. The tips of the tubes rise above the surface of the honeycomb mesh to keep the flamelets away from the honeycomb surface. Hence, the oxidizer stream cools the walls of the tubes. The tips of the tubes above the surface of the honeycomb mesh also facilitate alignment of the burner for optical access, an important consideration for subsequent chapters on ignition. Fuel and oxidizer gases are introduced into separate chambers and are isolated by gasket materials. There are four chambers in the burner. Fuel for the inner flame enters from the bottom chamber and is delivered to the burner surface through eighteen fuel tubes. These tubes are sealed on the gasket to prevent mixing between fuel and oxidizer streams. The oxidizer stream for the inner flame is delivered to the chamber above the bottom fuel chamber. This sequence of bottom-fuel-chamber, top-oxidizer-chamber is repeated for the outer flame; hence, combustible mixtures can occur only downstream of fuel tube outlets.

A central tube with a 2 mm ID passes through the burner for solid fuel feeding. The central tube is set to about 2 mm above the hypodermic tubes. So, in all experiments, the zero value is defined to be at the top of the central tube. A quartz tube (150 mm in height) is set above the burner to isolate the burner from the outside environment, decrease heat loss, and provide optical access. A fine stainless-steel wire mesh on top of the quartz tube minimizes disturbances from ambient air and ensures steady convective flow of the post-flame gases. The wire mesh has slots for inserting a thermocouple and gas sampling probe into the burner for measurements. The probe is connected to Horiba PG-250 gas analyzer, which measures the post-flame O_2 concentration based on the galvanic cell method. In this method, gold is used as the anode and lead as the cathode with potassium hydroxide as the electrolyte. When a suitable load resistance is connected to the

electrodes, gas passes through a permeable membrane and the oxygen inside such gas is reduced by the anode to form hydroxide ions. Thus, the electromotive force generated by the electrochemical reaction is measured and the oxygen concentration is determined.

2.2.2 Gas supply

Airgas and Praxair Inc. supplied chemical grade gases and liquids. Rotameters are used to control gas flows. All rotameters are calibrated prior to use, and periodic several-point checks are conducted to ensure consistency in flow rates. A supply pressure of 20 psig is used on each gas line. Gases flow to the four chambers in the two-stage Hencken burner, with each chamber supplied with nitrogen gas for purging prior to experimental runs and for control of gas temperatures and compositions.

2.2.3 Gas temperature measurements

Fine bare wire thermocouples, supported by a ceramic tube, are widely used in measuring flame temperatures because of their simplicity, cost-effectiveness, good response time, and high spatial resolution.[81-83] The measurement is based on convective heat transfer from the gas phase to the thermocouple bead. As a result, the gas temperature determined from the measured bead temperature is prone to error from two other modes of heat transfer, i.e., conduction and radiation. The accuracy of temperature measurement, especially in a high-gas temperature environment, is dependent on the relative magnitude of radiative heating in comparison to the convective heating on the bead surface. In other words, the heat from the gas is conducted and radiated, and some energy is stored in the thermocouple itself. In the steady state, the rate of change of energy stored in the thermocouple must be zero, as illustrated in Eq. (1):

$$Q_{conv} + Q_{rad} + Q_{cond} = 0 \qquad (2.1)$$

where Q_{conv} is the convective heat to the thermocouple bead, Q_{rad} is the radiation heat energy, and Q_{cond} is the conduction heat energy. Expressed in terms of the bead temperature, T_b, and the lead/base temperature, T_{base}, Eq. (2.1) becomes

$$h_g A_{surf}(T_g - T_b) - \varepsilon_b \sigma A_{surf}(T_b^4 - T_w^4) - \frac{k_b A_c}{L}(T_b - T_{base}) = 0 \tag{2.2}$$

where h_g is the convective heat transfer coefficient, A_{surf} is the surface area of the bead, A_c is the cross sectional area of the bead, L is the lead wire length, k_b is the thermal conductivity, d_b is the bead diameter, ε_b is the emissivity and σ is the Stefan-Boltzmann's constant. Thus, the difference between the true gas temperature, T_g, and the measured bead temperature, T_b, is given by:

$$T_g - T_b = \frac{1}{h_g}\left(\varepsilon_b \sigma (T_b^4 - T_w^4) + \frac{k_b d_b (T_b - T_{base})}{4L^2}\right) \tag{2.3}$$

Most studies usually neglect conduction loss in comparison to radiation. Heat is transferred by conduction from the bead to the thermocouple wire or lead, and the loss is directly proportional to the difference between the bead temperature and the lead/base temperature. On the other hand, radiation loss has a fourth power dependence on the gas temperature. Still, previous studies [81, 82] have also shown that conduction losses in Eq. (2.3) can be significant depending on wire diameters, wire length, and the difference between the bead temperature and the base temperature. With the Y-shaped butt-welded thermocouple design shown in Fig. 2-3, both radiation and conduction losses can be minimized since it is designed to have a small bead size, a thin wire diameter, a long wire length [81, 84], and a minimal temperature difference between the bead temperature and the base temperature (See Eq. 2.3). A two-hole ceramic tube is used to support 200 μm thermocouple bare

wires, and 50 μm lead wires are welded to the proper ends, positive or negative, of the 200 μm thermocouple wires. The 50 μm lead wires are fusion-welded together to form a thermocouple with an ~80 μm bead diameter. For all the nominal gas temperatures considered, the deviation from the true gas temperatures range from 12 K to 62 K.

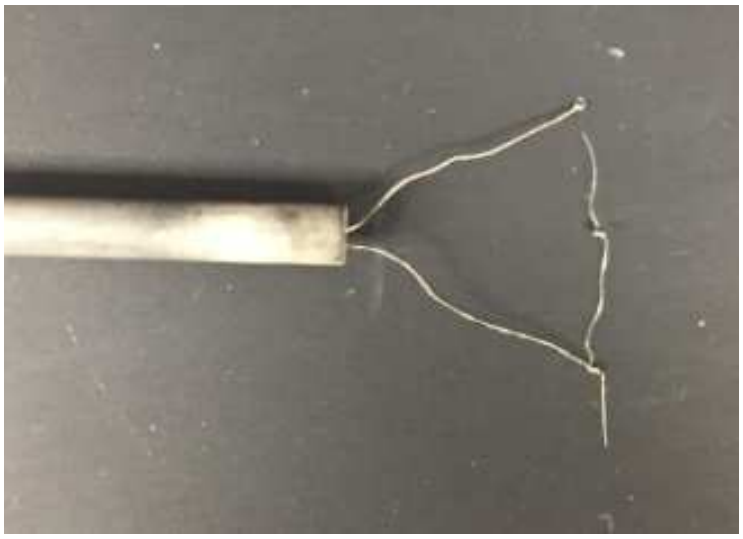

Figure 2-3. Y-shaped butt-welded thermocouple, used for flame characterization

2.2.4 Normal and inverse flame configurations

For this study, the fuel is methane and the oxidizer is a mixture of O_2 and N_2. The burner is tested under two configurations, both of which have post-flame oxygen concentrations of about 20% on a wet basis. In one configuration, the mixture of O_2 and N_2 is fed through the unoccupied honeycomb channels, and the fuel is fed through the tubes. This is referred to as the normal flame configuration. Alternatively, if the oxidizer is introduced through the tubes and the fuel through the unoccupied honeycomb channels, this is an inverse flame configuration. Either way, the flame structure can be characterized by the stoichiometric mixture fraction, Z_{st} [85-90], given by Eq. (2.4).

$$Z_{st} = (1+Y_{F,0}W_O\upsilon_O/\ Y_{O,0}W_F\upsilon_F)^{-1}, \quad (2.4)$$

where Y denotes the mass fraction, W is the molecular mass, and υ is the stoichiometric coefficient. The subscripts F, O, and 0 refer to the fuel stream, oxidizer stream, and inlet state respectively. For the methane/air diffusion flame, this stoichiometry is given by Eq. (2.5).

$$CH_4 + 2O_2 + 7.52N_2 \longrightarrow \text{products} \quad (2.5)$$

If the stoichiometry in Eq. (2.5) is maintained, nitrogen can be introduced with the fuel only, with the oxidizer only, or split between both the fuel and the oxidizer, all without a change in the adiabatic flame temperature. However, the flame structure, which refers to the relationship between the local temperature and the local gas composition, is altered.[86] Pure CH_4 burning in an O_2/N_2 mixture corresponds to the lowest Z_{st}, and CH_4/N_2 burning in pure O_2 corresponds to the highest. A high Z_{st} yields more oxygen-containing species and less fuel-based species in the high temperature reaction zone. Several studies have demonstrated that increasing Z_{st} by oxygen enrichment and fuel dilution can inhibit soot formation in diffusion flames, even at high temperatures.[89, 91, 92] High Z_{st} can also lead to stronger flames with more resistance to extinction, resulting in a greater extinction scalar dissipation rate and lower extinction temperature.[85] Based on this flame-design theory, normal and inverse diffusion flames corresponding to low Z_{st} and high Z_{st} are considered in this work.

Studies using a Hencken burner for fundamental coal studies typically report the axial profiles of temperature and oxygen concentration along the centerline of the burner, operated in low Zst mode.[45, 93, 94] However, coal particles are dispersed in a jet, expanding out from the coal feed tube. Therefore, a more detailed characterization, including radial profiles, is needed to describe the burner accurately. Also, a radial profile characterization can provide information on the axial diffusion length over which the radial flatness assumption holds. Thus, results from burner

characterization are presented here, including axial and radial profiles, to establish the degree of uniformity and radial flatness that are attainable in the new two-stage Hencken flat-flame burner.

2.3 Oxidizing flame characterization

2.3.1 Flame characterization at low Z_{st}

Pulverized coal particles in the near-burner region typically experience combustion environments with high local gas temperatures[30], and most fundamental studies that use the Hencken burner to study the early stage of coal combustion are conducted up to 1800 K.[52, 59, 60, 62] Table 2-1 presents the flow rates in standard conditions, with the corresponding superficial gas velocities. Here, three nominal gas temperatures of 1300 K, 1600 K, and 1800 K are achieved by adjusting the flow rates of the fuel and the oxidizer gas streams. The cold superficial flow gas velocities for the inner and outer flames are kept nearly equal to avoid shear-induced radial momentum transfer that can be caused by radial velocity gradients. Three gas temperatures are evaluated at a fixed oxygen concentration of 20%, and all reported oxygen concentration measurements are within 10% standard deviation.

Table 2-1. Flow rates and superficial gas velocities in oxidizing environment

Temperature (K)	Flame	Volumetric flow rates (SLPM)				Superficial Gas velocity (m/s)
		CH_4	Fuel N_2	O_2	Oxidizer N_2	
1300	inner	0.10	-	0.90	1.74	0.24
	outer	2.86	6.54	23.82	33.33	0.23
1600	inner	0.27	-	1.13	1.74	0.28
	outer	3.60	6.54	25.51	31.18	0.23
1800	inner	0.35	-	1.04	1.64	0.27
	outer	6.86	15.90	37.71	33.33	0.32

Figure 2-4 shows measured centerline temperatures and oxygen compositions for nominal gas temperatures of 1300 K, 1600 K, and 1800 K. The centerline temperatures remain fairly constant above 2 cm height for all temperatures. The lower temperatures below 2 cm are due to the presence of the cold nitrogen carrier gas in the central tube that is used to transport coal particles. A fixed carrier gas flow rate of 130 cm^3/min is used for all conditions, thus, its influence on centerline gas temperatures decreases near the burner as the nominal gas temperature increases from 1300 K to 1800 K.

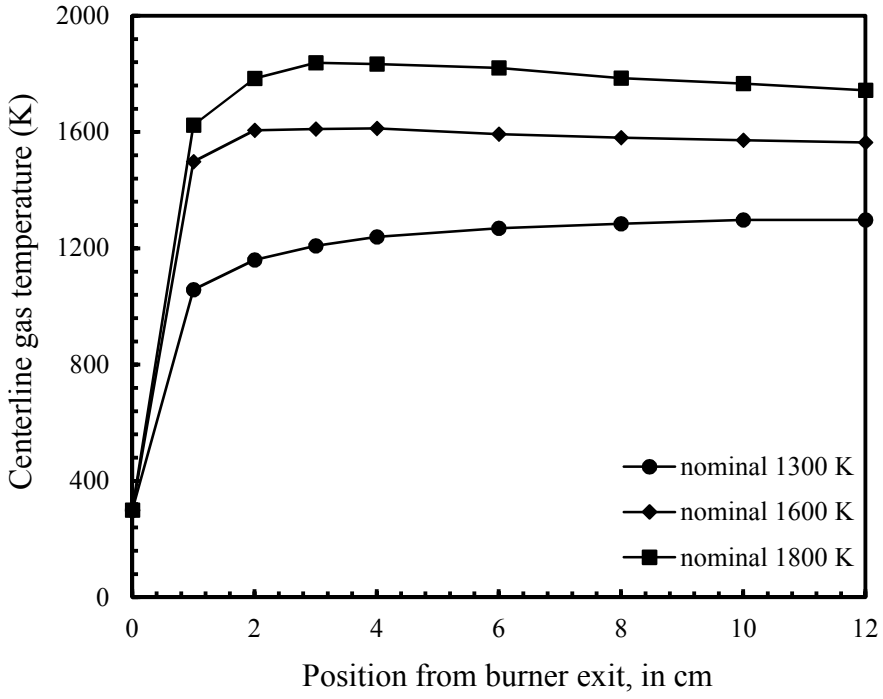

Figure 2-4. Measured centerline gas temperature profile, with the burner exit at 0 cm

Figure 2-5 shows that the profiles of oxygen composition for the three different temperatures follow similar trends. Thus, with such a relatively constant oxygen concentration profile, the effect of post-combustion gas temperatures on ignition and aerosol formation can be studied using the new two-stage Hencken flat-flame burner.

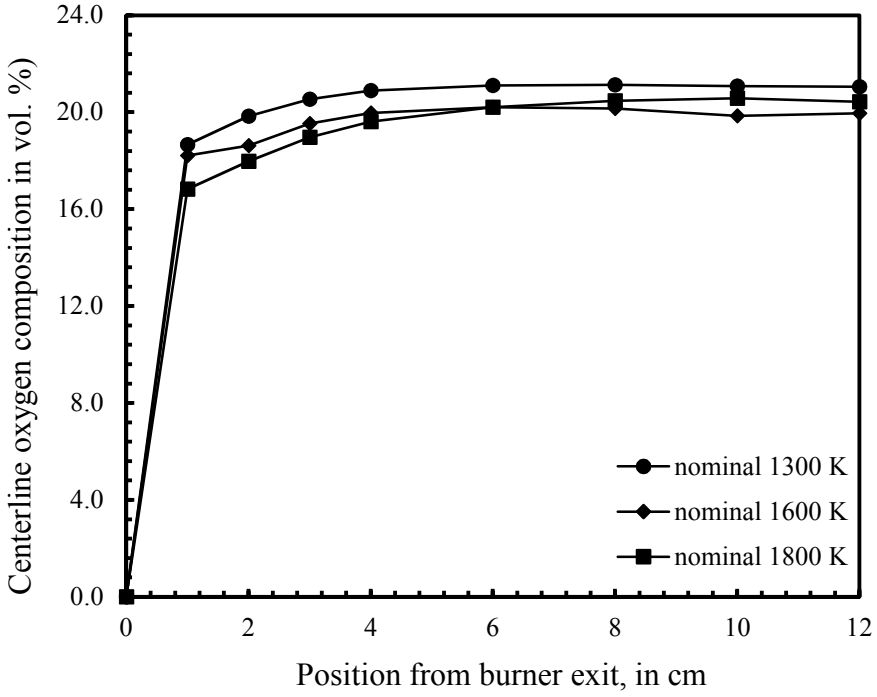

Figure 2-5. Measured centerline oxygen concentration profile, with the burner exit at 0 cm.

Experimental measurements were taken radially over 30 mm. The inner flame spans the region between -7 mm to +7 mm, with the central tube corresponding to the zero position. Radial measurements are taken at four axial positions (1, 3, 6, and 9 cm from the burner exit). In Fig. 2-6, black symbols represent measured gas temperatures for a nominal 1300 K condition at different

axial positions while the blue symbols represent measured gas temperatures for a nominal 1800 K gas condition at the same axial positions. The experimental data show that the post-flame combustion environment is symmetric about the central tube and that the radial flatness usually assumed for a Hencken burner is a valid assumption. The deviation from the desired nominal temperature is within ±150 K.

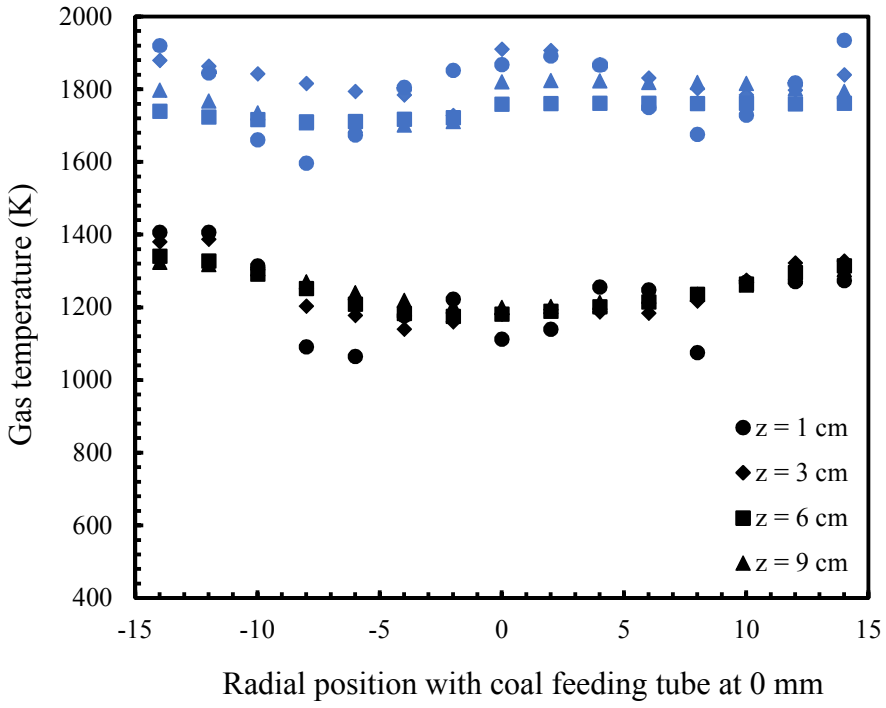

Figure 2-6. Measured radial gas temperature profile for nominal 1300 K (black symbols) and 1800 K (blue symbols) gas conditions. z is vertical height above burner exit.

For measurements at 1 cm above the burner exit, there are low temperature regions at radial positions between 6 to 10 mm and -6 to -10 mm, due to heat loss to the central 14-mm ID stainless steel tube that separates the inner flame and the outer flame. These low temperatures in Fig. 2.6,

which deviate from nominal value up to 225 K, and the high oxygen compositions observed for 1300 K (Fig. 2-7) and 1800 K (Fig. 2-8) near this central 14-mm ID tube, are due to the absence of combustion over the tube. Above the 1 cm axial position for both nominal gas temperatures, the profiles are symmetric radially and uniform axially with height above the micro-diffusion flames. Thus, the results in Figure 2-6 to Figure 2-8 show that the two-stage Hencken burner is suitable for fundamental studies of coal combustion when the micro-diffusion flames are operated in the normal flame configuration (i.e., at low Z_{st}).

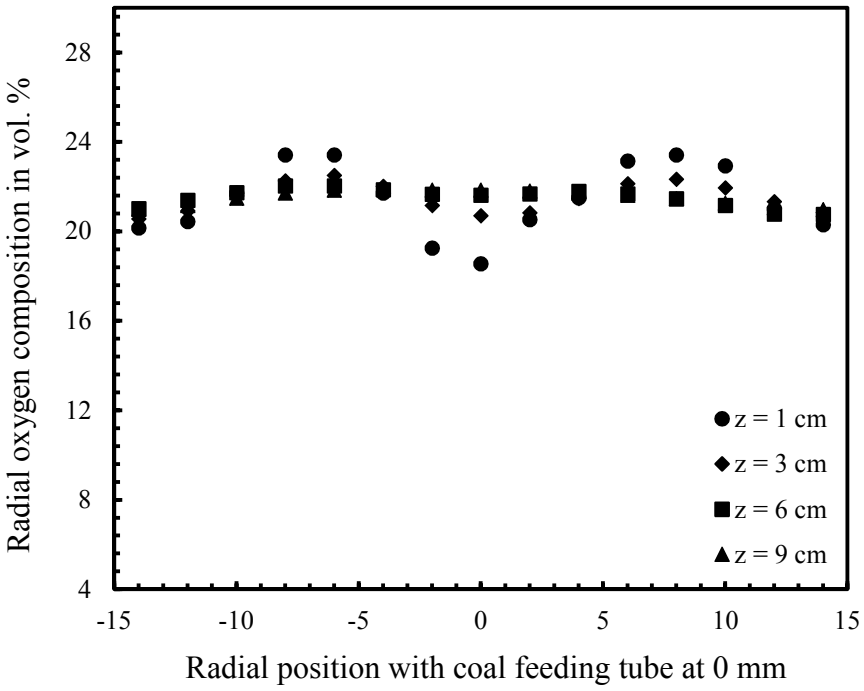

Figure 2-7. Measured radial oxygen composition for a nominal 1300 K gas temperature

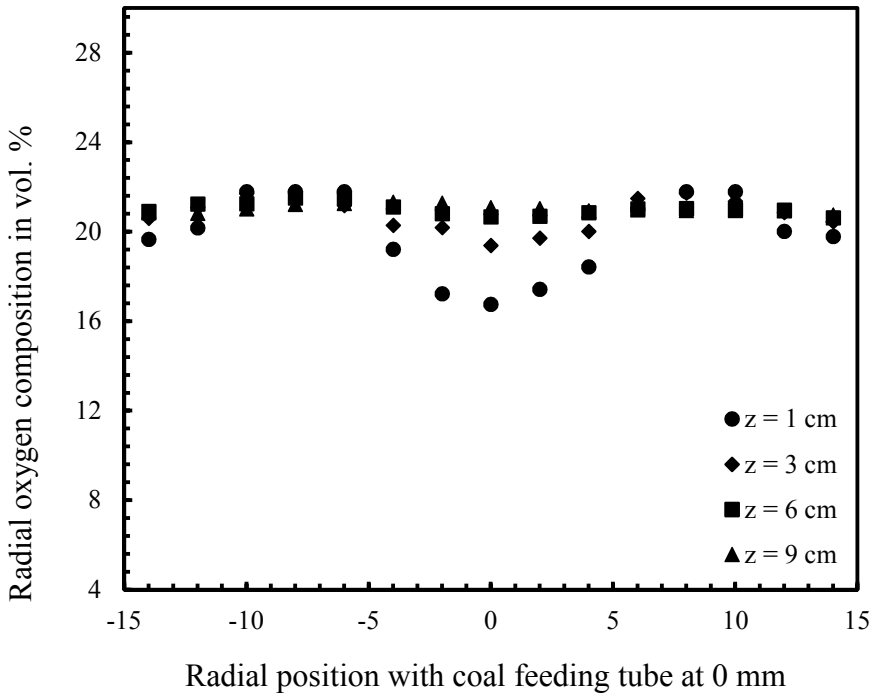

Figure 2-8. Measured radial oxygen composition for a nominal 1800 K gas temperature

2.3.2 Flame characterization at high Z_{st}

Low Z_{st} flames are prone to soot formation, particularly when using sooty fuels, such as ethylene.[95] On the other hand, high Zst inhibits soot formation.[89, 91, 92] Thus, high Zst flames can provide a soot-free system in the Hencken burner even at very high temperatures and with sooty fuels. Figure 2-9 shows flame images taken for two different flame configurations. The high Z_{st} flame (Fig. 2-9a) has no yellow emissions while the low Z_{st}-normal flame (Fig. 2-9b) shows a slightly yellow flame. Since methane is not a sooty fuel, yellow emissions are not particularly obvious in the high Z_{st} flame. But if sooty fuels were to be used, it suffices to say that soot from the micro-diffusion flames can interfere with the soot formed from coal volatiles during the early-stage of coal combustion, thus making it difficult to interpret experimental data on ultrafine particle

size distribution. Therefore, a high Z_{st} flame configuration would be more appropriate in a scenario where both sooty fuels and high-temperature gas environments are desired in a Hencken flat-flame burner.

In the normal, low Z_{st} flame configuration, the mixture of O_2 and most of the N_2 dilution gas is fed through the honeycomb, and CH_4, with a little dilution gas, is fed through the tubes. In other words, the smaller flowrate is fed through the 1.2 mm ID tubes and the larger flow rate through the larger area of the honeycomb. If a high Z_{st} flame were operated in the normal configuration, the oxygen enrichment and fuel dilution would imply that a larger gas volume must flow through the 1.2 mm ID tubes with small area, making it difficult to obtain a stable flame. To address this concern, an inverse flame configuration is used for a high Z_{st} flame in the Hencken burner. In the inverse flame configuration, the fuel mixture is fed through the unoccupied honeycomb channels, as opposed to the tubes. For high Zst, the flow rates remain the same as in Table 2.1 since the only change is that the nitrogen for dilution is moved from oxidizer side to fuel side.

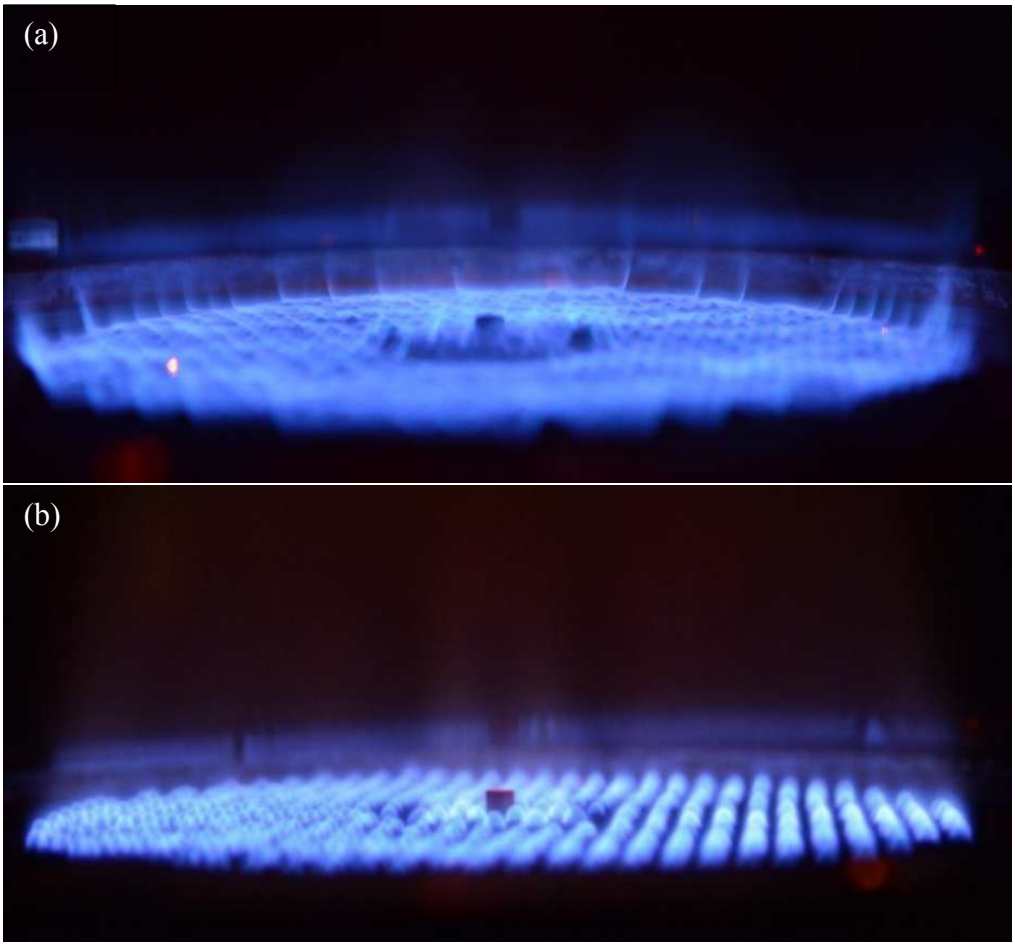

Figure 2-9. 1800 K flame images, comparing (a) high Z_{st} and (b) low Z_{st} flame configurations

Figure 2-10 and Fig. 2-11 show the centerline temperature and oxygen concentration measurements for the low Z_{st} and high Z_{st} configurations respectively. Since nitrogen gas is used as the coal carrier gas at the center, the oxygen concentration at burner exit is zero. The results for both flame configurations are similar and agree well. These uniform profiles demonstrate that the two-stage Hencken burner can be used in both the inverse and normal flame configurations.

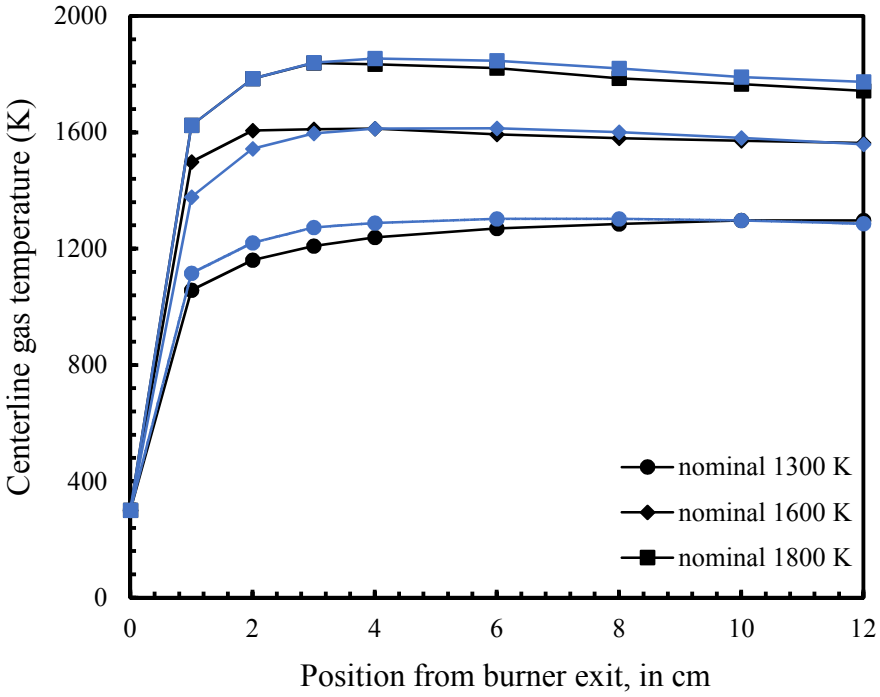

Figure 2-10. Comparison of centerline gas temperature for low Z_{st} (black lines) and high Z_{st} (blue lines) flame configurations

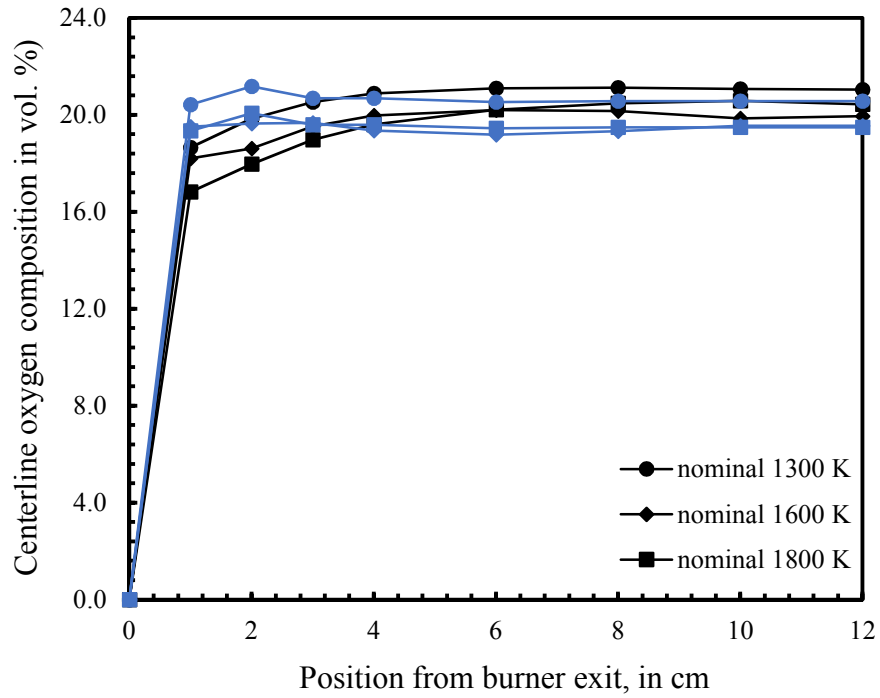

Figure 2-11. Comparison of centerline gas temperature for low Z_{st} (black lines) and high Z_{st} (blue lines) flame configurations

2.4 Reducing-oxidizing flame characterization

In a typical pulverized coal burner, the coal particles experience reducing environments in regions of high volatile release, despite the oxygen supplied to the coal carrier gas (primary oxidizer). Based on the approach described in the literature[96], a representative elemental composition of the volatile stream can be obtained from the coal ultimate and proximate analyses presented in Table 2-2. The approach involves subtracting the fixed carbon content given in the proximate analysis from the carbon content given in the ultimate analysis, with both quantities evaluated on a dry, ash free basis. The resulting quantity is the amount of carbon contained in the volatile. From this analysis, the C:H:O ratio that characterizes a reducing environment is approximately 2:3:1, with the oxygen content in the primary oxidizer. Thus, the inner flame composition was adjusted to give a reducing environment with this desired characteristic C:H:O ratio.

Table 2-2. Proximate and ultimate analysis of PRB sub-bituminous coal.

Proximate analysis (%wt)				Ultimate analysis (%daf)					HHV
M	VM	FC	Ash	C	H	O	N	S	(MJ/kg)
10	39	42.87	8.14	74.66	5.45	18.24	1.08	0.57	27.45

For convenience in comparing the effects of a reducing-to-oxidizing (R-O) atmosphere on combustion processes at different temperatures, the centerline height for the transition from the reducing to the oxidizing atmosphere is maintained at 2 cm for all temperatures. Depending on gas temperature, a height of 2 cm corresponds to an average residence time of 10 to 20 ms in the two-stage Hencken burner. The average residence time of particles in the near-burner region of a

pulverized coal boiler is about 10 to 20 ms.[97] Also, ignition occurs at these time scales, an average residence time of 10 to 20 ms was deemed appropriate for characterizing the two-stage Hencken burner. Table 2.3 presents the flow rates in standard conditions for the reducing-to-oxidizing atmosphere.

Table 2-3. Flow rates and superficial gas velocities in reducing-to-oxidizing environment

Temperature (K)	Flame	Volumetric flow rates (SLPM)			
		CH_4	Fuel N_2	O_2	Oxidizer N_2
1300	inner	0.13	-	0.23	1.86
	outer	2.86	6.54	23.82	33.33
1600	inner	0.16	-	0.22	1.74
	outer	3.60	6.54	25.51	31.18
1800	inner	0.27	-	0.29	1.74
	outer	6.86	15.90	37.71	33.33

Figure 2-12, Fig. 2-13, and Fig. 2-14 show the results of post-flame characterization for 1300 K, 1600 K, and 1800 K respectively. The results presented in these figures are the centerline temperatures and oxygen mole percentages in reducing-to-oxidizing (R-O) flame conditions, and further contrast the results with those of oxidizing (O) flame environments. The centerline temperature profiles for the R-O transition match with those of the oxidizing atmospheres for the 1600 K and 1800 K flames, to within 100 K difference. For the 1300 K gas flame, the temperature is about 200 K lower at 1 cm and about 200 K higher at 2 cm. Thus, the stoichiometric flame location at the 2-cm height influences the temperature profile below and at the reducing-to-oxidizing environment location more conspicuously at the low temperature of 1300 K. With the

results in Figure 2-12 to Figure 2-14, the O_2 concentrations in all the reducing-to-oxidizing environments remain very similar and peak at about 12 to 14 % on a volume basis. Well-controlled R-O and oxidizing flames at all temperatures are obtainable in the newly designed flat-flame burner. Thus, the new two-stage burner setup can be used effectively to evaluate the effect of this reducing-to-oxidizing environment on coal ignition.

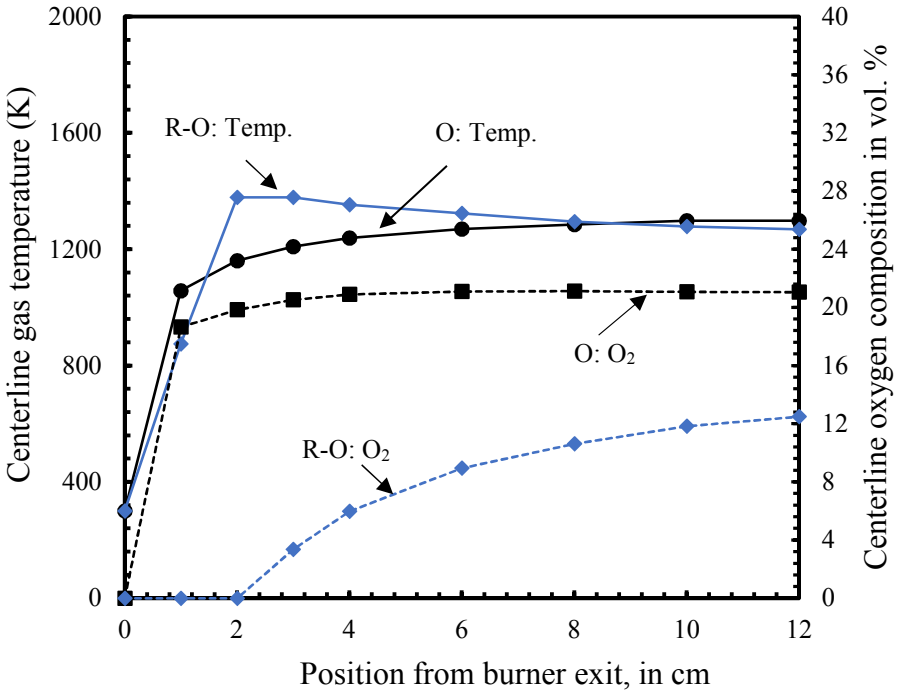

Figure 2-12. A plot of centerline gas temperatures and oxygen compositions for a nominal 1300 K gas condition with either an inner-oxidizing flame (black lines) or an inner-reducing flame (blue lines)

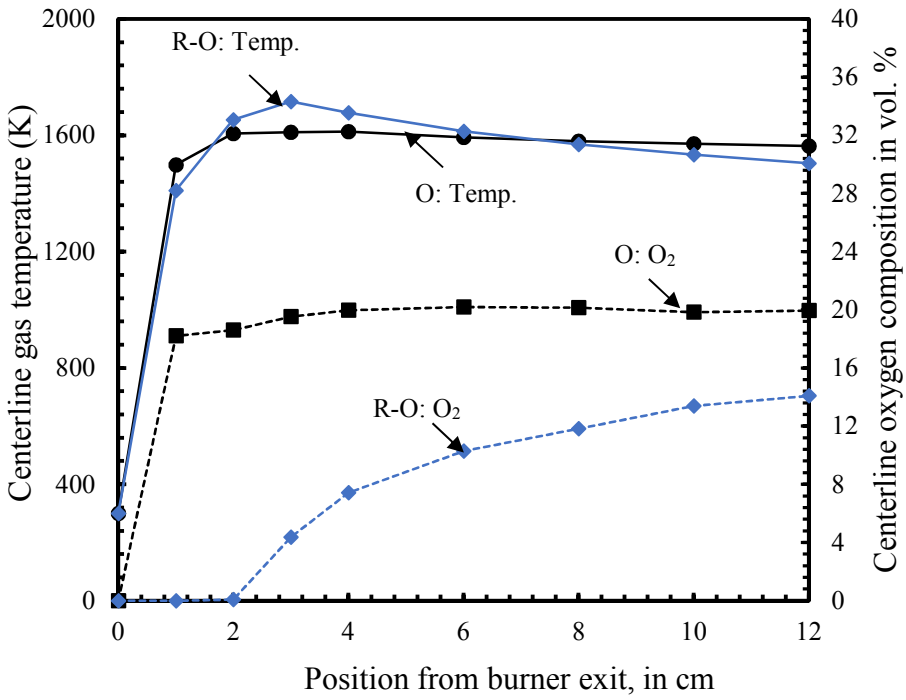

Figure 2-13. A plot of centerline gas temperatures and oxygen compositions for a nominal 1600 K gas condition with either an inner-oxidizing flame (black lines) or an inner-reducing flame (blue lines)

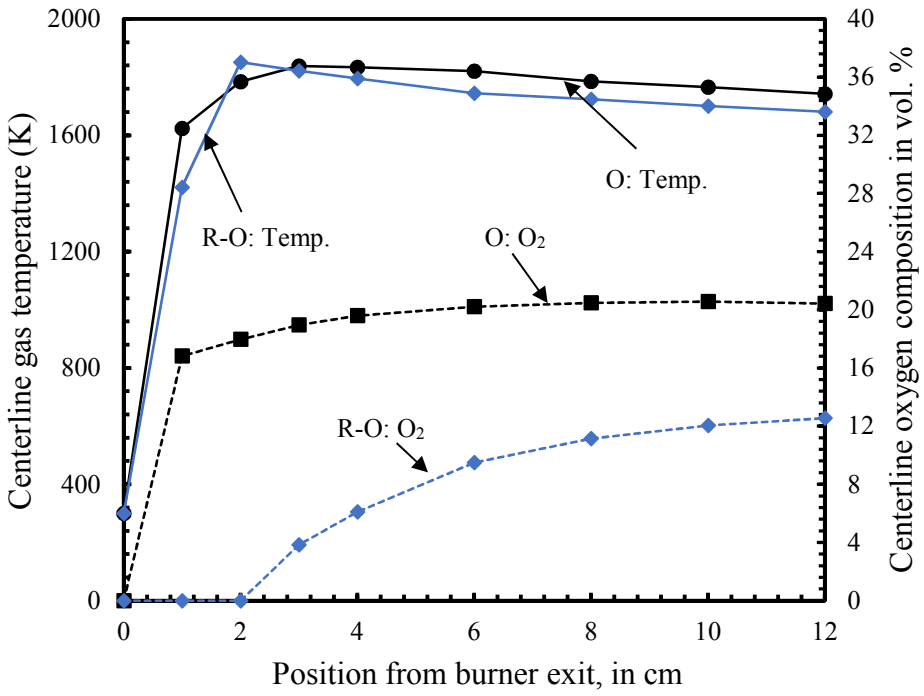

Figure 2-14. A plot of centerline gas temperatures and oxygen compositions for a nominal 1800 K gas condition with either an inner-oxidizing flame (black lines) or an inner-reducing flame (blue lines)

Figure 2-15 shows high-resolution images of the inner reducing flames and the outer oxidizing flames for the three nominal gas temperatures. Due to increase in temperature from 1300 K to 1800 K, the volume and radial spread of the hot gas corona around the flame location increases. While temperature is the primary cause of the spread away from the flame front, Dufour effect will also be stronger as temperature increases since flow rates increase with temperatures. This effect is caused by the sharp local concentration gradient between the inner-reducing and outer-oxidizing post-flame gas compositions. The result is hot combustion gases from the outer post-flame diffusing to the flame sheet. Heat energy is also transferred as species diffuse to the flame location, thus the corona around the flame location is created by both mass and thermal diffusion due, respectively, to a temperature gradient and a concentration gradient.

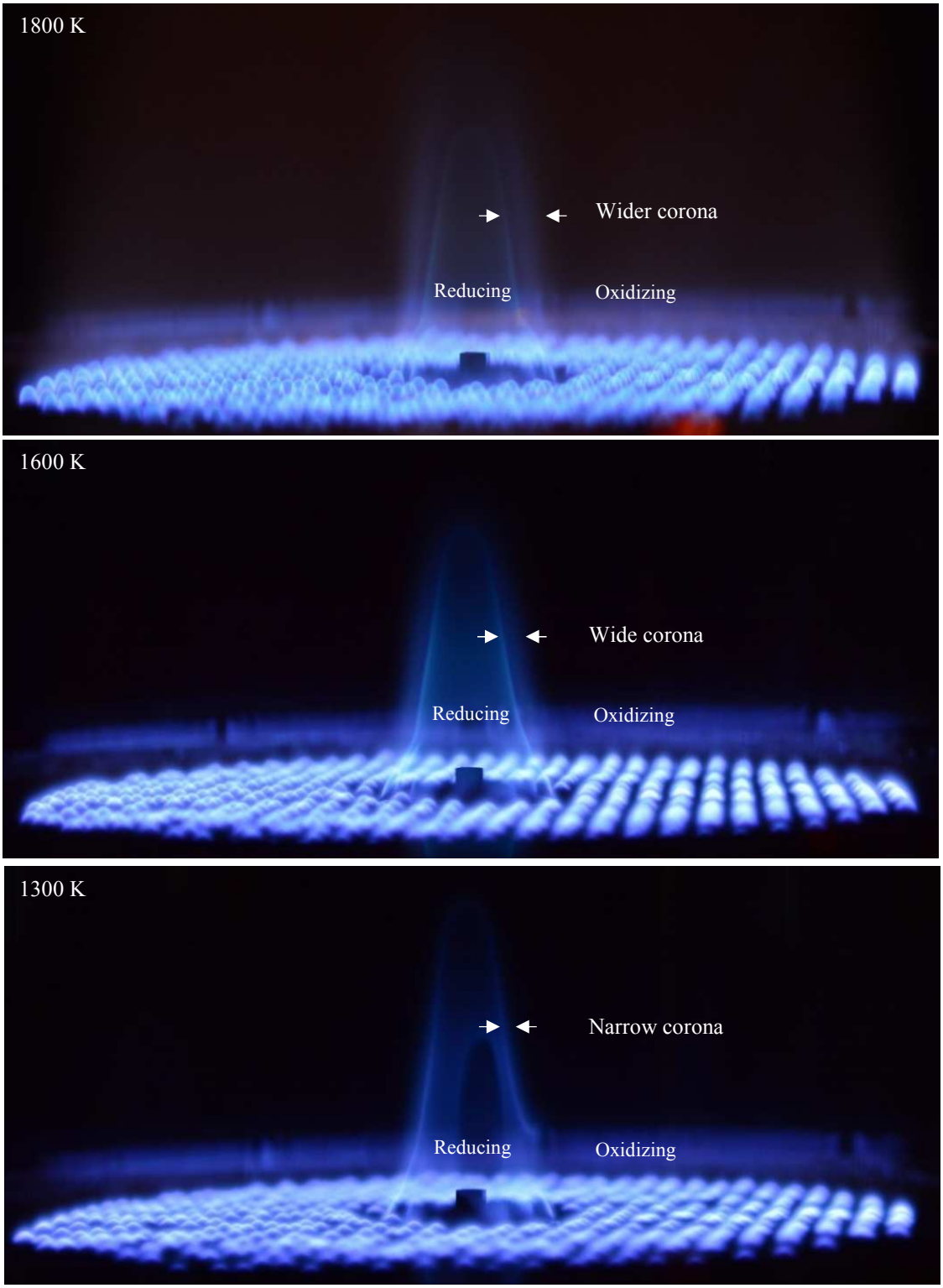

Figure 2-15. High resolution images of the reducing-to-oxidizing flames

2.5 Coal feeding system

There have been recent efforts to develop new particle feeders with well-dispersed coal particle streams for fundamental coal combustion studies. Yuan et al. [60] developed a novel particle feeder based on the principle of deagglomeration. In his design, a programmable piezoelectric ceramic plate vibrates the outlet of a syringe tube containing the coal particles. The high frequency vibration leads to particles impacting the wall of the syringe and then deagglomerating. Relatively good dispersion was achieved, with a feed rate of ~70 mg/min and a variance less than ±15%. Kim et al. [52] used a syringe pump to drive particles into a container at a known rate. A fixed nitrogen flow was then introduced into the container. Both feeders were not designed to supply steady particle feeding over the wide range necessary to evaluate single particle and coal stream ignition experiments. In addition, the requirement that the particles must be dried before being fed into the burner further limits the direct interpretation of ignition time scales, since moisture vaporization is not accounted for in the initial particle heating stage.

Hence, a new particle feeder is designed in this work that can be used to feed coal particles over a wide range without drying. Figure 2.16 shows a cross section of the coal feeder, which consists of ¾ in. and ½ in. ID tubes with the ½" tube driven by a syringe pump. A clear plastic tube containing coal particles is held to the ½ in. tube by Cajon O-ring fittings. The new coal feeder is designed with an 8-slot gas distributor, welded slightly above and surrounding the end of a stationary fine gauge 1 mm ID tube. The gas distributor fits snugly within the plastic tube, creating many high velocity and low momentum gas jets. As the jets emerge from the distributor, they impact the surface of the coal bed in the plastic tube, entraining the coal particles. Given the low momentum, packing of the particles is minimal.

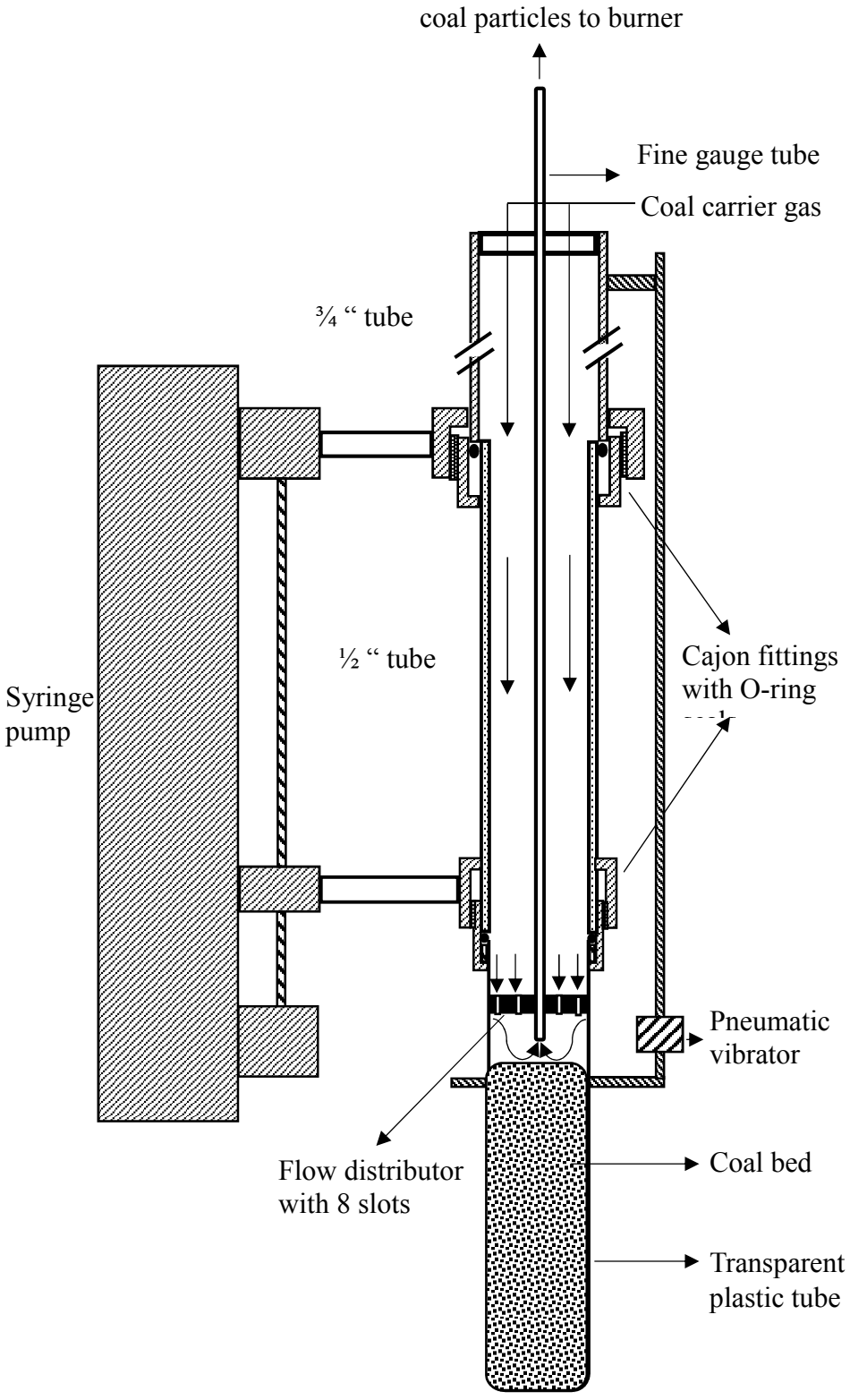

Figure 2-16. Cross section of the coal feeder.

With a high jet velocity, the particles can feed steadily from single particles to the coal stream. A pneumatic vibrator, attached to an annular plate and installed around the plastic tube, locally shakes the surface of the coal bed, which keeps the surface loose and enables the high velocity nitrogen gas jet to entrain the coal particles. Thus, by being able to adjust the location of the flow distributor relative to the inlet of the fine gauge tube and the coal bed surface and the benefits of the low-momentum, high-velocity jet flow with local vibration, the new coal feeder can be used effectively for feeding single particles (at rates as low as 25 mg/min) and coal streams (as high as 500 mg/min), with a variance of less than ±4% (See Fig. 2.17). The lower and the upper limits of feeding are constrained only by the syringe pump capacity. In this work, coal feeding rate below 100 mg/min is considered single particle feeding, consistent with literature on single particle ignition studies [52, 53, 60]. The outlet of the fine gauge tube is kept at a constant clearance above the coal bed surface in the plastic tube by matching the coal feed rate to the syringe pump speed. The rate of entrainment is controlled by the rate at which the plastic tube is driven towards the stationary fine gauge tube.

Figure 2.17 shows the coal particle feeder characterization for a fixed coal carrier (CC) gas of 130 cm^3/min of nitrogen and assuming 298 K. The resulting gas velocity is higher than the saltation velocity of the coal particles, as calculated by Carman-Kozeny fluidization equation [98]; hence, the particles are entrained continuously in the gas. With the fixed coal carrier gas flowrate, the particle spacing ratio can be as low as 6 at 298 K, where the particle spacing ratio (PSR) is defined as the dimensionless distance between two particles entrained in the carrier gas. As described in the literature [60], if the coal density is known, the particle volume fraction, f_{coal}, can be obtained by dividing the volumetric rate of the coal feed by the carrier gas volumetric flow rate. With that information, the particle spacing ratio can be obtained by applying the formula, $PSR = (\frac{\pi}{6f_{coal}})^{1/3}$.

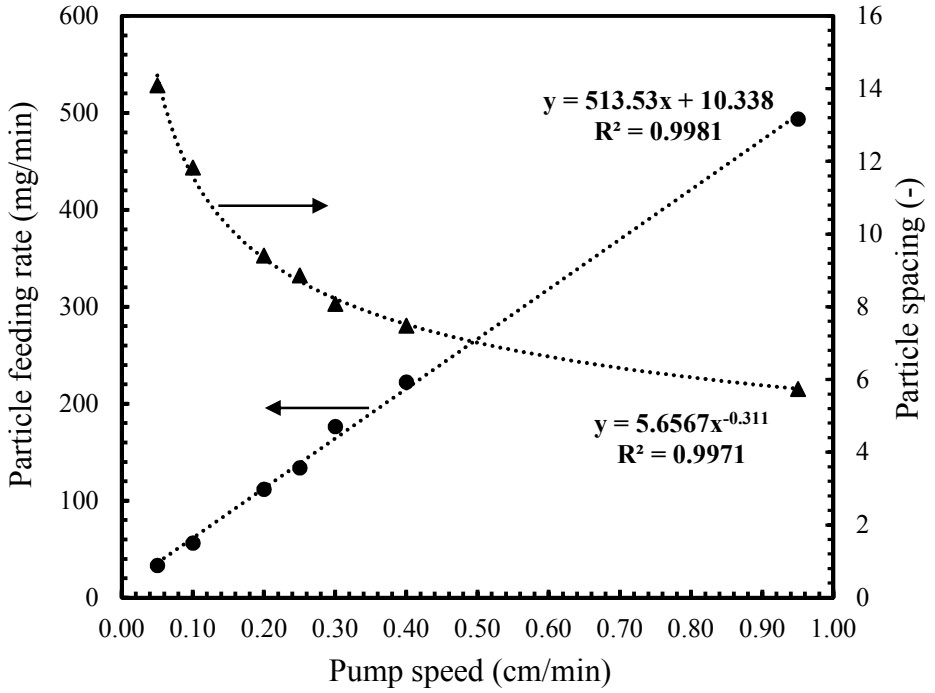

Figure 2-17. Coal feeder characterization relating pump speed to feeding rate and spacing.

Combustion images of particles from the feeder were obtained using a NAC MEMREMCAM HX-7 high-resolution, high-speed camera at a setting of 2,000 frames per second and a shutter speed of 20 μs. Figures 2-18(a & b) were taken for coal feed rates of 33 mg/min and 270 mg/min respectively. Both images were taken at a constant coal carrier gas flow rate of 130 cm^3/min. The particle interactions increase as the particle spacing ratio decreases, and these particle interactions will affect ignition, char burnout, and aerosol formation. The high particle spacing ratio of 14 at 33 mg/min leads to single particle feeding, and the low particle spacing ratio at the feeding rate of 270 mg/min leads to coal stream feeding. The coal feeder, together with the two-stage Hencken flat-flame burner, offers a unique experimental platform for studying single particle ignition and group ignition in both oxidizing and reducing-to-oxidizing environments.

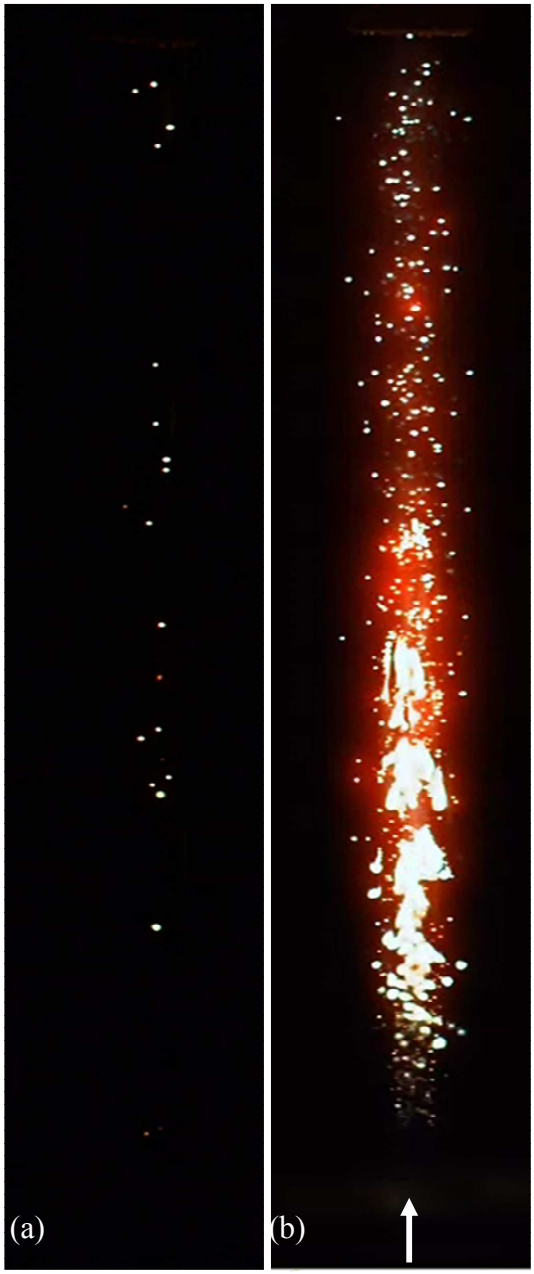

Figure 2-18. High speed camera imaging of coal combustion with different feed rates (a) 33 mg/min, (b) 270 mg/min. The arrow shows the direction of flow of gas and coal particles.

Figure 2-19 shows the results of changing the coal carrier (CC) gas flowrate for two different syringe pump speeds (PS). For a fixed pump speed, say 0.05 cm/min, doubling the coal carrier gas

flowrate from 130 ccm to 304 ccm does not change the coal feed rate. The increased gas flow does not affect the bed surface position relative to the fine gauge tube but only improves the particle fluidization at the coal bed surface. However, changing the pump speed from 0.05 cm/min to 0.20 cm/min leads to a four-time increase in coal feed rate. This increase suggests a linear dependence between the pump speed and particle feed rate. The increased speed drives more coal particles towards the fine gauge tube through which coal particles are transported to the flat-flame burner.

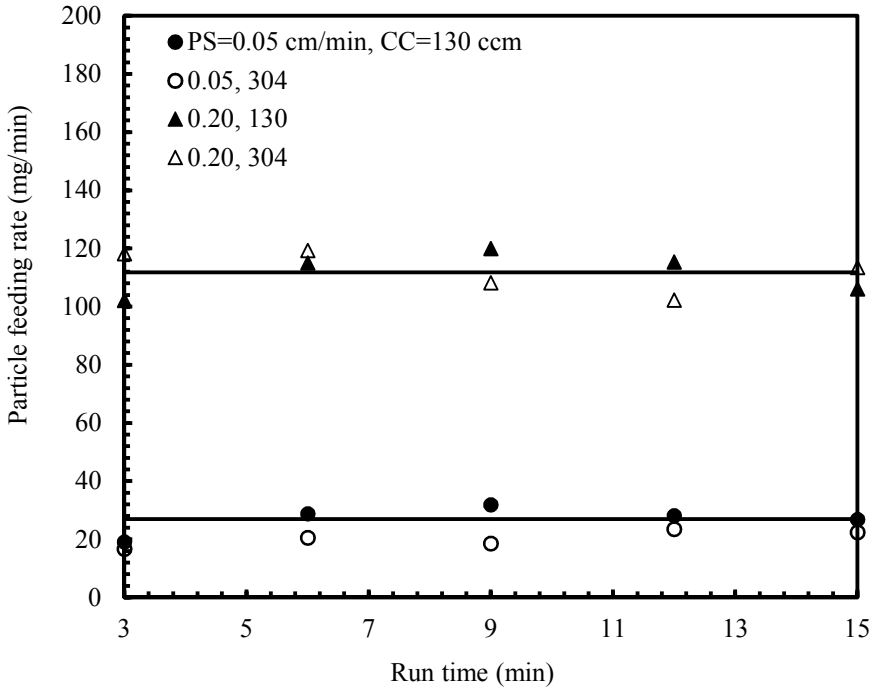

Figure 2-19. Effect of coal carrier gas flowrate on coal feed rate

2.6 Summary

A new Hencken burner (flat-flame) design was described, which can mimic the temperature-time-gas composition histories of coal particles in typical pc boilers. This burner has an inner methane flat-flame, which can be operated in a fuel-rich mode, and an outer methane flat-flame, which is operated in a fuel-lean mode, creating a reducing-to-oxidizing environment that mimics the near-burner environment of a typical pc furnace. The inner methane flat-flame and the outer methane flat-flame can both be operated in fuel-lean mode, creating an oxidizing environment. The new burner design and its full characterization were elaborated. In addition, a new coal feeding system was designed and described. Characterization of the feeding system shows that steady operation can be obtained over a wide range of particle feeding, allowing for fundamental studies of both single particle ignition and coal stream ignition. Thus, the two-stage flat-flame burner, together with its coal feeder, is suitable for systematic study of various processes of coal combustion, either in single particle mode or coal stream mode. Chapter 3 presents the results of single coal particle ignition studies using the burner-feeder setup.

Chapter 3

Effect of the reducing-to-oxidizing environment on single particle ignition

3.1 Introduction

Generally, fundamental studies on the early-stage processes of coal combustion have focused on either oxidizing conditions (mimicking the post-flame region) or reducing conditions (mimicking the devolatilization region). The effect of the reducing-to-oxidizing environment (R-O) on early-stage of coal combustion has, until now, not been considered. As presented in Chapter 2, the new two-stage burner offers well-controlled environments for fundamental coal studies in either an oxidizing environment or an R-O environment. Here, as a proof of concept, the effect of the R-O environment on single-particle ignition is evaluated.

3.2 Single particle ignition

Particle ignition has been studied extensively.[45, 51, 56, 67, 68, 94, 99-102] In a review of fundamental coal ignition studies, Essenhigh et al. [67] noted that most works have focused on understanding the mechanisms that control the ignition of single coal particles. Homogeneous ignition refers to the mechanism whereby the released volatiles burn in the gas phase, while heterogeneous ignition refers to direct particle surface combustion. Howard and Essenhigh [99] studied single-particle ignition and showed that coal particles can experience simultaneously both homogeneous and heterogeneous ignition, depending on the particle size and local combustion conditions.

Apart from being transient, particle ignition depends on many factors, including particle size, volatile matter content, gas composition, gas temperature, surface heating rate, and the volatile release rate.[44, 45, 103] Homogeneous ignition is dominant when the particle size is large and the heating rate is low. On the other hand, heterogeneous ignition is dominant for small particle sizes and high heating rates.[45, 56, 102, 103] In addition, two other mechanisms for ignition are possible. In hetero-homogeneous ignition, a particle experiences volatile oxidation along with char oxidation which can be due to similarity in particle heating time and pyrolysis time.[60] Hetero-homogeneous ignition can be the dominant mode over a wide spectrum of particle sizes, particularly in high-temperature environments.[60, 104] Alternatively, a coal particle can initially ignite homogeneously, and subsequently, after a delay, ignite heterogeneously; hence the term homogeneous-to-heterogeneous ignition.

Solomon et al. [105] were the first to observe homogeneous-to-heterogeneous ignition mode in which secondary ignition occurs after the dispersed coal particles have burned for a short time and the surfaces are then exposed to the surrounding hot gas stream. This later stage burning was observed to occur on the surface of the particle, as indicated by the fact that the width of the observed luminous emission was roughly equal to the particle diameter. Yuan et al. [59, 60] also experimentally observed the ignition characteristics of coal particles using in situ methods in an optical Hencken flat-flame burner. They argued that heterogeneous ignition is dominant at lower temperatures for 65-74 μm particles at 10% to 30% oxygen mole compositions. They concluded that coal combustion has two distinct light emission profiles, corresponding to a coherent volatile flame and to char combustion. Solomon et al. [105] studied ignition in a drop tube furnace at a low temperature of 1123 K and low heating rate. More recently, Yuan et al. [59, 60] studied ignition at high heating rate using a Hencken burner, but their analysis was based on the collective ignition

behavior of particles under oxidizing conditions, rather than on single-particle ignition. Additionally, the effect of the reducing-to-oxidizing environment on particle ignition was not considered. Direct observation of single particle ignition under the reducing-to-oxidizing environment is necessary to understand the significance of this transition on ignition.

While there are many studies on coal particle ignition [35, 43, 53, 60, 68, 94, 100, 101, 106-109], fundamental studies of hetero-homogeneous ignition and homogeneous-to-heterogeneous ignition are lacking, especially under conditions that simulate the reducing-to-oxidizing (R-O) environments found in practical pulverized coal burners. The locally reducing environment in the near-burner region is created by coal devolatilization occurring in a region where the particle number density is high.[8, 30] Beyond this region, the particles move into an oxidizing environment. Wall et al. [68, 109] have noted that, depending on the injected coal mass and coal carrier gas, particles transitioning from a reducing to oxidizing environment can strongly affect the combustion characteristics and the controlling mechanisms for ignition.

Herein, we employ the two-stage Hencken flat-flame burner, described in Chapter 2, along with high speed videography, to study the role of the reducing-to-oxidizing environment and the ambient gas temperature on both ignition delay and induction times. Induction time refers to the delay between when, following homogeneous ignition, the volatiles are oxidized completely, or the volatile flame is extinct, and char ignition begins. A MATLAB program is developed to track the coal particle history and give the particle's luminous intensity as a function of position (time). Thus, we can qualitatively evaluate the modes of ignition and determine the ignition delays and induction times.

3.3 Experimental methods

Figure 3-1 shows a schematic representation of the two-stage Hencken flat-flame burner. A detailed description can be found in Section 2.2. As shown in Figure 3-1, the key modification to Fig. 2-2 is the background lighting and the high-speed camera setup.

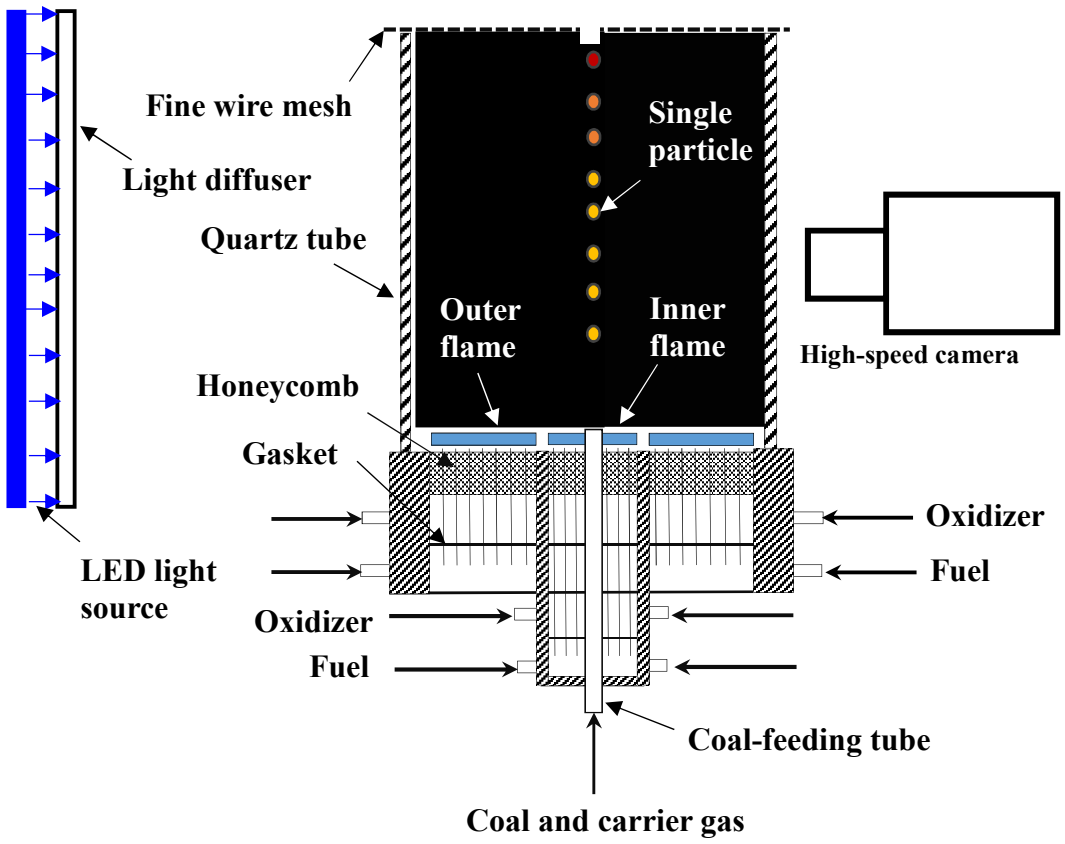

Figure 3-1. Cross section of a two-stage Hencken flat-flame burner, showing single particle combustion and the high-speed camera setup with a blue LED background light source

3.4 High-speed, high-resolution videography

Particle devolatilization on its own does not emit radiation, but volatile/soot oxidation and char oxidation do emit visible light. Thus, significant insight on ignition, which is a reaction process caused by either volatile oxidation or char oxidation, can be obtained from such radiation emissions. Video images of visible light emission were obtained using a NAC MEMRECAM HX-7 high-speed camera. The camera was fitted with a SIGMA APOMACRO 180 mm lens, used to obtain image magnification of 1:4. For the experiments, the camera was set to 8,000 frames per second (fps) and an exposure time of 50 μs to resolve the motion of the particles. To view non-emitting coal particles, a blue LED light with a light diffuser was used as a background light source. The resulting shadow allowed for observation of non-emitting coal and char. The background light allowed the blue sensors of the camera's RGB channels to be used to continuously observe the particle because the amount of emission in the blue wavelength is small except at high temperatures. Data from the red sensors of the camera's RGB channels gives the visible emission during both volatile and char combustion, from which qualitative and quantitative information on single particle ignition was obtained.

The visible image from the camera is multispectral, made of red, green, and blue bands. Such an image is an array of square pixels arranged in rows and columns, with each pixel indicating the intensity of light sensed by the camera's detector in the three-color bands. Thus, the image processing code uses built-in functions in commercially available MATLAB software to track particles and obtain spectral intensity signals up to a height of 6 cm from the burner exit. The flow chart in Fig. 3-2 succinctly displays the image processing steps for obtaining the red spectral intensity signal. The image processing algorithm is provided in Appendix A-1.

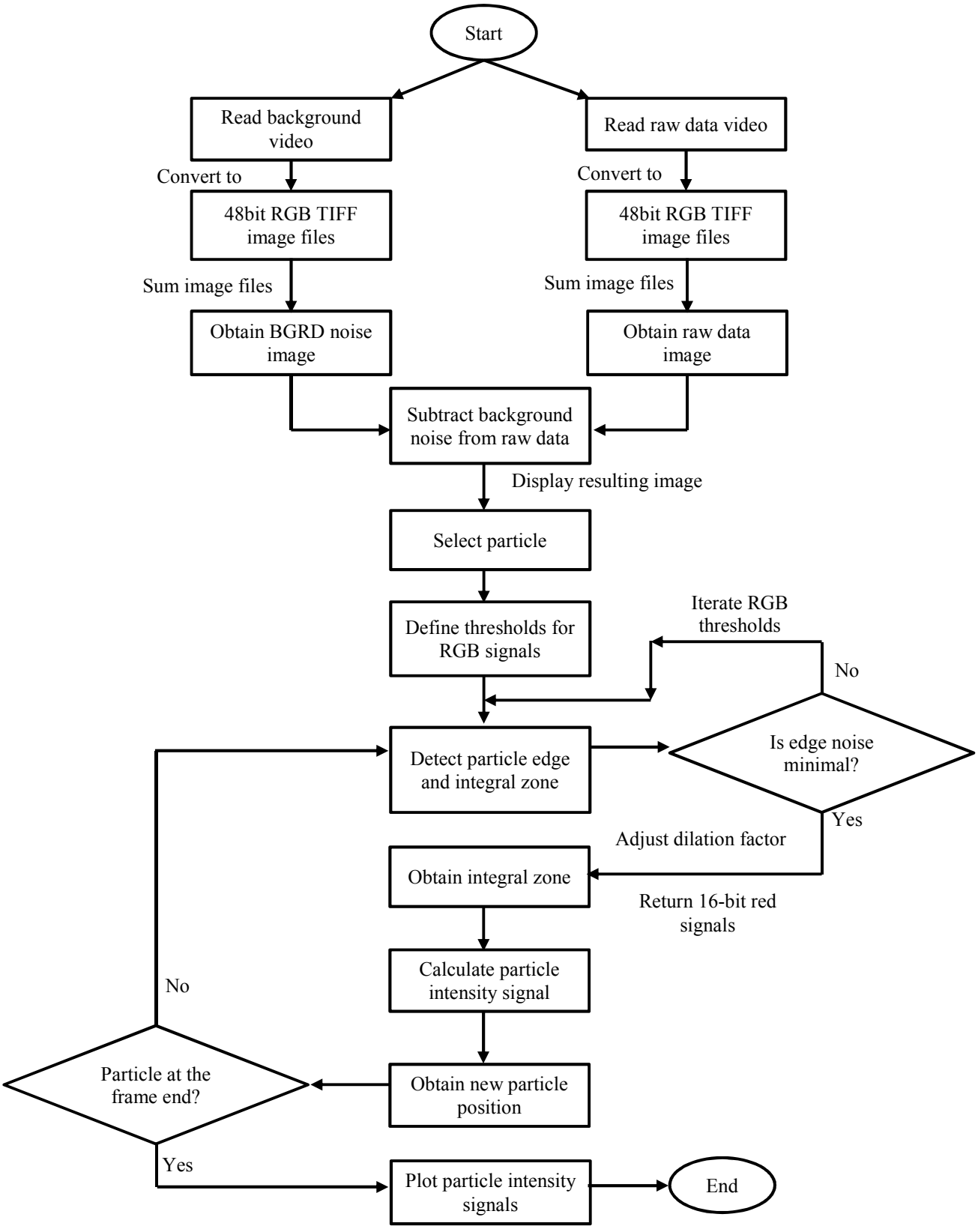

Figure 3-2. Flowchart of steps to extract spectral intensity from camera RGB sensor.

3.5 Coal properties

Powder River Basin (PRB) subbituminous coal was used in this study, and the proximate and ultimate analyses of the coal are presented in Table 2-2. Coal particle size has a strong influence on ignition.[8, 57, 67] Ignition studies are usually performed with particle sizes ranging up to 150 microns.[44, 45, 110] A particle size of 125-149 μm was selected for this single particle study, since the size is within the bracket and is also particularly suitable for high resolution videography of particle ignition.

3.6 Results and discussion

3.6.1 Effect of gas temperature on coal particle ignition

Levendis and coworkers [110] showed that the oxygen concentration in an oxidizing environment can significantly influence the single particle ignition. By implication, factors associated with combustion environments such as a reducing-to-oxidizing environment and gas temperature should be studied. Most fundamental investigations on early-stage processes of coal combustion have been conducted up to 1800 K.[52, 59, 60, 62] Here, single particle ignition studies were performed at nominal gas temperatures of 1300 K and 1800 K. These two temperatures span a range that is typical of the near-burner region where early-stage processes of coal combustion occur.[30] The effect of temperature on the early-stage process of ignition under oxidizing conditions is considered first, where the nominal oxygen composition is 20% by volume. High-speed, high-resolution videos of single particles were obtained at a coal feed rate of 30 mg/min. Several particles were tracked, and Figure 3.3 shows representative still images of a single particle's combustion, obtained in oxidizing conditions at 1800 K (Fig. 3-3a) and 1300 K (Fig. 3-3b) gas temperatures. The particle velocity and particle residence time were obtained from the camera's

frame speed and position-wise tracking of the particles. The displayed numbers in the figures denote the residence times of the particle in milliseconds. Arrows point to the single particle before ignition. Circles gives the time/location of homogeneous ignition, with the coal particle in the center of the volatile flame. A triangle represents the time/location of heterogeneous ignition.

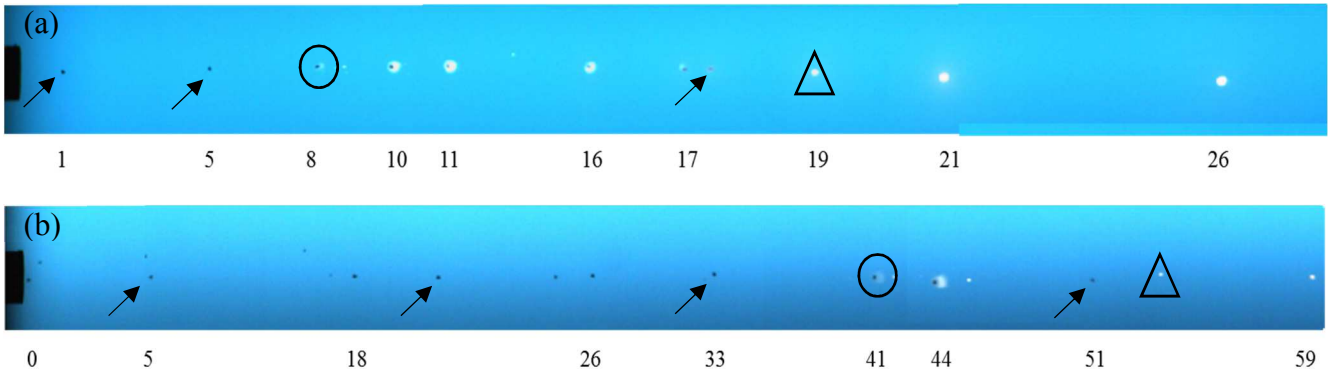

Figure 3-3. High-speed videography of the evolution of a single coal particle in a nominal 20 vol. % oxidizing condition at gas temperatures of (a) 1800 K, and (b) 1300 K. Numbers in ms

For the 1800 K oxidizing post-flame condition, devolatilization is fast. With a high heating rate and high local oxygen concentration, the coal particle ignites homogeneously at 8 ms, forming a diffusion flame around the coal particle. The particle is initially enveloped by the volatile flame, but a black particle emerges after complete combustion of volatiles. As seen in Figure 3-3a, the emerged black particle ignites heterogeneously after an induction time, so homogeneous ignition precedes heterogeneous ignition in an oxidizing condition at 1800 K. The particles require longer residence times for sufficient particle heating to remove moisture and release volatile species for a 1300 K gas temperature. Consequently, the particle ignites homogeneously in the 1300 K oxidizing environment as well, but after a longer residence time than for 1800 K. After the volatile

oxidation, the emerged particle ignites heterogeneously, just as it does in the 1800 K oxidizing condition. This observation is consistent with conclusions in the literature.[60, 74, 103, 110] Thus, in an oxidizing environment with 20% O_2 by volume, homogeneous-to-heterogeneous ignition prevails for both gas temperature environments.

Emission intensity-time histories were extracted for many particles. Figure 3-4 shows a typical representation of the particle combustion along the central axis. The signal size may differ among individual particles, but the characteristic times and trends are repeatable. For ease of comparison, the emission profiles are normalized by their respective peak intensities. There are two peaks for both temperatures. The first peak corresponds to volatile oxidation after homogeneous ignition, while second wider peak represents heterogeneous char oxidation after an induction time. The light intensity shows modulation during the induction time while the particle surface is heated to the required temperature for heterogeneous ignition. The modulation is from particle rotation and/or subsequent ejection of material as the char surface temperature rises. After heterogeneous ignition in the oxidizing condition at 1800 K, the emission intensity remains fairly constant with time, after which it declines. As char oxidation progresses, the particle size decreases and intensity declines because of the spreading ash coverage of the exterior surface and lower emissivity.[110] Also, char oxidation rate decreases as the carbon content decreases with time.

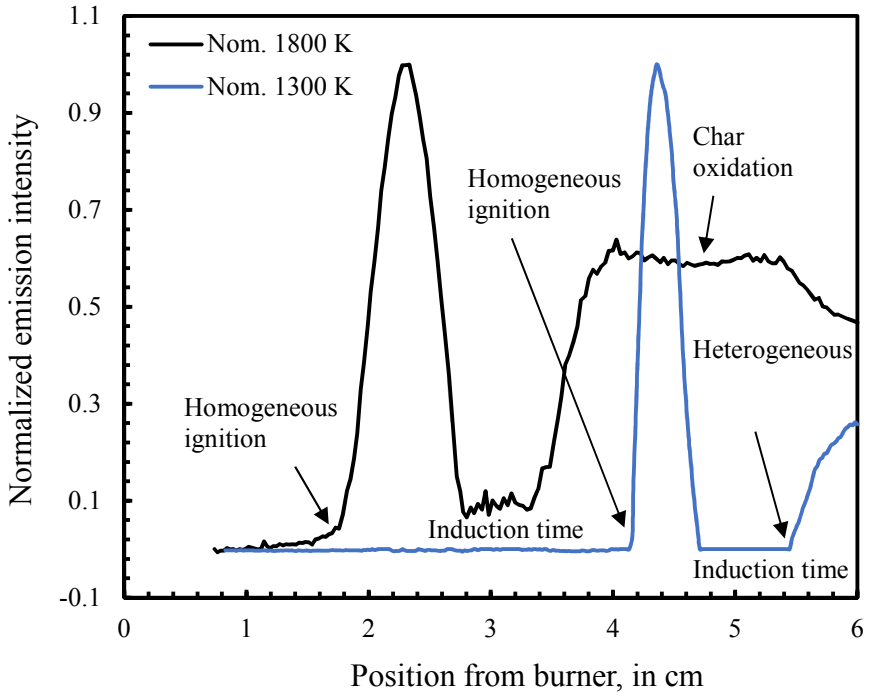

Figure 3-4. Normalized light emission intensity vs. height from the burner for oxidizing conditions at 1800 K and 1300 K

3.6.2 Effect of the reducing-to-oxidizing environment on coal particle ignition

At high gas temperatures of 1800 K, a high volatile release rate is expected. But the volatiles released will diffuse away from the surface of the unburned coal particle since there is no oxygen in the reducing zone. As heat continues to be transferred to the surface of the particle, volatile release is enhanced within the central reducing zone. Because the heating rate is high for the 1800 K gas temperature, both the volatiles and the char particle are hot and ignite once there is interaction with oxygen beyond the reducing zone (i.e. hetero-homogeneously, as defined by Juntgen et al. [111]). Unlike the oxidizing condition, a single peak is observed for the R-O condition at 1800 K gas temperature, as shown in Fig. 3-5.

As discussed in Section 2.4, particles transition to the oxidizing environment from the reducing environment through a flame sheet that raises the particle surface temperature in comparison to the oxidizing condition at the same gas temperature of 1300 K. A volatile reaction can be observed in Fig 3-5 for 1300 K gas temperature (blue line), but it is quenched almost immediately, suggesting that the volatile concentration may be below the lower flammability limit at this temperature. The wavy characteristic of the normalized intensity for the 1300 K gas temperature suggests a continuous but weak volatile oxidation, which later leads to heterogeneous oxidation.

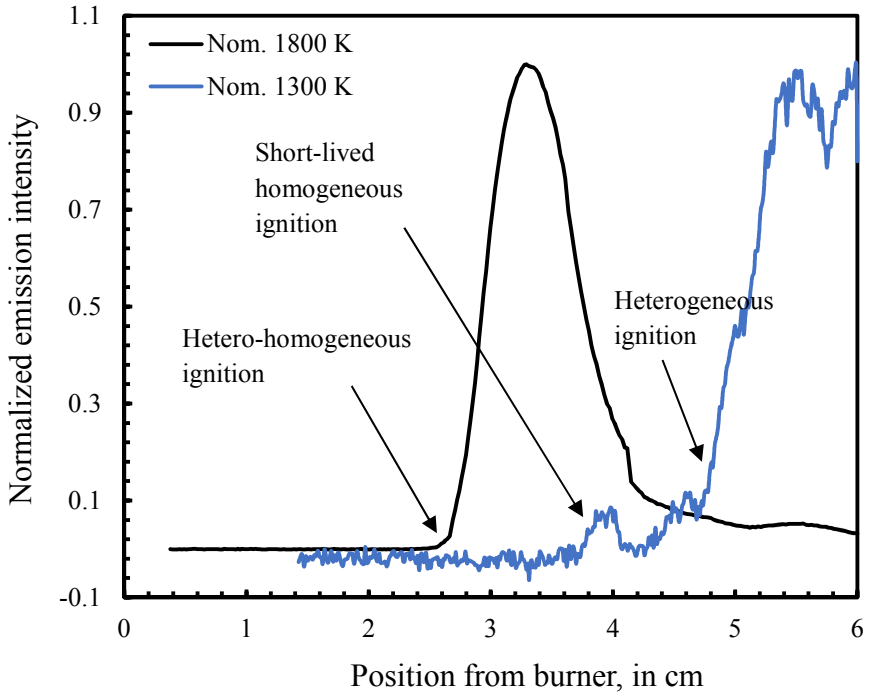

Figure 3-5. Normalized light emission intensity vs. height from the burner for reducing-to-oxidizing conditions at 1800 K and 1300 K

Similar to the work of Yuan et. al. [60], the ignition point is defined as the height above the burner corresponding to 10% of the maximum emission intensity. The induction time is obtained from the time difference between completed volatile oxidation and char ignition. Figure 3.6 shows the

ignition and induction times for the conditions studied in this work. The R-O environments have longer ignition delay times in comparison to the oxidizing environments. For the nominal 1300 K temperature, the characteristic ignition delay times for both oxidizing and reducing-to-oxidizing conditions are 30 and 36 ms respectively, an average of 20% increase in R-O environment over the value for the oxidizing environment. For the 1800 K gas temperature, the ignition delay time for the R-O environment increases by an average of 4 ms over that of the oxidizing (O) environment. While R-O environments cause longer ignition delay times than in oxidizing environments at the same nominal gas temperatures, the induction times in R-O environments are shorter. Under the conditions of this work, including temperatures and combustion environments, these experimental findings show that the characteristics of ignition in R-O environments are quite different from those in oxidizing environments.

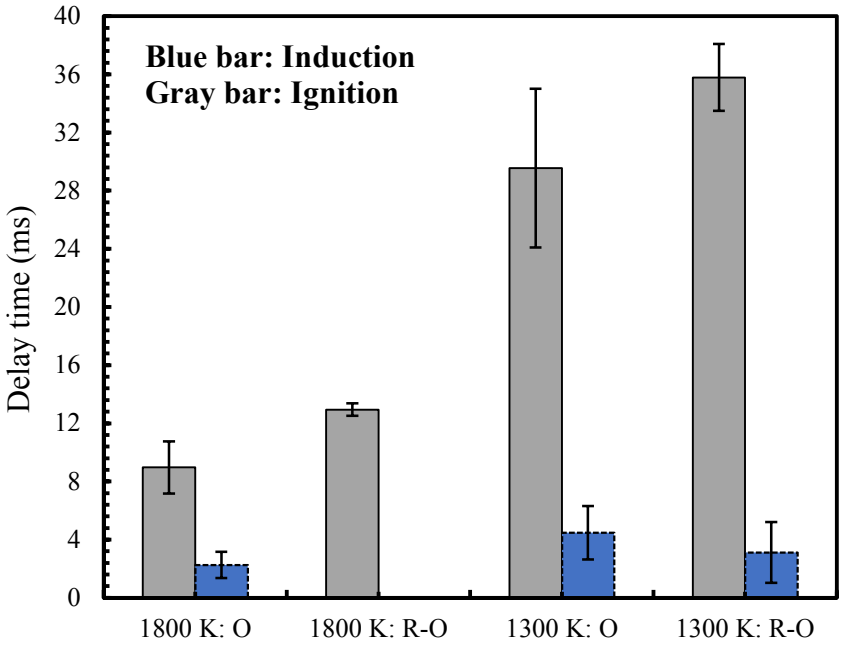

Figure 3-6. Effect of reducing-to-oxidizing environment and temperature on ignition and induction times

Given the experimental observations, Figure 3.7 sums up the controlling ignition mechanisms during the early-stage process of a single particle combusting in an oxidizing condition at 1300 K and 1800 K. The single particle is initially heated to a temperature high enough for moisture vaporization and devolatilization. The released volatiles either diffuse away from the particle surface or burn in the oxidizing environment. Then, time elapses while heat diffuses to the particle surface and the combustion products (i.e., H_2O and CO_2) diffuse away from particle surface, which is indicated by the induction time before char oxidation. After these steps, the particle then ignites heterogeneously.

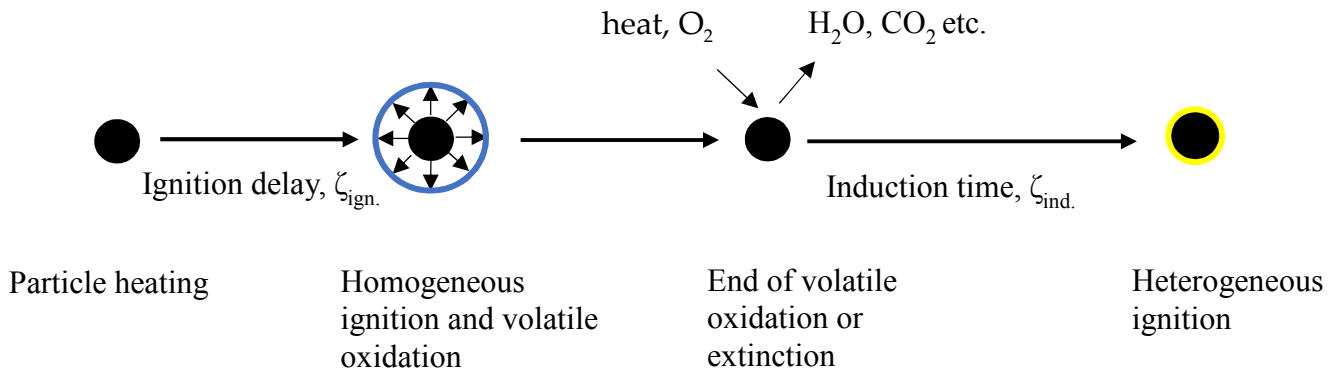

Figure 3-7. Homogeneous-to-heterogeneous ignition mechanism of single coal particle in oxidizing conditions

As illustrated in Fig. 3-8, a flame sheet separates the reducing zone from the oxidizing zone. In the reducing-to-oxidizing condition at 1800 K, devolatilization occurs significantly within the reducing zone. The released volatiles, however, become part of the reducing zone because there is no oxygen for combustion. Subsequent volatile release, which is low in concentration, burns at the coal particle surface once the particle transitions from the reducing zone to the oxidizing zone. The

particle surface oxidation occurs along with the volatile oxidation occurring at the surface (i.e., hetero-homogeneous ignition). However, at 1300 K, devolatilization occurs more after the particle has transitioned to the oxidizing zone, due to low heating rate. Thus, homogeneous ignition of the released volatiles occurs in the oxidizing zone. However, the gas phase ignition is short-lived because the low volatile concentration cannot sustain a combustible mixture in an environment with a low nominal oxygen concentration. Heterogeneous ignition occurs after the homogeneous ignition.

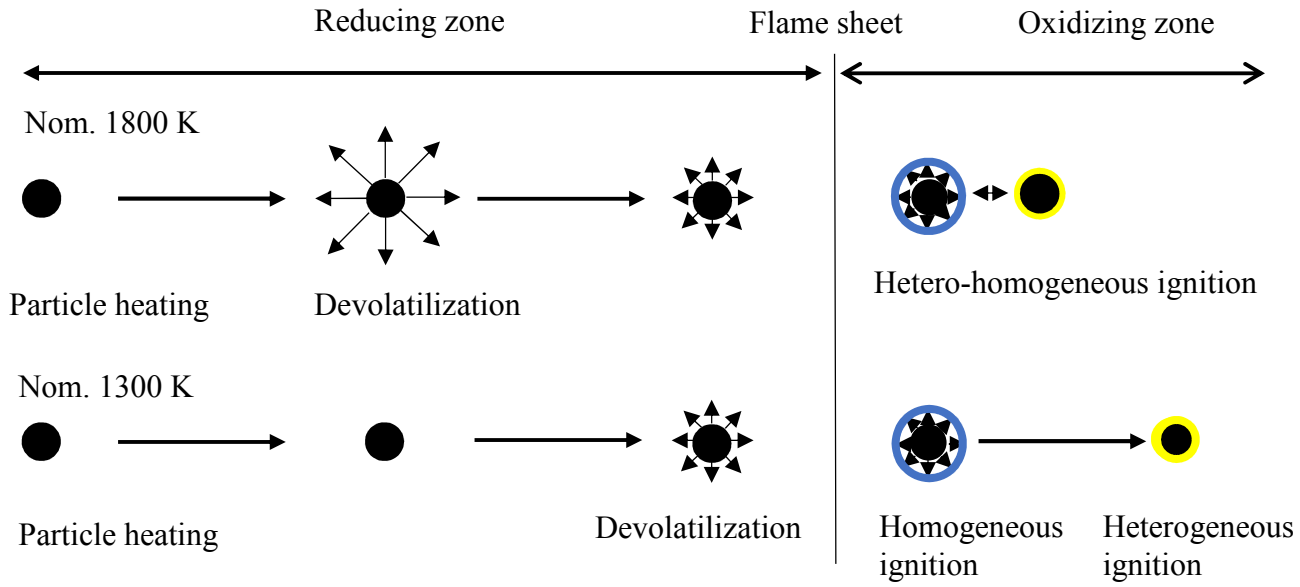

Figure 3-8. The controlling ignition mechanism in reducing-to-oxidizing conditions

3.7 Summary

Using high speed videography, single particle ignition of PRB sub-bituminous coal has been investigated experimentally in both reducing-to-oxidizing environments and oxidizing conditions.

Reducing-to-oxidizing environment promoted hetero-homogeneous ignition in an 1800 K gas temperature environment. Also, there was a significant increase in ignition delay due to the R-O environment. The traditionally studied oxidizing condition with 20 mole percent oxygen concentration led to homogeneous-to-heterogeneous ignition mode.

Chapter 4

The role of size on single particle ignition and the simultaneous determination of particle size and ignition time

4.1 Introduction

The previous chapter showed the impact of the reducing-to-oxidizing environment on ignition behavior, and, for simplification, a single particle size range was used. The chosen particle size range for that study allows for convenient particle ignition videography. Typically, coal particles are classified into narrow size ranges before single particle experiments. Ignition behavior of the narrow particle size range is then based on data from a few sampled particles, usually with no knowledge of what particle sizes are sampled within an entire given particle size range. Here, in addition to evaluating the role of various particle sizes on single particle ignition, a new algorithm is developed that allows for simultaneous determination of particle size before ignition and ignition delay time in an experiment using a wide particle size range. This algorithm eliminates the need to classify particles before ignition studies, and is thus valuable for validating a key assumption on which single particle experiments in the literature are based.

4.2 Particle size range and ignition studies

Experimental studies of ignition at a fundamental level involve single coal particles and are aimed at providing direct and unbiased information regarding particle ignition.[104] Earlier studies on single coal particles are performed to verify and explain findings from various theoretical models and calculations on coal particle ignition and combustion.[46, 50, 67, 68, 99, 100, 109] The agreements between model predictions and the experimental data reported in those studies have encouraged other researchers to continue to study single particles, albeit in experimental set-ups and conditions that are more relevant to practical furnaces with high heating rates.[44, 45, 52, 56, 59, 60, 74-76, 93, 102, 103, 110, 112, 113]

Many factors affect coal particle ignition, including the coal rank [45, 54, 102, 110, 112, 114], particle heating rate [47], coal feeding rate [93], gas temperature [60, 93], combustion environment [56, 60, 94, 102, 109, 112], and particle size.[52, 93, 99] As shown in Chapter 3, the mode of ignition strongly depends on the combustion environment. Khatami et al. [44, 112] observed that all particle sizes, independent of coal rank, ignite more intensely and with an increased tendency of volatile flame closer to the char surface as oxygen concentration increases. Thus, a local combustion condition with higher oxygen concentration leads to shorter ignition delay and devolatilization times.[56]

As noted by Kim et. al. [52], the ignition behavior of pulverized coal particles over a wide particle size range at high heating rates is yet to be thoroughly investigated. All previous single particle ignition studies were performed for a given particle size range, such as 63-74 μm [59, 60], 75-90 μm [76, 112], 75-105 μm [56, 93], 97-105 μm [115, 116], 106-125 μm [94], 75-150 μm [44, 45, 53, 112], and 150-180 μm [52, 74]. Coal particles of the same size, let alone different sizes within a given size range, behave differently depending on the proximate and ultimate analyses. It is also well established that coal particle size has a strong influence on the ignition delay times and mechanisms.[8, 57, 67] Therefore,

to ensure accurate interpretation of experimental findings, it is important to validate the assumption that ignition of a few sampled particles represents the ignition of an entire given particle size range.

Herein, experimental investigations of ignition behaviors of different particle size ranges are reported and compared to the results of studies without size classifications. This work provides valuable information as to the validity of the assumption and the accuracy of the conclusion regarding ignition behavior drawn based on this assumption. First, experiments were conducted for particle size classifications, including 75-89 μm, 90-105 μm, 106-124 μm, and 125-149 μm. Afterwards, a separate experiment was conducted for 75-149 μm particles, i.e., without size classification. In both cases, high-speed, high-resolution videography was used to observe ignition of individual particles. A new algorithm, developed in MATLAB, offers a way to determine simultaneously the specific size of particle at ignition and the corresponding ignition delay time, without the need to size-classify the coal particles beforehand. The algorithm provides particle size-ignition time statistics with average particle ignition delay times that can be compared to those obtained from experiments using the four narrow particle size cuts. The experiments were performed at the same conditions as discussed in Chapter 3, i.e., nominal 1300 K and 1800 K gas temperatures and two environments (oxidizing (O) and reducing-to-oxidizing (R-O)). The two-stage burner and the high-speed camera settings have been described in Sections 2.2, 3.3 and 3.4 and will not be repeated in this chapter.

4.3 Coal proximate and ultimate analyses

Table 4-1 presents the proximate and ultimate analyses of the bituminous coal used for this study, with as received values calculated based on standard test methods (ASTM D3172-5). Ignition studies are usually performed with particle size up to 150 microns.[44, 45, 110] Coal particles

are screened to obtain specific size classifications including 75-89 μm, 90-105 μm, 106-124 μm, and 125-149 μm in diameter.

Table 4-1. Proximate and ultimate analyses of West Elk bituminous coal

Proximate analysis (%wt)				Ultimate analysis (%daf)					HHV(daf)
M	VM	FC	Ash	C	H	O	N	S	(MJ/kg)
3.55	33.72	48.07	9.65	79.05	5.42	13.15	1.73	0.63	32.34

4.4 Simultaneous determination of particle size and ignition delay time

Videos of unclassified particles (i.e., 75-149 μm particles) were obtained using a NAC MEMRECAM HX-7 high-speed video camera, set at 8000 frames per second. The videos were post-processed to obtain high quality tagged image files, with each individual graphic file having three 16-bit channels corresponding to the red, green and blue (RGB) spectra. Here, 48-bit sequence tagged image files are preferred because they suffer no-loss of quality when compressed to graphic files. Before experimental measurement and for a given post-flame gas condition and temperature, videos of the field of view of the camera without particles, illuminated by a blue LED light source, were taken for background correction during image processing. Then, 500 tagged image files were extracted and used for each experimental condition to obtain a good average of the background effects for use with the actual particle data. The 500 graphics were read using commercially available MATLAB software and are then converted to string representations on a

double precision basis. The string representations were then summed and concatenated, turning the graphical data into a double array dataset matrix, which was then averaged by the number of images processed. Using the same image-processing methods, raw data from experiments was converted to matrices and the background corrections were then subtracted.

The Wiener method, a 2-D pixelwise adaptive noise-removal filtering, was adopted to further reduce noise in the actual experimental data [117]. This method is based on statistics estimated from the local neighborhood of each pixel constituting the particle (i.e., n_1-by-n_2). For a specific image, there are N-by-M total local neighborhoods, and for which n_1-by-n_2 are elements. The local image mean, $\overline{n}$, and standard deviation, σ, are calculated using Eq. (4.1) and Eq. (4.2) respectively.

$$\overline{n} = \frac{\sum_{n_1, n_2 \in \eta} a(n_1, n_2)}{NM} \tag{4.1}$$

$$\sigma = \frac{\sum_{n_1, n_2 \in \eta} a^2(n_1, n_2)}{NM} - \left(\frac{\sum_{n_1, n_2 \in \eta} a(n_1, n_2)}{NM} \right)^2 \tag{4.2}$$

Based on these estimates, a lowpass Wiener filter, described by Eq. (4.3), is created to remove any degradation in quality due to additive noise, with ν^2 being the average of all the local estimated variances.

$$b(n_1, n_2) = \overline{n} + \frac{\sigma^2 - \nu^2}{\sigma^2}(a(n_1, n_2) - \overline{n}) \tag{4.3}$$

Before ignition, the particles were detected based on RGB information in the 48-bit tagged image files. As the particle moved and burned, pixel area covered by the particle increases due to volatile

oxidation or particle swelling. With a dilation factor and application of other parameters (e.g., the background correction matrix, the Wiener filter correction matrix), the integral area of the image for a selected particle was obtained, and the edge of the dilated image was monitored over the particle time history (i.e., 7 cm view length of the camera).

The initial x-y position of the selected particle was defined in a given frame. With the estimated pixel velocity, the new positions of the particle were obtained and stored. The first dilation occurred at the point of particle ignition. Thus, integral area changed as the combustion progressed with new x-y coordinates. The signal intensity profile in the red channel as a function of time was then obtained by multiplying the double array datasets of the image with the corresponding integration area at a given time. To obtain the average projected area of the particle, an exponential curve was fitted for the red channel signal intensities, up to the position corresponding to 10% of the maximum intensity for a given particle. An exponential curve fit was deemed acceptable for determining particle size if the corresponding absolute value from the curve fit fell within 3 times the standard deviation of the red channel data. Assuming spherical symmetry of the particle before ignition, the particle size, d_p, at the ignition point was then determined using Eq. (4.4) based on the corresponding number of pixels covered by the particle, N_{pixel}, at the position before 1% of the maximum intensity. A_{pixel} is the unit pixel area, based on the resolution and the view length of the high-speed camera. A flow chart representation of the algorithm, summarizing the process described above, is presented in Fig. 4-1, and the MATLAB code is provided in Appendix A-2.

$$d_p = \sqrt{A_{pixel} \cdot N_{pixel} \cdot 4/\pi} \tag{4.4}$$

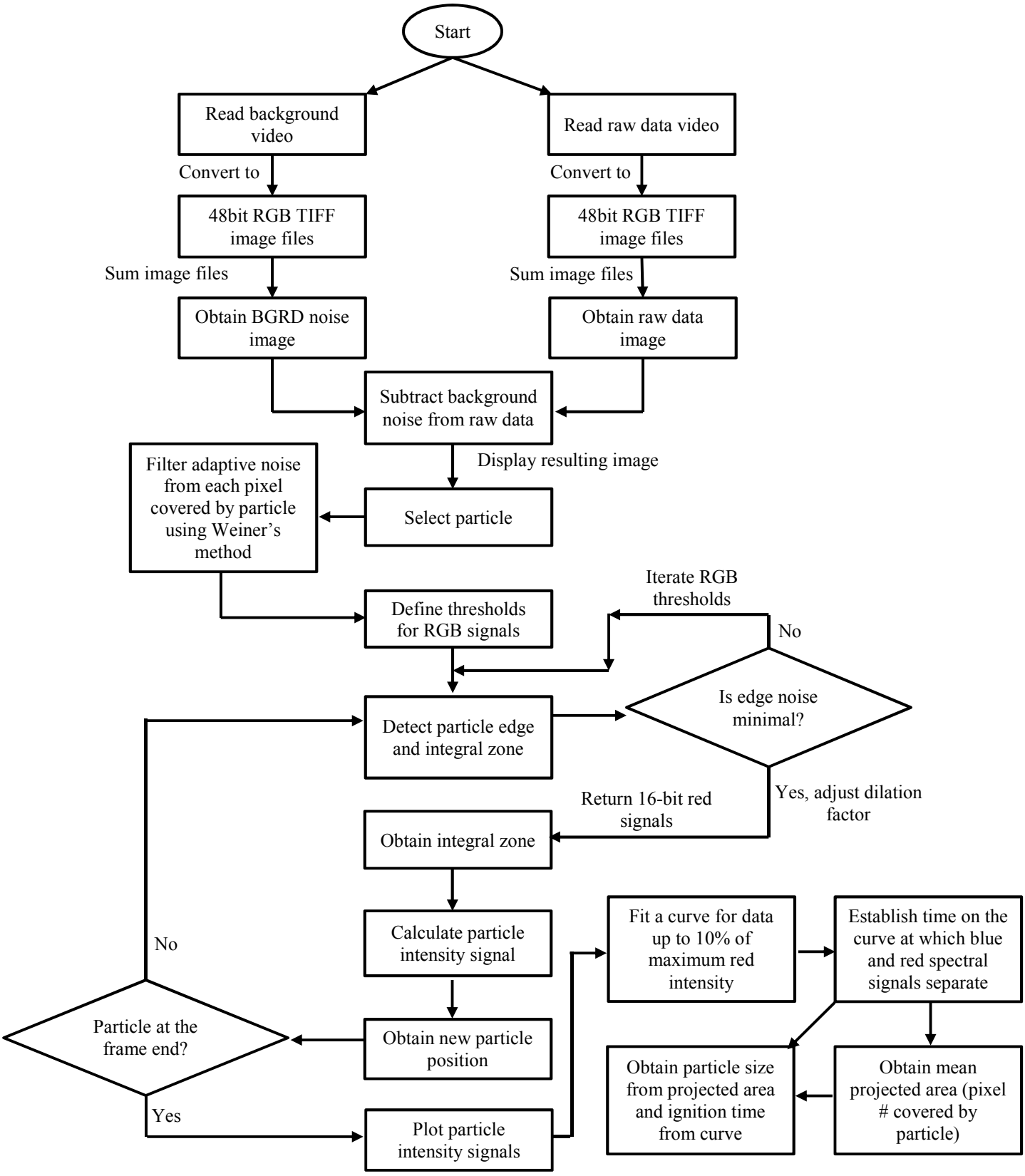

Figure 4-1. Flow chart describing simultaneous particle size and ignition delay time determination.

4.5 Results and discussion

4.5.1 Effect of particle size on ignition in oxidizing conditions

Figures 4-2(a-c) show photographs of a single particle tracked as it undergoes various combustion events. The figures present single particles for three different narrow size classifications in oxidizing condition. Particles are suspended and transported in the hot gas with a nominal gas temperature of 1800 K. The particle velocity and particle residence time are obtained from the camera's frame speed, frame number, and the camera total view length. The displayed numbers in the figures denote residence times of the particle in milliseconds. The arrow points to the particle before ignition, and the location of ignition is shown in the figures by circles. As expected, the ignition delay time decreases as particle size decreases, with 125-149 μm particles igniting after 15.4 ms and 90-105 μm particles after 5.8 ms. The volatile flame size increases with particle size. Thus, volatile flame in large particles requires a longer time before extinction. For 90-105 μm sizes, particles beyond 15.3 ms residence time correspond to char oxidation, given that the widths of the luminosity of the particle emerging from the volatile flame are about the same as the particle size.

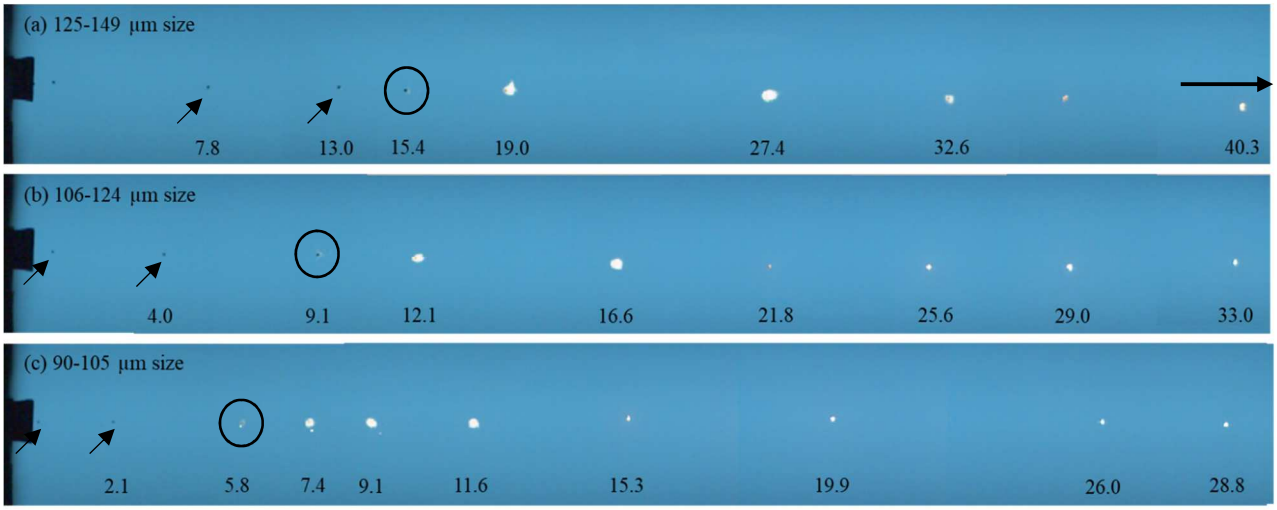

Figure 4-2. High-speed videography of a single coal particle ignition in oxidizing conditions at a nominal gas temperature of 1800 K for (a) 125-149 µm, (b) 106-124 µm, and (c) 90-105 µm particle size ranges. The flow is from left to right, as shown by the arrow.

At a lower gas temperature, the particle surface temperature is low, and so is the volatile release. Thus, the ignition delay times in 1300 K nominal gas temperature presented in Figures 4-3(a-c) are significantly higher than those reported in Figures 4-2(a-c), where the nominal gas temperature is 1800 K. The experiments show that the ignition delay times are 50 ms for 125-149 µm particles, 44.6 ms for 106-124 µm particles, and 23.4 ms for 90-105 µm particles. Even though the trend of the ignition time as a function of particle size is the same in both gas temperatures, the heating rates at an 1800 K gas temperature can reduce the ignition time by a factor of 3 to 5 times over those of a 1300 K environment for the same particle size under the same experimental settings.

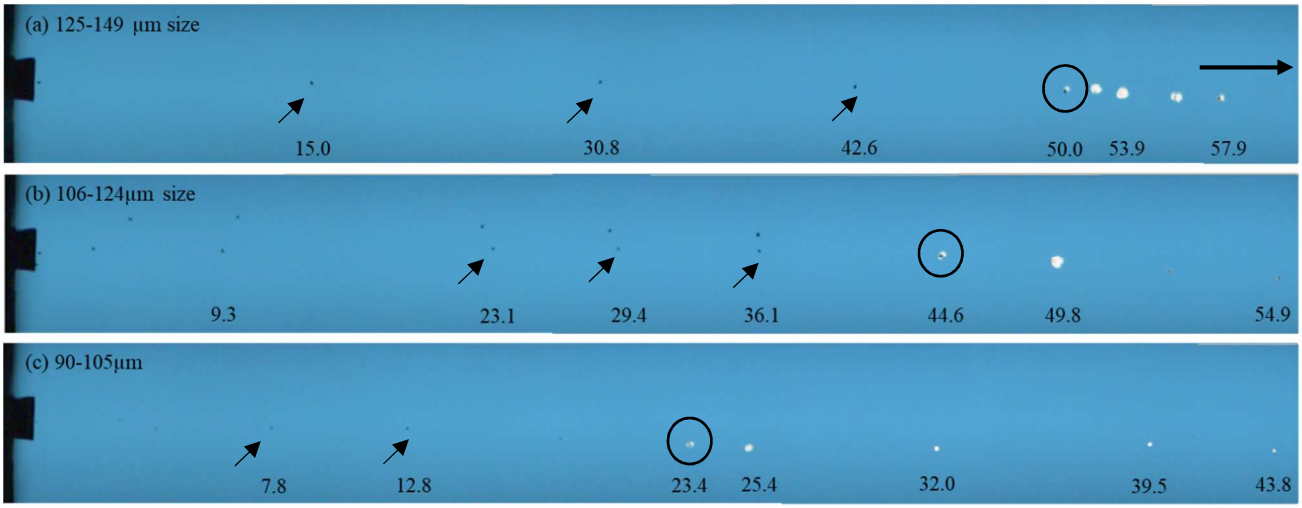

Figure 4-3. High-speed videography of a single coal particle ignition in oxidizing conditions at a nominal gas temperature of 1300 K for (a) 125-149 µm, (b) 106-124 µm, and (c) 90-105 µm particle size ranges. The flow is from left to right.

4.5.2 Effect of particle size on ignition in reducing-to-oxidizing conditions

The ignition behavior of a particle size range was shown in Section 4.5.1 to be significantly affected by the temperature of the combustion gas environment in the presence of excess oxygen. Here, the effect of transition from a reducing-to-oxidizing environment is evaluated for the same nominal gas temperatures. The results in Figures 4-4(a-c) show that the transition from reducing environment to an oxidizing environment leads to ignition delays of 21.8 ms, 22.9 ms and 12.4 ms for 125-149 µm, 106-124 µm and 90-105 µm particles, respectively. Compared to the oxidizing condition with ignition delay times of 15.8 ms, 9.1 ms, and 5.8 ms for the same particle size respectively, it is thus clear that ignition behavior of a particle depends not only on the gas temperature in the which the particle is suspended but also on the local oxygen composition. For the oxidizing condition, the ignition delay times increase monotonically with particle size. However, in the R-O condition, the ignition delay times for 125-149 µm and 106-124 µm particle

size range are nearly the same. Ignition is oxygen-limited in the R-O condition, but no such limitation exists in the oxidizing condition. Since volatile flux is high for large particle sizes due to the high gas temperature, homogeneous ignition occurs as soon as the particle with its volatile transitions to the oxidizing environment from the reducing environment. This behavior suggests that, in a high-temperature environment, when the surface flux of the volatiles is small, gas-phase combustion of the volatiles can occur simultaneously with surface heterogeneous combustion.

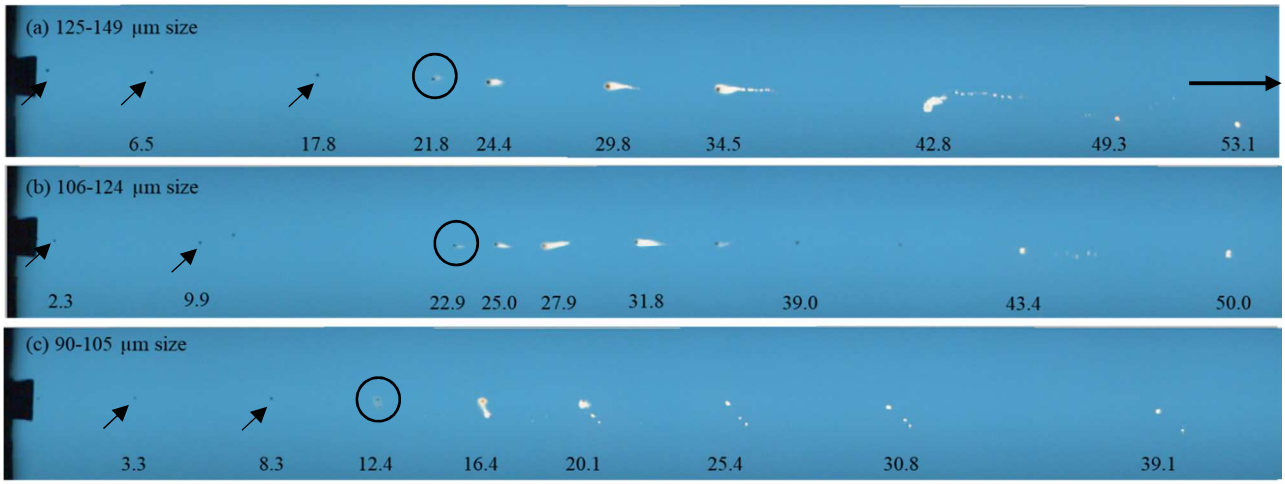

Figure 4-4. High-speed videography of a single coal particle ignition in R-O conditions at a nominal gas temperature of 1800 K for (a) 125-149 µm, (b) 106-124 µm, and (c) 90-105 µm particle size ranges. The flow is from left to right.

The impact of the reducing-to-oxidizing environment combined with a low gas temperature is considered next and presented in Figures 4-5(a-c). In contradistinction to the differences in ignition behavior between the O and R-O conditions at 1800 K, the ignition delay times at a nominal gas temperature of 1300 K in the R-O condition are nearly the same with those of 1300 K in the O condition (See Section 4.5.1). For example, the ignition delay times for 125-149 µm particles at

1300 K are 50.0 ms and 45.4 ms in the O and R-O conditions, respectively. For 90-105 µm particles, the ignition delay times at 1300 K are 23.4 ms and 25.9 ms in the O and R-O conditions respectively. The low heating rate limits particle or volatile ignition in 1300 K, despite the high oxygen concentration around the particles in the O condition. However, in the R-O condition, there exists a flame sheet that demarcates the transition from the reducing to the oxidizing environment. At a low nominal gas temperature of 1300K, the flame sheet in the R-O condition heats the particle, a process that is absent in the O condition. This heating compensates for or negates the effect of the lower oxygen concentration in the R-O condition. Hence, similar ignition delays are observed in both conditions.

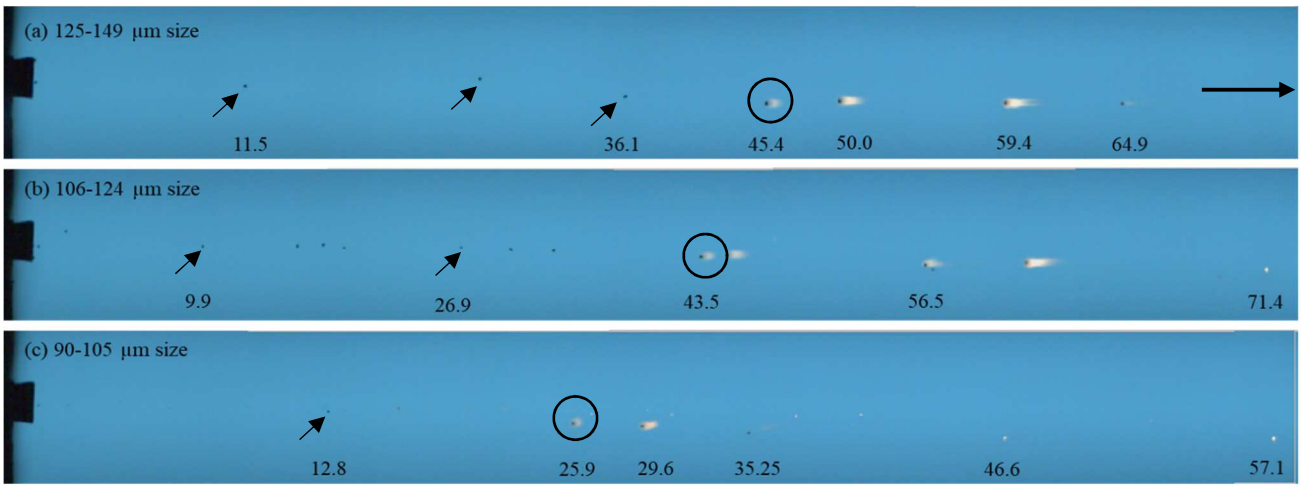

Figure 4-5. High-speed videography of a single coal particle ignition in R-O conditions at a nominal gas temperature of 1300 K for (a) 125-149 µm, (b) 106-124 µm, and (c) 90-105 µm particle size ranges. The flow is from left to right.

Particles in the 75-89 µm classification are difficult to visualize among the others presented in Fig. 4-2 to Fig. 4-5. Thus, the results of this size range for the four conditions (i.e., O at 1800 K, O at 1300 K, R-O at 1800 K, and R-O at 1300 K) are presented in terms of particle emission

intensities. Luminous emissions due to both volatile and char combustion are normalized by the maximum intensities and presented in Figure 4-6. The magnitude of the emission intensity may differ for individual particles, but the characteristic times and trends are repeatable. The results show that ignition delays in the O and R-O conditions at 1800 K are 5 ms and 13 ms, respectively. Thus, the difference in ignition delays can be attributed to the different oxygen concentrations in O and R-O conditions. However, at a low nominal gas temperature of 1300 K, the normalized emission intensities in both R-O and O are very similar, and the ignition delay is not significantly different (green and red profiles in Fig. 4-6). Consistent with other larger sizes, this result shows that particle heating to a sufficient temperature is critical to ignition in 1300 K gas temperature, irrespective of the oxygen concentration.

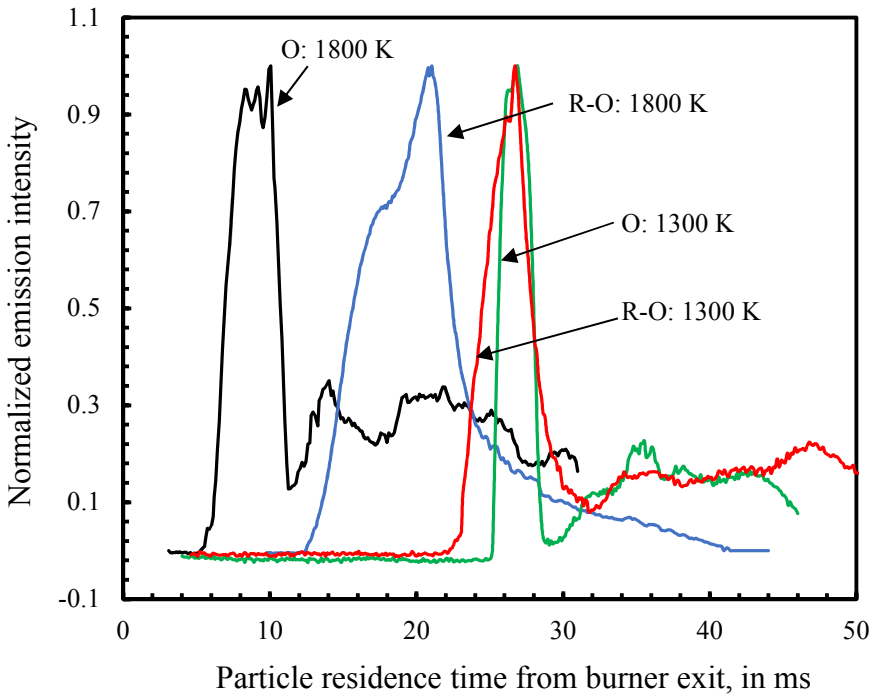

Figure 4-6. Normalized light emission intensity vs. particle residence time.

4.5.3 Ignition time and particle size statistical results

This section presents the data obtained from the algorithm developed in MATLAB and discussed in Section 4.4 for simultaneous determination of particle size and ignition delay time. Figure 4-7, a scatter plot, shows ignition delay times on the vertical axis and the corresponding particle sizes on the horizontal axis. The plot shows data for two conditions, which are 1800 K gas temperature in O condition, and 1800 K gas temperature in the R-O condition. The exact size of each particle at its ignition point is obtained. Figure 4-7 suggests that particle ignition delay time is strongly independent of particle size for an 1800 K gas temperature in the O condition, since the ignition delay times remain almost constant as particle size changes from 75 μm to 150 μm. With high excess oxygen and a high gas temperature, the particles ignite irrespective of their sizes.

However, for 1800 K gas temperature in the R-O condition, ignition delay times fairly but weakly correlate with particle size, with significant variance about the mean. Also, the ignition delay times are longer than those at 1800 K gas temperature in the O condition. The difference between the O and R-O conditions is the reducing-to-oxidizing environment and its characteristic oxygen composition profile. Thus, as seen in Figure 4-7, the effect of this transition on ignition delay times is not pronounced at a high heating rate for all particle sizes, further affirming one of the conclusions in Chapter 3 and Section 4.5.2, which is that heating rate has a first order effect on ignition delay time.

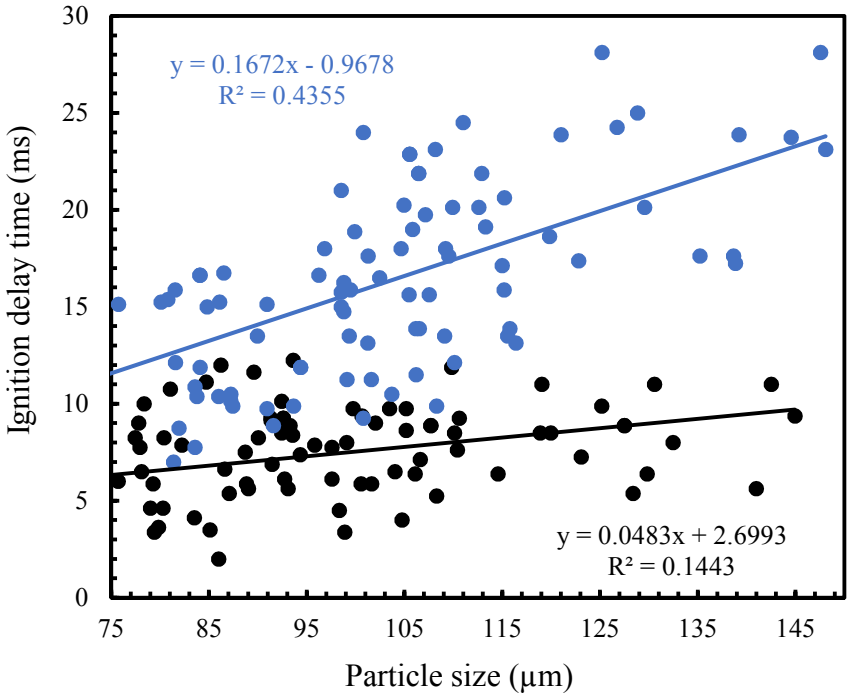

Figure 4-7. Scatter plots of ignition delay time vs. particle size before ignition. Black scatter data corresponds to nominal 1800 K gas temperature and O condition, and the blue scatter data corresponds to nominal 1800 K gas temperature and R-O condition.

Each of the 100-scatter data presented in Figure 4-7 corresponds to a specific size with its characteristic ignition delay time. To verify the accuracy of the usual basis of fundamental ignition studies, which involves the use of a narrow size range, the scatter data are arranged into four size classes (i.e., 75-89 μm, 90-105 μm, 106-124 μm, and 125-149 μm). Then statistical averages of ignition delay times based on these size classifications are compared to those obtained from direct experiments involving those particle size ranges, as described in Sections 4.5.1 to Section 4.5.4.

To give the same basis of comparison, twenty particles from each size cut were tracked and used to obtain the average ignition delay times. As shown in Figure 4-8, the results from the use of a narrow particle size classification in evaluating the ignition behavior of single coal particle (i.e., Figure 4-2 to Figure 4-6) compare well on average to the statistical ignition results. However,

the results from narrow particle size ranges do not capture the variations in ignition delay times, which are associated with the entire given particle size range. As shown in Fig. 4-8, the standard deviations for the ignition-time-vs-actual-size plot are significantly higher than those obtained from experiments using narrow size ranges. Results with and without classifications both show that ignition is fairly independent of particle size for the O condition at 1800 K. As noted before, the dependence of ignition delay time on particle size correlates very weakly in the R-O condition. Thus, if the heating rate is high, devolatilization will be fast and ignition delay time will be independent of the local oxygen concentration.

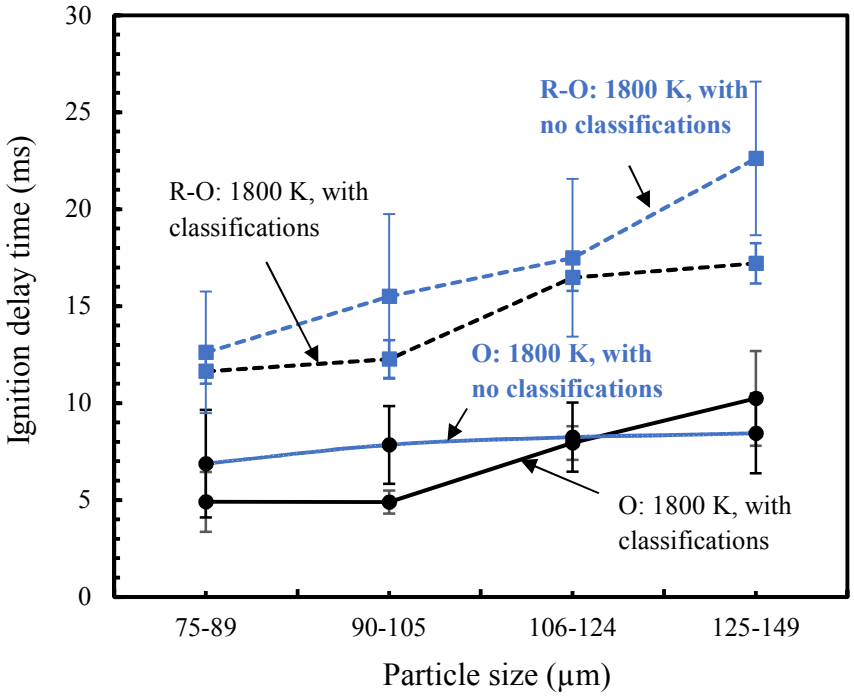

Figure 4-8. Comparison of the average ignition delay times for experimental cases with and without particle size classifications.

4.6 Summary

Using a two-stage flat-flame burner, the effect of particle size on pulverized coal ignition was studied in an oxidizing environment and in a reducing-to-oxidizing environment. Gas temperature had a first order effect on particle ignition. The trend in the ignition time as a function of particle size was the same in both 1300 K and 1800 K gas temperatures. The heating rates at an 1800 K gas temperature reduced the ignition time by a factor of 3 to 5 times over those of a 1300 K environment for the same particle sizes. The ignition delay times increased monotonically as particle size increased in the oxidizing condition at high temperatures. However, in the R-O condition where ignition is oxygen-limited, the ignition delay times were nearly the same for large particle sizes at 1800 K. For a nominal 1300 K gas temperature, ignition delay times were similar in both atmospheres (O and R-O), further affirming that gas temperature (i.e., heating rate) has a first order effect on particle ignition.

The use of narrow size classifications in estimating ignition behavior of coal particles compared well on average to the statistical data obtained from experiments using 75-149 μm particles. This finding confirmed for the first time the common assumption that the ignition behavior of a few sampled particles from a given particle size range provides an accurate representation of the ignition characteristics of the entire particle size range.

An investigation of the role of different particle sizes and the transition from a reducing-to-oxidizing environment on ignition of a pulverized coal stream is presented in Chapter 5.

Chapter 5

The effects of particle size and the transition from a reducing-to-oxidizing environment on pulverized coal stream ignition

5.1 Introduction

Single particle ignition study was the subject of Chapter 3 and Chapter 4. Here in Chapter 5, attention is directed to fundamental studies of coal particle stream ignition in a reducing-to-oxidizing environment using high-speed videography and scanning electron microscopy. Most theoretical and experimental studies of ignition at a fundamental level have concentrated on single coal particles.[45, 46, 56, 67, 94, 100, 118, 119] However, experimental evaluation of particle stream ignition is more relevant to pulverized coal burners than single particle ignition because such particle stream experiments consider the effects of particle interactions on early-stage coal combustion. Also, particle stream ignition affects other processes, such as char burnout and pollutant formation.[120-124]

This explains why there has been numerous work done to model coal particle stream ignition in oxidizing conditions.[69-71, 125, 126] Ryan and Annamalai developed transient ignition models for dense clouds and dilute clouds of coal particles with size ranging from 50 μm to 100 μm and gas

temperature ranging from 1100 K to 1900 K, all at 23% O_2 by mass [71, 72]. Their findings showed that homogeneous ignition occurs in a dense cloud, while single particles in dilute cloud undergo heterogeneous ignition. In addition, quasisteady and transient results obtained for coal particle stream ignition showed that the burning rate of a single particle in the cloud is lower than the burning rate of the same particle in isolation.[51, 70] These modeling efforts have provided great insights on the ignition of particle clouds and computational predictions of group burning rates and flame structures. However, to date, there have been few experimental studies on coal particle stream ignition.[50, 93, 127] Thus, numerical solutions can be confirmed only qualitatively [70], and such confirmation must be approached with caution since conditions and geometries in the available experiments may be widely different from those in the numerical studies.

Ruiz et al. [127] conducted an experimental study evaluating ignition delay for continuous flow of particle stream of high-volatile bituminous coal particles injected into a 9% oxygen environment. Their work showed that ignition time first decreases with increasing particle density, and then increases with further particle loading in a laminar flow reactor. Their work was based on photographs of luminous emission from the burning particles for temperatures between 1023 and 1150 K. Liu et al. [93] conducted experiments on the ignition properties of different coals with different particle loadings, using a laminar entrained flow reactor at gas temperatures between 1200 K and 1670 K. A fixed particle size of 75-105 μm was used for their experiments in oxygen concentration from 12% to 20%. They found that ignition delay time is very sensitive to the temperature of the hot coflow into which the coal stream is introduced. Yuan et al. [59] investigated the ignition behaviors of dispersed coal particle streams using in situ methods in an optical Hencken flat-flame burner. They argued that heterogeneous ignition is dominant at lower temperatures for 65-74 μm particles at 10% to 30% oxygen mole fractions. In a separate work [60],

they studied the collective ignition behavior of dispersed coal particle streams and observed transitions from heterogeneous ignition to hetero-homogeneous ignition for gas temperatures of 1500 K and 1800 K. Volatile evolution and heterogeneous surface chemistry during the hetero-homogeneous mode is discussed based on pyrolysis and heating timescales.

While these experimental studies provide data for computational model validation, none of them addresses coal stream ignition in a combustion environment typical of conventional pc burners with characteristic transition from a reducing-to-oxidizing environment in the near-burner region. Combustion characteristics and ignition can be strongly affected by particles transitioning from reducing to oxidizing atmospheres [68, 109]. Thus, to provide information aimed at addressing flame instability in pc burners, fundamental studies in experimental platform where coal particle stream ignition can be evaluated in the reducing-to-oxidizing environment are important. Furthermore, data of more relevance to burner design and optimization can be obtained if fundamental ignition studies simultaneously consider coal particle streams (as opposed to single-particle studies) in the reducing-to-oxidizing environment.

To this end, the novel two-stage Hencken flat-flame burner described fully in Chapter 2 is used as the experimental platform. Using this burner and with the aim of improving upon the limited data on ignition of coal particle streams, this chapter presents new experimental findings isolating the effects of: (1) particle size, and (2) reducing-to-oxidizing environment (R-O) on ignition of a coal stream. Results are presented for gas temperatures of 1300 K and 1800 K. High-speed, back-lit high-resolution videography is employed to image the particles under oxidizing (O) and R-O conditions for four different particle sizes.

5.2 Experimental methods

Figure 5-1 shows a cross section of the two-stage Hencken burner showing coal particle stream combustion, high speed camera set-up with blue LED background light source. While the burner and the high-speed camera settings stay the same as described in Chapter 4, a new image processing code was developed to extract and average the radially binned vertical profile along the reactor from the exit of the coal feeder up to a height of 9 cm from the burner.

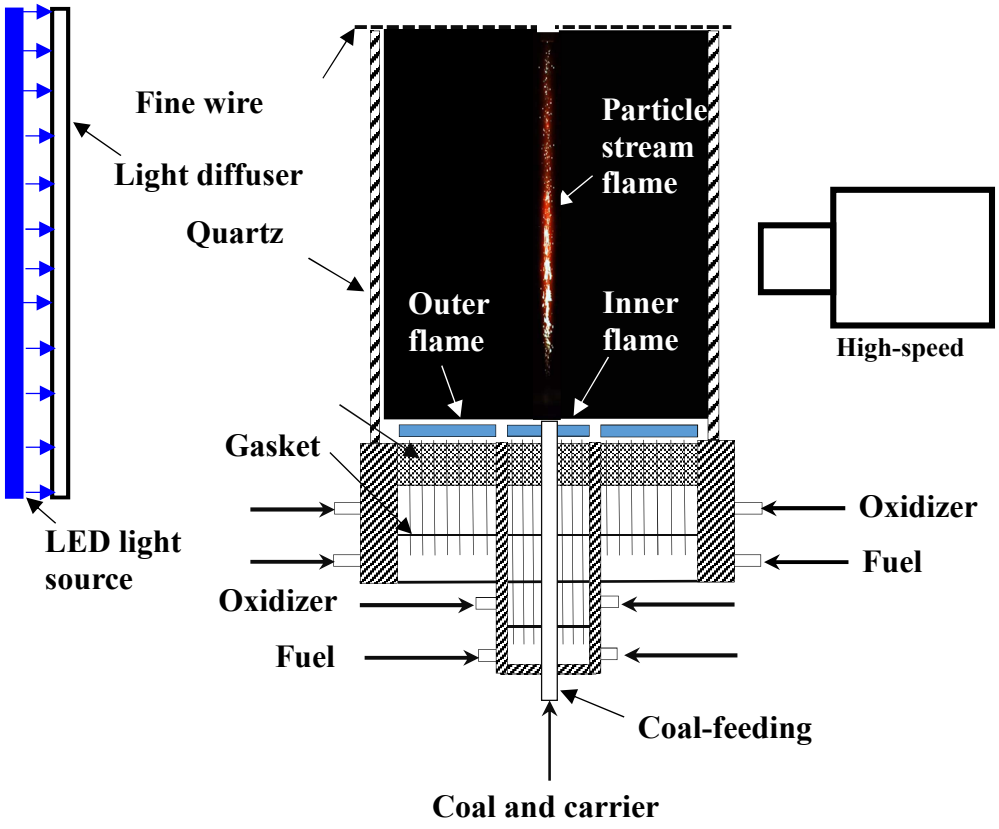

Figure 5-1. Cross section of a two-stage Hencken flat-flame burner, showing coal particle stream combustion, high speed camera set-up with blue LED background light source.

The MATLAB code allows for a quantitative evaluation of the coal stream ignition as determined for each combustion condition using 6000 images. As the coal particle stream is convected from the burner exit, the coal particles ignite and emit visible light. Both gas-phase reactions and char surface oxidation will increase the visible light intensity, as captured by the red sensor of the camera's RGB filter array sensor. The signal from each image represents the visible light intensity. The code is provided in Appendix A-3.

5.3 Particle size used for this study

Powder River Basin (RPB) subbituminous coal was used for this study, and the proximate and ultimate analyses of the coal has been provided in Table 2.2. Coal particles are screened to four size cuts: 63-74 μm, 75-89 μm, 90-124 μm, and 125-149 μm in diameter, to study the effect of particle size. The mass feed rate was similar for all particle sizes.

5.4 Results and discussion

5.4.1 Effect of particle size on coal stream ignition in the 1300 K oxidizing condition

The video frames in Fig. 5-2 show the combustion of coal particle streams for the four size classifications in an environment having a 20 vol.% O_2 composition and a nominal gas temperature of 1300 K. As discussed in Chapter 2, the particles are fed into the reactor through a central coal feeding tube, and the background in the figure is from the blue LED light source. The coal particles leaving the tube can be seen as black particles in the backlit image. The released volatiles ignite, creating a bright volatile flame, which is followed by char oxidation. Given that the diameters of luminosity of the individual particles emerging from the volatile flames are about the same as the

initial particle diameters, the emerging particles are assumed to be char particles. As expected, the char burnout is fastest for the smallest particles. While Fig. 5-2 shows qualitative trends for the four particle classifications using a single frame, Fig. 5-3 presents a plot of normalized intensity with height, obtained from averaging signals from 6000 frames. For the 63-74 µm particles in Fig. 5-2a, thermal emissions from volatiles oxidation can be observed before char oxidation. Hence, homogeneous-to-heterogeneous ignition prevails in coal stream combustion for the 63-74 µm particles. Figures 5-2 b&c show similar qualitative observations with respect to the mode of ignition for 75-89 µm and 90-124 µm particle sizes, respectively. For the 125-149 µm particles, the standoff height is significantly longer due to slower particle heating, with homogeneous particle combustion occurring almost at the end of the optical view of the high-speed camera.

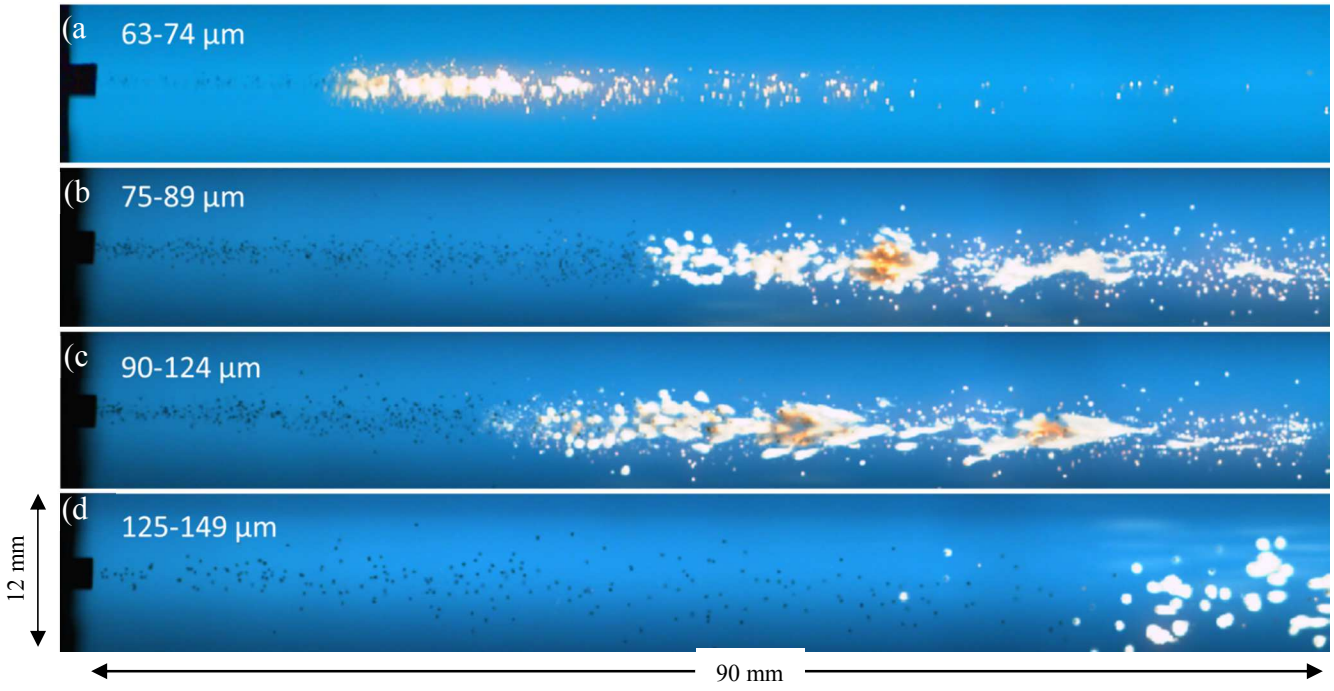

Figure 5-2. Coal stream ignition for different particle sizes in in an environment of 20 vol.% O_2 and a 1300 K gas temperature. The flow is from left to right.

The normalized light intensities shown in Fig. 5-3 reveal more general characteristics of ignition for each particle size range, and the results are consistent with Fig. 5-2, in that the location of rapid increase in light emission, which corresponds to coal stream ignition, depends on particle size, and that the relationship is not monotonic with size. For the 63-74 μm and 125-149 μm particles, the location of rapid increase in emission intensity is at 2 cm and 7 cm, respectively. As expected [45, 100, 118, 119], the standoff height should increase with particle size due to slower particle heating, and delayed devolatilization. Figure 5-3 agrees with this expectation except for the 90-124 μm particle stream, where the location of the rise in emission intensity is between those of the 63-74 μm and 75-89 μm coal streams, as can also be observed in Fig. 5-2. This exception is consistent with earlier findings on single particle ignition done by Essenhigh et al. [67, 119] and Juntgen et al.[111, 128] Those works showed that coal particle sizes well below 110 μm ignite heterogeneously and that homogeneous ignition becomes prevalent for particles well above 110 μm. However, 90-124 μm particles are able to produce significant amount of volatiles (about an order of magnitude above smaller particles), and yet small enough that temperature is not a barrier to high volatile flux. Thus, the significant reduction in the standoff height can be attributed to the enhancement of the homogeneous combustion.

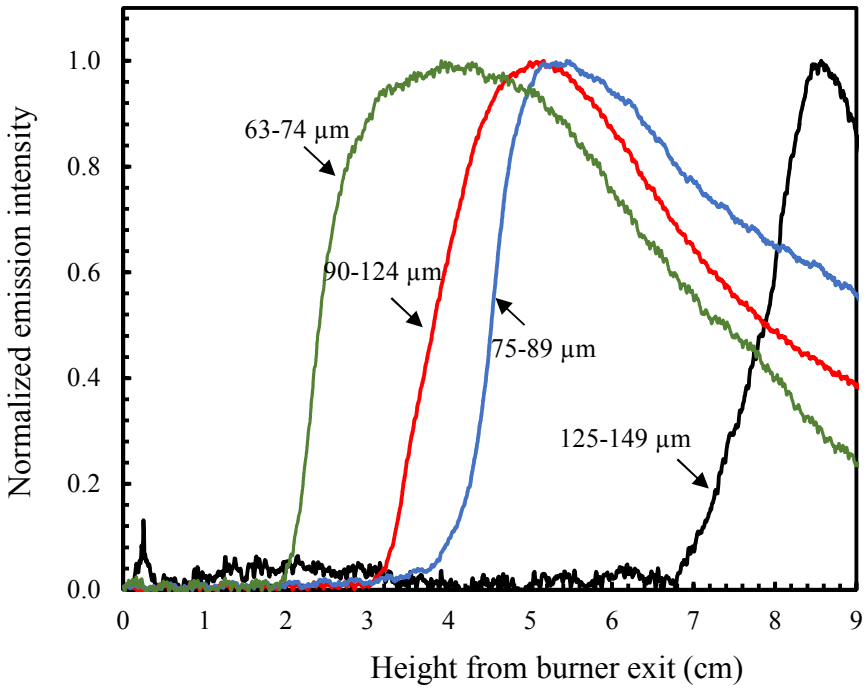

Figure 5-3. Normalized emission intensities for different particle sizes in an environment of 20 vol.% O_2 and a 1300 K gas temperature.

5.4.2 Effect of particle size on coal stream ignition in the 1800 K oxidizing condition

Now we consider coal particle streams injected into a combustion environment of nominally 20 vol.% O_2 and 1800 K. Video images of coal particle combustion in this condition for the four particle size classifications are presented in Fig. 5-4. The trend and the mode of ignition of the particle streams in this higher-temperature environment is similar to that in the lower-temperature environment for the four particle sizes; this is in contradistinction to the single particle experiment were hetero-homogeneous ignition has been reported for this particle size range and in high gas temperature.[60] There are significant reductions in standoff heights at this temperature for all four

particle sizes but no differences in trends, suggesting that the higher heating rate affects ignition times but not ignition modes. The length of the volatile flame can be seen directly in Fig. 5-4 (as labeled) and by the broad region of high emission intensity in Fig. 5-5. The length increases with particle size due to the increase in volatile mass with particle size. Prior to the extinction of the volatile flame in Fig. 5-4(d), long tar tail combustion, oriented along the gas flow streamline, is seen for the 125-149 size μm particles. The tail flame is tar combustion, as indicated in previous studies.[54, 129]

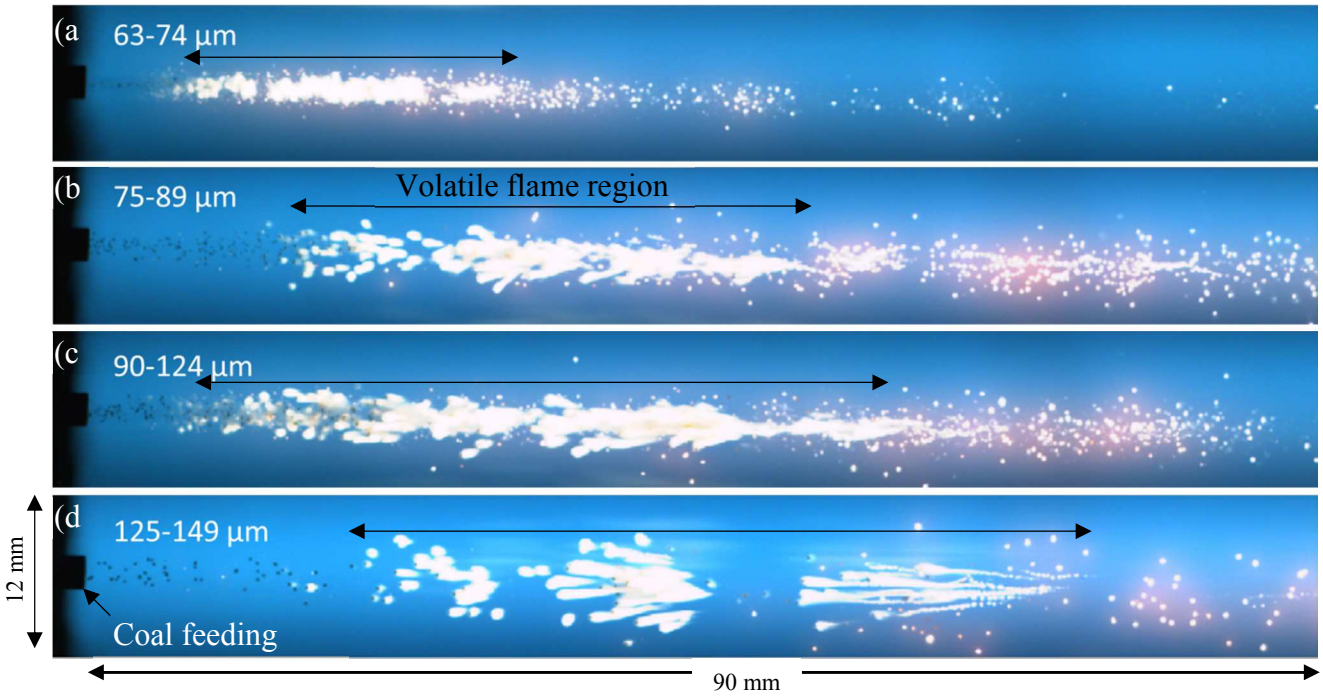

Figure 5-4. Coal stream ignition for different particle sizes in an oxidizing environment at 1800 K. Flow is from left to right.

The results in Fig. 5-5 are qualitatively consistent with the lower gas temperature results presented in Fig. 5-3, with the smallest particle size having the lowest ignition delay and fastest char burnout. Single particle theories have shown that ignition mode should be different as

temperature increases.[35, 130, 131] However, theories that include particle interactions and group devolatilization showed that minimum ignition temperature ignition which would increase with size under single particle studies decreases with size under coal stream ignition.[69] On ignition mode, theory has shown that ignition that will be heterogeneous in single particle studies become homogeneous in coal stream under the same ambient conditions.[68-70, 125] Thus, group devolatilization as a result of particle interactions is at play on the mode of coal stream ignition observed at different temperatures. The interactions between the volatiles of many particles could easily reach the lower flammability limit to support homogeneous ignition, irrespective of the gas temperatures. We observed this experimentally with homogeneous ignition mode for all sizes for both temperatures but the time at which these events happened are very different at different temperatures. With the higher gas temperature, the standoff height is shorter, and the evolution of the entire lifetime of the particle can now be observed in the available field of view for the 125-149 μm particles. The particles initially ignite homogeneously, as they did in the lower gas temperature environment. Subsequently, after the first flame extinguishes due to depletion of volatiles, a second ignition involving char oxidation occurs, leading to the two-peak normalized emission intensity profile in Fig. 5-5.

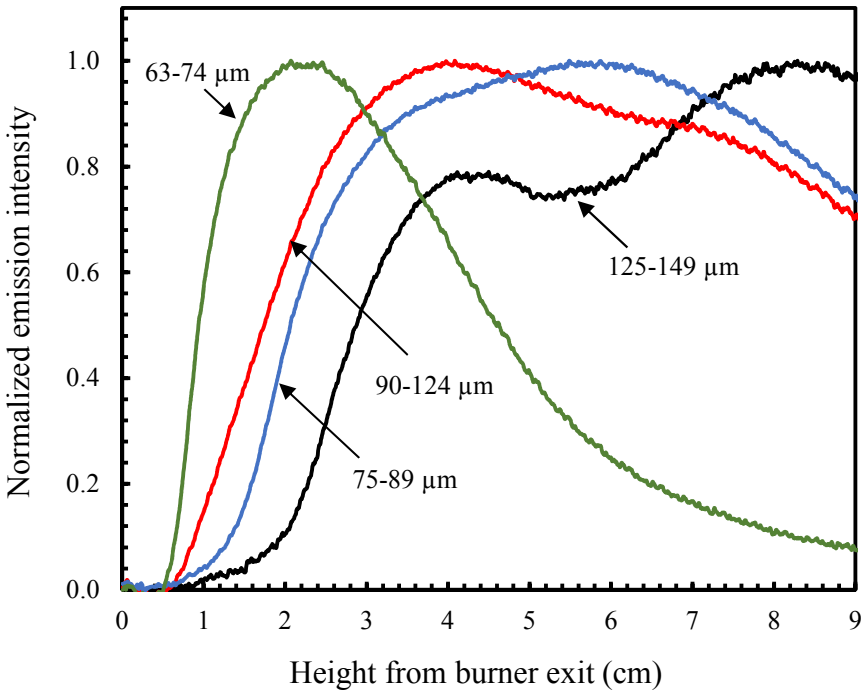

Figure 5-5. Normalized emission intensities for different particle sizes in an environment of 20 vol.% O_2 and a 1800 K gas temperature.

Particle tracking was used to obtain particle residence time. The particle stream ignition delay time is defined as the time corresponding to the maximum rate of change of slope in the normalized emission intensity. This criterion has been shown to give similar results to those with a criterion in which half of the injected coal particles have ignited (as approximated by the time corresponding to 50% of the maximum intensity[93]). Figure 5-6 shows the ignition delay times for different particle size classifications. Ignition delay times are significantly shorter at 1800 K than 1300 K, however the trends are the same for both gas temperatures. With high oxygen concentration, the ignition delay time increases with size from 63-74 µm to 75-89 µm. Since the 90-124 µm particle stream has characteristically lower minimum ignition temperature, the ignition delay time for 90-124 µm particles is even lower than that of 75-89 µm particles at the same temperature. This is consistent

with other results in Fig. 5-2 and Fig. 5-4; the ignition delay time increases generally with particle size, apart from the 90-124 μm particles.

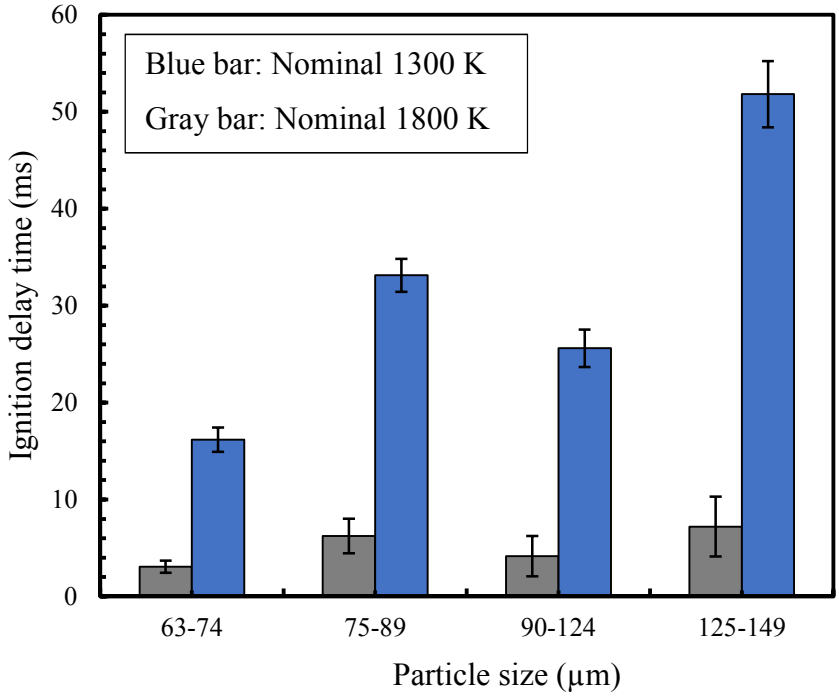

Figure 5-6. Ignition delay times as a function of particle sizes in an environment of 20 vol.% O_2 for nominal gas temperatures of 1300 K and 1800 K.

5.4.3 Effect of particle size on coal stream ignition in the 1300 K reducing-to-oxidizing environment

The role of particle size on ignition in an environment where the particles experience a reducing-to-oxidizing environment is now presented. Figure 5-7 shows the video images in the R-O environment at 1300 K for the different particle sizes. The flame shown in Fig. 2-15, which results from combustion of the products of incomplete combustion of the flat flame, is 2 cm high, and is identified in Fig 5-7a. The height of this flame stands for the characteristic length of the reducing zone and it is the same height for the other three video images in Fig. 5-7.

The characteristic of ignition in the R-O environment are quite different from that of the oxidizing environment (cf. Figs 5-2 and 5-4). Plots of the normalized emission intensities for the four particle sizes in Fig. 5-8 show the differences more clearly, with a standoff height of 2 cm for the 90-124 μm coal stream and about 3 cm for other particle sizes. Compared with the oxidizing environment, there are differences in the locations of ignition, the trends in standoff height, and the emission intensities. Referring to Fig. 2-12, Fig. 2-13 and Fig 2-14 for the axial distributions of oxygen and temperature, it is clear that the differences are not due to temperature, but rather the very different composition histories that the particles experience. As the particles enter the burner and are rapidly heated, they experience a reducing environment, resulting from the products of the rich inner flame. The volatiles that are released in this zone mix with the products of the rich flame and the mixture is burned in the diffusion flame. When the particles pass through this flame, they continue to devolatilize but the oxygen concentration is low, as the composition is primarily products of combustion from the diffusion flame. Traveling downstream, the oxygen and volatile concentrations increase with distance and, at some point, the concentrations are sufficiently high to support combustion, and the volatiles burn homogeneously. Visible flames can be observed at nearly the same standoff heights for all but the 90-124 μm coal stream. Similar standoff heights suggest that ignition in the R-O environment is strongly influenced by the location at which volatiles mix with sufficient oxygen, about 4-7 vol.% oxygen for this gas temperature. Thus, this trend in the standoff height suggests that homogeneous ignition prevails in R-O environments with nominal gas temperature of 1300 K.

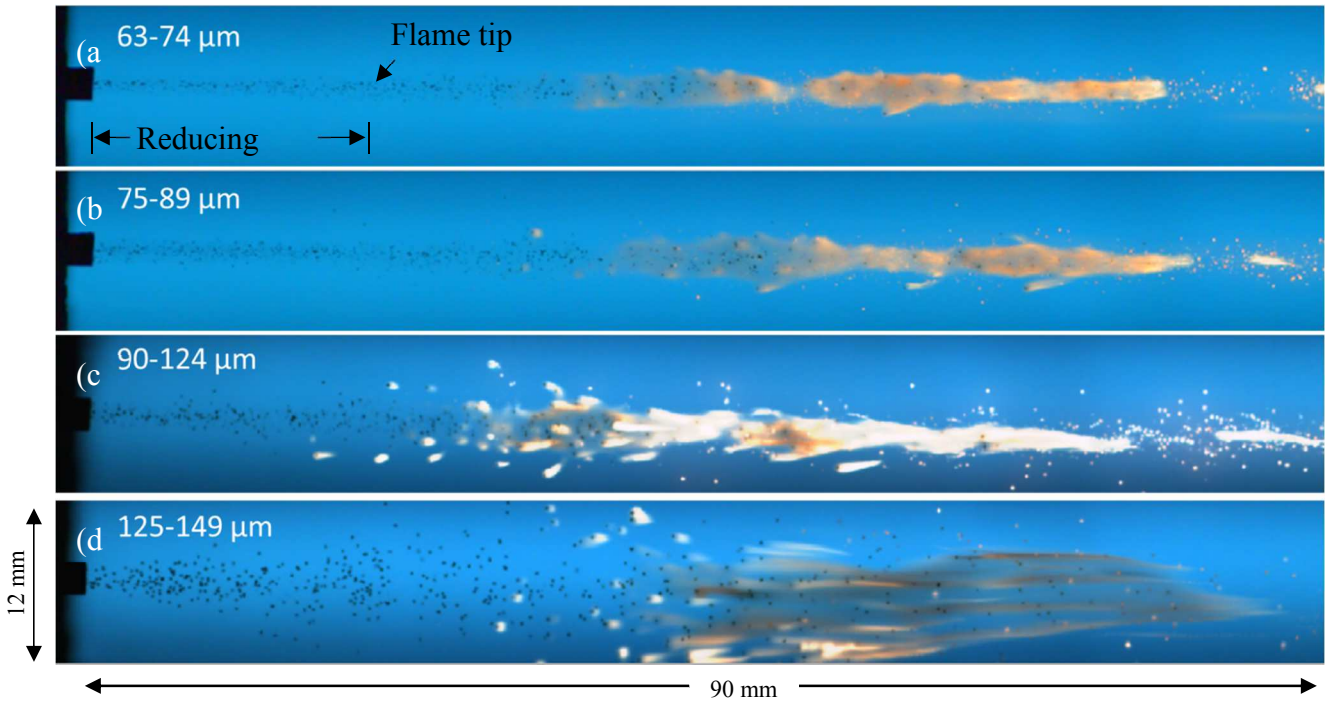

Figure 5-7. Coal stream ignition for different particle sizes in a reducing-to-oxidizing environment at 1300 K. The flow is from left to right.

As discussed previously in Sections 5.4.1 and 5.4.2, high volatile flux enhances homogeneous ignition for the 90-124 µm coal particles. Thus, the early oxidation of volatiles released by particles in the 90-124 µm coal stream reduces the standoff height. Surprisingly, the standoff height for the 125-149 µm coal stream decreases from about 7 cm in oxidizing environment to 3 cm in the R-O environment. Note that the burner is up-fired. So, inertial effect on particle trajectory increases with particle size. Larger particles, with higher volatile flux, particle rotation will increase with particle size due to higher volatile flux. This, together with inertial effect, will contribute to longer time before the particles relax to the vertical gas velocity field. Thus, the larger particle sizes show more dispersion from the centerline gravity, particularly noticeable in the 125-149 size µm particles. Noting the shape of the diffusion flame in the reducing-to-oxidizing environment, this

explains why ignition can be seen in Figs 5-7c&d, in regions away from the centerline, and this partially explains why ignition is seen to occur earlier for larger sizes. The transition of particles through a diffusion flame leads to enhanced release of volatiles that are subsequently oxidized. Thus, the standoff height is shorter for the 125-149 µm coal stream in the R-O environment compared to the oxidizing environment. Although there is no significant difference between the intensity profiles for the 63-74 µm and 75-89 µm particles, the standoff heights are higher in the R-O environment than in the oxidizing environment, indicating the significance of oxygen volume percent on ignition for these smaller particle sizes. Thus, in addition to particle size, the standoff height for different particle size classifications can be affected by the local oxygen volume percent in a low gas temperature environment.

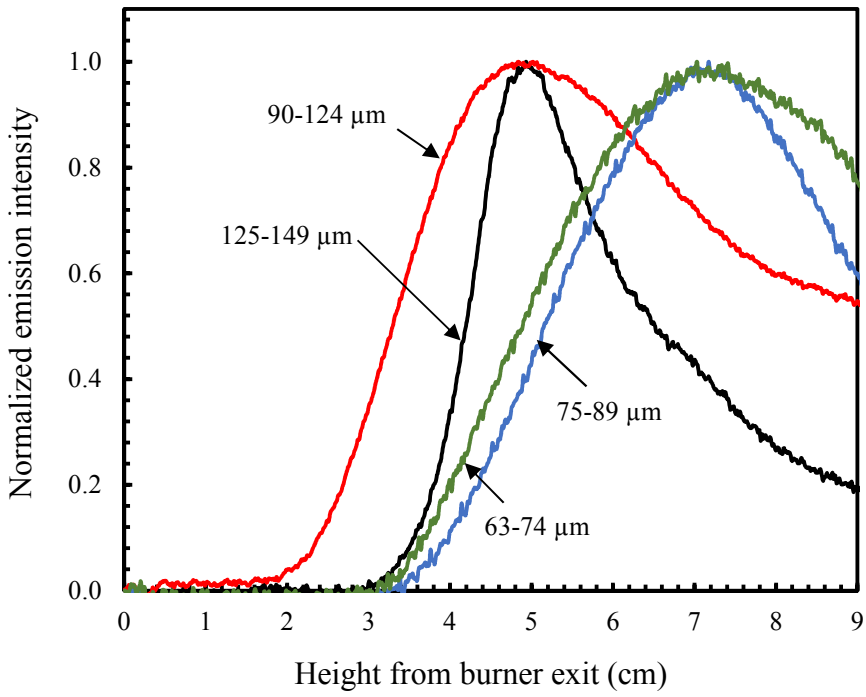

Figure 5-8. Normalized emission intensities for different particle sizes in an environment with a reducing-to-oxidizing environment and a 1300 K gas temperature.

5.4.4 Effects of particle size on coal stream ignition in the 1800 K in reducing-to-oxidizing environment

Figure 5-9 shows the video images for the different particle sizes in the R-O environment at 1800 K nominal gas temperature. In this higher-temperature environment, ignition occurs at about the same height for all particle sizes. Figure 5-10 clearly shows this observation with the plots of emission intensities in the high temperature R-O condition. As noted above, there are marked differences in the emission intensity profiles at 1800 K under oxidizing conditions (Fig. 5-5). Under oxidizing conditions, the volatiles ignite locally as they are released, leading to distinct ignition curves as a function of size (Fig. 5-5), since the rate of heating, and thus volatile release, is dependent on particle size. Under R-O condition, volatiles begin to release within the reducing zone due to the high heating rate, but the volatiles cannot ignite until after the reducing zone, when the oxygen concentration has increased sufficiently for combustion. As the particles stream through the high-temperature flame sheet and mix with oxygen, the volatiles ignite, leading to the observed similarity in the emission intensity profiles for the different particle sizes (Fig. 5-10).

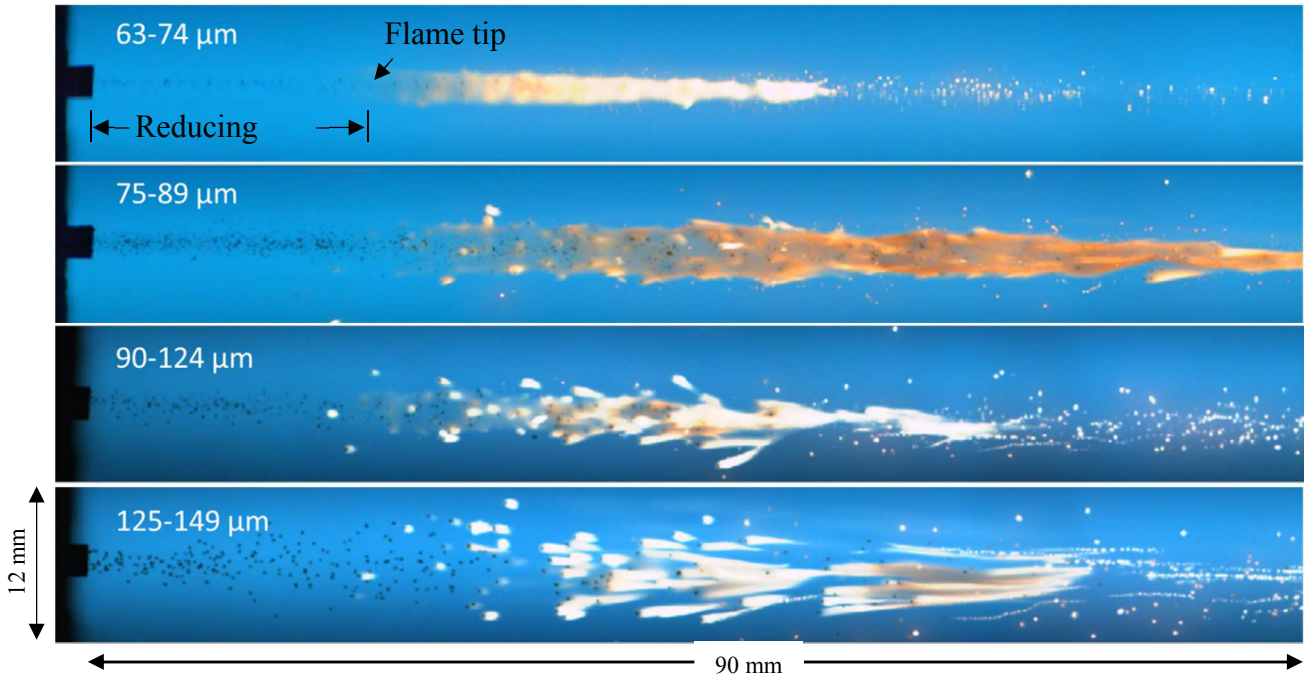

Figure 5-9. Coal stream ignition for different particle sizes in a reducing-to-oxidizing environment at 1800 K. The flow is from left to right.

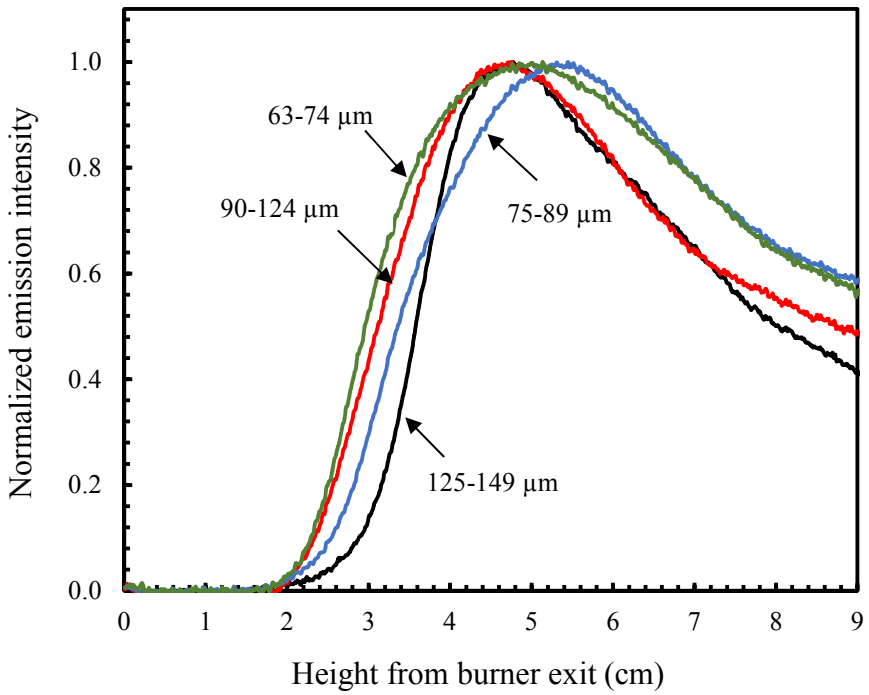

Figure 5-10. Normalized emission intensities for different particle sizes in an environment with a reducing-to-oxidizing environment and a 1800 K gas temperature

5.4.5 Particle size and ignition delay in reducing-to-oxidizing environment

Figure 5-11 is a plot of ignition delay time as a function of particle size in a reducing-to-oxidizing environment for nominal gas temperatures of 1300 K and 1800 K. In contradistinction to the results at 1300 K for oxidizing conditions (Fig. 5-6), there is no significant difference in the ignition delay times as particle size increases from 63-74 μm to 75-89 μm under reducing-to-oxidizing conditions. For the smaller particle sizes (i.e., 63-74 μm and 75-89 μm), ignition is thus oxygen dependent at this gas temperature, i.e., ignition of the released volatiles is limited by the availability of oxygen for the small particles.

At 1300 K, the ignition time for the 63-74 μm size increases from an average of 16 ms for the oxidizing condition to 34 ms in the reducing-to-oxidizing condition. As particle size increases in the lower gas temperature environment, ignition becomes particle-temperature dependent. Since the diffusion flame sheet characterizes the reducing-to-oxidizing environment, particles flow through the flame sheet with a relatively higher temperature than those in oxidizing conditions. The local temperature at the flame sheet enhances volatile release and the released volatiles then ignite as they mix with oxygen. From the blue bars in Fig. 5-11, a decrease in ignition delay is observed as particle size changes from 75-89 μm to 90-124 μm. Thus, there is a crossover from oxygen-dependent ignition to particle-temperature-dependent ignition. However, compared to the oxidizing conditions with no flame sheet in Fig. 5-6, the ignition delay time for 125-149 μm in the oxidizing condition is significantly higher than in reducing-to-oxidizing condition, further affirming that heating rate has a strong effect on ignition. However, ignition of the released volatiles is limited by the availability of oxygen for all particle sizes at the 1800 K gas temperature; hence ignition delay times are higher in the R-O condition than in oxidizing conditions (Fig.5-6).

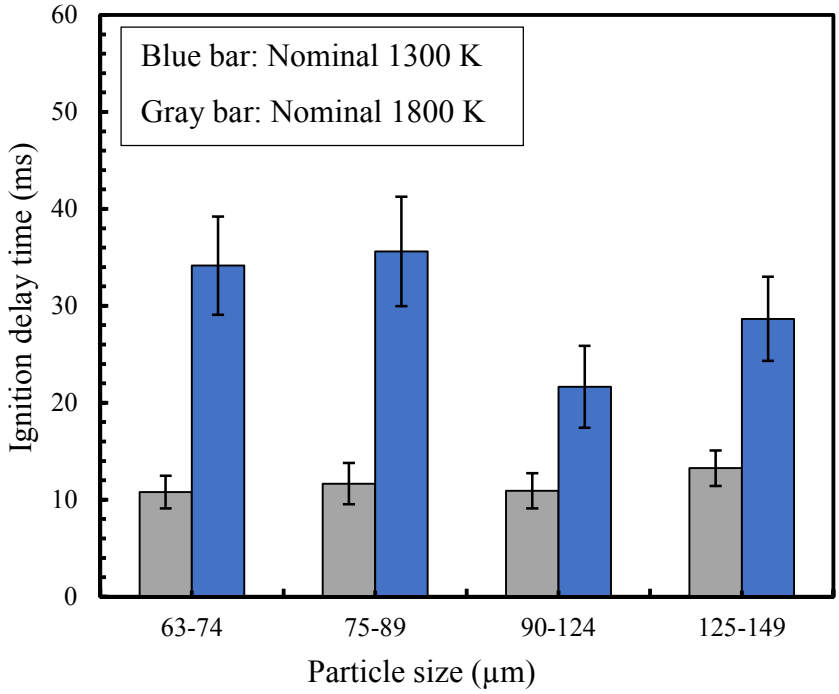

Figure 5-11. Ignition delay times as a function of particle sizes in the reducing-to-oxidizing environment for nominal gas temperatures of 1300 K and 1800 K.

5.5 Scanning electron microscopic analysis of particles: Effect of particle size, temperature and oxygen composition

5.5.1 Micrographs of particles in the 1300 K oxidizing and R-O conditions

Scanning electron microscopy (SEM) was used to characterize the 63-74 μm and 125-149 μm particles, sampled at a residence time of 50 ms, corresponding to a time that is post ignition [59]. Samples are obtained at the same residence time of 50 ms for all conditions by changing the heights accordingly. The scanning electron micrographs presented are representative of many particles surveyed. Insights into the controlling ignition modes of ignition can be gained from these micrographs. Figure 5-12 presents SEM images at a 1300 K gas temperature for the 63-74 μm

particles under a) oxidizing and b) reducing-to-oxidizing conditions. Small volumetric release of volatiles means more direct oxygen attack on the particle surface. Thus, for the 63-74 μm particles under oxidizing conditions, particle surface oxidation is dominant at this residence time, as indicated by the rough surfaces with varying depths and apparent porosities. On the other hand, under reducing-to-oxidizing conditions, the particles show a surface lacking macroporosity, which is expected for particles with no significant surface oxidation. This implies devolatilization is still significant at this residence time. Thus, in the R-O environment at 1300 K, the ignition of particles below this sampling time must be homogeneous since the particle surface is shielded from the limited supply of oxygen by the released volatiles.

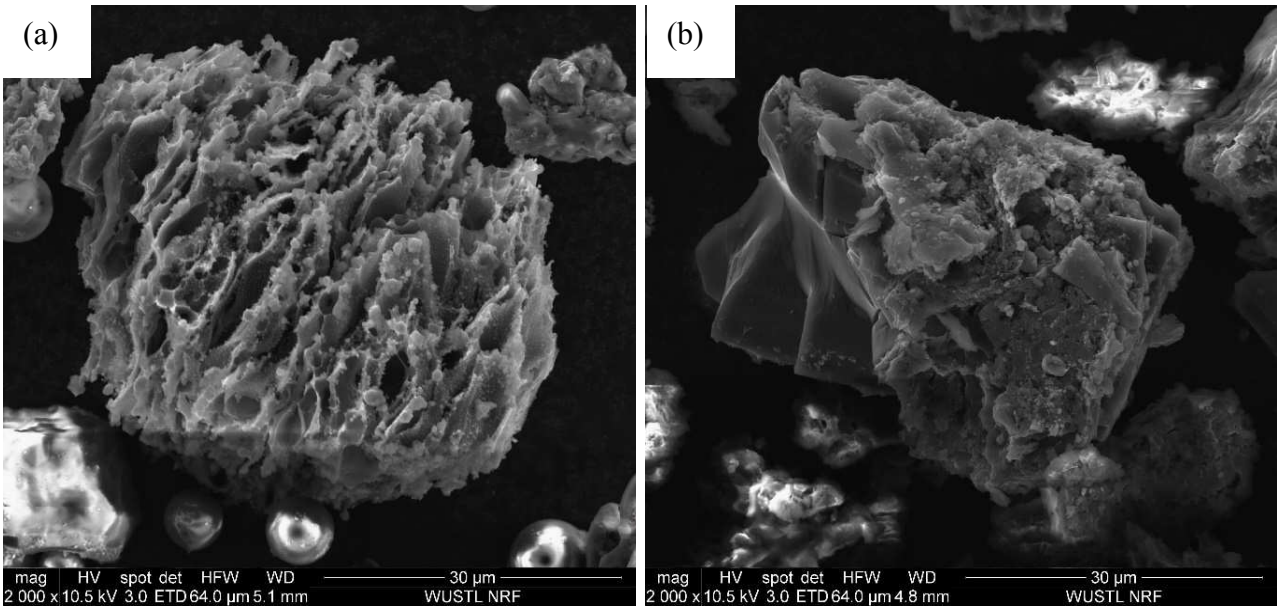

Figure 5-12. SEM images of 63-74 μm particles in (a) an oxidizing condition, and (b) a reducing-to-oxidizing condition at a 1300 K gas temperature.

Micrographs of the 125-149 μm particles are also obtained. Figure 5-13 presents SEM images taken for a) oxidizing and b) reducing-to-oxidizing conditions. Similar to the results in [45], significant particle devolatilization is still taking place after ignition and the particle can be classified as inertoid with characteristically low porosity and high volatile layer thickness [132, 133]. Thus, the particle surface is not accessible to oxygen for oxidation. Hence, since the volatiles must ignite and burn before particle surface oxidation, homogeneous ignition prevails for the large particles irrespective of whether combustion is in an oxidizing or reducing-to-oxidizing condition.

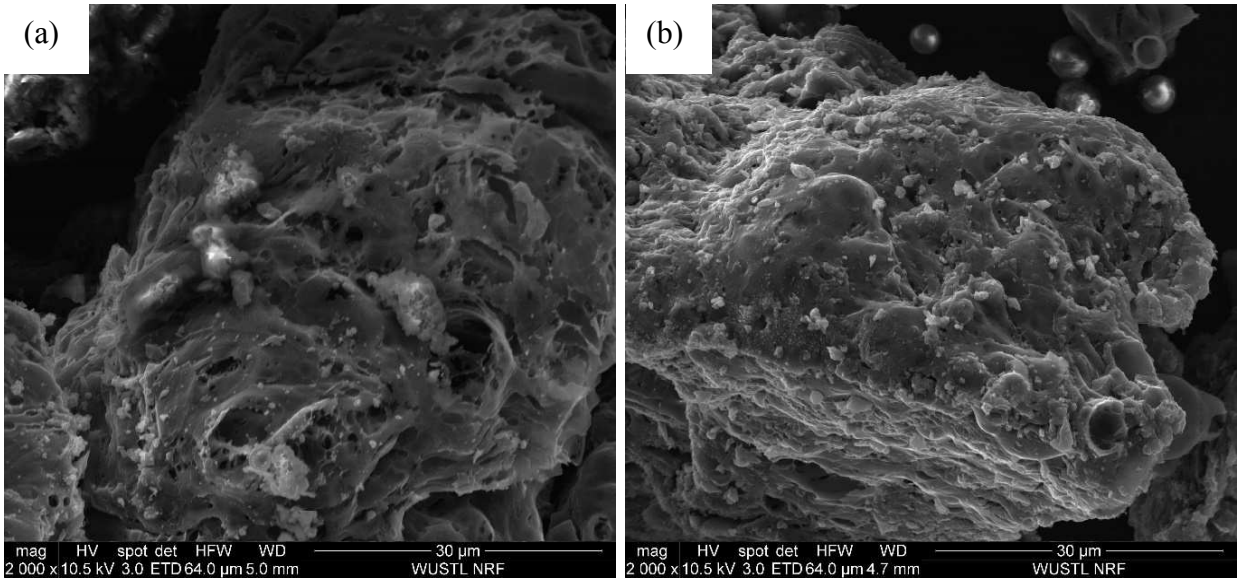

Figure 5-13. SEM images of 125-149 μm particles in (a) an oxidizing condition, and (b) a reducing-to-oxidizing condition at a 1300 K gas temperature.

5.5.2 Micrographs of particles in the 1800 K oxidizing and R-O conditions

Figure 5-14 shows SEM images from the 63-74 μm particles for the 1800 K nominal gas temperature. Unlike the results for the lower gas temperature, oxidizing environment shown in

Fig. 5-12a, Fig. 5-14a shows that at the higher gas temperature, the surface is smooth, suggesting fusion of mineral matter after complete combustion of char.[134] However, Fig. 5-14b shows that combustion is not complete at 50 ms for the R-O environment, with the particle displaying a significantly rough surface. Thus, the incomplete combustion is an indication that particles in the R-O environment have longer homogeneous ignition delay times and longer char burnout times than those in the oxidizing environment, a consequence of the delayed exposure to oxygen.

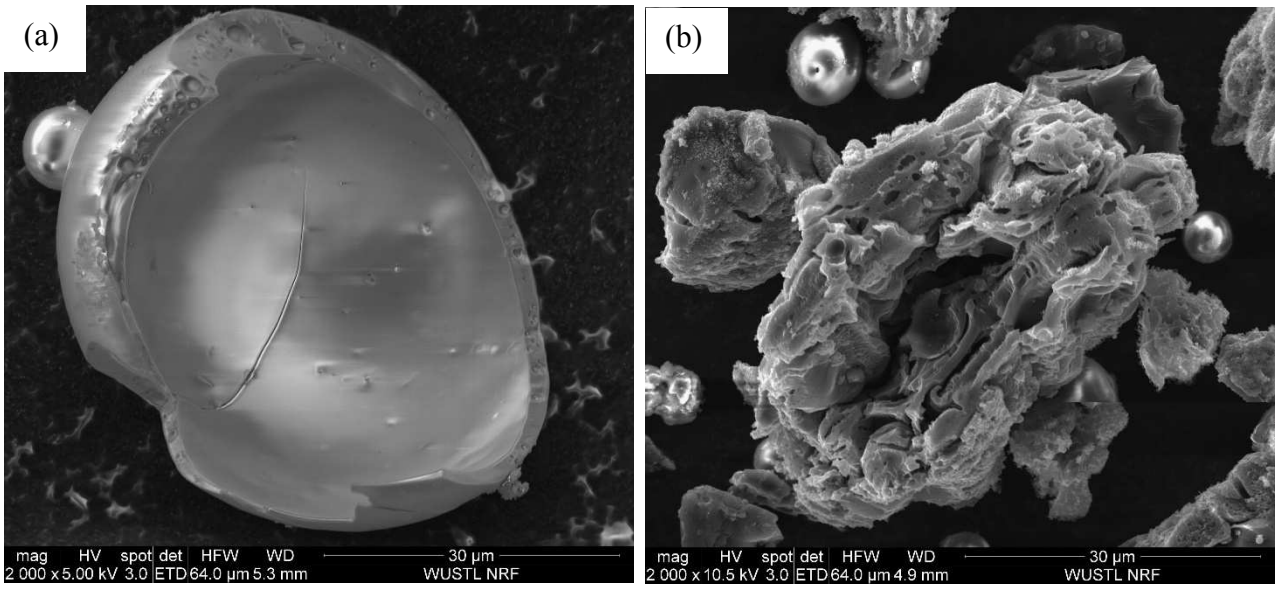

Figure 5-14. SEM images of 63-74 µm particles in (a) an oxidizing condition, and (b) a reducing-to-oxidizing condition at a 1800 K gas temperature.

SEM photographs of the 125-149 µm particles are shown in Fig. 5-15. For both environments, sponge-like, irregular surface structures are observed, indicating char surface oxidation [132, 135]. Based on the videography in Fig. 5-4 and Fig. 5-9, we observe that for the 125-149 µm particles, the volatiles ignite first, after which the char particles undergo an induction period and then ignite

heterogeneously. Thus, the similarity in the morphologies in Figs. 5-15a and b suggest that the particles are sampled at the stage in which the homogeneous mode is complete and the heterogeneous mode is ongoing.

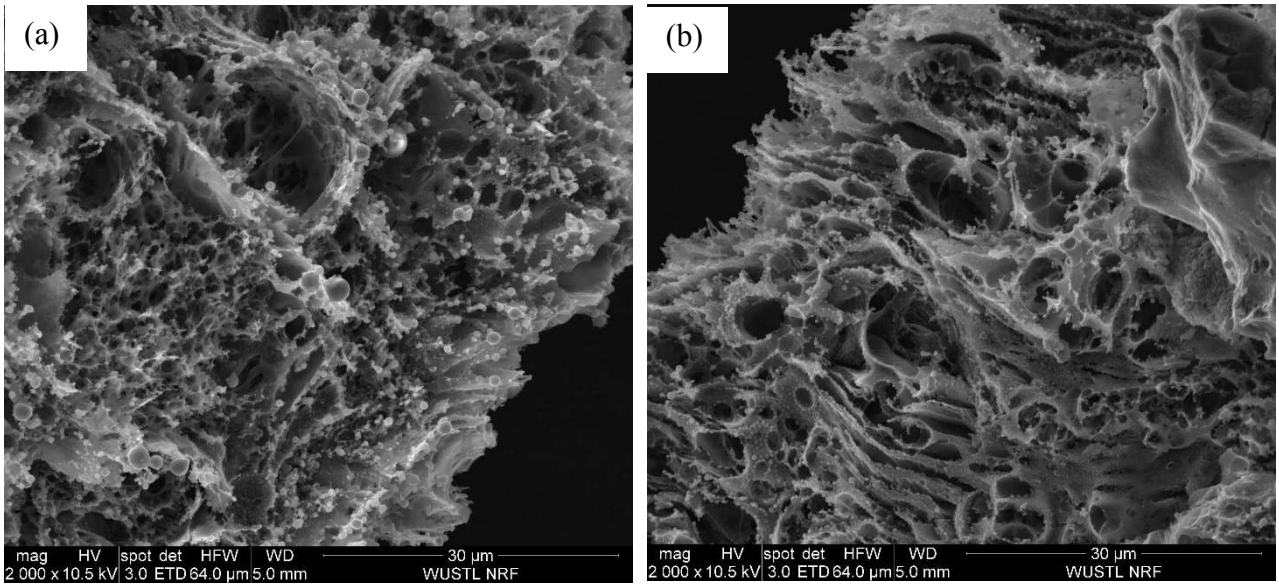

Figure 5-15. SEM images of 125-149 µm particles in (a) an oxidizing condition, and (b) a reducing-to-oxidizing condition at a 1800 K gas temperature.

5.6 Summary

In an effort to replicate the characteristics of the near-burner region of a conventional pulverized coal furnace, we employed a two-stage Hencken flat-flame burner, and studied the effects of the reducing-to-oxidizing environment on ignition modes and ignition delays for coal particle streams as a function of particle size. The results showed that ignition in the reducing-to-oxidizing environment can be quite different from those in the oxidizing environment, especially for small particles. For all particle size ranges considered, homogeneous-to-heterogeneous ignition is observed. Ignition delay times are independent of particle size at 1800 K gas temperatures but

depend significantly on particle size at 1300 K. This suggests that ignition delay is determined by the amount of volatiles released (depending on particle size and gas temperature) and the local oxygen concentration. For the 1800 K nominal gas temperature in either the oxidizing or the reducing-to-oxidizing environment, ignition delay time is independent of particle size. However, the reducing-to-oxidizing environment increases ignition delay times by 100% on average over those of oxidizing conditions at 1800 K gas temperature. In the reducing-to-oxidizing environment, longer ignition delay times are due to the oxidation of volatiles released before the particles exit the volatile flame front at the flame front. Hence, for homogeneous ignition to occur, more volatiles must be generated downstream of the reducing-to-oxidizing environment zone. On the other hand, in 1300 K nominal gas temperature, ignition delay times strongly depend on particle size in the stream. Interestingly though, there exists a crossover at which the ignition delay times in reducing-to-oxidizing environment are less than those of oxidizing conditions for large particles (i.e., 90-124 μm and 125-149 μm) at 1300 K.

Chapter 6

Coal combustion modeling and analysis

6.1 Introduction

Based on the unique features of the two-stage Hencken flat-flame burner presented in Chapter 2, the role of combustion environments (i.e. oxidizing or reducing-to-oxidizing environments), particle size, and gas temperature have been explored in Chapters 3-5. Those results show that ignition of coal particles is strongly dependent on gas temperature, i.e., the heating rate affects the ignition delay time. Depending on the gas temperature, other factors become significant as well. For example, particle size becomes an important factor for ignition at a gas temperature of 1300 K, and the controlling mechanism shifts from oxygen-dependent to temperature-dependent as particle size increases. In an 1800 K gas environment, the ignition delay time in the reducing-to-oxidizing environment increases compared to that in the oxidizing environment.

In this chapter, attention is directed towards theoretically modeling both the pre-ignition and the post-ignition stages of particle combustion. The pre-ignition modeling evaluates quantitatively early-stage processes of coal combustion without volatile and char oxidation (i.e., before ignition). These processes include particle heating, demoisturization, and devolatilization. To clarify the effect of gas temperature and particle size on the volatile release rate and ignition, particle temperature-time history and devolatilization times are compared for different particle sizes. Then, the roles of particle size and environments on char ignition and char burnout are evaluated in the post-ignition modeling. With a methane-fueled flat-flame, there is a significant amount of steam

and carbon dioxide around the particles. Hence, the model evaluates the significance of char gasification along with char oxidation on particle burnout.

6.2 Pre-ignition model description

A theoretical model on the early-stage of coal combustion is presented here. Figure 6.1 shows particle heating, demoisturization, and devolatilization as early-stage processes. The goal is to understand the significance of gas temperature on particle heating, demoisturization and volatile release without particle reactions in an oxidizing environment. Since there is no oxidation step in the pre-ignition model, the results for the O condition are the same as for the R-O condition. In other words, gas temperature, and not the oxygen composition, controls particle heating, demoisturization, and devolatilization.

By proximate analysis, a coal particle consists of moisture, volatile, char, and ash. Since volatile release leads to char structure evolution, a dry-ash-free mass variable, $m_{u,}$ was used to represent the unreacted combustible mass.[33] Assumptions made include spherical symmetry, constant properties, unity Lewis number, and no interaction between particles. Assuming plug flow in the reactor, especially for the short residence time during which pre-ignition processes occur, it is reasonably accurate to assume that single particles are effectively suspended in the gas medium.[57]

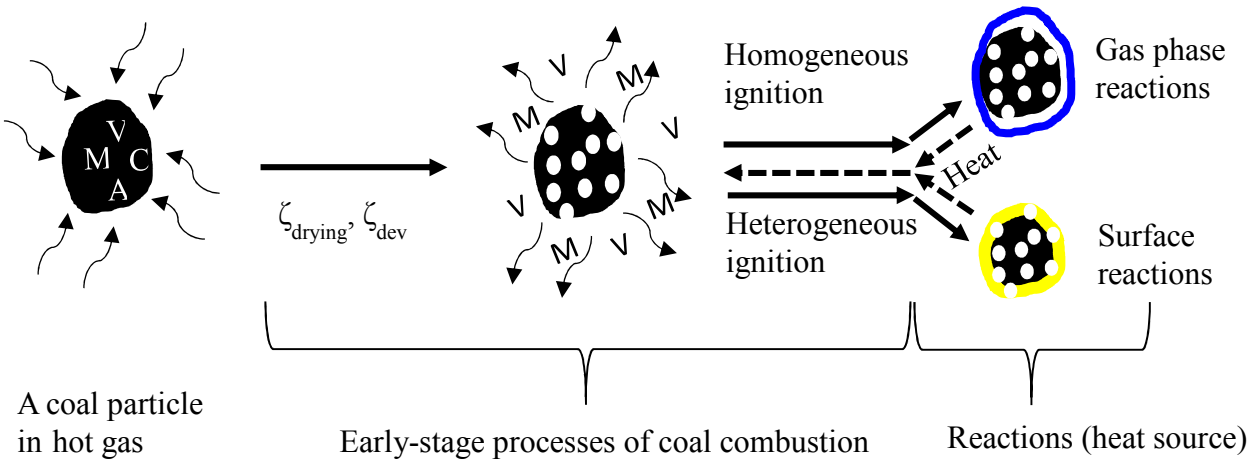

M: Moisture, V: Volatile, C: Char, A: Ash

Figure 6-1. A coal particle undergoing early-stage processes of coal combustion.

Particle size, d_p, is assumed constant during devolatilization [60], but particle density changes as given by Eq. (6.1),

$$\frac{d\rho_p}{dt} = -\frac{6}{\pi d_p^{\,3}}\frac{dm_p}{dt} \tag{6.1}$$

where m_p is the particle mass at a given residence time, and ρ_p is the particle density. The mass balance is given by Eq. (6.2), based on the components that change with time,

$$\frac{dm_p}{dt} = \frac{dm_{H_2O}}{dt} + \frac{dm_u}{dt} \tag{6.2}$$

where m_{H_2O} and m_u are the mass of moisture and unreacted combustible mass (i.e., volatile and char) respectively. Moisture release is based on mass transfer of the moisture in the particle to the gas phase, and Eq. (6.3) describes this transfer [106], where $P_{m,sat}$ is the saturation pressure of water

at a particle temperature T_p, P_{H_2O} is the partial pressure of water in the gas phase, T_g is the gas temperature, A_p is the particle surface area, and M_{w,H_2O} is the molecular weight of water. k_{H_2O} is the mass transfer coefficient of moisture into the gas phase, defined based on a Sherwood number of 2 with the moisture diffusivity depending on residence time, particle mass, and gas temperature.[106, 136]

$$\frac{dm_{H_2O}}{dt} = -k_{H_2O}\left(\frac{P_{m,sat}}{RT_g} - \frac{P_{H_2O}}{RT_g}\right)A_p M_{w,H_2O} \tag{6.3}$$

The devolatilization rate, $\Re_{dev}$, is modeled by using the single step first-order Arrhenius model, given by Eq. (6.4). This model has been used extensively to study coal devolatilization, with the kinetic parameters drawn from experiments [34, 100, 130, 131, 137, 138]. In this work, methane is used as a single pseudo-organic species, as in other works.[100, 106]

$$\Re_{dev} = -\frac{dm_v}{dt} = A\exp\left(-\frac{E_a}{RT_p}\right)\cdot m_v \tag{6.4}$$

Since the particle is immersed in a continuously flowing gas stream, the concentration of volatiles in the gas phase around the particle is proportional to the devolatilization rate [35]. Hence, the volatile mole fraction in the gas phase at the particle surface can be expressed as

$$x_{s,vol} = \frac{\Re_{dev}\cdot m_v}{MW_{vol}\cdot \dot{n}_g} \tag{6.5}$$

Heat transfer to a cold coal particle from a hot gas is through convection, radiation, and heat requirement for demoisturization of the particle. Thus, the energy balance determining the particle

temperature is given by Eq. (6.6). The particle size of interest is between 63 μm and 150 μm, and the Biot number for this particle size range is 0.07 (i.e. Bi <<1) indicates no resistance to heat transfer inside of the particle, so the particle's temperature is uniform.

$$m_p C_p \frac{dT_p}{dt} = hA_p(T_g - T_p) + \varepsilon\sigma A_p({T_w}^4 - {T_p}^4) + \frac{dm_{H_2O}}{dt} L_{H_2O} \tag{6.6}$$

In this pre-ignition model, the coal particle thermochemistry is divided into vaporization and devolatilization both due to particle heating from the surrounding hot gas at nominal gas temperatures of 1300 K and 1800 K. The model is constrained so that there is no volatile release before the moisture is fully removed from the particle, and so that heat addition to the particle provides the latent heat of vaporization, expressed mathematically in Eq. (6.7).

$$-\frac{dm_{H_2O}}{dt} L_{H_2O} = hA_p(T_g - T_p) + \varepsilon\sigma A_p({T_w}^4 - {T_p}^4) \tag{6.7}$$

The equations are solved using a MATLAB program whose algorithm is presented in Appendix A-4. The volatile mole fraction in the gas phase at the particle surface and the particle temperature-time profiles are discussed below.

6.3 Lower flammability limits (LFLs) and ignition

Flammability limits for various alkane and alkene fuels have been extensively studied for ambient temperatures up to ~1800 K.[139-141] Based on experimental and numerical analyses, these studies established a dimensionless correlation known as the Zabetakis equation that relates the lower flammability limits to the ambient temperature and the initial fuel temperature. This equation

is given in Eq. 6.8, where $LFL_{T_f} / LFL_{T_\infty}$ is the ratio of the lower flammability limit at the fuel temperature, T_f, to the lower flammability limit at the ambient temperature, T_∞.

$$\frac{LFL_{T_f}}{LFL_{T_\infty}} = 1 - k_c \cdot (T_f - T_\infty) \tag{6.8}$$

The volatile temperature, T_f, is assumed to be the same as the particle surface temperature, T_p, since the volatile is released from the surface of the particle. Here, k_c is a correlation factor that depends on the heating value and the thermophysical properties of the volatiles. The ambient temperature is the gas phase temperature in which the coal particle is suspended, i.e. 1300 K or 1800 K for the experimental results in preceding chapters. The volatile mole fraction at the surface of the particle can be compared to the lower flammability limits (LFLs), where both parameters are functions of the volatile temperature (residence time). Thus, plots comparing the LFL of the volatile (assumed to be methane) with the particle surface temperature (assumed to be the volatile temperature) and the volatile mole fraction at the surface of the particle are appropriate for understanding ignition.

6.4 Pre-ignition model predictions and analysis

6.4.1 Particle size, volatile composition, and ignition in a gas temperature of 1300 K

Figure 6-2 shows plots of the volatile mole fraction at the surface of the particle and the LFL for five different particle sizes at 1300 K. For particles below 75 μm, the volatile mole fraction in the gas phase next to the particle surface is significantly lower than the lower flammability limits, which indicates that the volume of volatile release from small particles is not sufficient to form a

combustible mixture. Thus, heterogeneous ignition is the controlling mechanism, since volatile oxidation cannot occur. For a 75 µm particle, the volatile fraction first meets the lower flammability limit curve. In addition to this, the volatile mole fraction exceeds the lower flammability limit for about 2 ms for a 90 µm particle. Hence, for the 75-90 µm size range, volatile oxidation can only be sustained for a brief time around the particle surface. Thus, its effect on ignition delay time will be minimal for particles in the 75-90 µm range. However, for particles above 90 µm, a larger volatile flux, sustained for several milliseconds, signifies strong homogeneous ignition, forcing the reaction zone away from the solid surface.

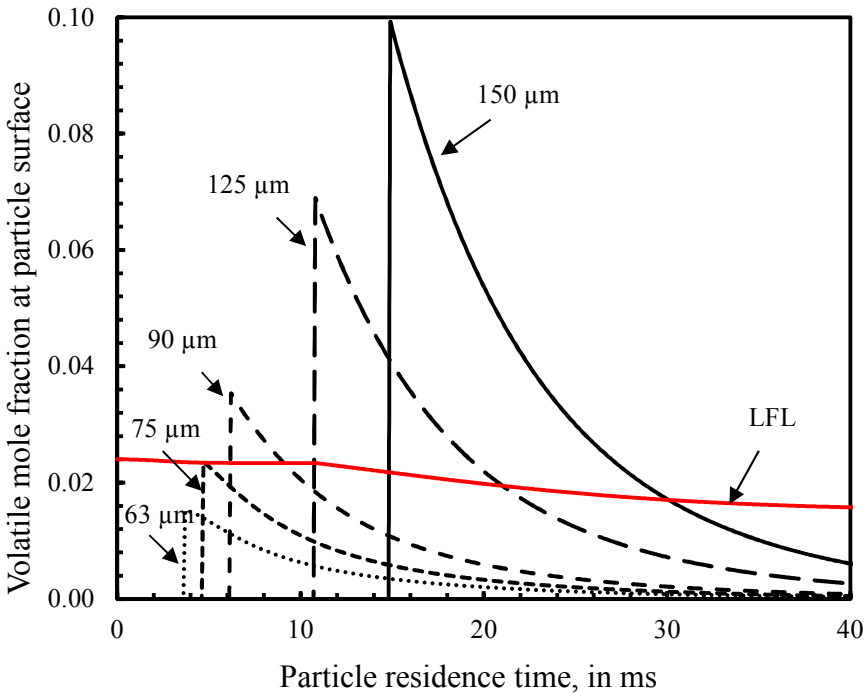

Figure 6-2. A plot comparing volatile mole fractions on particle surface for different particle sizes to the lower flammability limit (LFL) for a nominal 1300 K gas temperature.

In Fig. 5-4 of Chapter 5, it was noted that the 90-124 μm particle size range was an exception to the expectation that the ignition delay time would increase with particle size. This exception is consistent with earlier findings on single particle ignition done by Essenhigh et al. [67, 119] and Juntgen et al. [111, 128] The results of this model, as presented in Figure 6-2, clarify the reason for this non-monotonic behavior. Above 90 μm, there is a significant volatile composition in the gas phase around the particle. For example, the volatile mole fractions between 90 μm and 125 μm are almost triple the lower flammability limit. In addition, during the early-stage of devolatilization, the residence time of the volatile above the lower flammability limit extends for as long as 15 ms. There is therefore sufficient volatile concentration to sustain homogeneous ignition and to impose a transition from heterogeneous mode to homogeneous mode.

Also, as indicated by the histories of the particle devolatilization (Fig. 6-2) and temperature (Fig. 6-3), both low concentrations of volatiles in the gas phase and a higher temperature in particles smaller than 90 μm (i.e., the 63-74 μm and 75-89 particle size ranges) show that heterogeneous ignition is favored. Consistent with the results in Fig. 5-3, the ignition delay time for 75-89 μm particle sizes is expected to be higher than the ignition delay time for 63-74 μm particle sizes, since heterogeneous ignition prevails for both particle size ranges. With the transition to homogeneous ignition for particles above 90 μm, due to the high volume of released volatile, the results in Fig. 6-2 for a 90 μm particle and for a 125 μm particle suggests that the reduction in ignition delay time for 90-124 μm size range (See Fig. 5-4) can be attributed to the enhancement from homogeneous combustion. The findings in this dissertation showed that particle ignition modeling and flammability limit analysis are valuable for interpreting experimental data either from single particle ignition studies or coal stream ignition studies.

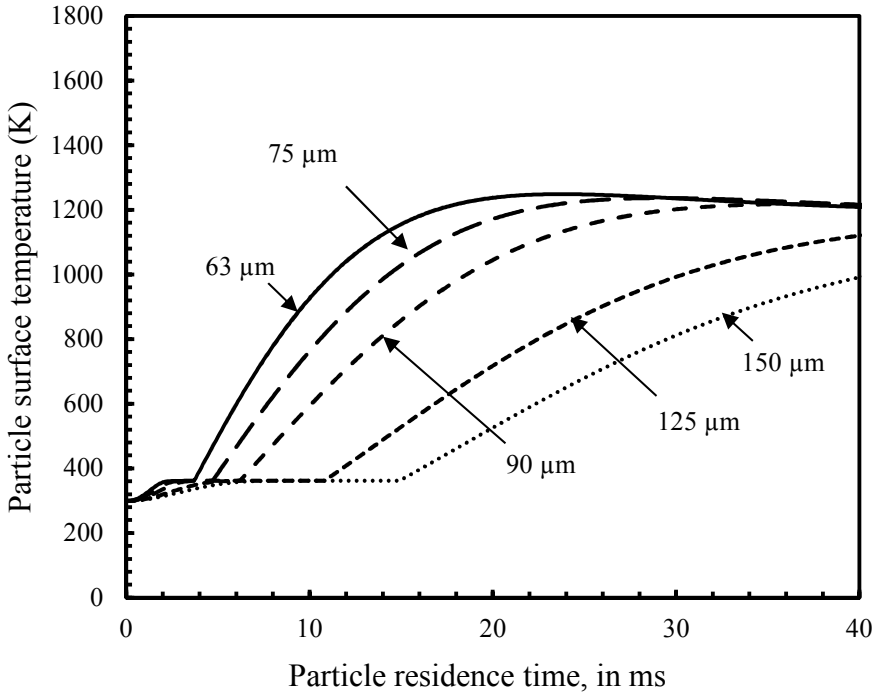

Figure 6-3. Profiles of particle surface temperatures for different particle sizes at a nominal 1300 K gas temperature.

6.4.2 Particle size, volatile composition, and ignition in a gas temperature of 1800 K

At low temperature (1300 K), the lower flammability limit is 2.5 mole percent on average. In comparison, as shown in Fig. 6-4, the lower flammability limit (LFL) decreases significantly to 0.05 mole percent (50 times lower) on average at a nominal gas temperature of 1800 K. As expected, the residence time at which devolatilization starts increases with particle size (increase in thermal mass). As shown in Fig. 6-4, the extremely low LFL indicates that volatile oxidation precedes char oxidation for all the particle sizes. Hence, in contradistinction to the observations at low gas temperature of 1300 K, all particle, irrespective of size, support homogeneous ignition. According to Mitchell et al. [142, 143], char consumption through oxidation accelerates significantly

at particle temperatures above ~873 K. As shown in Fig. 6-5, the surface temperature reaches this value only after some residence time, subsequent to homogeneous ignition. Although the sharp rise in particle surface temperatures at all sizes indicates that particle heating time and volatile oxidation time are within the same order of magnitude at high heating rate, especially for particles with size below 125 µm. This idea is consistent with experimental observations in Chapter 5, where it was noted that homogeneous ignition mode is dominant at high gas temperature of 1800 K, in which a particle experiences volatile oxidation and then char oxidation.

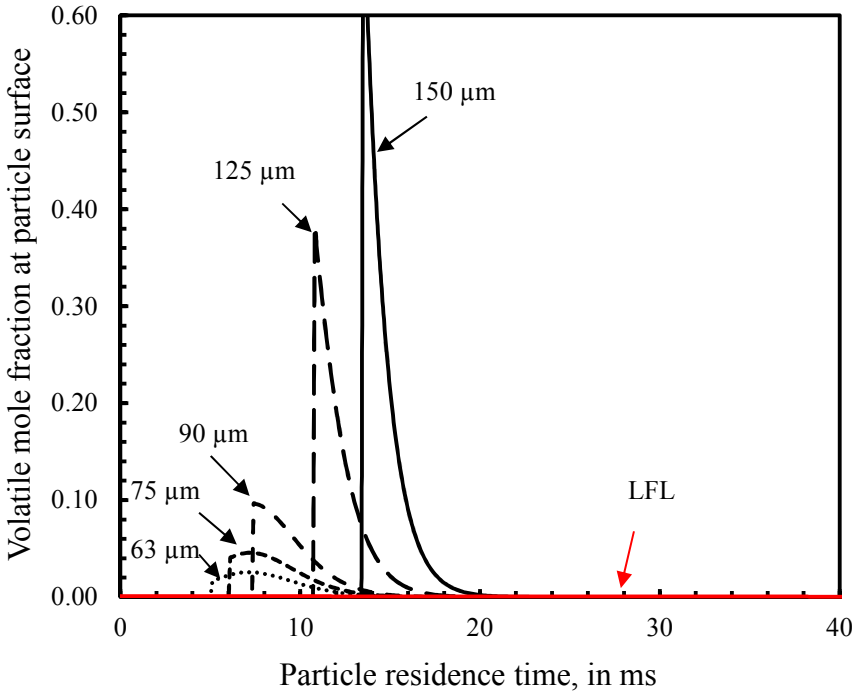

Figure 6-4. A plot comparing volatile mole fractions on the particle surface for different particle sizes to the lower flammability limit (LFL) for a nominal 1800 K gas temperature.

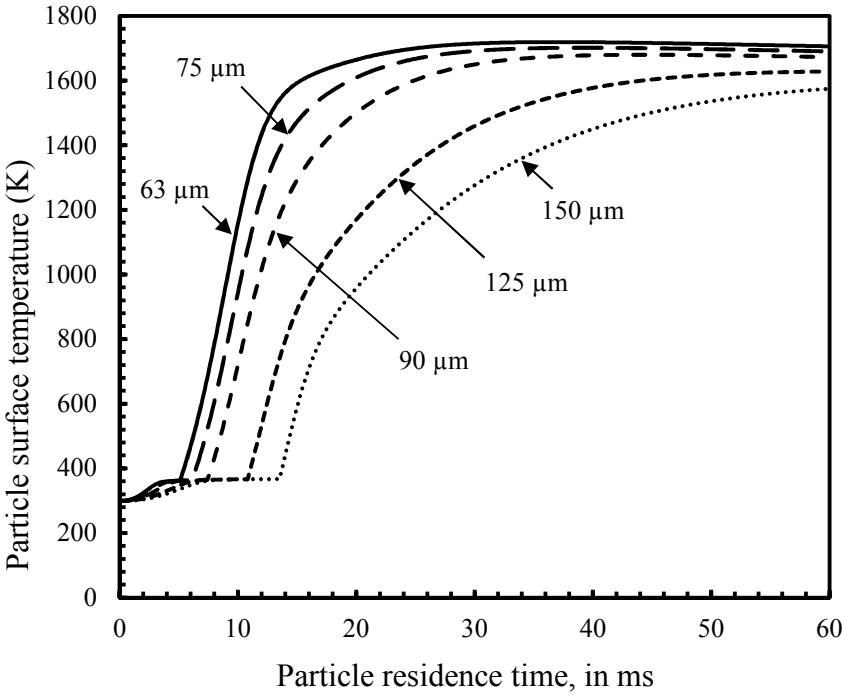

Figure 6-5. Particle surface temperature-time history for different particle sizes at a nominal 1800 K gas temperature.

6.5 Combustion model description

The models for moisture vaporization and devolatilization described in Section 6.1 stay the same for the combustion model, while volatile oxidation, char oxidation, and gasification models are incorporated. The volatile combustion rate, $\Re_{vol,rxn}$, in kg/s, can be defined using a one-step global chemistry [100],

$$\Re_{vol,rxn} = -\frac{dm_{vol,rxn}}{dt} = \left(\frac{P_g}{RT_g}\right)^2 \cdot x_{O_2} \cdot x_{vol} \cdot M_{w,vol} \cdot A_{vol} \exp(-E_{vol}/RT_g) \qquad (6.8)$$

where P_g is the gas pressure. x_{vol} is the mole fraction of the volatile in the gas phase, and x_{O_2} is the mole fraction of oxygen. The Arrhenius parameter, A_{vol}, and the activation energy for the volatile oxidation, E_{vol}, are obtained from.[100, 144] $M_{w,vol}$ is the molecular weight of the volatile. D_g is the gas diffusivity, defined as a function of gas temperature [145]. The volatile release into the gas phase is assumed to be quasi-steady, which implies that at any instant of time the process can be described as if it were steady state. This assumption eliminates the need to deal with partial differential equations.[146]

In this combustion model, Stefan flow is neglected since it has been shown in the literature to be of no influence on mass and heat transfer in air-fired combustion.[147-149] Char gasification by steam or carbon dioxide requires high activation energies. However, with a significant steam fraction in the gas composition, the contribution of gasification to the char burning rate may be significant. The steam-rich environment due to the methane-fueled flat-flame can lead to increased diffusivity, thus promoting steam gasification. Although char oxidation is known to dominate over gasification in high oxygen environments, the contribution of gasification to char burnout is not fully understood especially in a high-steam environment.[31, 150] Thus, for complete description, char gasification is considered in the model.

Char combustion is described using a kinetic/diffusion-limited rate model where the surface reaction rate is determined either by the chemistry or by the diffusion rate. The rate of heterogeneous combustion of char, $\Re_{char,rxn}$, is given by Eq. (6.11). The diffusion rate coefficient, R_c, and the kinetic rate coefficient, R_d, are defined by Eq. (6.12) and Eq. (6.13), respectively.[136, 151, 152]

$$\Re_{char,rxn} = -\frac{dm_{char}}{dt} = A_p\left(\frac{P_{O_2,s}R_{c,O_2}R_{d,O_2}}{R_{c,O_2}+R_{d,O_2}} + \frac{P_{H_2O,s}R_{c,H_2O}R_{d,H_2O}}{R_{c,H_2O}+R_{d,H_2O}} + \frac{P_{CO_2,s}R_{c,CO_2}R_{d,CO_2}}{R_{c,CO_2}+R_{d,CO_2}}\right) \quad (6.11)$$

$$R_d = C_{R,d}\frac{\left(\frac{1}{2}(T_p+T_g)\right)^{0.75}}{d_p} \quad (6.12)$$

$$R_c = C_{R,c}\exp\left(-\frac{E_c}{RT_p}\right) \quad (6.13)$$

The kinetic and diffusion parameters for the char gasification reactions and the char oxidation are obtained from Chen's work.[150] In the model, char kinetics assumes first order and the rate is evaluated using the external surface area of the particle. For high temperature environments, diffusion or mass transfer will always dominate over chemistry for char oxidation.[152] Thus, the diffusion-limited reaction rate constant, $C_{R,d}$, accounts for the effect of volatile release on mass transfer.[153, 154] Char is consumed if the particle temperature is high enough (constrained to be > 873 K [143]). The rate of heterogeneous combustion of a coal particle can be defined using Eq. (6.14) and the associated kinetic parameters.[35, 130] Hence, by comparing the combustion rates from Eq. (6.11) and Eq. (6.14), the significance of gasification over oxidation can be determined:

$$\Re_{coal,rxn} = -A_p\left(\frac{P_{O_2,s}R_{c,O_2}R_{d,O_2}}{R_{c,O_2}+R_{d,O_2}}\right) \quad (6.14)$$

The energy balance is presented in Eq. (6.15), where h is the convective heat transfer coefficient.

$$\frac{dT_p}{dt} = \frac{1}{m_pC_p}\left(hA_p(T_g-T_p) + \varepsilon\sigma A_p(T_w{}^4 - T_p{}^4) + \alpha\cdot\dot{m}_{char}h_{char} - \dot{m}_{H_2O}L_{H_2O}\right) \quad (6.15)$$

The release of moisture and volatile translates to changes in temperature. Since h is a function of gas temperature through gas thermal conductivity and particle size, the effect of mass change on h is accounted for through its dependency on temperature. For convection, Nu = 2 is assumed due to the low Reynolds number in the reactor. Further, ε is the particle emissivity, with a constant value of 0.8 [155]; σ is the Stefan-Boltzmann's constant; T_w is the wall temperature (assumed 300 K); $\dot{m}_{char}$ is the char loss rate; $\dot{m}_{vol}$ is the volatile loss rate; and h_{char} is the heating value for heterogeneous coal combustion.[60] Also, h_{vol} is the heat of combustion of volatiles [100], and α, taken to be 0.3 [106], denotes the fraction of the heat from char consumption absorbed by the particle. $\dot{m}_{H_2O}$ and L_{H_2O} refer to the demoisturization rate and the latent heat of vaporization respectively. These equations are solved using MATLAB, and the solutions are discussed in Section 6.5. Various kinetic parameters used for both the pre-ignition model and combustion model are provided in Table 6-1.

Table 6-1. Kinetic parameters used in the models

Type of reaction	Pre-exponential factor	Activation energy (kJ/mole)	References
Devolatilization	1.34E4 (1/s)	74.1	34, 131
Volatile oxidation	3.88E8 (m^3/mol/s)	159.0	35, 100
Char oxidation	0.0045 (kg/m^2/s/Pa)	69.0	31, 34, 100, 130
Coal oxidation	0.016 (kg/m^2/s/Pa)	149.0	31, 35, 104, 116, 130
Char steam gasification	0.00192 (kg/m^2/s/Pa)	147.0	31, 35, 104, 116, 130
Char CO_2 gasification	0.00635 (kg/m^2/s/Pa)	162.0	31, 35, 104, 116, 130

6.5 Combustion model predictions

6.5.1 Effect of particle size on char burnout

As particle size increases, devolatilization is delayed due to the high heating time. However, once devolatilization starts, the gas-phase volatile mole fraction increases significantly with size, as shown in Fig. 6-2 and Fig. 6-4. Hence, the particle surface may be shielded from combustion because the volatile mole fraction on the particle surface increases with particle size. Thus, heterogeneous ignition, which is the onset of char burnout, may be delayed significantly. Since char burnout rate increases with gas temperature, and gasification reactions are important only at high temperatures, only the results for 1800 K are presented.

Figure 6-6 shows the char mass fraction profiles for different particle sizes as particle residence time increases in an oxidizing condition. As expected, the heterogeneous ignition time (i.e., the time at which char burning starts) increases as particle size increases. Given the temperature constraint for heterogeneous ignition, char burnout starts at about 12 ms and 36 ms for 63 μm and 150 μm particles, respectively. Char is burnt completely at 28 ms, 44 ms, and above 100 ms for 63 μm, 90 μm, and 150 μm particles, respectively. With its sharp slope, as seen in Fig. 6-6, the char burnout rate is highest for 63 μm particles. The char burning rate of the particle decreases as particle size increases.

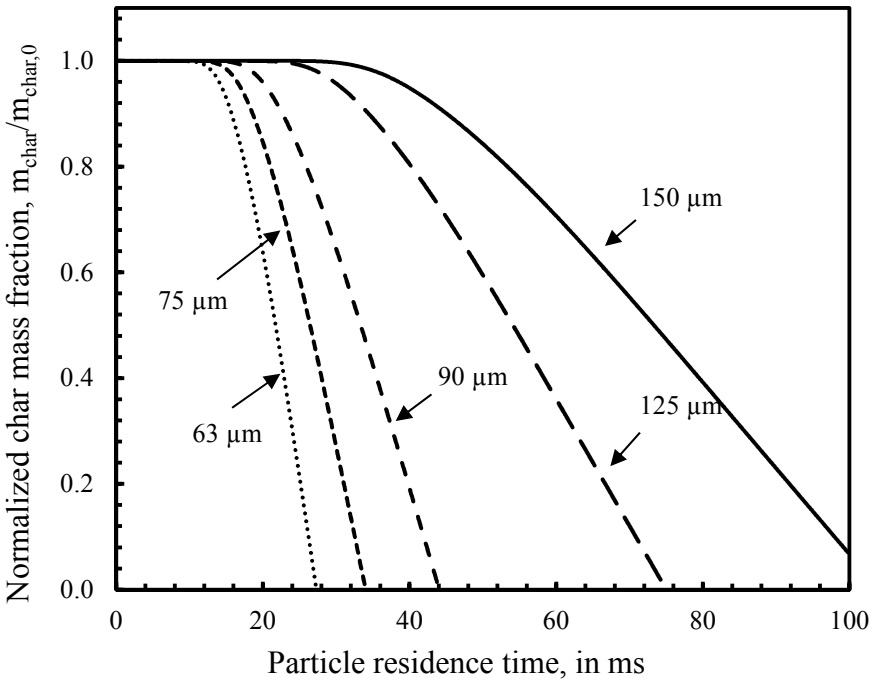

Figure 6-6. Particle char mass fraction-time history in an oxidizing condition for different particle sizes at nom. 1800 K gas temperature.

6.5.2 Effect of reducing-to-oxidizing environment on char burnout

Figure 6-6 shows the effect of particle size on char burnout in an oxidizing condition. Figure 6-7, on the other hand, compares char burnout in a reducing-to-oxidizing environment (R-O) with those in an oxidizing environment for three particle sizes (represented in three colors). The profiles show that the initial delays in char oxidation in the R-O environment are identical at about 28 ms, even with increasing particle size (see the dashed lines in Fig. 6-7). This observation is consistent with the expectation that the onset of char combustion (heterogeneous ignition) must occur after the flame sheet that demarcates the reducing zone from the oxidizing zone. However, in oxidizing conditions where excess oxygen is available at all positions, the onset of char combustion is dependent on particle size. There are distinct residence times at which the char mass fraction starts

to fall off, increasing from 12 ms for 63 µm, to 20 ms for 90 µm, and to 38 ms for 150 µm particles respectively. But with the lower oxygen concentration in an R-O environment, the rates of char burnout are slower than in an oxidizing environment, leading to the observed changes in the char mass fraction profiles as particle size increases. The char burnout time is 28 ms for 63 µm particle in oxidizing environment, and 62 ms for the same particle size in an R-O environment. This model result agrees with the scanning electron micrograph in Fig. 5-14, which shows that combustion is complete at 50 ms for the oxidizing environment but still ongoing for the same particle in an R-O environment.

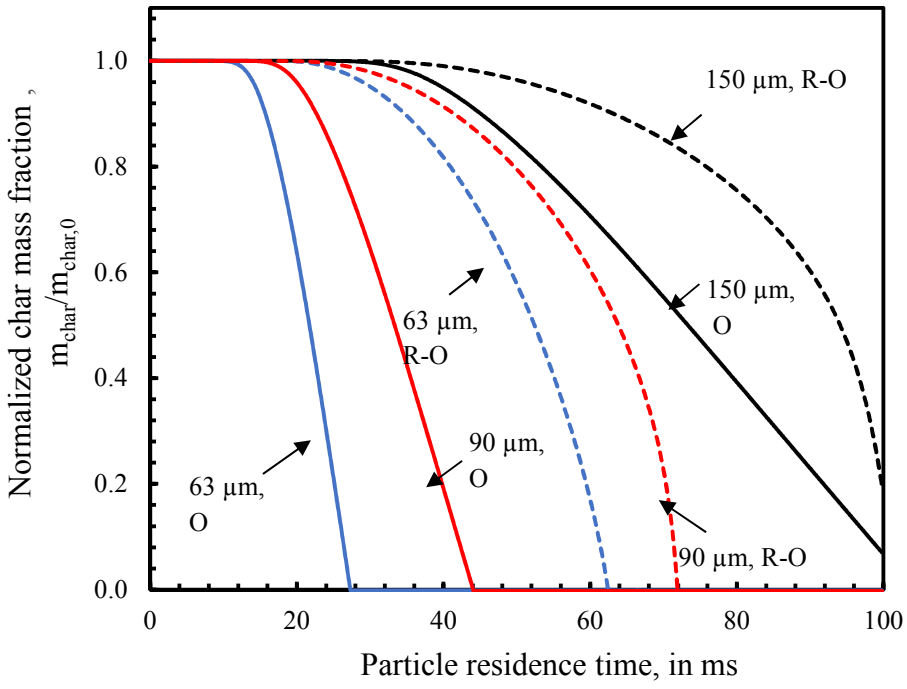

Figure 6-7. Comparison between particle char mass fraction-time histories in O and R-O conditions for different particle sizes at nominal 1800 K gas temperature.

6.5.3 Contribution of char gasification to char burnout

The effects of gasification reactions on char consumption in oxy-fuel or steam combustion has attracted much interest in recent years.[156-162] A simplified multi-surface model is usually used to estimate the contribution of char gasification by steam (Eq. 6.16) and by CO_2 (Eq. 6.17) to char burnout.

$$C(s)+H_2O \rightarrow CO+H_2 \quad (6.16)$$

$$C(s)+CO_2 \rightarrow 2CO \quad (6.17)$$

Figure 6-8 shows the results of a char burnout model that considers char oxidation along with gasification (WG) to the results of a char burnout model with no gasification (NG) is considered. Comparisons are made for three different particle sizes at nominal gas temperature of 1800 K. Figure 6-8 shows that the contribution of gasification to overall char burnout is insignificant, and gasification decreases the overall char burnout rate with time as the particle size increases from 63 μm to 150 μm. This decrease occurs because gasification reactions are endothermic processes.[31] Hence, as reaction energies are extracted from the particle surface for the gasification reactions, the particle surface temperature decreases. The cooling leads to the observed decrease in the char consumption rate with time. Second, the gasification reactions are kinetically controlled under most combustion conditions; however, the orders of magnitude of steam- and CO_2-gasification reactions are roughly four times lower than that of char oxidation.[31, 158] The results in Fig. 6-8 further affirm the dominance of oxidation over gasification, as reported in the literature for a high oxygen environment.[31, 156]

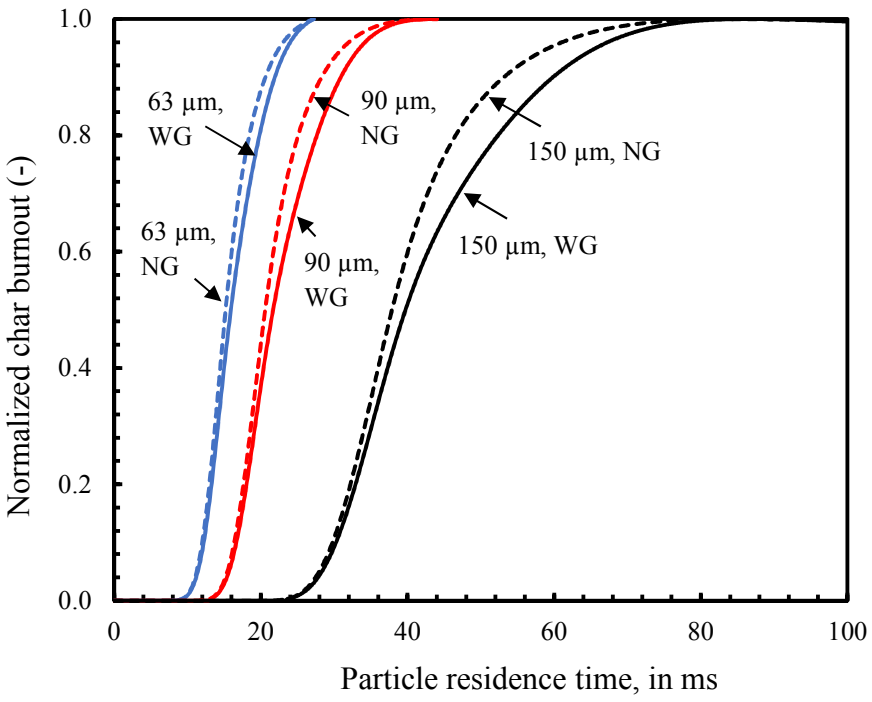

Figure 6-8. A plot comparing char burnout in nominal 1800 K gas temperature, 20% oxygen composition condition with (WG) and no gasification (NG) for different particle sizes.

Fig. 6-9 shows the char burnouts for three different particle sizes with (WG) and no (NG) gasification in the R-O environment. For the three particle sizes, char burnout occurs mainly through char oxidation, and gasification decreases the overall char burnout rate significantly in the R-O environment. This behavior is contrary to what happens in an oxidizing environment where gasification has no effect. The energy required for char gasification is usually provided from the heat released by char oxidation.[156, 158, 161] With low oxygen concentration in the R-O environment, char oxidation is weaker than in an oxidizing environment. Heat extraction for gasification has a stronger cooling effect in the R-O than in an oxidizing environment. Figure 6-9 shows that the cooling effect also increases with particle size.

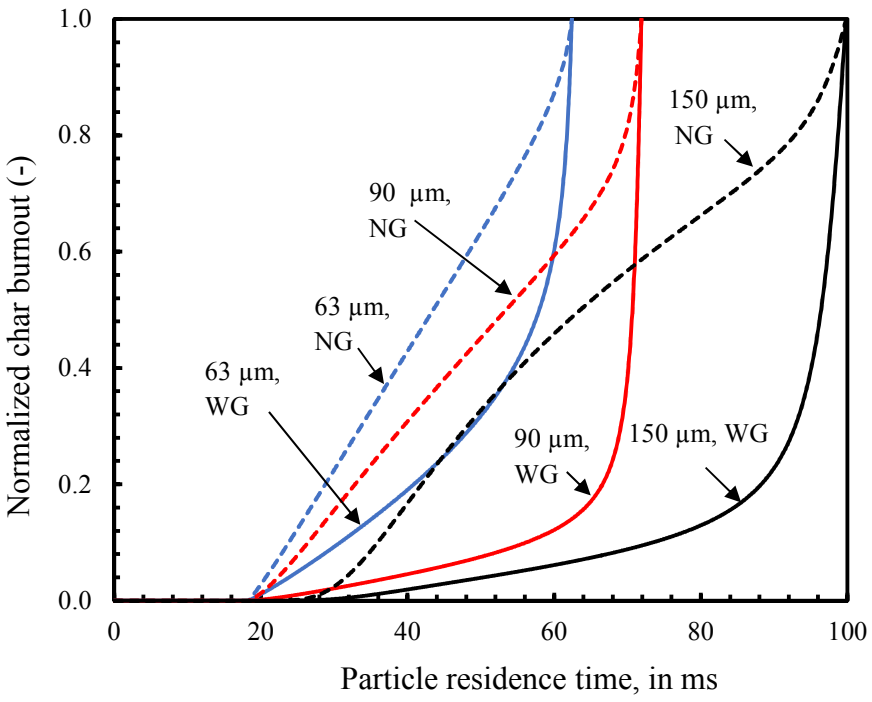

Figure 6-9. A plot comparing char burnout in a nominal 1800 K gas temperature, R-O condition with (WG) and no gasification (NG) for different particle sizes.

6.6 Summary

Simplified model predictions for both pre-ignition events and the combustion of single particles agree well with experimental findings. As particle size increases, the flux of volatile on particle surface increases. At a low 1300 K gas temperature, the model showed that there was a transition from heterogeneous ignition to homogeneous ignition as particle sizes increased. At a high temperature of 1800 K, the extremely low lower flammability limits indicated that volatile oxidation precedes heterogeneous ignition. Char burning rates were slower in an R-O environment than in an O environment. Gasification reactions retarded char burnout in both environments, but more significantly in R-O.

Chapter 7

Submicron particle formation during pulverized coal combustion in a flat-flame burner

7.1 Introduction

The previous chapters described pulverized coal ignition. The ignition studies considered the effects of various factors, such as particle size, heating rate, particle interaction, and the transition from a reducing to an oxidizing environment for both single particle and coal stream ignition. As stated in Chapter 2, apart from ignition, the formation of submicron aerosols is also an early-stage process of coal combustion. Hence, in this Chapter, the formation and evolution of sub-micron particles during the early-stage of pulverized coal combustion is investigated in the new flat-flame Hencken burner under well-controlled oxidizing conditions.

Figure 7-1 shows a schematic of a typical coal-fired boiler. The near-burner region, labeled as zone 2 in the figure, is where the early-stage processes of coal combustion take place. These processes influence particle reactions, including volatile oxidation, char oxidation, and char gasification.[95, 163] These early-stage processes also determine ash deposition initiation, which is a critical step preceding high-temperature fouling and slag deposit formation in coal-fired boilers from inorganic impurities or minerals.[30] Boiler fouling and slagging are severe especially for power plants using low rank coals such as sub-bituminous or lignite with high alkaline, alkaline-

earth metals (AAEMs), and iron.[164-166] Boiler fouling and slagging cause major problems, including frequent shutdown for cleaning, decrease in efficiency, and equipment failure.[167-170] Thus, fundamental studies on ultrafine evolution will be indeed valuable to developing innovative solutions, such as in-flame aerosol control technologies.

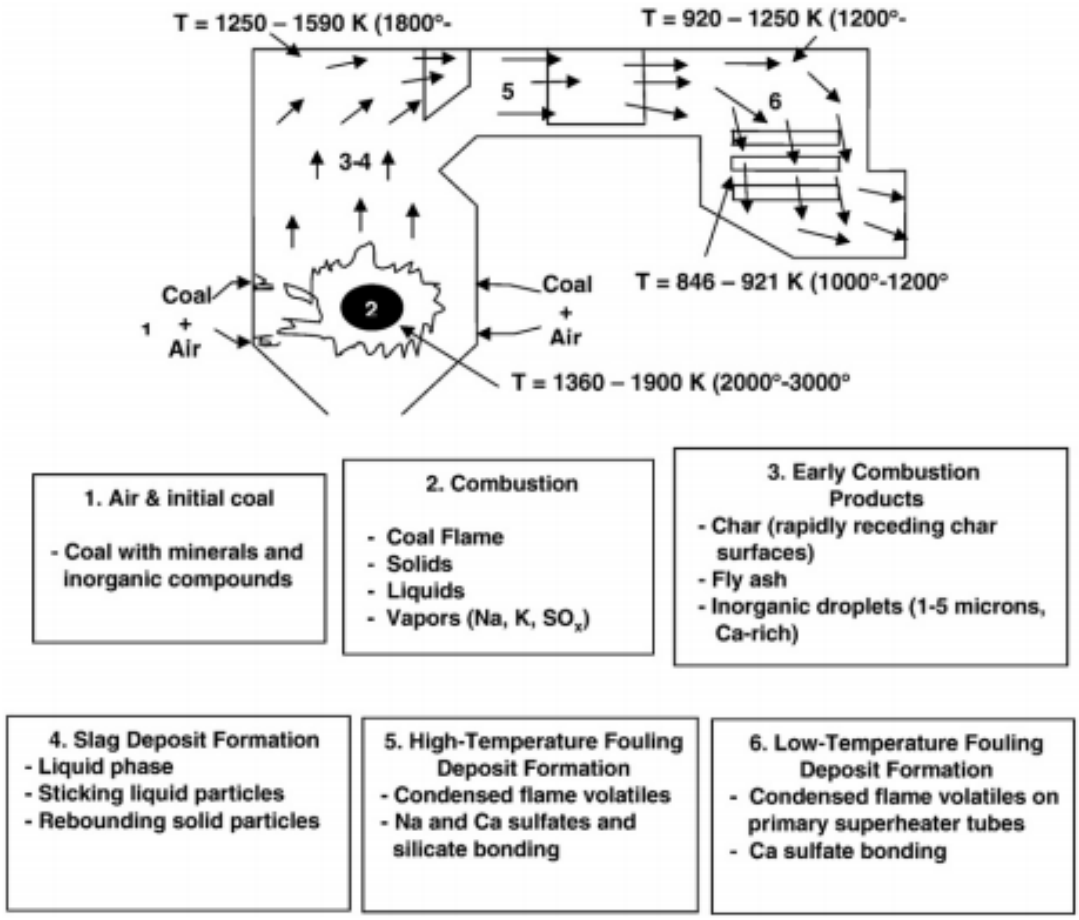

Figure 7-1. Schematic of coal combustion processes in a typical coal-fired boiler.

Formation of sub-micron ash particles depends on the properties of the parent coal, its size distribution and rank, and the local combustion conditions experienced by the coal/char/mineral

particles.[171, 172] Sub-micron particles from coal combustion can be classified into mineral and carbonaceous particles.[173] The mineral matters, which are organic-bound, are released during the devolatilization and form sub-micron particles.[174]. Soot particles are also formed from tar during the devolatilization. Most studies on submicron aerosol formation during coal combustion have investigated particle emission at the exit of the combustion furnace to deduce the formation and evolution processes.[173, 174] Recently, a flat-flame Hencken burner has been employed to investigate sodium release and particle formation during the early-stage of combustion for a low-rank coal.[20, 163] A competition between sodium release and nascent particulate coagulation during the early-stage processes of devolatilization of both AAEMs and tar was found to affect the ultrafine particle size distribution and mode.[163] The impact of early-stage processes on particulate evolution and mechanisms has not been fully explored. However, to facilitate in-flame control of aerosol emission, better understanding on submicron aerosol evolution is required.

In this work, the formation of sub-micron particles in the early-stage of coal combustion was investigated in a Hencken flat-flame burner under a well-controlled oxidizing condition. The particle size distribution (PSD) was measured for PRB sub-bituminous coal at three temperatures (1100, 1400, and 1700 K) and two residence times (~15 and ~31 ms). A tube furnace was operated in a tandem DMA configuration to oxidize the soot particles so that mineral residuals can be distinguished from soot. The PSD results for different temperatures were compared and discussed to understand the evolution of sub-micron particle during the early-stage of coal combustion.

7.2 Experimental methods

7.2.1 Coal properties

A sub-bituminous Powder River Basin (PRB) coal was used in these experiments. Table 7-1 lists select coal properties. PRB coal is a high-volatile coal where the dominant ash compositions

are silicon (Si), aluminum (Al), calcium (Ca), sulfur (S) and iron (Fe). The coal particles were dried and sieved to a size range of 63 to 75 μm for the combustion experiments.

Table 7-1 Properties of PRB sub-bituminous coal

Proximate analysis (wt %, dry basis)				Ultimate analysis (wt %, dry and ash free basis)					
FC	VM	Ash	HHV (MJ/kg)	C	H	O (Diff.)	N	S	
47.63	43.33	9.04	27.45	74.66	5.45	18.24	1.08	0.57	
Ash composition analysis (wt %)									
SiO_2	Al_2O_3	Fe_2O_3	CaO	MgO	TiO_2	SO_3	P_2O_5	K_2O	Na_2O
37.44	16.50	5.15	16.20	3.05	1.06	16.90	0.40	0.65	1.21

7.2.2 Combustion system

An up-fired flat-flame Hencken burner, described in Chapter 2, was used for the study, and the approach for particle sampling is schematically illustrated in Fig. 7-2. Rather than the quartz tube that is set typically above the burner for ignition studies where optical access is desired, a ceramic heater with a 15-cm length was used. The ceramic wall, heated and maintained at about 873 K, isolated the burner from the outside environment and decreased heat loss. Methane (CH_4) was used as the fuel, and a mixture of oxygen (O_2) and nitrogen (N_2) as the oxidizer. The post-flame temperature and gas composition were well controlled, and the gas velocity was ~1.5 m/s. Three characteristic gas temperatures of 1100 K, 1400 K, and 1700 K were considered in the experiments, and the post-flame O_2 composition was about 10%. The oxidizing atmosphere was particle-free to keep a clean background for particle measurements.

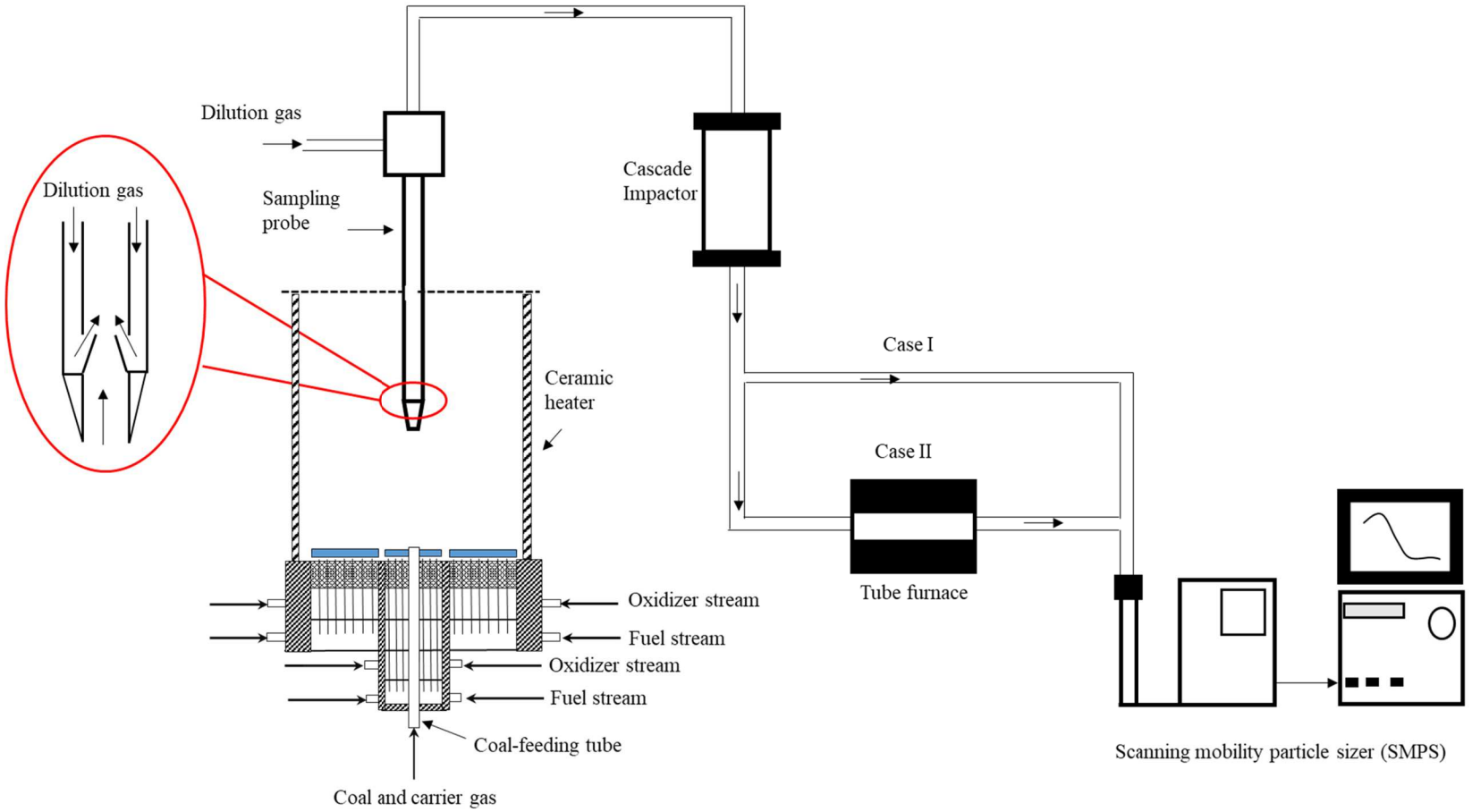

Figure 7-2. Experimental setup showing particle sampling from flat-flame burner.

Figure 7-3 shows the axial temperature profiles measured with an S-type thermocouple and corrected for radiation loss. The temperature is reasonably constant within the height of 12 cm. Figure 7-4 and Fig. 7-5 show the post-flame gas composition profiles in the axial direction along the centerline and radial direction at different heights, respectively. The gas compositions are measured using Horiba PG-250 gas analyzer, described in Chapter 2. Uniform high-temperature gas environments can be obtained in the Hencken flat-flame burner, as shown in Fig. 7-4, and Fig. 7-5, and aerosol evolution and formation can be fundamentally investigated under such controlled conditions.

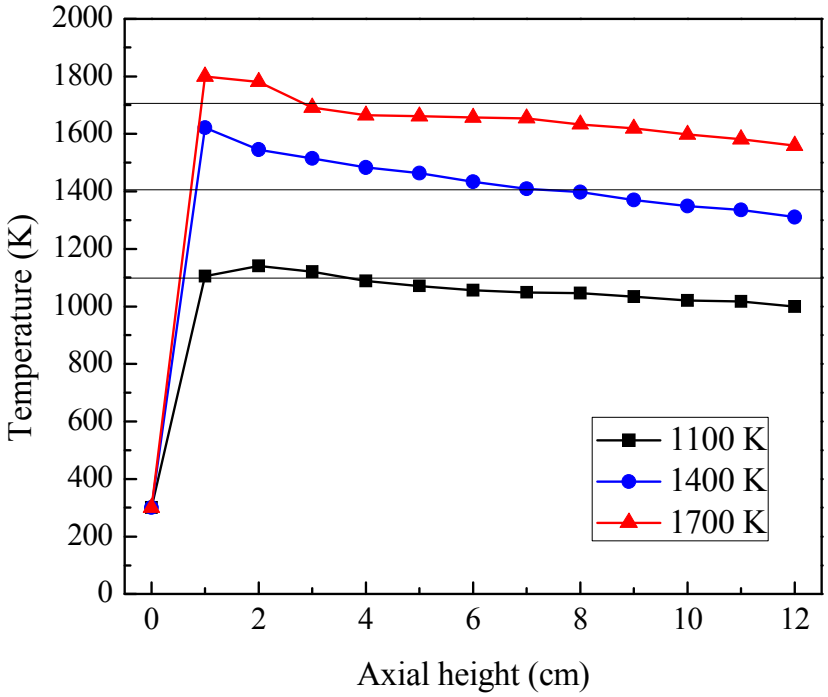

Figure 7-3. Axial temperature profiles along the centerline.

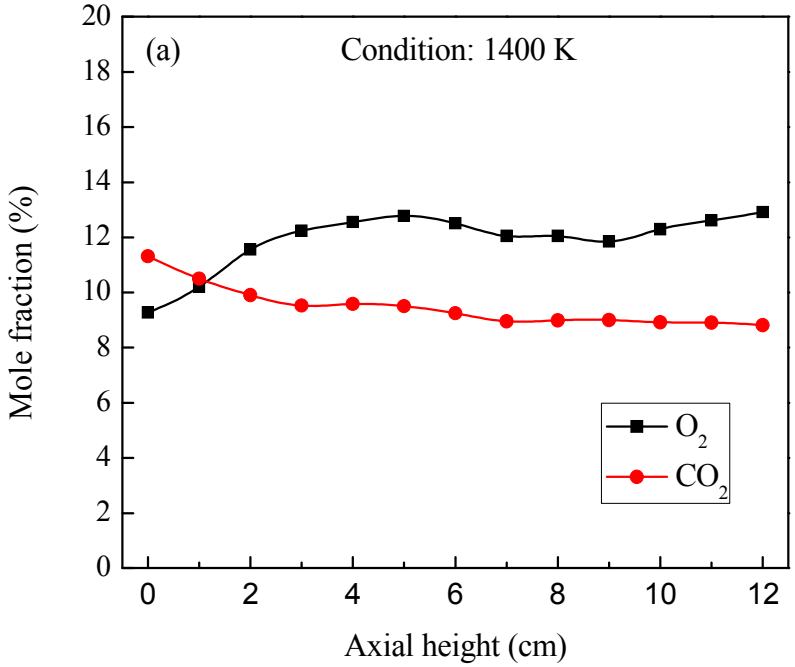

Figure 7-4. Post-flame gas composition in the axial direction along the centerline.

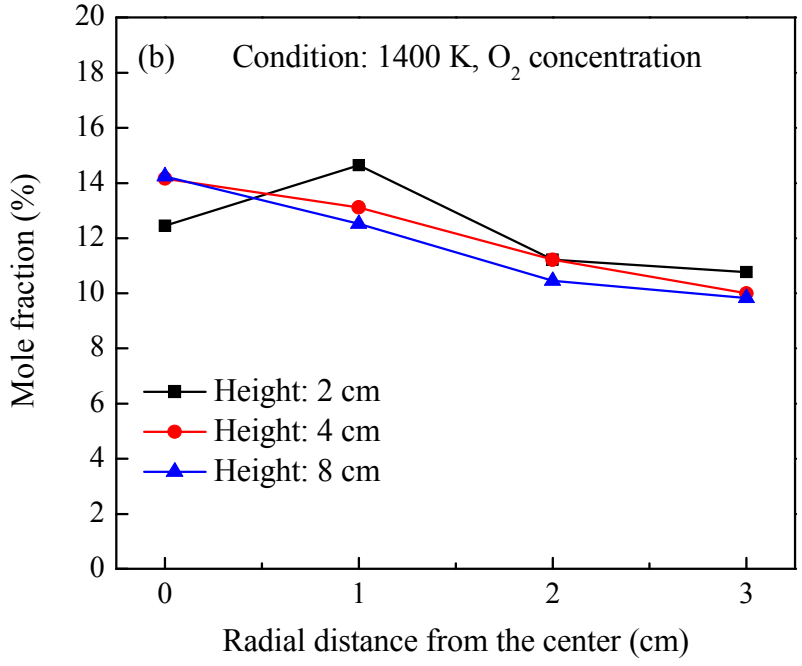

Figure 7-5. Post-flame oxygen composition in the radial direction at different heights.

Coal particles were entrained in N_2 and fed into the central tube of the burner with a flow rate of 0.13 SLPM. The feed rate of coal was from 2.0 g/h for the different runs. The coal particle stream was steady with the particles traveling upward and burning. Photographs, taken with a high-speed camera were analyzed to determine the coal particle velocity and residence time under the different conditions, and the results are shown in Fig. 7-6. The inset figure shows the residence time of coal particles as a function of height. Particle sampling was done at two residence times of about 15 ms and 31 ms, common to the three gas temperatures.

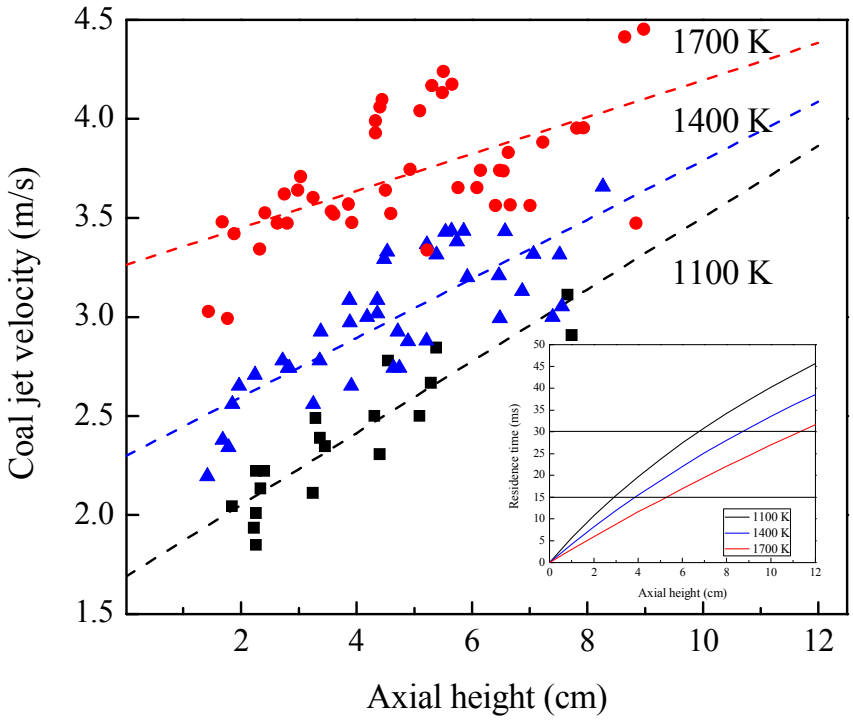

Figure 7-6. Coal particle velocity and residence time.

7.2.3 Submicron particle measurement

The particles are sampled with a nitrogen-dilution probe at two residence times of ~15 and ~31 ms. As shown in Fig. 7-2. The probe was seated on a holder attached to a motor-driven slide that

could change the axial position. The flow of dilution N_2 through the annulus gap provided the negative pressure needed to sample the flue gas as well as to cool and dilute the particle-laden flow. The dilution ratio (DR) was controlled by the nitrogen flow rate and the physical dimensions of the annulus gap. CO_2 was chosen as the tracer gas for dilution ratio calculations. A high flow rate of nitrogen dilution (~ 45 SLPM) was applied, and the dilution ratio was controlled to a range of 30 – 200. The probe sampled the whole coal particle stream while maintaining quasi-isokinetic sampling, and so was expected to introduce little bias into the sub-micron particle measurements [175]. The estimated residence time for sampled gas in the probe was less than 5 ms. The diluted gas flowed through a cascade impactor with a final cut-off size of 0.7 μm. The number concentration of sub-micron particles was measured with a scanning mobility particle sizer (SMPS, model 3080, TSI Inc.), with a size range from 14.3 nm to 673.2 nm.

Figure 7-7 shows the measured particle number size distributions (PSD) at 1400 K and 31 ms residence time for two dilution ratios. The presented particle number concentrations were normalized to the same coal feed rate (2 g/h) for all cases. The results showed a consistency in results for the two dilution ratios. To eliminate error in the gas analyzer measurement while keeping the number PSD accurate, a dilution ratio of 30–50 was used.

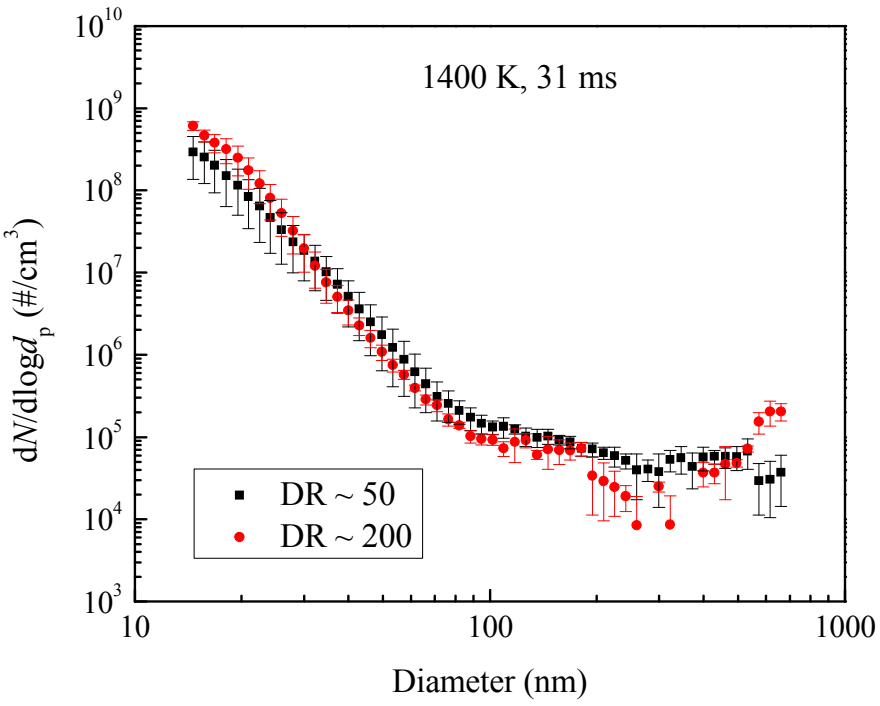

Figure 7-7. Particle number size distribution for different dilution ratios (DR) measured at 1400 K and 9 cm height (31 ms residence time).

7.2.4 Tube furnace

To distinguish mineral particulate matter from carbonaceous matter in the early-stage of pulverized coal combustion, an electrically-heated alumina tube furnace was introduced downstream of the impactor to burn out soot particles or carbonaceous matter. As shown in Fig. 7-8, the furnace tube, a 10-mm ID has a constant temperature of 1373 K for ~25 cm in length. To burn off carbonaceous matter the flue gas was mixed with O_2 (at 0.3 SLPM) before entering the furnace. The gas mixture, with an oxygen mole fraction as high as ~50%, had a residence time of ~1.8 s in the high temperature zone. The calculated time for 90% oxidization of a 700 nm diameter carbon particle at 1373 K is 1.2 s, based on the widely used Nagle and Strickland-Constable (NSC)

model [176, 177]. Given this information, the tube is capable of removing sub-micron carbonaceous particles and providing information on the mineral residuals.

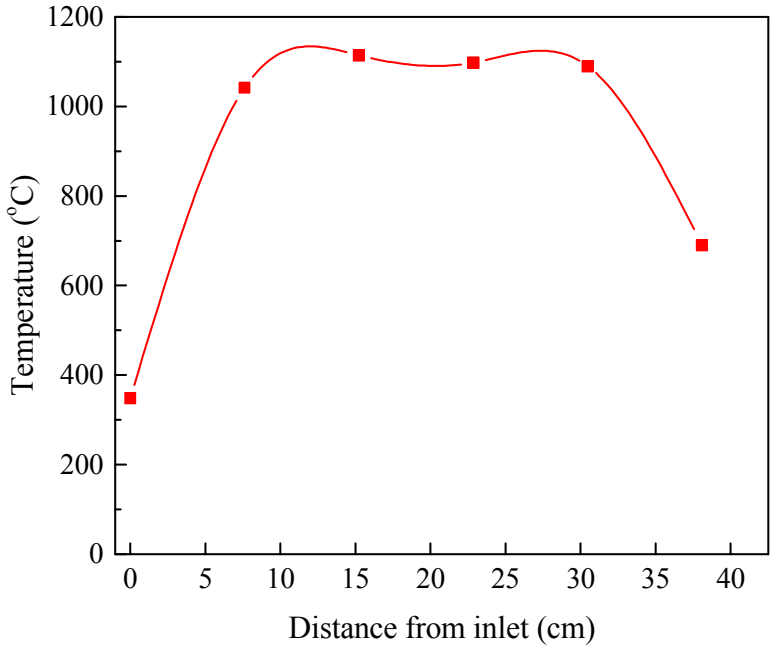

Figure 7-8. Gas temperature profile in the furnace tube

Before any experiments, it was first verified from background measurements that the tube furnace, whether heated or not, does not generate particles. Figure 7-9 shows the number PSD measured for the two particle-sampling connections. The conventional connection with no furnace (Case I in Fig. 7.2), described as “no-furnace connection” in Fig. 7-8, refers to the case in which the sample goes straight to the SMPS from the impactor. The second case (Case II in Fig. 7-2) is in Fig. 7-9 described as “furnace-off connection”. In this case, the gas flow to the SMPS goes through the tube furnace but the furnace is not heated. The measured PSD in both cases matched

reasonably well, although there is some particle loss attributed to deposition on the tube furnace wall.

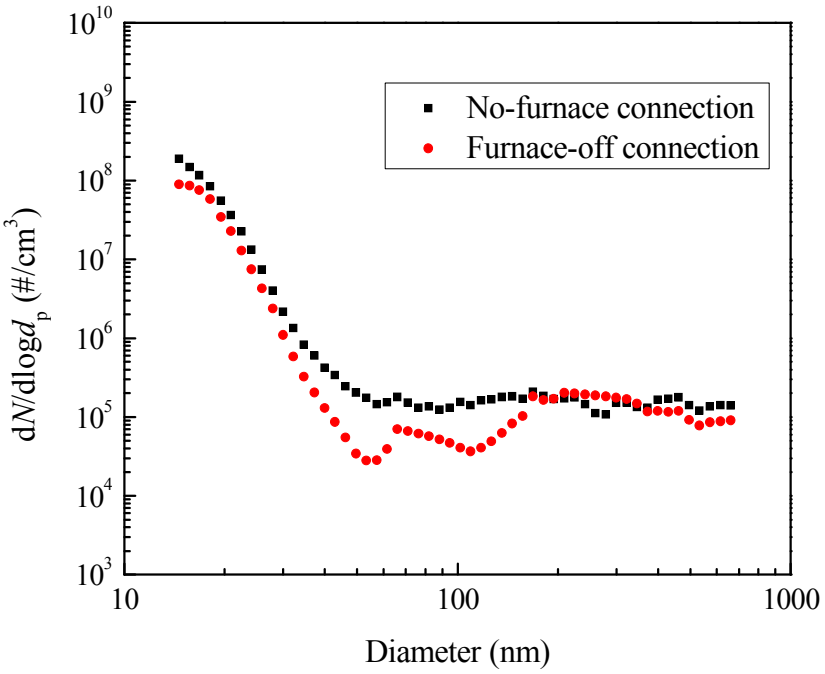

Figure 7-9. Particle number size distributions for tube furnace bypassed and tube furnace connected but off, measured at 1400 K and 31 ms residence time.

7.3 Results and discussion

7.3.1 Sub-micron particle evolution in the early stage

Figure 7-10, Fig. 7-11, and Fig. 7-12 show the measured particle number PSDs at two residence times (15 ms and 31 ms) for the three different temperature conditions (1100 K, 1400 K, and 1700 K) respectively. Different behaviors are observed during the early-stage combustion of PRB coal. At a low temperature condition (1100 K), the number concentration of $PM_{0.1}$ at 31 ms of residence time is 2–3 orders of magnitude larger than that at 15 ms. At a high temperature condition (1700

K) the trend is reversed, i.e., the number concentration at 31 ms is an order of magnitude lower than that at 15 ms, and the mean diameter is also decreased. At the intermediate temperature condition (1400 K), the larger mode particles decrease in number concentration with time, while the finest mode experiences an increase. The experiment thus reveals the significant effect of temperature on sub-micron particle evolution in the early stage of coal combustion.

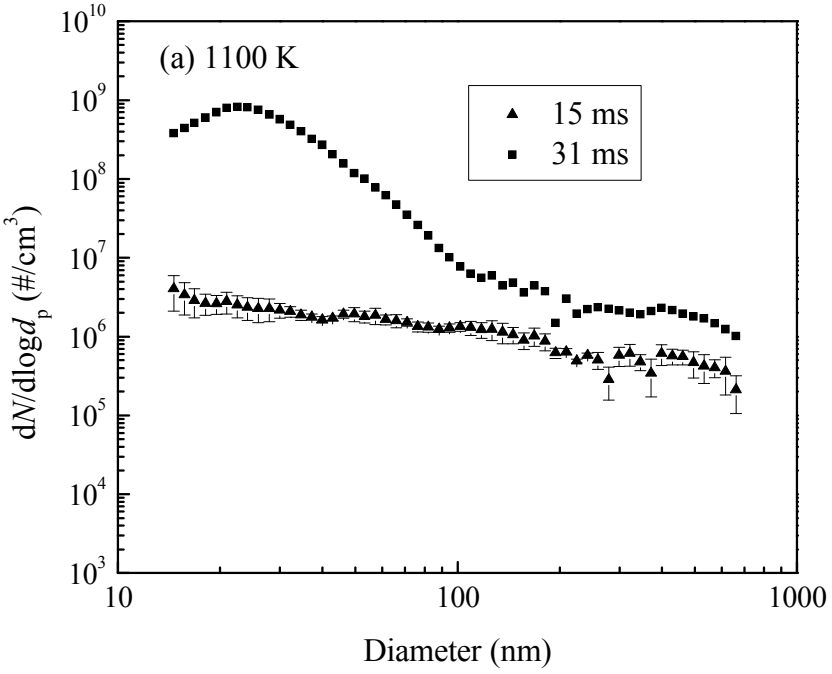

Figure 7-10. Particle number size distributions generated by PRB coal at gas temperatures of 1100 K.

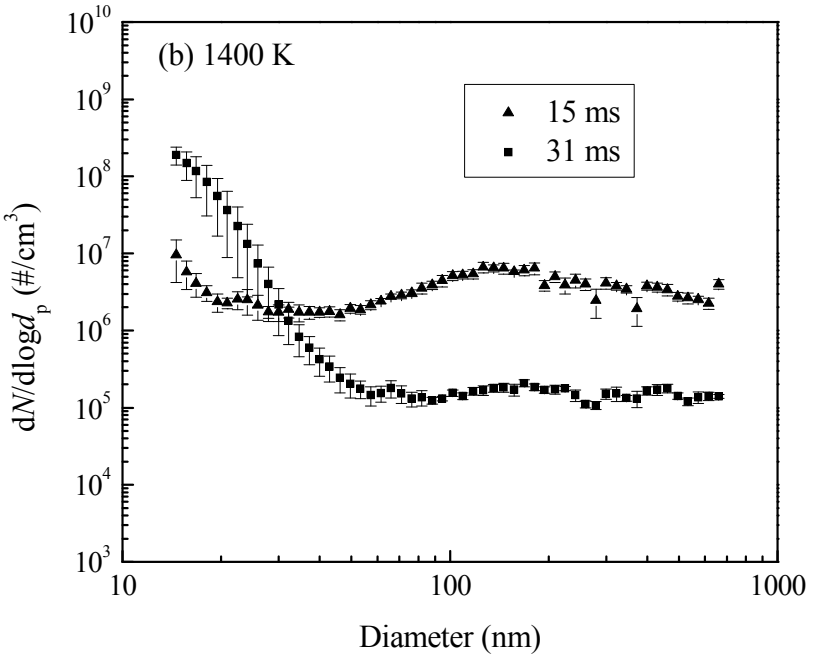

Figure 7-11. Particle number size distributions generated by PRB coal at gas temperatures of 1400 K.

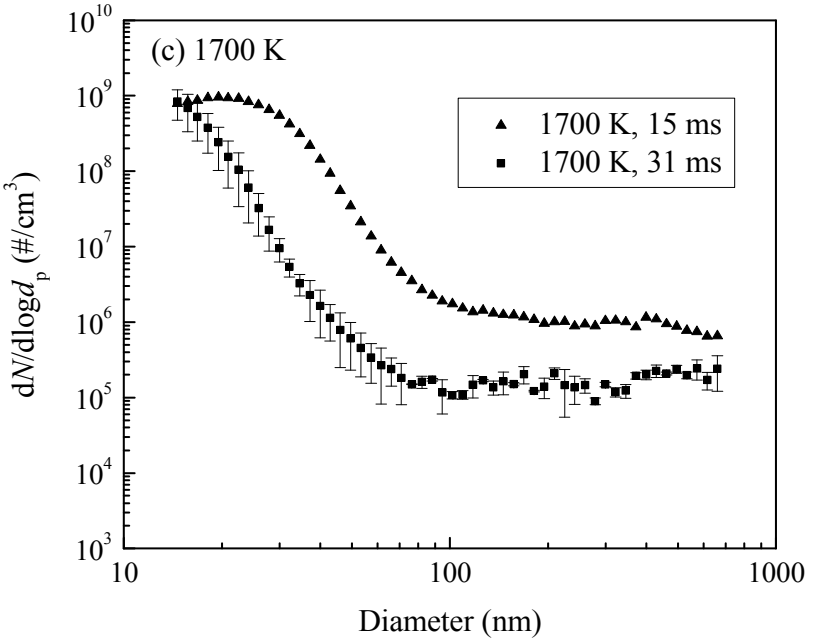

Figure 7-12. Particle number size distributions generated by PRB coal at gas temperatures of 1700 K.

To distinguish the source of particles, the tube furnace was used to burn out the carbonaceous particles. Figure 7-13 shows the number size distributions of particles sampled a residence time of 31 ms for two nominal gas temperatures of 1400 K and 1700 K. The number size distributions for samples with and without the furnace were compared. The figure shows a reduction in number concentration of the ultrafine particles, while the coarser $PM_{0.1+}$ are almost constant. The results imply, that at 31 ms residence time, the finest particles (smaller than ~30 nm) are dominated by soot particles, and the coarser particles are composed primarily of mineral residuals for both temperatures. At the largest recorded size, a carbonaceous component reappears, presumably due to unburned char fragments.

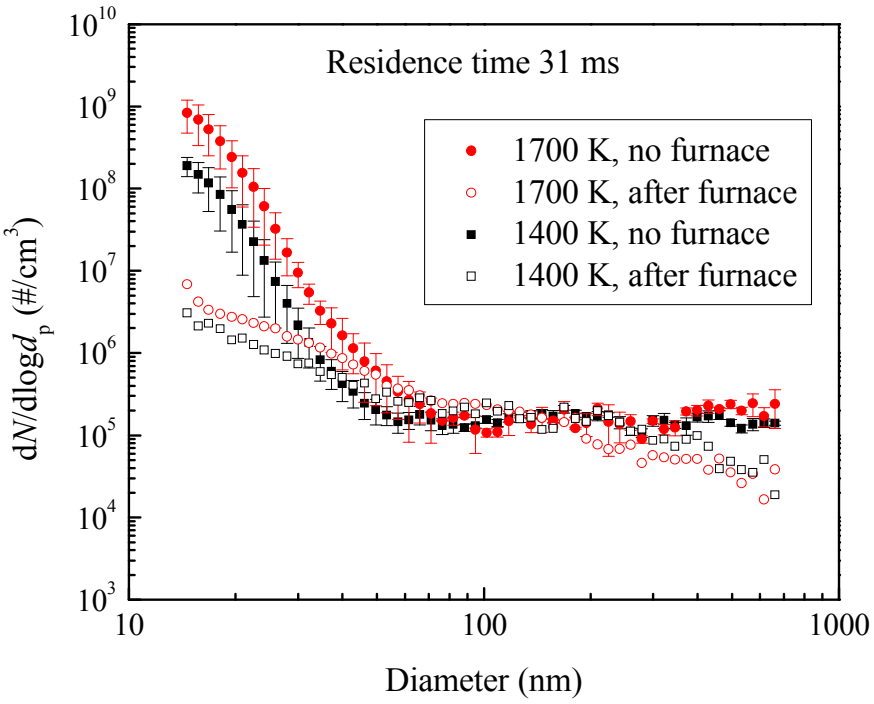

Figure 7-13. Particle number size distributions generated without and with the tube furnace.

7.3.2 Mechanism for submicron particle evolution in the early stage

The submicron particles in the early-stage of coal combustion consists of nucleation-generated ultrafine particles ($PM_{0.1}$) and small coal/char/mineral fragments ($PM_{0.1\text{-}1.0}$). The measured number PSD after the tube furnace is always reduced by more than an order of magnitude, showing the dominance of carbonaceous particles in the early-stage for PM_1 particles. Local temperature is a dominant factor affecting the devolatilization rate in the early-stage of coal combustion. In the low temperature case (1100 K), the devolatilization time is much larger than 31 ms. Therefore, during the volatile release process, soot particles are expected to form from tar in the vicinity of coal particles within the locally reducing atmosphere.[176] At the same time, soot oxidation is not kinetically favored at the low temperature. As a result, the measured PSD at 31 ms increases. At higher temperature (1700 K), however, the devolatilization time is shorter than 15 ms and a larger number of soot particles are formed. The subsequent oxidation process consumes some of the soot particles, decreasing the number concentration and the mean diameter. In the medium temperature case (1400 K), both soot formation and oxidation play roles. Larger $PM_{0.1\text{-}1.0}$ particles are partially oxidized, resulting in a dramatic decrease in number concentration for that size, but the shrinking/breaking residuals contribute to $PM_{0.03}$, along with the nucleated nascent soot particles. For temperatures higher than 1400 K, the results indicate that after 31 ms, the $PM_{0.1\text{-}1.0}$ particles are mainly mineral residuals. An ultrafine mineral residual in ($PM_{0.03}$) is also observed, implying nucleation of vaporized elements.

7.4 Summary

The ultrafine particle formation and evolution processes were investigated in a flat-flame Hencken burner during the early-stage combustion of sub-bituminous PRB coal. The particle size

distribution (PSD) was measured by scanning mobility particle sizer (SMPS) for PRB sub-bituminous coal at three temperatures (1100, 1400 and 1700 K) and two residence times (15 and 31 ms). A tube furnace was operated in a tandem DMA configuration to oxidize the soot particles so that mineral residuals could be distinguished from soot. In the early-stage of pulverized coal combustion, the ultrafine PM_1 included soot and minerals. At a high gas temperature of 1700 K, devolatilization was fast, leading to a drop in the $PM_{1.0}$ concentration. At a low temperature of 1100 K, the residence time was too low for significant devolatilization, which led to continuous formation of $PM_{1.0}$ without consumption. However, at an intermediate temperature of 1400 K, both soot oxidation and formation were significant. $PM_{0.1\text{-}1.0}$ particles were partially oxidized at higher residence times to form more $PM_{0.1}$. For the 1400 K and 1700 K cases, at a residence time of 31 ms, the $PM_{0.1\text{-}1}$ particles were mainly minerals.

Chapter 8

Submicron particle formation during biomass combustion in a flat-flame burner

8.1 Introduction

In Chapter 7, submicron particle formation from coal was studied. Here, in Chapter 8, an evaluation of biomass combustion is presented, with specific focus on the role of water-leaching on submicron particle formation and ignition in the flat-flame burner. Biomass is considered carbon-neutral, and its use as a primary energy source can reduce carbon footprints and help meet renewable energy targets.[178] By far, the largest consumption of biomass is still via small-scale domestic stoves, where combustion efficiencies are low and fine particle emissions are severe [179]. The use of biomass in large-scale industry furnaces to produce heat and electricity has been of interest in recent years.[180] However, the potassium and chlorine content in biomass is high, which induces severe fouling and corrosion problems, and leads to large emissions of potassium-containing particulate matter with an aerodynamic diameter less than 2.5 μm ($PM_{2.5}$).[181-183]

One approach to solve these problems in biomass-fired furnaces is to lower the potassium content in the feedstock, and water-leaching has proven highly effective at this for agricultural biomass.[184] Water-leaching of biomass-waste also widely occurs in nature, where the water-soluble minerals in biomass are washed away largely by natural processes. On the other hand, many studies have shown that potassium is a catalyst for both pyrolysis and carbon oxidation, and thus its removal could affect biomass particle ignition and biomass char burning rate.[185, 186]

There are many studies of the effects of water-leaching pretreatment, and subsequent potassium doping, on biomass pyrolysis, ignition, and bio-char oxidation. Most of these works found that potassium accelerated thermochemical processes of biomass.[187-189] It is noteworthy that all these studies were conducted using thermogravimetric analysis (TGA), at a heating rate 4-5 orders of magnitude lower than that in practical furnaces. Generally, in TGA, both volatile and char oxidation during biomass combustion are completed before 550 °C due to the limited heating rate of 5-100 °C·min^{-1}, while the dominant inorganic-potassium remains in the solid residuals until 600-800 °C.[190] In a practical furnace, the heating rate is as high as 10^5 °C·s^{-1}, so it will certainly reach the temperature needed for potassium release before complete combustion. Thus, TGA experiments at a low heating rate cannot provide relevant information about the effect of potassium on biomass burning in a practical furnace.

In contrast to TGA, a flat-flame reactor has a heating rate comparable to that of a conventional furnace and is convenient for in-situ optical measurements. This reactor is becoming more popular for particle ignition studies.[52, 60, 94] Flat-flame reactors have been predominantly used for studying coal combustion, while biomass particle ignition studies are rare. Wornat et al.[191] were the first to measure the combustion rate of biomass char in a flat-flame burner reactor, using a two-color optical pyrometer and a video camera. Their work showed that biomass char burned over a much wider range of particle temperatures than for coal particles, and biomass particles were somewhat less reactive than low-rank lignite and sub-bituminous coal particles. The most recent study on biomass combustion was done using an optically accessible McKenna burner.[192] It showed that the biomass had a longer ignition delay time than high-volatile bituminous coal due to its high inherent moisture content. In addition, biomass might have longer ignition delay time than coal when water-leaching treatment has removed potassium. However, no prior studies using a flat-

flame burner, have reported on the changes in biomass particle ignition before and after potassium removal by water-leaching. In addition, there are no studies of the impact of water-leaching on reduction of fine particles, which would help to quantitatively determine the contribution of water-soluble substances to the formation of submicron particles during biomass combustion.

This chapter demonstrates the effect of water-leaching on $PM_{1.0}$ emission and ignition during biomass combustion. Using the Hencken flat-flame burner, we can attain a heating rate comparable to that of a practical furnace. A high-speed video camera and electrical low-pressure impactor (ELPI) are respectively employed to study ignition and $PM_{1.0}$ along the height above the burner. The mineral composition of residual solid particles along the height is measured to quantify potassium release in the early-stage of biomass combustion. The results of $PM_{1.0}$ emission and biomass ignition from the flat-flame burner are compared with the $PM_{1.0}$ emissions from a drop tube furnace and the ignition data from thermogravimetric analysis (TGA).

8.2 Experimental methods

8.2.1 Fuel samples and leaching method

The biomass used in this study was wheat straw, with less than 100 μm particle size. The proximate and ultimate analyses of the biomass can be found in [193]. Biomass samples were leached with deionized water at 80 °C for 6 hours, filtrated, and then dried in an oven at 80 °C for 24 hours. The elemental compositions of the raw and leached biomass ash are shown in Table 8-1. After water leaching, the content of potassium and sulfur in the ash decreased from 13.5% to 3.1%, and from 2.6% to 0.8%, respectively, and no chlorine was detected. Since the ash content was lowered by about half, 90% of the potassium and all the chlorine was removed by water-leaching. The surface functional groups of samples were analyzed using a Fourier transform infrared

spectrometer as shown in Fig. 8-1. The pore structural parameters including BET surface area and pore volume were determined using a Tristar 3020 volumetric analyzer. The changes in the pore structural parameters before and after washing treatments are summarized in Table 8-1. The results of FTIR and BET show that the water-leaching treatment does not affect the functional groups in biomass, but increases the surface area and pore volume. A thermogravimetric analyzer was used to compare combustion of the biomass samples before and after water leaching, at a heating rate of 20 °C·min^{-1} and a gas flow rate of 200 ml·min^{-1} (20 vol.% O_2).

Table 8-1. Ash elemental compositions and pore volume of raw and water-leached biomass

Samples	Ash chemical compositions (wt. %)										BET surface area	Pore volume
	K	Cl	S	Ca	Mg	P	Fe	Si	Al	O	(m^2/g)	(cm^3/g)
Raw biomass	13.5	2	2.6	15	5.2	1.9	3.1	15.8	2.3	38.7	3.7	6.3×10^{-3}
Water leached	3.1	0	0.8	13.1	3.8	1.4	4.5	27.1	3.2	43	8.4	9.1×10^{-3}

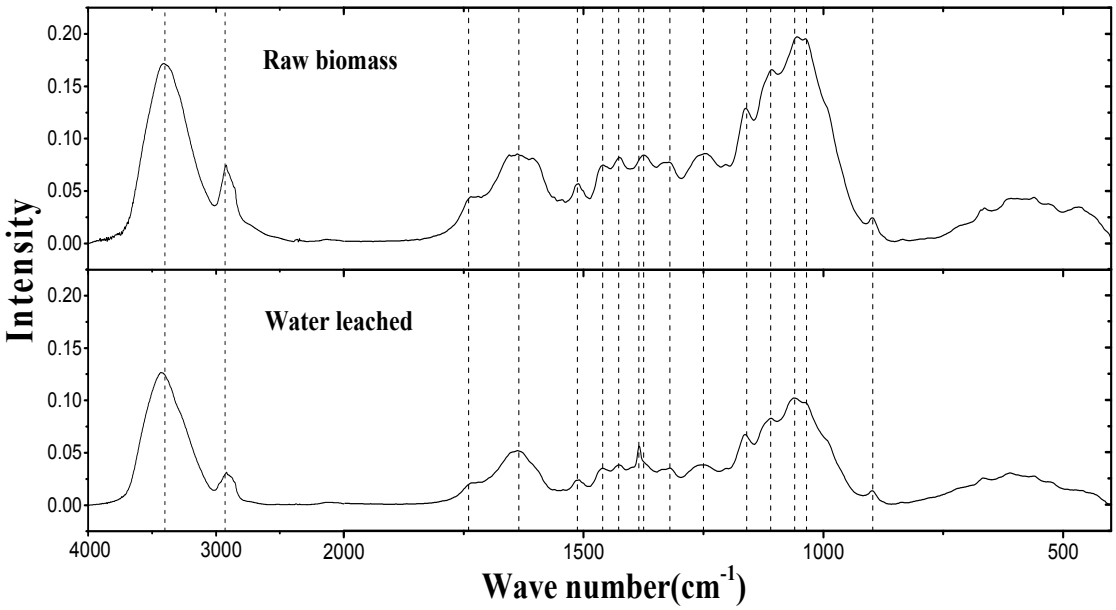

Figure 8-1. FTIR spectra of raw and water-leached biomass samples.

8.2.2 Hencken flat-flame burner

A schematic of the flat-flame burner is shown in Fig. 8-2 with various instrumentations for particle size distribution measurements and ignition studies. It consists of the Hencken flat-flame burner described in Chapter 2, a feeding unit, optical diagnostics unit, and a particle/gas sampling unit. The biomass particles were fed at a stable rate of ~50 mg·min^{-1}. A high-resolution high-speed video camera (MEMRECAM HX-7, NAC) captured the ignition. An ELPI was employed to measure the particle size distributions (PSDs) of $PM_{1.0}$ from the gas sampled at 12 cm above burner. A high-dilution probe was used to sample particles. Particles larger than 10 μm (PM_{10+}) were cut off before the ELPI. Then, the particles passed through a second-stage dilution before the ELPI. Particles were collected at different heights, and their morphology and elemental composition were obtained using scanning electron microscopic technique with an electron dispersive X-ray spectroscopy (SEM-EDS). This study was performed at two temperatures

(1000 °C and 1300 °C) and one oxygen composition (20 vol.%). Particle residence times were determined by tracking the motion of more than twenty particles. In the flat-flame burner, a particle residence time is short, making it particularly suitable for studying early-stage processes of coal combustion. On the other hand, a drop tube furnace provides a residence time longer than 3s, making it suitable for studying conditions typical of a practical furnace exit.

8.2.3 Ignition delay time determination

Determining the ignition time for a solid particle at a high heating rate is challenging. In this study, the ignition criterion is based on the visible light signal, following the procedures used by Yuan et al. [60]. To obtain a normalized visible light-signal intensity, 10,000 continuous pictures are averaged and post-processed in MATLAB. Yuan et al.[60] defined the ignition time for a single coal particle as the residence time when the light intensity reached 10% of the maximum peak intensity, while a later study by the same group for the ignition process of single biomass particles selected a criterion of 15%.[192] In this chapter, to quantitatively present the ignition time for different conditions, ignition time is defined as the inflection point of the emission intensity profile. This method is comparable to those used in previous studies in terms of the effect of water-leaching on ignition time.[60, 192]

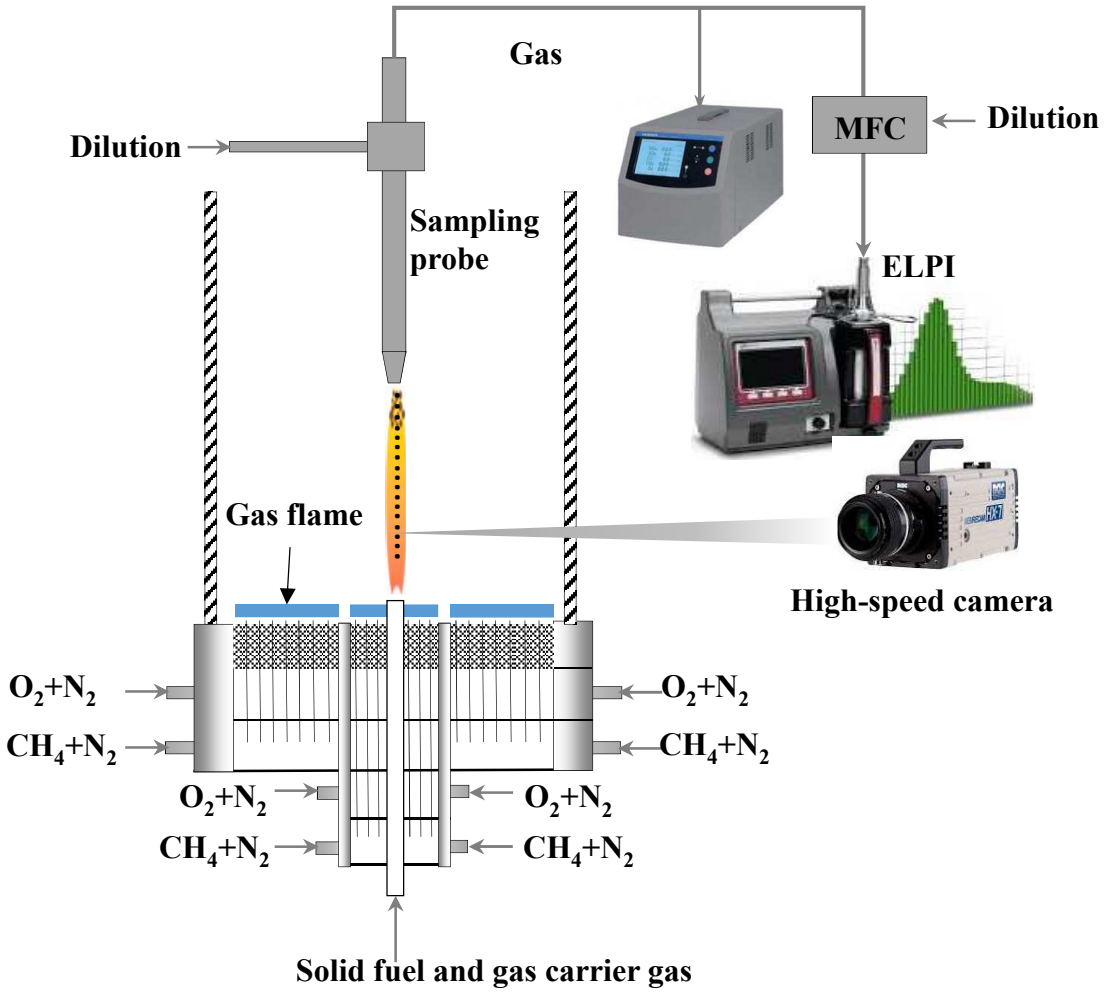

Figure 8-2. Flat-flame burner with various instruments for particle sampling, particle size distribution measurement, and particle videography.

8.3 Results and discussion

8.3.1 Effect of feedstock water-leaching on $PM_{1.0}$ emissions

The mass PSDs of $PM_{1.0}$ from biomass combustion in the drop tube furnace are presented in Fig. 8-3(a). In the drop tube furnace, before water-leaching, the PSDs show peaks around 274 nm and 97 nm at 1000 °C and 1300 °C, respectively. The difference in the peak locations at the two

temperatures is mainly due to the particle composition. As shown in Fig. 8-4, the sulfur content in fine particles at 1000 °C is much higher than that at 1300 °C. A higher K_2SO_4(g) partial pressure in the flue gas at the moderate temperature of 1000 °C results in more nucleation of potassium vapor, and thus a larger particle size.[193] Fig. 8-4 also shows the distribution of the K/(Cl+2S) mole ratios in $PM_{1.0}$. The ratio is about 1 for $PM_{1.0}$ smaller than 397 nm, showing that all the potassium reacts with chlorine and sulfur to form potassium salts. For particles larger than 397 nm, the K/(Cl+2S) mole ratio linearly increases with particle size, suggesting that more potassium exists as insoluble salts, e.g. silicates and aluminosilicates.

After water-leaching, as shown in Fig. 8-3(a), the $PM_{1.0}$ emission is reduced by approximately 90%. So, the peak location of the submicron PSD curve shifts from 274 nm to a smaller size of ~57 nm for the 1000 °C gas temperature. The effect of water-leaching on particle size can also be directly observed in the SEM images in Fig. 8-4, where the morphologies of $PM_{1.0}$ from biomass combustion at 1000 °C before and after water-leaching are presented. Before water-leaching, significantly large agglomerates of regular crystals of KCl are observed. After water-leaching, smaller particles with irregular shapes are observed.

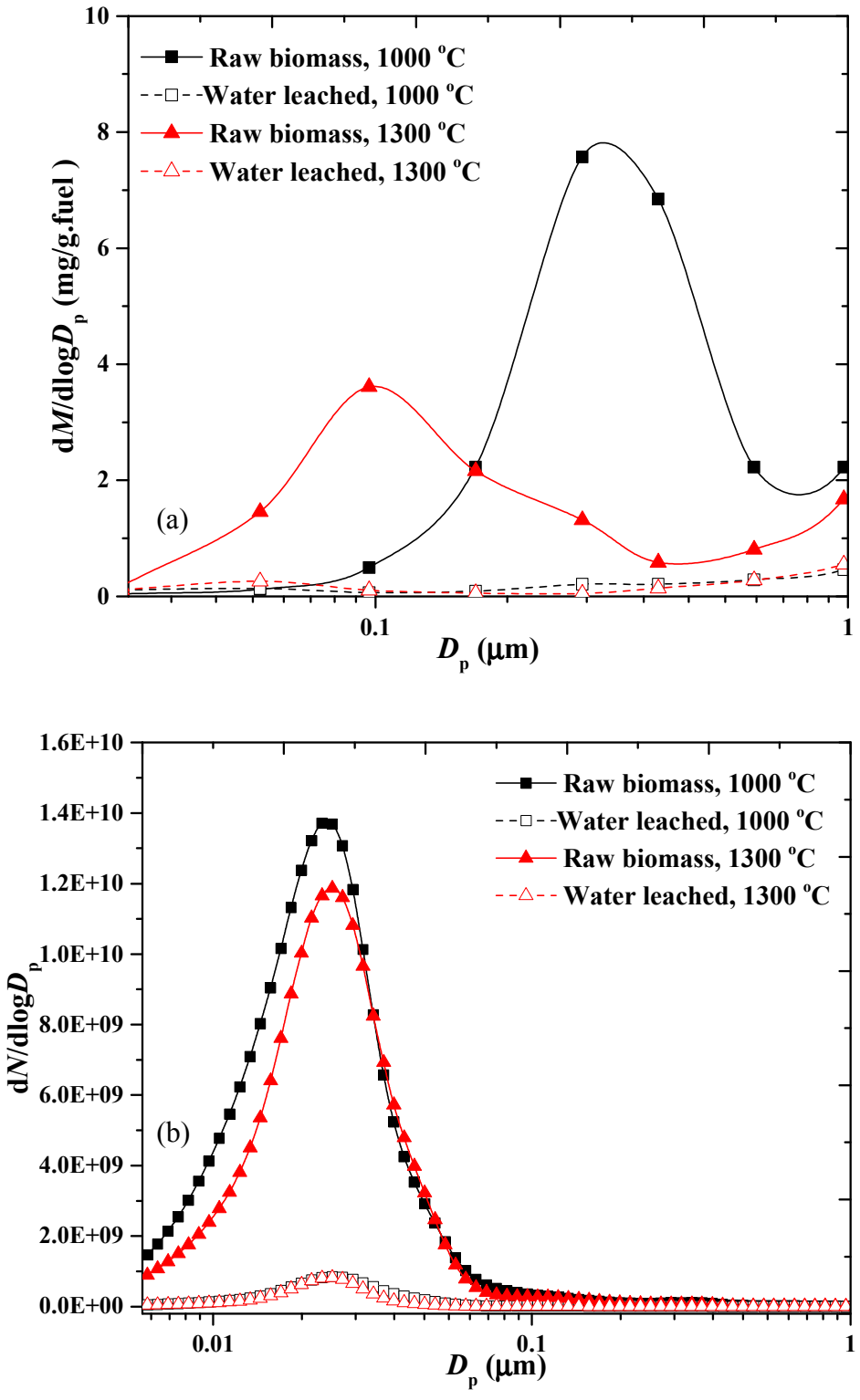

Figure 8-3. PSDs of $PM_{1.0}$ from raw and water-leached biomass combustion in (a) drop tube furnace and (b) Hencken flat-flame burner.

The effect of feedstock water-leaching on the $PM_{1.0}$ emission from biomass combustion can also be observed from the elemental compositions in Fig. 8-4. At 1000 °C, before water-leaching, the sum of the K, Cl, and S contents in $PM_{1.0}$ is beyond 95%, while the sum of the Si, Ca, Mg, P, and Fe content is correspondingly small. Water-leaching removes most of the K and Cl from fuel. In contrast, the less soluble Si, Ca, Mg, P, and Fe minerals are difficult to remove by water-leaching. Therefore, after water-leaching, the KCl and K_2SO_4 contents in $PM_{1.0}$ decrease to about 40%, but the other insoluble substances account for about 60%. The $PM_{1.0}$ emissions of biomass combusted in the flat-flame burner, before and after water-leaching, are shown in Fig. 8-3(b). Approximately 94% of the $PM_{1.0}$, especially $PM_{0.1}$, is removed through water-leaching, consistent with results from the drop tube furnace. The temperature of the flue gas sampled in the flat-flame burner is high (1000 °C and 1300 °C), so the potassium in flue gas exists as vapor. Therefore, to a certain extent, the $PM_{1.0}$ is formed through condensation during cold nitrogen dilution. It can be concluded that water-soluble potassium dominates $PM_{1.0}$ emission, and feedstock water-leaching is an efficient route to remove potassium and control fine particle emissions from biomass combustion.

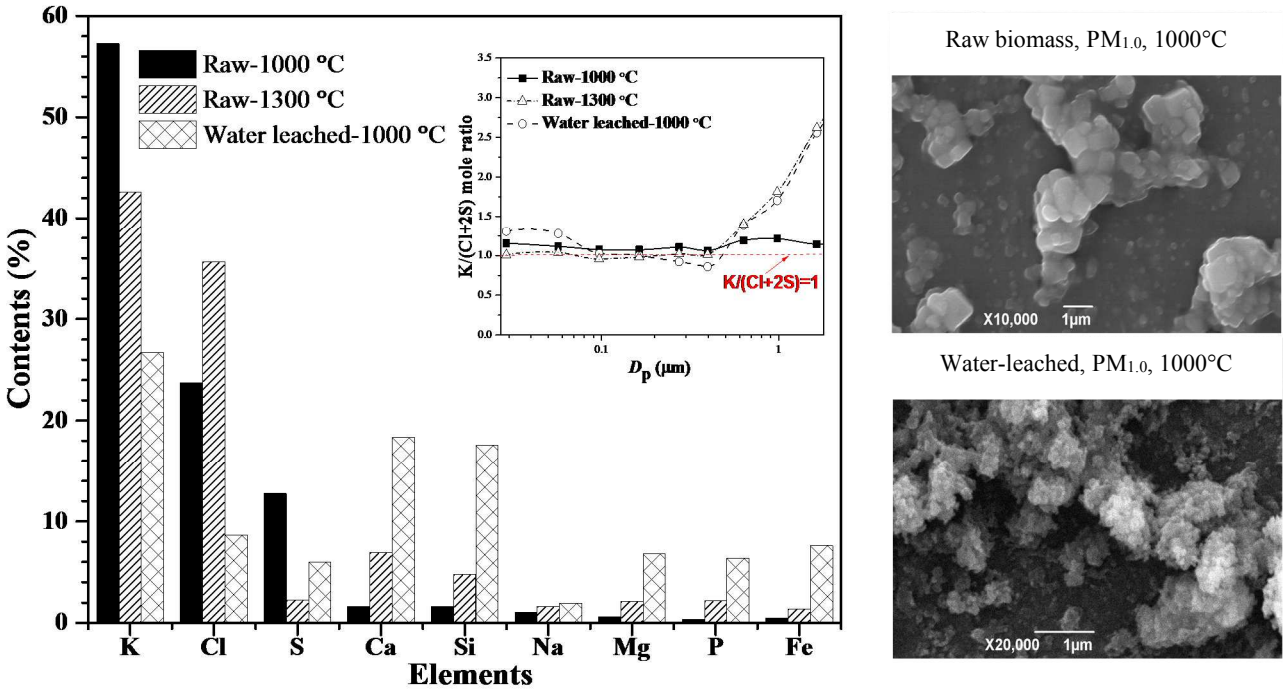

Figure 8-4. Elemental composition and morphology of PM1.0 from biomass combustion.

8.3.2 Effect of feedstock water-leaching on ignition

Biomass particle ignition was studied in the flat-flame burner to observe the effect of potassium on ignition when the heating rate was on the order of 10^5 °C/s. Using the method described in Section 8.2.3, reconstructed flame luminosities are shown in Fig. 8-5. From the overall mapping of light intensity, it was observed that the ignition of biomass particles at 1300 °C occurred much earlier than that at 1000 °C. After water-leaching, the ignition of biomass particles at 1000 °C was significantly delayed compared to that of raw biomass. However, when the gas temperature was increased to 1300 °C, the ignition delay from water-leaching was marginal.

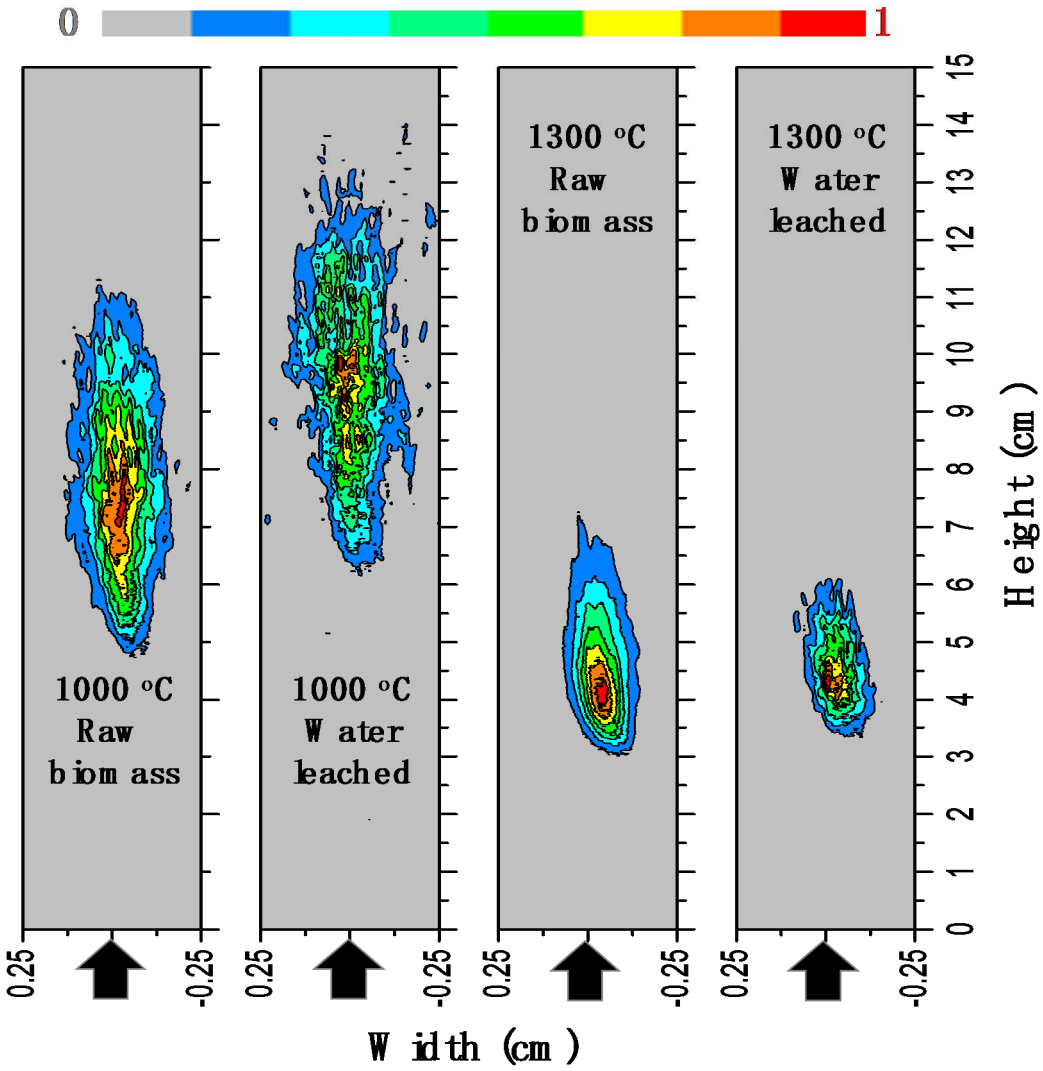

Figure 8-5. Contour of biomass flames at different temperatures. False color indicates emission intensity

To quantitatively present the ignition time of different conditions, light intensity contour plots as a function of burner height were obtained. For raw biomass, the ignition of biomass particles at 1000 °C occurred at 20 ms (Fig. 8-6), which is over two times later than that at 1300 °C (9.2 ms), and the light intensity distribution at 1000 °C was much wider. This result indicated that the biomass particle heating time was longer at lower temperatures, with longer ignition and burnout

times. After water-leaching, the ignition time was delayed from 20 ms to 24 ms for 1000 °C and from 9.2 ms to 10.2 ms for 1300 °C. In addition, in contrast with the ignition delay by feedstock water-leaching, the biomass burnout time was shorter after feedstock water-leaching, especially at 1300 °C (Fig. 8-7). This difference can have two causes. As shown in Table 8-1, water-leaching increases the surface area and pore volume, and thus promotes solid phase burnout. Alternatively, after water-leaching, biomass particles have a higher melting temperature, which benefits the biochar burnout [187].

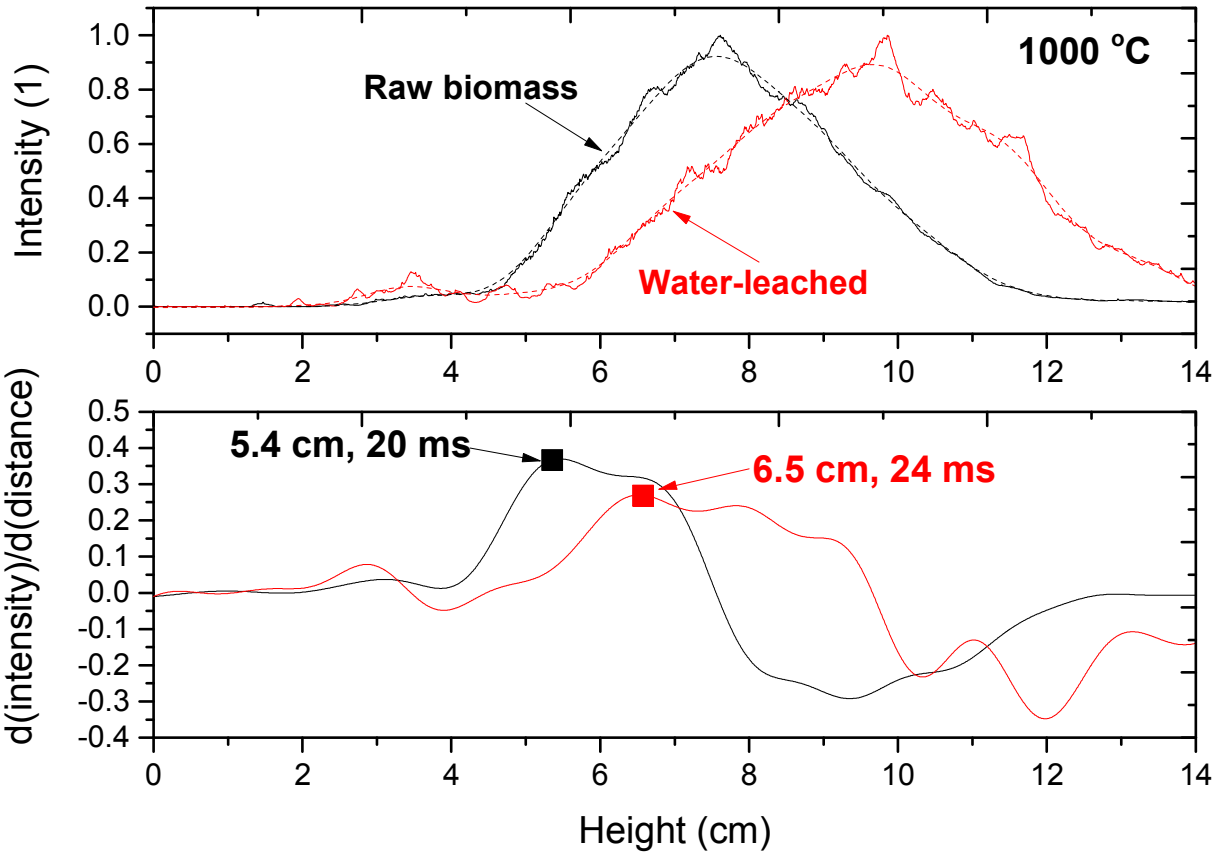

Figure 8-6. Ignition times of biomass particles at 1000 °C.

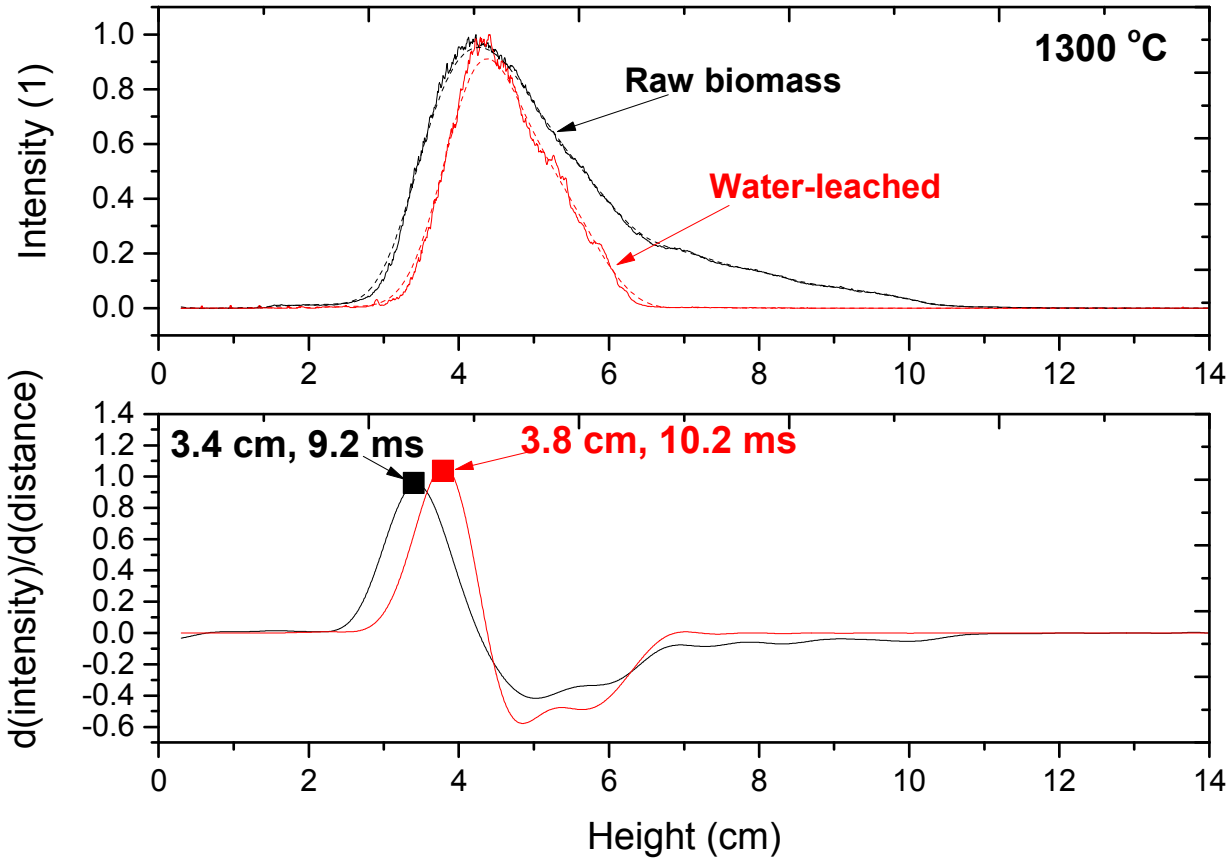

Figure 8-7. Ignition times of biomass particles at 1300 °C.

Simoes et al.[192] recently compared the ignition modes and times for five kinds of biomass. Their results showed that the ignition mode (homogeneous or heterogeneous) strongly depends on temperatures and fuel properties. They pointed out that at temperatures less than 1377 °C, wheat straw particles experienced heterogeneous ignition. The effect of feedstock washing on ignition delay was observed in a recent study on the combustion characteristics of high-sodium lignite. The sodium ions were detected in the flame, and were believed to have promoted catalytic cracking of large tar species.[194] However, these studies were conducted with a larger, static coal particle (2.5 mm) heated in a tube furnace at a low heating rate (100 °C·s^{-1}). To show how water-soluble

minerals affect the ignition of biomass particles in a pulverized combustion furnace, it is essential to track the mineral release before ignition under realistic conditions.

8.3.3 Thermogravimetric analysis and results

The ignition property of straw before and after water-leaching is further measured by TGA, and the TG-DTG curves are shown for comparison in Fig. 8-8. The TG-DTG curve shows two stages: 1) devolatilization and 2) char oxidation. After water-leaching, the devolatilization shifts to higher temperature, increasing the ignition temperature by 17 °C and the char oxidation by 28 °C. This result is consistent with previous studies which reported that alkaline metals, particularly potassium, act as catalysts to promote volatile release.[187-189] *Ab initio* modeling also showed that potassium ions can chelate in the ring of cellulose structures and interact with hydroxyl and ether groups to enhance cracking reactions.[195]

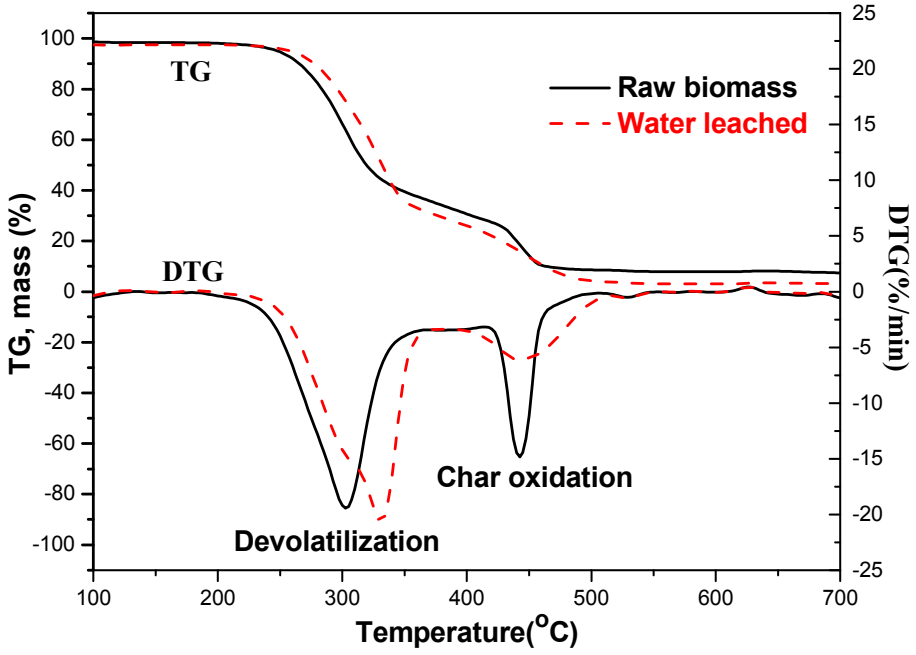

Figure 8-8. TG-DTG curves of raw and water-leached biomass combustion.

No obvious change is observed in the peak temperature of char oxidation in the DTG curves, however, the DTG peak height can also indicate the burning rate of biomass fuels.[196] As shown in Fig. 8-8, after water-leaching, the valley of char oxidation in the DTG curve is much shallower, indicating that water-leaching significantly inhibits the oxidation of biomass char. The catalytic oxidation of char by metal ions can be explained by oxygen-transfer theory.[197] Alkali metal atoms on carbon surfaces act as active sites for the chemisorption of oxygen, thereby weakening C=C surface bonds and promoting the desorption of CO and CO_2 products.[198] In conclusion, at a low heating rate, such as in a TGA, the water-soluble substances in biomass promote the devolatilization and accelerate the oxidation of biochar.

8.3.4 Potassium release at the early stage of biomass combustion

As shown in Fig. 8-8 and discussed in 8.3.3, under TGA conditions of a low heating rate, the combustion process stops at ~500 °C. However, a significant amount of potassium is released from biomass at a higher temperature, starting at 600-700 °C.[190] Thus, below 500 °C, potassium remains within the biomass particle and catalyzes the pyrolysis and char oxidation, as was observed in our TGA experiments. However, recently developed on-line diagnostics offer the option to measure the release kinetics of potassium and other minerals from biomass pyrolysis, gasification, and combustion at a realistically high heating rate.[195, 199, 200] These on-line diagnostic results show that a certain amount of potassium is released during devolatilization and char oxidation, depending on the biomass type and temperature. The release ratios of potassium in the devolatilization and char oxidation stages are in the range of 2-20% and 10-60%, respectively. However, these previous studies employed a much bigger particle size (4-8 mm), which resulted in a lower heating rate ($<10^3$ °C $\cdot s^{-1}$) and a longer burnout time (15-80 s). In the present study, the particle size was <100

μm, with a much higher heating rate of $>10^5$ °C ·s^{-1}. However, it is challenging to perform on-line diagnostics of mineral vapor release from a moving particle on a millisecond time scale.

To evaluate the extent of potassium release during biomass combustion, especially before ignition, we sampled larger particles (PM_{10+}) at 2 cm, 4 cm, and 6 cm above the flat-flame burner. These heights represented positions before, at, and after ignition respectively. The mineral composition of these samples along the reactor height was then analyzed and presented in Fig. 8-9(a). Before ignition, the K, Cl, and Ca contents decrease as the height above the reactor increases from 0 cm to 4 cm. In contrast, the Si and Al contents increase. However, when the sampling position increases from 4 cm to 6 cm, (post-ignition locations), a significant decrease of Si and Al contents can be observed. Especially at 1300 °C, the relative contents of Si and Al decrease by over 50 wt%, leading to a significant increase in Ca content. Thus, after particle ignition, Si and Al are still being released due to the high particle temperature and reducing atmosphere on the particle surface. However, at 6 cm, even for 1000°C, the relative content of K remains nearly constant after ignition. With the continuous release of Si and Al after ignition, a stable K content in biomass particles indicates a continuous release of K as well. Through the data analysis of Fig. 8-9(a), since the composition of Ca increases as K, Si, Al compositions decrease, Ca can be regarded as a relatively stable tracer in the particle post-ignition. Therefore, a plot of the K/Ca mass ratio is appropriate to show the continuous release of K. Figure 8-9(b) confirms this expectation of continuous release of K through the preheating and ignition process.

Comparing the ignition curves (Fig. 8-6 and Fig. 8-7) and K release curve (Fig. 8-9b), it can be concluded that a large amount of K has been released before biomass ignition. This further supports the conclusion that the catalytic promotion by potassium of biomass ignition is mainly through its effect during the devolatilization stage.

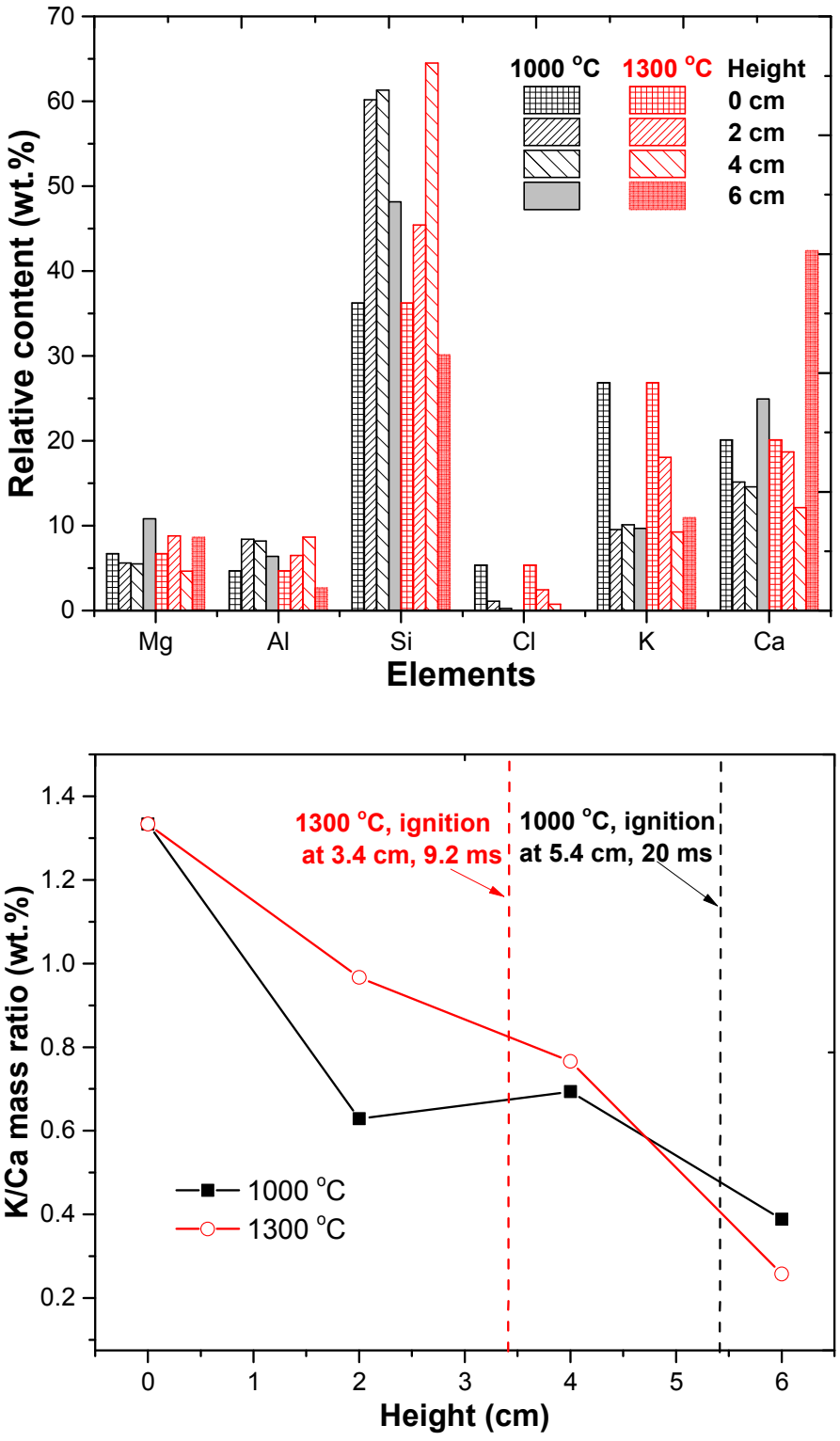

Figure 8-9. Profiles of (a) elemental content and (b) K/Ca mass ratio along the reactor height.

8.4 Summary

In this work, for the first time, the effects of feedstock water-leaching on $PM_{1.0}$ emission and ignition during biomass combustion were studied using a flat-flame burner. A high-speed video camera and electrical low-pressure impactor were employed to study ignition and $PM_{1.0}$ respectively. In addition, the mineral composition of PM_{10+} along the flat-flame burner height were measured to assess the potassium release during the early-stage of biomass combustion. The results show that water-leaching does not change the functional groups of biomass, but increases the BET surface area and pore volume. Thus, KCl and K_2SO_4 are the dominant species in $PM_{1.0}$ emissions from biomass burning, and water-leaching removes 90% of the potassium and all the chlorine, correspondingly reducing the same amounts of $PM_{1.0}$ emission.

Using the flat-flame burner, a longer ignition delay is observed for water-leached biomass particles, which agrees with the delay of biomass-devolatilization in TGA. The profile of mineral compositions in PM_{10+} along the flat-flame burner height shows a high potassium release ratio before biomass ignition. The high release ratio indicates that the catalytic effect of potassium as a water-soluble mineral on biomass on ignition is primarily through enhancement of devolatilization. The catalytic promotion by potassium of on biochar oxidation at a high heating rate is much complex, and needs further study.

Chapter 9

Conclusions and future work

9.1 Key conclusions

A systematic study of coal particle ignition in different combustion environments has been presented, with emphasis on the effects of the reducing-to-oxidizing environment, particle size, particle-to-particle interaction, and particle size classifications. The effects are all benchmarked against a typically studied post-flame oxygen composition of 20% on a mole basis. Key conclusions from this research work include the following:

1. The newly designed two-stage Hencken burner is an effective platform for fundamental studies of the early-stage processes of coal combustion.
2. The two-stage flat-flame burner with the inner stage flame operating fuel-rich mimics the temperature-time history of coal particles in the near-burner region of pulverized coal boilers.
3. High-speed videography with appropriate image-processing techniques is an effective tool to study ignition and combustion processes.
4. The ignition behavior of coal particles is strongly affected by the reducing-to-oxidizing environment. Heating rates at nominal 1800 K gas temperatures can reduce the ignition time by a factor of 3 to 5 over those of 1300 K environment for the same particle size.
5. For single particle studies, ignition delay times increase monotonically as particle size increases in an oxidizing condition. However, in the reducing-to-oxidizing condition where

particle reaction is oxygen-limited, ignition delay times are nearly the same for large particle sizes in high gas temperatures.

6. In a nominal 1300 K gas temperature, the oxygen concentration in which the particles burn has a secondary effect on single particle ignition behavior for small particles; hence, there is a similar ignition delay time in both oxidizing and reducing-to-oxidizing conditions.
7. Predictions of ignition behavior based on sampled particles from experiments using narrow particle size ranges are fairly comparable, on average, to statistical ignition predictions. This, thus, confirms for the first time the assumption that the ignition behavior of a few sampled particles is representative of a given size classification.
8. For particle stream ignition, ignition delay time is independent of particle size for 1800 K nominal gas temperature in either the oxidizing or the reducing-to-oxidizing environment. However, the reducing-to-oxidizing environment increases ignition delay times by 100% on average over those of oxidizing conditions at 1800 K gas temperature.
9. For particle stream ignition at 1300 K nominal gas temperature, ignition delay times strongly depend on particle size in the stream, with a characteristic crossover at which the ignition delay times in reducing-to-oxidizing environment are less than those of oxidizing conditions for large particles.
10. The model predictions here are consistent with experimental results. The presented model shows that homogeneous ignition depends on temperature, particle size, and the volatile concentration at the particle surface. Based on a lower flammability limit comparison, homogeneous ignition occurs in large particles (above 90 μm), while heterogeneous ignition is dominant in smaller particles (below 75 μm) for nominal gas temperature of 1300 K.

11. In high temperature environment though, homogeneous ignition precedes heterogeneous ignition, as indicated by the lower flammability analysis.
12. In high-temperature and high-oxygen environment, overall char burnout is controlled by oxidation, and the contribution of gasification reactions is insignificant.
13. In high temperature environment, the particle surface cooling due to gasification reactions in reducing-to-oxidizing environment reduces the rate of char burnout significantly.

Regarding submicron particle formation, considering coal and biomass particles, the following are the key findings:

14. As an early-stage of coal combustion, $PM_{1.0}$ formation, including soot and minerals, is significantly affected by temperature and residence time.
15. At an intermediate temperature of 1400 K, both organic formation and oxidation are significant. With a higher residence time, $PM_{0.1\text{-}1.0}$ particles are partially oxidized to form more $PM_{0.1}$ particles.
16. At 1400 K and 1700 K, PM $_{0.1\text{-}1}$ come dominantly from inorganic mineral matter sources as opposed to organic sources, even at a low residence time of 31 ms.
17. Water-soluble potassium dominates $PM_{1.0}$ emission from the studied wheat straw biomass, consistent with findings in the literature.
18. Water-leaching is an efficient way to remove potassium and control fine particle emissions from biomass combustion.
19. The catalytic effects of potassium on biomass ignition is primarily through its enhancement of volatile release in high temperature environments.

9.2 Future work

The works presented in this dissertation have shown the significance of reducing-to-oxidizing environment on coal particle ignition as an early-stage process of coal combustion. These works have been done in nitrogen environments, such as are found in air-fired boilers. The following are some suggestions for future research:

1. The inner flame region could be improved to provide longer residence time, which is needed for the refractory oxide pathway for ultrafine aerosol formation.
2. Assuming a flame product temperature of 2000 K for near-zero excess oxygen, a gas mixture of 1100 K (about the minimum temperature used for fundamental ash studies) will be associated with an oxygen concentration of 12 %. Thus, a well-controlled environment with 8% to 12% oxygen concentration is the right base-case for ultrafine aerosol studies. [201, 202] A study on the effects of oxygen composition on the nucleation of suboxides to form ultrafine aerosol in a reducing-to-oxidizing environment would be interesting.
3. Along the same line of thought, the gas temperature could be characterized for higher temperatures such as 2000 K, which would promote the vaporization of the refractory oxides. Such high temperatures would be appropriate for modern coal-fired boilers which involve the use of high oxygen concentration. One example of such boilers is the Staged, Pressurized Oxy-combustion Technology under development at Washington University in St Louis.
4. Along with high speed videography, further ignition studies with particle surface temperature measurements can provide data valuable for improving numerical model predictions of ignition mechanism. For example, using multi-vision high-speed, high-resolution imaging technique, temperature of the gas phase could be determined at the

standoff height where ignition occurs. Such measurements will provide information on the minimum gas temperature required for ignition and can allow for theoretical determination of a difficult-to-measure variable such as volatile concentration at ignition point. Assuming that volatile combustion reaction can be simplified to a one-step global reaction rate in Arrhenius form, then accurate volatile concentration at ignition point can be determined analytically.[31] Also, such gas temperature measurements can be used to verify a theoretical prediction of ignition based on modified Semenov thermal explosion analysis and to improve predictions of activation energies, frequency factor, and specific reaction rates for different particle sizes, as described in the literature.[50]

References

1. Editor *BP Statistical Review of World Energy*; BP PLC: 1 St James's Square, London SW1Y 4PD 2017.
2. International Energy Outlook. https://www.eia.gov/outlooks/ieo/exec_summ.php (October 12, 2017),
3. Energy Technology Perspective https://www.iea.org/publications/freepublications/publication/ETP2012_free.pdf
4. Outlook for Energy: Journey to 2040. http://corporate.exxonmobil.com/en/energy/energy-outlook/highlights (October 14, 2017),
5. Coal Facts 2015. https://www.worldcoal.org/sites/default/files/resources_files/Coal%20Facts%202015.pdf (October 13, 2017),
6. U.S. Energy Information Adminidtration Independent Statistics and Analysis https://www.eia.gov/outlooks/ieo/exec_summ.php
7. Bhat, S.; Agarwal, P. K., The effect of moisture condensation on the spontaneous combustibility of coal. *Fuel* **1996,** 75, (13), 1523-1532.
8. Smoot, L. D.; Smith, P. J., *Coal combustion and gasification*. Springer Science & Business Media: 2013.
9. Reid, W., Coal Ash-Its Effect on Combustion Systems. In Wiley: New York: 1981; pp 1389-1445.
10. van der Zwaan, B., Coal and Climate Change. **2004**.
11. Change, I. C., Mitigation of climate change. *Summary for Policymakers* **2007,** 10, (5.4).
12. Nakicenovic, N.; Alcamo, J.; Grubler, A.; Riahi, K.; Roehrl, R.; Rogner, H.-H.; Victor, N., *Special Report on Emissions Scenarios (SRES), A Special Report of Working Group III of the Intergovernmental Panel on Climate Change*. Cambridge University Press: 2000.
13. Myhrvold, N. P.; Caldeira, K., Greenhouse gases, climate change and the transition from coal to low-carbon electricity. *Environmental Research Letters* **2012,** 7, (1), 014019.

14. Hegerl, G. C.; Hasselmann, K.; Cubasch, U.; Mitchell, J.; Roeckner, E.; Voss, R.; Waszkewitz, J., Multi-fingerprint detection and attribution analysis of greenhouse gas, greenhouse gas-plus-aerosol and solar forced climate change. *Climate Dynamics* **1997,** 13, (9), 613-634.

15. Forster, P.; Ramaswamy, V.; Artaxo, P.; Berntsen, T.; Betts, R.; Fahey, D. W.; Haywood, J.; Lean, J.; Lowe, D. C.; Myhre, G., Changes in atmospheric constituents and in radiative forcing. Chapter 2. In *Climate Change 2007. The Physical Science Basis*, 2007.

16. Do not write off coal amid India's solar boom. https://www.worldcoal.org/don%E2%80%99t-write-coal-amid-india%E2%80%99s-solar-boom (October 15,2017),

17. Bittanti, S.; Calloni, L.; Canevese, S.; De Marco, A.; Prandoni, V., A Clean-Coal Control Technology Application Study: Modelling and Control Issues for a Coal Gasifier. **2009**.

18. Boer, G.; Flato, G.; Ramsden, D., A transient climate change simulation with greenhouse gas and aerosol forcing: projected climate to the twenty-first century. *Climate Dynamics* **2000,** 16, (6), 427-450.

19. Davis, K. A.; Hurt, R. H.; Yang, N. Y.; Headley, T. J., Evolution of char chemistry, crystallinity, and ultrafine structure during pulverized-coal combustion. *Combustion and Flame* **1995,** 100, (1-2), 31-40.

20. Xiao, Z.; Shang, T.; Zhuo, J.; Yao, Q., Study on the mechanisms of ultrafine particle formation during high-sodium coal combustion in a flat-flame burner. *Fuel* **2016**.

21. Baxter, L. L., The evolution of mineral particle size distributions during early stages of coal combustion. *Progress in Energy and Combustion Science* **1990,** 16, (4), 261-266.

22. Lu, L.; Kong, C.; Sahajwalla, V.; Harris, D., Char structural ordering during pyrolysis and combustion and its influence on char reactivity. *Fuel* **2002,** 81, (9), 1215-1225.

23. Senior, C.; Panagiotou, T.; Sarofim, A. F.; Helble, J. J., Formation of ultra-fine particulate matter from pulverized coal combustion. **2000**.

24. Senior, C. L.; Bool Iii, L. E.; Srinivasachar, S.; Pease, B. R.; Porle, K., Pilot scale study of trace element vaporization and condensation during combustion of a pulverized sub-bituminous coal. *Fuel Processing Technology* **2000,** 63, (2–3), 149-165.

25. Spörl, R.; Paneru, M.; Babat, S.; Stein-Brzozowska, G.; Ott, S.; Maier, J.; Scheffknecht, G., Fly Ash and Deposit Transformations in Air and Oxy-Fuel Combustion. **2014**.

26. Viskanta, R.; Mengüç, M., Radiation heat transfer in combustion systems. *Progress in Energy and Combustion Science* **1987,** 13, (2), 97-160.

27. Suriyawong, A.; Gamble, M.; Lee, M.-H.; Axelbaum, R.; Biswas, P., Submicrometer Particle Formation and Mercury Speciation Under O_2−CO_2 Coal Combustion. *Energy & Fuels* **2006,** 20, (6), 2357-2363.

28. Quann, R.; Sarofim, A. In *Vaporization of refractory oxides during pulverized coal combustion*, Symposium (international) on combustion, 1982; Elsevier: 1982; pp 1429-1440.

29. Quann, R. J.; Neville, M.; Janghorbani, M.; Mims, C. A.; Sarofim, A. F., Mineral matter and trace-element vaporization in a laboratory-pulverized coal combustion system. *Environmental science & technology* **1982,** 16, (11), 776-781.

30. Huque, Z.; Ali, M. R.; Kommalapati, R., Application of pulse detonation technology for boiler slag removal. *Fuel Processing Technology* **2009,** 90, (4), 558-569.

31. Chen, L.; Yong, S. Z.; Ghoniem, A. F., Oxy-fuel combustion of pulverized coal: Characterization, fundamentals, stabilization and CFD modeling. *Progress in Energy and Combustion Science* **2012,** 38, (2), 156-214.

32. Smoot, L. D.; Brown, B. W., Controlling mechanisms in gasification of pulverized coal. *Fuel* **1987,** 66, (9), 1249-1256.

33. Annamalai, K.; Ryan, W., Interactive processes in gasification and combustion—II. Isolated carbon, coal and porous char particles. *Progress in Energy and Combustion Science* **1993,** 19, (5), 383-446.

34. Cai, L.; Zou, C.; Guan, Y.; Jia, H.; Zhang, L.; Zheng, C., Effect of steam on ignition of pulverized coal particles in oxy-fuel combustion in a drop tube furnace. *Fuel* **2016,** 182, (Supplement C), 958-966.

35. Ponzio, A.; Senthoorselvan, S.; Yang, W.; Blasiak, W.; Eriksson, O., Ignition of single coal particles in high-temperature oxidizers with various oxygen concentrations. *Fuel* **2008,** 87, (6), 974-987.

36. Prationo, W.; Zhang, J.; Cui, J.; Wang, Y.; Zhang, L., Influence of inherent moisture on the ignition and combustion of wet Victorian brown coal in air-firing and oxy-fuel modes: Part 1: The volatile ignition and flame propagation. *Fuel Processing Technology* **2015,** 138, (Supplement C), 670-679.

37. Xia, F.; Yang, Z.; Adeosun, A.; Kumfer, B. M.; Axelbaum, R. L., Staged, pressurized oxy-combustion: computational fluid dynamic simulations of radiant boilers. In *The 8th International Symposium on Coal Combustion*, Beijng, China, 2015.

38. Umeki, K.; Yamamoto, K.; Namioka, T.; Yoshikawa, K., High temperature steam-only gasification of woody biomass. *Applied Energy* **2010,** 87, (3), 791-798.

39. Xiao, R.; Zhang, M.; Jin, B.; Huang, Y.; Zhou, H., High-temperature air/steam-blown gasification of coal in a pressurized spout-fluid bed. *Energy & Fuels* **2006,** 20, (2), 715-720.

40. Noor, M.; Wandel, A. P.; Yusaf, T. In *The development of MILD combustion open burner experimental setup*, Proceedings of the 2nd International Conference of Mechanical Engineering Research (ICMER 2013), 2013; Universiti Malaysia Pahang: 2013; pp 1-19.

41. Sorrentino, G.; Sabia, P.; de Joannon, M.; Cavaliere, A.; Ragucci, R., The Effect of Diluent on the Sustainability of MILD Combustion in a Cyclonic Burner. *Flow, Turbulence and Combustion* **2016,** 96, (2), 449-468.

42. Neville, M.; Sarofim, A. In *The stratified composition of inorganic submicron particles produced during coal combustion*, Symposium (international) on combustion, 1982; Elsevier: 1982; pp 1441-1449.

43. Khare, S. P.; Wall, T. F.; Farida, A. Z.; Liu, Y.; Moghtaderi, B.; Gupta, R. P., Factors influencing the ignition of flames from air-fired swirl pf burners retrofitted to oxy-fuel. *Fuel* **2008,** 87, (7), 1042-1049.

44. Khatami, R.; Levendis, Y. A., An overview of coal rank influence on ignition and combustion phenomena at the particle level. *Combustion and Flame* **2016,** 164, 22-34.

45. Riaza, J.; Khatami, R.; Levendis, Y. A.; Álvarez, L.; Gil, M. V.; Pevida, C.; Rubiera, F.; Pis, J. J., Single particle ignition and combustion of anthracite, semi-anthracite and bituminous coals in air and simulated oxy-fuel conditions. *Combustion and Flame* **2014,** 161, (4), 1096-1108.

46. Timothy, L. D.; Sarofim, A. F.; Béer, J. M., Characteristics of single particle coal combustion. *Symposium (International) on Combustion* **1982,** 19, (1), 1123-1130.

47. Chen, Y.; Mori, S.; Pan, W.-P., Studying the mechanisms of ignition of coal particles by TG-DTA. *Thermochimica Acta* **1996,** 275, (1), 149-158.

48. Zhang, D.-K., Laser-induced ignition of pulverized fuel particles. *Combustion and flame* **1992,** 90, (2), 134-142.

49. Prationo, W.; Zhang, L., Influence of steam on ignition of Victorian brown coal particle stream in oxy-fuel combustion: In-situ diagnosis and transient ignition modelling. *Fuel* **2016,** 181, (Supplement C), 1203-1213.

50. Chen, M.-R.; Fan, L.-S.; Essenhigh, R. H., Prediction and measurement of ignition temperatures of coal particles. *Symposium (International) on Combustion* **1985,** 20, (1), 1513-1521.

51. Du, X.; Annamalai, K., The transient ignition of isolated coal particle. *Combustion and Flame* **1994,** 97, (3), 339-354.

52. Kim, R.-G.; Li, D.; Jeon, C.-H., Experimental investigation of ignition behavior for coal rank using a flat flame burner at a high heating rate. *Experimental Thermal and Fluid Science* **2014,** 54, 212-218.

53. Lee, H.; Choi, S., An observation of combustion behavior of a single coal particle entrained into hot gas flow. *Combustion and Flame* **2015,** 162, (6), 2610-2620.

54. McLean, W. J.; Hardesty, D. R.; Pohl, J. H., Direct observations of devolatilizing pulverized coal particles in a combustion environment. *Symposium (International) on Combustion* **1981,** 18, (1), 1239-1248.

55. Prationo, W.; Zhang, J.; Cui, J.; Wang, Y.; Zhang, L., Influence of inherent moisture on the ignition and combustion of wet Victorian brown coal in air-firing and oxy-fuel modes: Part 1: The volatile ignition and flame propagation. *Fuel Processing Technology* **2015**.

56. Shaddix, C. R.; Molina, A., Particle imaging of ignition and devolatilization of pulverized coal during oxy-fuel combustion. *Proceedings of the Combustion Institute* **2009,** 32, (2), 2091-2098.

57. Liu, Y.; Geier, M.; Molina, A.; Shaddix, C. R., Pulverized coal stream ignition delay under conventional and oxy-fuel combustion conditions. *International Journal of Greenhouse Gas Control* **2011,** 5, Supplement 1, S36-S46.

58. Sahu, A. K.; Joshi, K. A.; Raghavan, V.; Rangwala, A. S., Comprehensive numerical modeling of ignition of coal dust layers in different configurations. *Proceedings of the Combustion Institute* **2015,** 35, (2), 2355-2362.

59. Yuan, Y.; Li, S.; Zhao, F.; Yao, Q.; Long, M. B., Characterization on hetero-homogeneous ignition of pulverized coal particle streams using CH∗ chemiluminescence and 3 color pyrometry. *Fuel* **2015**.

60. Yuan, Y.; Li, S.; Li, G.; Wu, N.; Yao, Q., The transition of heterogeneous–homogeneous ignitions of dispersed coal particle streams. *Combustion and Flame* **2014,** 161, (9), 2458-2468.

61. Li, S.; Ren, Y.; Biswas, P.; Tse, S. D., Flame aerosol synthesis of nanostructured materials and functional devices: Processing, modeling, and diagnostics. *Progress in Energy and Combustion Science* **2016,** 55, 1-59.

62. Yuan, Y.; Li, S.; Yao, Q., Dynamic behavior of sodium release from pulverized coal combustion by phase-selective laser-induced breakdown spectroscopy. *Proceedings of the Combustion Institute* **2015,** 35, (2), 2339-2346.

63. Wooldridge, M. S.; Torek, P. V.; Donovan, M. T.; Hall, D. L.; Miller, T. A.; Palmer, T. R.; Schrock, C. R., An experimental investigation of gas-phase combustion synthesis of SiO2 nanoparticles using a multi-element diffusion flame burner. *Combustion and Flame* **2002,** 131, (1), 98-109.

64. Baxter, L. L.; DeSollar, R. W., A mechanistic description of ash deposition during pulverized coal combustion: predictions compared with observations. *Fuel* **1993,** 72, (10), 1411-1418.

65. Boow, J.; Goard, P., Fireside deposits and their effect on heat transfer in a pulverized fuel-fired boiler-3. Influence of physical characteristics of deposit on its radiant emittance and effective thermal conductance. *Journal of the Institute of Fuel* **1969,** 42, (346), 412-8.

66. Annamalai, K.; Ryan, W., Interactive processes in gasification and combustion. Part I: Liquid drop arrays and clouds. *Progress in Energy and Combustion Science* **1992,** 18, (3), 221-295.

67. Essenhigh, R. H.; Misra, M. K.; Shaw, D. W., Ignition of coal particles: A review. *Combustion and Flame* **1989,** 77, (1), 3-30.

68. Wall, T.; Gupta, R.; Gururajan, V.; Zhang, D.-k., The ignition of coal particles. *Fuel* **1991,** 70, (9), 1011-1016.

69. Annamalai, K.; Ryan, W.; Dhanapalan, S., Interactive processes in gasification and combustion—Part III: Coal/char particle arrays, streams and clouds. *Progress in Energy and Combustion Science* **1994,** 20, (6), 487-618.

70. Du, X.; Gopalakrishnan, C.; Annamalai, K., Ignition and combustion of coal particle streams. *Fuel* **1995,** 74, (4), 487-494.

71. Ryan, W.; Annamalai, K., Group Ignition of a Cloud of Coal Particles. *Journal of Heat Transfer* **1991,** 113, (3), 677-687.

72. Ryan, W.; Annamalai, K.; Caton, J., Relation between group combustion and drop array studies. *Combustion and Flame* **1990,** 80, (3), 313-321.

73. Bejarano, P. A.; Levendis, Y. A., Combustion of coal chars in oxygen-enriched atmospheres. *Combustion Science and Technology* **2007,** 179, (8), 1569-1587.

74. Bejarano, P. A.; Levendis, Y. A., Single-coal-particle combustion in O_2/N_2 and O_2/CO_2 environments. *Combustion and Flame* **2008,** 153, (1), 270-287.

75. Khatami, R.; Levendis, Y. A., On the deduction of single coal particle combustion temperature from three-color optical pyrometry. *Combustion and Flame* **2011,** 158, (9), 1822-1836.

76. Khatami, R.; Levendis, Y. A.; Delichatsios, M. A., Soot loading, temperature and size of single coal particle envelope flames in conventional-and oxy-combustion conditions (O_2/N_2 and O_2/CO_2). *Combustion and Flame* **2015,** 162, (6), 2508-2517.

77. Sarroza, A. C.; Bennet, T. D.; Eastwick, C.; Liu, H., Characterising pulverised fuel ignition in a visual drop tube furnace by use of a high-speed imaging technique. *Fuel Processing Technology* **2017,** 157, (Supplement C), 1-11.

78. Li, S.; Ren, Y.; Biswas, P.; Stephen, D. T., Flame aerosol synthesis of nanostructured materials and functional devices: Processing, modeling, and diagnostics. *Progress in Energy and Combustion Science* **2016,** 55, 1-59.

79. Campbell, M.; Bohlin, G.; Schrader, P.; Bambha, R.; Kliewer, C.; Johansson, K.; Michelsen, H., Design and characterization of a linear Hencken-type burner. *Review of Scientific Instruments* **2016,** 87, (11), 115114.

80. Barlow, R.; Dibble, R.; Chen, J.-Y.; Lucht, R., Effect of Damköhler number on superequilibrium OH concentration in turbulent nonpremixed jet flames. *Combustion and Flame* **1990,** 82, (3-4), 235-251.

81. Hindasageri, V.; Vedula, R.; Prabhu, S., Thermocouple error correction for measuring the flame temperature with determination of emissivity and heat transfer coefficient. *Review of Scientific Instruments* **2013,** 84, (2), 024902.

82. Bradley, D.; Matthews, K., Measurement of high gas temperatures with fine wire thermocouples. *Journal of Mechanical Engineering Science* **1968,** 10, (4), 299-305.

83. De, D., Measurement of flame temperature with a multi-element thermocouple. *Journal of the Institute of Energy* **1981,** 54, 113-16.

84. Heitor, M. V.; Moreira, A. L. N., Thermocouples and sample probes for combustion studies. *Progress in Energy and Combustion Science* **1993,** 19, (3), 259-278.

85. Chen, R.; Axelbaum, R., Scalar dissipation rate at extinction and the effects of oxygen-enriched combustion. *Combustion and Flame* **2005,** 142, (1), 62-71.

86. Du, D. X.; Axelbaum, R. L.; Law, C. K., The influence of carbon dioxide and oxygen as additives on soot formation in diffusion flames. *Symposium (International) on Combustion* **1991,** 23, (1), 1501-1507.

87. Kumfer, B.; Skeen, S.; Axelbaum, R., Soot inception limits in laminar diffusion flames with application to oxy–fuel combustion. *Combustion and Flame* **2008,** 154, (3), 546-556.

88. Kumfer, B.; Skeen, S.; Chen, R.; Axelbaum, R., Measurement and analysis of soot inception limits of oxygen-enriched coflow flames. *Combustion and Flame* **2006,** 147, (3), 233-242.

89. Skeen, S.; Yablonsky, G.; Axelbaum, R., Characteristics of non-premixed oxygen-enhanced combustion: II. Flame structure effects on soot precursor kinetics resulting in soot-free flames. *Combustion and Flame* **2010,** 157, (9), 1745-1752.

90. Xia, F.; Yablonsky, G. S.; Axelbaum, R. L., Numerical study of flame structure and soot inception interpreted in carbon-to-oxygen atom ratio space. *Proceedings of the Combustion Institute* **2013,** 34, (1), 1085-1091.

91. Kumfer, B. M.; Skeen, S. A.; Axelbaum, R. L., Soot inception limits in laminar diffusion flames with application to oxy–fuel combustion. *Combustion and Flame* **2008,** 154, (3), 546-556.

92. Skeen, S.; Yablonsky, G.; Axelbaum, R., Characteristics of non-premixed oxygen-enhanced combustion: I. The presence of appreciable oxygen at the location of maximum temperature. *Combustion and Flame* **2009,** 156, (11), 2145-2152.

93. Liu, Y.; Geier, M.; Molina, A.; Shaddix, C. R., Pulverized coal stream ignition delay under conventional and oxy-fuel combustion conditions. *International Journal of Greenhouse Gas Control* **2011,** 5, S36-S46.

94. Molina, A.; Shaddix, C. R., Ignition and devolatilization of pulverized bituminous coal particles during oxygen/carbon dioxide coal combustion. *Proceedings of the Combustion Institute* **2007,** 31, (2), 1905-1912.

95. Gao, Q.; Li, S.; Yuan, Y.; Zhao, Y.; Yao, Q., Role of Minerals in the Evolution of Fine Particulate Matter during Pulverized Coal Combustion. *Energy & Fuels* **2016,** 30, (3), 1815-1821.
96. ANSYS, I. Modeling Coal Combustion Using the Non-Premixed Model. http://www.afs.enea.it/project/neptunius/docs/fluent/html/ug/node560.htm#sec-coal-inputs-pdf (06-01),
97. Liu, H.; Liu, Y.; Yi, G.; Nie, L.; Che, D., Effects of Air Staging Conditions on the Combustion and NOx Emission Characteristics in a 600 MW Wall Fired Utility Boiler Using Lean Coal. *Energy & Fuels* **2013,** 27, (10), 5831-5840.
98. Coulson, J.; Richardson, J.; Backhurst, J.; Harker, J., *Vol. 2: Particle technology and separation processes*. Oxford [etc.]: Butterworth-Heinemann: 1991.
99. Howard, J. B.; Essenhigh, R. H., Mechanism of solid-partical combustion with simultaneous gas-phase volatiles combustion. *Symposium (International) on Combustion* **1967,** 11, (1), 399-408.
100. Gururajan, V. S.; Wall, T. F.; Gupta, R. P.; Truelove, J. S., Mechanisms for the ignition of pulverized coal particles. *Combustion and Flame* **1990,** 81, (2), 119-132.
101. Zou, C.; Cai, L.; Wu, D.; Liu, Y.; Liu, S.; Zheng, C., Ignition behaviors of pulverized coal particles in O_2/N_2 and O_2/H_2O mixtures in a drop tube furnace using flame monitoring techniques. *Proceedings of the Combustion Institute* **2015,** 35, (3), 3629-3636.
102. Khatami, R.; Stivers, C.; Levendis, Y. A., Ignition characteristics of single coal particles from three different ranks in O_2/N_2 and O_2/CO_2 atmospheres. *Combustion and Flame* **2012,** 159, (12), 3554-3568.
103. Maffei, T.; Khatami, R.; Pierucci, S.; Faravelli, T.; Ranzi, E.; Levendis, Y. A., Experimental and modeling study of single coal particle combustion in O_2/N_2 and Oxy-fuel (O_2/CO_2) atmospheres. *Combustion and Flame* **2013,** 160, (11), 2559-2572.
104. Marek, E.; Stańczyk, K., Case Studies Investigating Single Coal Particle Ignition and Combustion. *Journal of Sustainable Mining* **2013,** 12, (3), 17-31.
105. Solomon, P.; Chien, P.; Carangelo, R.; Serio, M.; Markham, J., New ignition phenomenon in coal combustion. *Combustion and Flame* **1990,** 79, (2), 214-215.
106. Goshayeshi, B.; Sutherland, J. C., A comparison of various models in predicting ignition delay in single-particle coal combustion. *Combustion and Flame* **2014,** 161, (7), 1900-1910.

107. Moroń, W.; Rybak, W., Ignition behaviour and flame stability of different ranks coals in oxy fuel atmosphere. *Fuel* **2015,** 161, 174-181.

108. Prationo, W.; Zhang, J.; Cui, J.; Wang, Y.; Zhang, L., Clarifying the influence of moisture on the ignition and combustion of wet Victorian brown coal in air-firing and oxy-fuel modes: Part 2: Contribution of gasification reaction to char oxidation rate. *Fuel Processing Technology* **2015**.

109. Zhang, D.-k.; Wall, T. F., Ignition of coal particles: the influence of experimental technique. *Fuel* **1994,** 73, (7), 1114-1119.

110. Levendis, Y. A.; Joshi, K.; Khatami, R.; Sarofim, A. F., Combustion behavior in air of single particles from three different coal ranks and from sugarcane bagasse. *Combustion and Flame* **2011,** 158, (3), 452-465.

111. Jüntgen, H.; Van Heek, K. H., An update of german non-isothermal coal pyrolysis work. *Fuel Processing Technology* **1979,** 2, (4), 261-293.

112. Khatami, R.; Stivers, C.; Joshi, K.; Levendis, Y. A.; Sarofim, A. F., Combustion behavior of single particles from three different coal ranks and from sugar cane bagasse in O_2/N_2 and O_2/CO_2 atmospheres. *Combustion and Flame* **2012,** 159, (3), 1253-1271.

113. Xu, Y.; Li, S.; Yuan, Y.; Yao, Q., Measurement on the Surface Temperature of Dispersed Chars in a Flat-Flame Burner Using Modified RGB Pyrometry. *Energy & Fuels* **2016**.

114. Gieras, M.; Klemens, R.; Wolański, P., Experimental and theoretical study of ignition of single coal particles at zero gravity. *Acta Astronautica* **1986,** 13, (5), 231-239.

115. Zou, C.; Cai, L.; Wu, D.; Liu, Y.; Liu, S.; Zheng, C., Ignition behaviors of pulverized coal particles in O 2/N 2 and O 2/H 2 O mixtures in a drop tube furnace using flame monitoring techniques. *Proceedings of the Combustion Institute* **2015,** 35, (3), 3629-3636.

116. Zou, C.; Cai, L.; Zheng, C., Numerical research on the homogeneous/heterogeneous ignition process of pulverized coal in oxy-fuel combustion. *International Journal of Heat and Mass Transfer* **2014,** 73, 207-216.

117. Lim, J. S., Two-dimensional signal and image processing. In Prentice Hall: Englewood Cliffs, NJ, 1990; p 548.

118. Wall, T. F.; Gupta, R. P.; Gururajan, V. S.; Zhang, D.-k., The ignition of coal particles. *Fuel* **1991,** 70, (9), 1011-1016.

119. Howard, J. B.; Essenhigh, R. H., The mechanism of ignition of pulverized coal. *Combustion and Flame* **1965,** 9, (3), 337-339.

120. Sheng, C.; Li, Y.; Liu, X.; Yao, H.; Xu, M., Ash particle formation during O_2/CO_2 combustion of pulverized coals. *Fuel Processing Technology* **2007,** 88, (11–12), 1021-1028.

121. Wang, C. a.; Zhang, X.; Liu, Y.; Che, D., Pyrolysis and combustion characteristics of coals in oxyfuel combustion. *Applied Energy* **2012,** 97, 264-273.

122. Wang, X.; Guo, H.; Liu, F.; Hu, R.; Wang, M., Effects of CO_2 on sulfur removal and its release behavior during coal pyrolysis. *Fuel* **2016,** 165, 484-489.

123. Xu, M.; Yu, D.; Yao, H.; Liu, X.; Qiao, Y., Coal combustion-generated aerosols: Formation and properties. *Proceedings of the Combustion Institute* **2011,** 33, (1), 1681-1697.

124. Yu, Y.; Xu, M.; Yao, H.; Yu, D.; Qiao, Y.; Sui, J.; Liu, X.; Cao, Q., Char characteristics and particulate matter formation during Chinese bituminous coal combustion. *Proceedings of the Combustion Institute* **2007,** 31, (2), 1947-1954.

125. Annamalai, K.; Durbetaki, P., A theory on transition of ignition phase of coal particles. *Combustion and flame* **1977,** 29, 193-208.

126. Zhao, Y.; Kim, H. Y.; Yoon, S. S., Transient group combustion of the pulverized coal particles in spherical cloud. *Fuel* **2007,** 86, (7–8), 1102-1111.

127. Ruiz, M.; Annamalai, K.; Dahdah, T., An experimental study on group ignition of coal particle streams. *Heat and Mass Transfer in Fires and Combustion Systems* **1990,** 148, 19-26.

128. Jüntgen, H., Review of the kinetics of pyrolysis and hydropyrolysis in relation to the chemical constitution of coal. *Fuel* **1984,** 63, (6), 731-737.

129. Seeker, W. R.; Samuelsen, G. S.; Heap, M. P.; Trolinger, J. D., The thermal decomposition of pulverized coal particles. *Symposium (International) on Combustion* **1981,** 18, (1), 1213-1226.

130. Jovanovic, R.; Milewska, A.; Swiatkowski, B.; Goanta, A.; Spliethoff, H., Numerical investigation of influence of homogeneous/heterogeneous ignition/combustion mechanisms on ignition point position during pulverized coal combustion in oxygen enriched and recycled flue gases atmosphere. *International Journal of Heat and Mass Transfer* **2011,** 54, (4), 921-931.

131. Cai, L.; Zou, C.; Liu, Y.; Zhou, K.; Han, Q.; Zheng, C., Numerical and experimental studies on the ignition of pulverized coal in O_2/H_2O atmospheres. *Fuel* **2015,** 139, 198-205.

132. Yu, J.; Lucas, J.; Wall, T.; Liu, G.; Sheng, C., Modeling the development of char structure during the rapid heating of pulverized coal. *Combustion and Flame* **2004,** 136, (4), 519-532.

133. Benfell, K. E.; Liu, G.-S.; Roberts, D. G.; Harris, D. J.; Lucas, J. A.; Bailey, J. G.; Wall, T. F., Modeling char combustion: The influence of parent coal petrography and pyrolysis pressure on

the structure and intrinsic reactivity of its char. *Proceedings of the Combustion Institute* **2000,** 28, (2), 2233-2241.

134. Neville, M.; Quann, R. J.; Haynes, B. S.; Sarofim, A. F., Eighteenth Symposium (International) on CombustionVaporization and condensation of mineral matter during pulverized coal combustion. *Symposium (International) on Combustion* **1981,** 18, (1), 1267-1274.

135. Yu, J.; Lucas, J. A.; Wall, T. F., Formation of the structure of chars during devolatilization of pulverized coal and its thermoproperties: A review. *Progress in Energy and Combustion Science* **2007,** 33, (2), 135-170.

136. Fluent, A., 14.0: Theory guide, ansys. *Inc., Canonsburg, PA* **2011**.

137. Álvarez, L.; Gharebaghi, M.; Jones, J.; Pourkashanian, M.; Williams, A.; Riaza, J.; Pevida, C.; Pis, J.; Rubiera, F., CFD modeling of oxy-coal combustion: prediction of burnout, volatile and NO precursors release. *Applied Energy* **2013,** 104, 653-665.

138. Jovanovic, R.; Milewska, A.; Swiatkowski, B.; Goanta, A.; Spliethoff, H., Sensitivity analysis of different devolatilisation models on predicting ignition point position during pulverized coal combustion in O_2/N_2 and O_2/CO_2 atmospheres. *Fuel* **2012,** 101, 23-37.

139. Jaimes, D. J. Determination of lower flammability limits of mixtures of air and gaseous renewable fuels at elevated temperatures and pressures. UC Irvine, 2017.

140. Van den Schoor, F., Influence of pressure and temperature on flammability limits of combustible gases in air. **2007**.

141. Burgess, M. J.; Wheeler, R. V., CCXXVIII.—The lower limit of inflammation of mixtures of the paraffin hydrocarbons with air. *Journal of the Chemical Society, Transactions* **1911,** 99, 2013-2030.

142. Mitchell, R. E.; Hurt, R.; Baxter, L.; Hardesty, D. *Compilation of Sandia coal char combustion data and kinetic analyses. Milestone report*; Sandia National Labs., Livermore, CA (United States): 1992.

143. Mitchell, R. E.; Ma, L.; Kim, B., On the burning behavior of pulverized coal chars. *Combustion and Flame* **2007,** 151, (3), 426-436.

144. Vandenabeele, H.; Corbeels, R.; Van Tiggelen, A., Activation energy and reaction order inmethane-oxygen flames. *Combustion and Flame* **1960,** 4, 253-260.

145. Poling, B. E.; Prausnitz, J. M.; O'connell, J. P., *The properties of gases and liquids*. Mcgraw-hill New York: 2001; Vol. 5.

146. Law, C. K., *Combustion physics*. Cambridge University Press: 2006.

147. Field, M.; Gill, D.; Morgan, B.; Hawksley, P., Reaction rate of carbon particles. *Combustion of Pulverised Coal, BCURA, Leatherhead, England* **1967**, 186.

148. Paterson, W. R., Mass transfer to, and reaction on, a sphere immersed in a stationary or flowing gas. *Chemical Engineering Science* **2000,** 55, (17), 3567-3570.

149. Zhou, K.; Yu, J.; Ou, W., Effects of Stefan Flow on Ignition and Heat Transfer of a Char Particle in O_2/CO_2 Atmospheres. *Energy & Fuels* **2013,** 27, (6), 3454-3459.

150. Chen, L. Computational fluid dynamics simulations of oxy-coal combustion for carbon capture at atmospheric and elevated pressures. Massachusetts Institute of Technology, 2013.

151. Baum, M.; Street, P., Predicting the combustion behaviour of coal particles. *Combustion science and technology* **1971,** 3, (5), 231-243.

152. Field, M. A., Rate of combustion of size-graded fractions of char from a low-rank coal between 1200 K and 2000 K. *Combustion and Flame* **1969,** 13, (3), 237-252.

153. Smith, I. In *The combustion rates of coal chars: a review*, Symposium (International) on combustion, 1982; Elsevier: 1982; pp 1045-1065.

154. Toporov, D.; Bocian, P.; Heil, P.; Kellermann, A.; Stadler, H.; Tschunko, S.; Förster, M.; Kneer, R., Detailed investigation of a pulverized fuel swirl flame in CO_2/O_2 atmosphere. *Combustion and Flame* **2008,** 155, (4), 605-618.

155. Yin, C., On gas and particle radiation in pulverized fuel combustion furnaces. *Applied Energy* **2015,** 157, 554-561.

156. Hecht, E. S.; Shaddix, C. R.; Geier, M.; Molina, A.; Haynes, B. S., Effect of CO_2 and steam gasification reactions on the oxy-combustion of pulverized coal char. *Combustion and Flame* **2012,** 159, (11), 3437-3447.

157. Hecht, E. S.; Shaddix, C. R.; Molina, A.; Haynes, B. S., Effect of CO_2 gasification reaction on oxy-combustion of pulverized coal char. *Proceedings of the Combustion Institute* **2011,** 33, (2), 1699-1706.

158. Kim, D.; Choi, S.; Shaddix, C. R.; Geier, M., Effect of CO_2 gasification reaction on char particle combustion in oxy-fuel conditions. *Fuel* **2014,** 120, 130-140.

159. Minchener, A., Coal gasification for advanced power generation. *Fuel* **2005,** 84, (17), 2222-2235.

160. Roberts, D.; Harris, D., Char gasification with O_2, CO_2, and H_2O: Effects of pressure on intrinsic reaction kinetics. *Energy Fuels* **2000,** 14, (2), 483-489.

161. Shaddix, C. R., Coal combustion, gasification, and beyond: Developing new technologies for a changing world. *Combustion and Flame* **2012,** 159, (10), 3003-3006.

162. Stanmore, B. R.; Visona, S. P., The contribution to char burnout from gasification by H_2O and CO_2 during pulverized-coal flame combustion. *Combustion and Flame* **1998,** 113, (1?2), 274-276.

163. Gao, Q.; Li, S.; Yuan, Y.; Zhang, Y.; Yao, Q., Ultrafine particulate matter formation in the early stage of pulverized coal combustion of high-sodium lignite. *Fuel* **2015,** 158, 224-231.

164. Couch, G. *Understanding Slagging and Fouling During PF Combustion, IEACR/72*; 01/08/1994, 1994.

165. Eddings, E. G.; Davis, K. A.; Heap, M. P.; Valentine, J. R.; Sarofim, A. F., Mineral Matter Transformation During Pulverized Coal Combustion. *Developments in Chemical Engineering and Mineral Processing* **2001,** 9, (3-4), 313-327.

166. Huang, L.; Norman, J.; Pourkashanian, M.; Williams, A., Prediction of ash deposition on superheater tubes from pulverized coal combustion. *Fuel* **1996,** 75, (3), 271-279.

167. Fan, J. R.; Zha, X. D.; Sun, P.; Cen, K. F., Simulation of ash deposit in a pulverized coal-fired boiler. *Fuel* **2001,** 80, (5), 645-654.

168. Naganuma, H.; Ikeda, N.; Kawai, T.; Takuwa, T.; Ito, T.; Igarashi, Y.; Yoshiie, R.; Naruse, I., Control of ash deposition in pulverized coal fired boiler. *Proceedings of the Combustion Institute* **2009,** 32, (2), 2709-2716.

169. Richard W, B., Fireside slagging, fouling, and high-temperature corrosion of heat-transfer surface due to impurities in steam-raising fuels. *Progress in Energy and Combustion Science* **1996,** 22, (1), 29-120.

170. Walsh, P. M.; Sarofim, A. F.; Beer, J. M., Fouling of convection heat-exchangers by lignitic coal ash. *Energy & Fuels* **1992,** 6, (6), 709-715.

171. Damle, A.; Ensor, D.; Ranade, M., Coal combustion aerosol formation mechanisms: a review. *Aerosol Science and Technology* **1981,** 1, (1), 119-133.

172. Ramanathan, V.; Crutzen, P.; Kiehl, J.; Rosenfeld, D., Aerosols, climate, and the hydrological cycle. *science* **2001,** 294, (5549), 2119-2124.

173. Morris, W. J.; Yu, D.; Wendt, J. O., Soot, unburned carbon and ultrafine particle emissions from air-and oxy-coal flames. *Proceedings of the Combustion Institute* **2011,** 33, (2), 3415-3421.

174. Li, G.; Li, S.; Huang, Q.; Yao, Q., Fine particulate formation and ash deposition during pulverized coal combustion of high-sodium lignite in a down-fired furnace. *Fuel* **2015,** 143, 430-437.

175. Kulkarni, P.; Baron, P. A.; Willeke, K., *Aerosol measurement: principles, techniques, and applications*. John Wiley & Sons: 2011.

176. Ma, J.; Fletcher, T.; Webb, B. In *Conversion of coal tar to soot during coal pyrolysis in a post-flame environment*, Symposium (International) on Combustion, 1996; Elsevier: 1996; pp 3161-3167.

177. Ma, L. Soot Formation During Coal Pyrolysis. Brigham Young University, 1996.

178. Demirbas, M. F.; Balat, M.; Balat, H., Potential contribution of biomass to the sustainable energy development. *Energy Conversion and Management* **2009,** 50, (7), 1746-1760.

179. Fang, J.; Leavey, A.; Biswas, P., Controlled studies on aerosol formation during biomass pyrolysis in a flat flame reactor. *Fuel* **2014,** 116, 350-357.

180. Wang, X.; Tan, H.; Niu, Y.; Pourkashanian, M.; Ma, L.; Chen, E.; Liu, Y.; Liu, Z.; Xu, T., Experimental investigation on biomass co-firing in a 300MW pulverized coal-fired utility furnace in China. *Proceedings of the Combustion Institute* **2011,** 33, (2), 2725-2733.

181. Wang, X.; Liu, Y.; Tan, H.; Ma, L.; Xu, T., Mechanism Research on the Development of Ash Deposits on the Heating Surface of Biomass Furnaces. *Industrial & Engineering Chemistry Research* **2012,** 51, (39), 12984-12992.

182. Yani, S.; Gao, X.; Wu, H., Emission of Inorganic PM10 from the Combustion of Torrefied Biomass under Pulverized-Fuel Conditions. *Energy & Fuels* **2015,** 29, (2), 800-807.

183. Gao, X.; Yani, S.; Wu, H., Emission of Inorganic PM10 during the Combustion of Spent Biomass from Mallee Leaf Steam Distillation. *Energy & Fuels* **2015,** 29, (8), 5171-5175.

184. Wang, Y.; Wang, X.; Tan, H.; Du, W.; Qu, X., Extraction and quantitation of various potassium salts in straw ash. *Environmental Progress & Sustainable Energy* **2015,** 34, (2), 333-338.

185. Jones, J. M.; Darvell, L. I.; Bridgeman, T. G.; Pourkashanian, M.; Williams, A., An investigation of the thermal and catalytic behaviour of potassium in biomass combustion. *Proceedings of the Combustion Institute* **2007,** 31, (2), 1955-1963.

186. Wang, X.; Li, S.; Adeosun, A.; Li, Y.; Vujanović, M.; Tan, H.; Duić, N., Effect of potassium-doping and oxygen concentration on soot oxidation in O_2/CO_2 atmosphere: A kinetics study by thermogravimetric analysis. *Energy Conversion and Management* **2017**.

187. Deng, L.; Zhang, T.; Che, D., Effect of water washing on fuel properties, pyrolysis and combustion characteristics, and ash fusibility of biomass. *Fuel Processing Technology* **2013,** 106, 712-720.

188. Vamvuka, D.; Sfakiotakis, S., Effects of heating rate and water leaching of perennial energy crops on pyrolysis characteristics and kinetics. *Renewable Energy* **2011,** 36, (9), 2433-2439.

189. Fahmi, R.; Bridgwater, A. V.; Darvell, L. I.; Jones, J. M.; Yates, N.; Thain, S.; Donnison, I. S., The effect of alkali metals on combustion and pyrolysis of Lolium and Festuca grasses, switchgrass and willow. *Fuel* **2007,** 86, (10–11), 1560-1569.

190. Johansen, J. M.; Jakobsen, J. G.; Frandsen, F. J.; Glarborg, P., Release of K, Cl, and S during Pyrolysis and Combustion of High-Chlorine Biomass. *Energy & Fuels* **2011,** 25, (11), 4961-4971.

191. Wornat, M. J.; Hurt, R. H.; Davis, K. A.; Yang, N. Y. In *Single-particle combustion of two biomass chars*, Symposium (international) on Combustion, 1996; Elsevier: 1996; pp 3075-3083.

192. Simões, G.; Magalhães, D.; Rabaçal, M.; Costa, M., Effect of gas temperature and oxygen concentration on single particle ignition behavior of biomass fuels. *Proceedings of the Combustion Institute* **2017,** 36, (2), 2235-2242.

193. Wang, X.; Hu, Z.; Adeosun, A.; Liu, B.; Ruan, R.; Li, S.; Tan, H., Particulate matter emission and K/S/Cl transformation during biomass combustion in an entrained flow reactor. *Journal of the Energy Institute* **2017**.

194. Zhang, Z.; Zhu, M.; Zhang, Y.; Setyawan, H. Y.; Li, J.; Zhang, D., Ignition and combustion characteristics of single particles of Zhundong lignite: Effect of water and acid washing. *Proceedings of the Combustion Institute* **2017,** 36, (2), 2139-2146.

195. Saddawi, A.; Jones, J.; Williams, A., Influence of alkali metals on the kinetics of the thermal decomposition of biomass. *Fuel processing technology* **2012,** 104, 189-197.

196. Haykırı-Açma, H., Combustion characteristics of different biomass materials. *Energy Conversion and Management* **2003,** 44, (1), 155-162.

197. Shen, B.; Qin, L., Study on MSW catalytic combustion by TGA. *Energy Conversion and Management* **2006,** 47, (11), 1429-1437.

198. Freriks, I. L.; van Wechem, H. M.; Stuiver, J. C.; Bouwman, R., Potassium-catalysed gasification of carbon with steam: a temperature-programmed desorption and Fourier Transform infrared study. *Fuel* **1981,** 60, (6), 463-470.

199. Fatehi, H.; Li, Z.; Bai, X.; Aldén, M., Kinetics of alkali metal release during biomass pyrolysis. *Proceedings of the Combustion Institute* **2016**.

200. Mason, P. E.; Jones, J. M.; Darvell, L. I.; Williams, A., Gas phase potassium release from a single particle of biomass during high temperature combustion. *Proceedings of the Combustion Institute* **2016**.

201. He, Y.; Zhu, J.; Li, B.; Wang, Z.; Li, Z.; Aldén, M.; Cen, K., In-situ measurement of sodium and potassium release during oxy-fuel combustion of lignite using laser-induced breakdown spectroscopy: effects of O_2 and CO_2 concentration. *Energy & Fuels* **2013,** 27, (2), 1123-1130.

202. Jiménez, S.; Ballester, J., Study of the evolution of particle size distributions and its effects on the oxidation of pulverized coal. *Combustion and Flame* **2007,** 151, (3), 482-494.

Appendix A

MATLAB codes

A.1 Single particle emission intensity extraction code

```
prefix='BackgroundFILENAME_';
Num_start=0;
Num_end=500;

im=double(imread(strcat(prefix,num2str(Num_start,'%08d'),'.tif')));
% Read the video files and convert each frame to tiff image files
for i=1:(Num_end-Num_start)
   % Sum of the images files after string concatenation to obtain average image data file
   im=im+double(imread(strcat(prefix,num2str(Num_start+i,'%08d'),'.tif')));
end
im=im/(Num_end-Num_start+1);
im_background=im;
save('background.mat','im_background');

% load the code below on a separate script

% Obtaining parameters for particle tracking and edge detection
prefix='DataFILENAME_';
load('background.mat');
Num_start=0;

% threshold for particle detection
threshold_R=400;
threshold_G=200;
threshold_B_negative=30;
threshold_B_positive=100;
filter_size=10;
% filter size, smaller than half of particle size
dilate_size=1;
% expansion factor for signal integration

% read image
im=double(imread(strcat(prefix,num2str(Num_start,'%08d'),'.tif'))); % read file
imsize=size(im);
```

```
im_nobg=im-im_background; % substract background
im_denoise=zeros(imsize);
im_denoise(:,:,1)=wiener2(im_nobg(:,:,1),[filter_size filter_size]); % reduce noise
im_denoise(:,:,2)=wiener2(im_nobg(:,:,2),[filter_size filter_size]);
im_denoise(:,:,3)=wiener2(im_nobg(:,:,3),[filter_size filter_size]);

imsize=size(im);

% display statistics of image after denoise and threshold
histogram(round(im_nobg(:,:,1)));
hold on;
histogram(round(im_denoise(:,:,1)));
hold off;
pause;

% display statistics of image after denoise and threshold
histogram(round(im_nobg(:,:,2)));
hold on;
histogram(round(im_denoise(:,:,2)));
hold off;
pause;

% display statistics of image after denoise and threshold
histogram(round(im_nobg(:,:,3)));
hold on;
histogram(round(im_denoise(:,:,3)));
hold off;
pause;

% convert to BW information
im_BW_R=abs(im_denoise(:,:,1))>threshold_R;
im_BW_G=abs(im_denoise(:,:,2))>threshold_G;
im_BW_B= (im_denoise(:,:,3)<-threshold_B_negative) |
(im_denoise(:,:,3)>threshold_B_positive);
% dilate integral area
SE = strel('sphere',dilate_size);
im_BW=imdilate(im_BW_R | im_BW_G | im_BW_B, SE);
% edge of integral area
im_edge=edge(im_BW);

% display image for edge detection
im_display=zeros(imsize(1)*5,imsize(2),3);
im_display(:,:,1)=[im_BW_R;im_BW_G;im_BW_B;im_BW;im(:,:,1)/max(max(max(im)))+im_
edge];
im_display(:,:,2)=[im_BW_R;im_BW_G;im_BW_B;im_BW;im(:,:,2)/max(max(max(im)))-
im_edge];
```

```
im_display(:,:,3)=[im_BW_R;im_BW_G;im_BW_B;im_BW;im(:,:,3)/max(max(max(im)))-
im_edge];

imshow(im_display);

% load the code below on a separate script

% track particles and obtain integral signal for each channel
prefix='DataFILENAME_';
Num_start=0;

pixel_velovity=7;
% estimated velocity of particles; Adjust accordingly
search_distance=2;
% estimated uncertainty of particle velocity; adjust accordingly

% parameters from test_parameters
threshold_R=360; % threshold for particle detection
threshold_G=150;
threshold_B_negative=60;
threshold_B_positive=60;
filter_size=4;
% filter size, smaller than half of particle size
dilate_size=2;
% expansion factor for signal integration
%
position_X=zeros(1000,1);
position_Y=zeros(1000,1);
signal_R=zeros(1000,1);
signal_G=zeros(1000,1);
signal_B=zeros(1000,1);

% read background file
load('background.mat');

% get image information
im=double(imread(strcat(prefix,num2str(Num_start,'%08d'),'.tif')));
imsize=size(im);

% specify particle to be tracked in image
imshow(im(:,1:round(imsize(2)/3),:)./max(max(max(im(:,1:round(imsize(2)/3),:)))));
initial_position=round(ginput(1));
position_X(1)=initial_position(1);
position_Y(1)=initial_position(2);

%
```

```
i=1;
while position_X(i) - search_distance > 0 ...
       && position_X(i)+ search_distance < imsize(2) ...
       && position_Y(i)- search_distance > 0 ...
       && position_Y(i)- search_distance < imsize(1) % tracking range is in the picture

   % read image
   im=double(imread(strcat(prefix,num2str(Num_start+i-1,'%08d'),'.tif')));
   im_nobg=im-im_background; % substract background
   im_denoise=zeros(imsize);
   im_denoise(:,:,1)=wiener2(im_nobg(:,:,1),[filter_size filter_size]); % reduce noise
   im_denoise(:,:,2)=wiener2(im_nobg(:,:,2),[filter_size filter_size]);
   im_denoise(:,:,3)=wiener2(im_nobg(:,:,3),[filter_size filter_size]);

   % detect integral zone
   im_BW_R=abs(im_denoise(:,:,1))>threshold_R;
   im_BW_G=abs(im_denoise(:,:,2))>threshold_G;
   im_BW_B= (im_denoise(:,:,3)<-threshold_B_negative) |
(im_denoise(:,:,3)>threshold_B_positive);
   SE = strel('sphere',dilate_size);
   im_BW=imdilate(im_BW_R | im_BW_G | im_BW_B, SE); % dilate integration area
   im_label=bwlabel(im_BW);

   % search local maximun signal for particle position
   search_area=im_denoise(...
         position_Y(i)+((-search_distance):search_distance),...
         position_X(i)+((-search_distance):search_distance),...
         :);
   search_area(:,:,3) =
search_area(:,:,3).*(1+(search_area(:,:,3)<0)/(threshold_B_negative*threshold_B_positive));%
intensify negative blue signal
   [~,temp]=max(...
      reshape(...
         sum( abs(search_area) , 3)...
         ,[(2*search_distance+1)^2 1] ...
      ));
   position_X(i)=position_X(i)+floor((temp-1)/(2*search_distance+1))-search_distance;
   position_Y(i)=position_Y(i)+mod(temp-1,2*search_distance+1)+1-search_distance;

   % calculate particle signal intensity and position
   if im_label(position_Y(i),position_X(i))==0 % lost particle
      % display tracking position
      im_display=im/3978;
      im_display(position_Y(i),:,1)=1;
      im_display(:,position_X(i),1)=1;
      im_display(position_Y(i),:,2)=0;
```

```
        im_display(:,position_X(i),2)=0;
        im_display(position_Y(i),:,3)=0;
        im_display(:,position_X(i),3)=0;
        imshow(imresize(im_display,0.5));

    else
        % calculate integral area
        integral_area=(im_label==im_label(position_Y(i),position_X(i)));

        % display integral area
        im_display=im/3978;
        integral_edge=edge(integral_area);
        im_display(:,:,1)=im_display(:,:,1)+integral_edge;
        im_display(:,:,2)=im_display(:,:,2)-integral_edge;
        im_display(:,:,3)=im_display(:,:,3)-integral_edge;
        imshow(imresize(im_display,0.5));

        % calculate signal intensity
        signal_R(i)=sum(sum(im_nobg(:,:,1).*integral_area))/sum(sum(integral_area));
        signal_G(i)=sum(sum(im_nobg(:,:,2).*integral_area))/sum(sum(integral_area));
        signal_B(i)=sum(sum(im_nobg(:,:,3).*integral_area))/sum(sum(integral_area));

        % calculate accurate position in current frame

position_X(i)=round(sum(sum(integral_area.*repmat(1:imsize(2),imsize(1),1)))/sum(sum(integr
al_area)));

position_Y(i)=round(sum(sum(integral_area.*repmat((1:imsize(1))',1,imsize(2))))/sum(sum(inte
gral_area)));
     end
    % estimate particle position in next frame
    position_X(i+1)=position_X(i)+pixel_velovity;
    position_Y(i+1)=position_Y(i);
    i=i+1;
end

% output result
num_of_frames=i-1;
position_X=position_X(1:num_of_frames,:);
position_Y=position_Y(1:num_of_frames,:);
signal_R=signal_R(1:num_of_frames,:);
signal_G=signal_G(1:num_of_frames,:);
signal_B=signal_B(1:num_of_frames,:);

Out2Excel=[...
    Num_start 0 0 0 0;...
```

```
    initial_position(1) 0 0 0 0 ;...
    initial_position(2) 0 0 0 0 ;...
    position_X position_Y signal_R signal_G signal_B;];
```

A.2 Code for simultaneous determination of particle size and ignition delay time

```
% calculate the average of images for background processing
prefix='BackgroundFILENAME_';
Num_start=0;
Num_end=500;

im=double(imread(strcat(prefix,num2str(Num_start,'%08d'),'.tif')));
% Read the video files and convert each frame to tiff image files
for i=1:(Num_end-Num_start)
    % Sum of the images files after string concatenation to obtain average image data file
    im=im+double(imread(strcat(prefix,num2str(Num_start+i,'%08d'),'.tif')));
end
im=im/(Num_end-Num_start+1);
im_background=im;
save('background.mat','im_background');

% load the code below on a separate script

% Obtaining parameters for edge detection and error corrections
prefix='DataFILENAME_';
load('background.mat');
Num_start=0;

% Initial thresholds for particle detection
threshold_R=500;
threshold_G=150;
threshold_B_negative=50;
threshold_B_positive=300;
filter_size=5;
% filter size, smaller than half of particle size
dilate_size=2;
% expansion factor for signal integration
save('parameters.mat','threashold_R','threashold_G','threashold_B_negative','threashold_B_positi
ve','filter_size','dilate_size');
```

```
% read image
im=double(imread(strcat(prefix,num2str(Num_start,'%08d'),'.tif'))); % read file
imsize=size(im);
im_nobg=im-im_background; % substract background
im_denoise=zeros(imsize);
im_denoise(:,:,1)=wiener2(im_nobg(:,:,1),[filter_size filter_size]); % reduce noise
im_denoise(:,:,2)=wiener2(im_nobg(:,:,2),[filter_size filter_size]);
im_denoise(:,:,3)=wiener2(im_nobg(:,:,3),[filter_size filter_size]);

imsize=size(im);

% display statistics of image after denoise and threshold
histogram(round(im_nobg(:,:,1)));
hold on;
histogram(round(im_denoise(:,:,1)));
hold off;
pause;

% display statistics of image after denoise and threshold
histogram(round(im_nobg(:,:,2)));
hold on;
histogram(round(im_denoise(:,:,2)));
hold off;
pause;

% display statistics of image after denoise and threshold
histogram(round(im_nobg(:,:,3)));
hold on;
histogram(round(im_denoise(:,:,3)));
hold off;
pause;

% convert to BW information
im_BW_R=abs(im_denoise(:,:,1))>threshold_R;
im_BW_G=abs(im_denoise(:,:,2))>threshold_G;
im_BW_B= (im_denoise(:,:,3)<-threshold_B_negative) |
(im_denoise(:,:,3)>threshold_B_positive);
% dilate integral area
SE = strel('sphere',dilate_size);
im_BW=imdilate(im_BW_R | im_BW_G | im_BW_B, SE);
% edge of integral area
im_edge=edge(im_BW);

% display image for edge detection
im_display=zeros(imsize(1)*5,imsize(2),3);
```

```
im_display(:,:,1)=[im_BW_R;im_BW_G;im_BW_B;im_BW;im(:,:,1)/max(max(max(im)))+im_
edge];
im_display(:,:,2)=[im_BW_R;im_BW_G;im_BW_B;im_BW;im(:,:,2)/max(max(max(im)))-
im_edge];
im_display(:,:,3)=[im_BW_R;im_BW_G;im_BW_B;im_BW;im(:,:,3)/max(max(max(im)))-
im_edge];

imshow(im_display);

% load the code below on a separate script

% track particles and obtain integral signal for each channel and calculate the projected area of
particle before ignition
prefix='DataFILENAME_';
Num_start=0;
pixel_velovity=9;
% estimated velocity of particles; adjust accordingly
search_distance=3;
% estimated uncertainty of particle velocity; adjust accordingly

% read parameters from parameters.mat
load('parameters.mat');
display_magnification=0.6;
%
position_X=zeros(1000,1);
position_Y=zeros(1000,1);
signal_R=zeros(1000,1);
signal_G=zeros(1000,1);
signal_B=zeros(1000,1);
projected_area=zeros(1000,1);

% read background file
load('background.mat');

% get image information
im=double(imread(strcat(prefix,num2str(Num_start,'%08d'),'.tif')));
imsize=size(im);

% specify particle to be tracked in image
imshow(im(:,1:round(imsize(2)/3),:)./max(max(max(im(:,1:round(imsize(2)/3),:)))));
initial_position=round(ginput(1));
position_X(1)=initial_position(1);
position_Y(1)=initial_position(2);
%
i=1;
while position_X(i) - search_distance > 0 ...
```

```
        && position_X(i)+ search_distance < imsize(2) ...
        && position_Y(i)- search_distance > 0 ...
        && position_Y(i)+ search_distance < imsize(1) % tracking range is in the picture

    % read image
    im=double(imread(strcat(prefix,num2str(Num_start+i-1,'%08d'),'.tif')));
    im_nobg=im-im_background; % substract background
    im_denoise=zeros(imsize);
    im_denoise(:,:,1)=wiener2(im_nobg(:,:,1),[filter_size filter_size]); % reduce noise
    im_denoise(:,:,2)=wiener2(im_nobg(:,:,2),[filter_size filter_size]);
    im_denoise(:,:,3)=wiener2(im_nobg(:,:,3),[filter_size filter_size]);

    % detect integral zone
    im_BW_R=abs(im_denoise(:,:,1))>threashold_R;
    im_BW_G=abs(im_denoise(:,:,2))>threashold_G;
    im_BW_B= (im_denoise(:,:,3)<-threashold_B_negative) |
(im_denoise(:,:,3)>threashold_B_positive);
    SE = strel('sphere',dilate_size);
    im_BW=imdilate(im_BW_R | im_BW_G | im_BW_B, SE); % dilate integration area
    im_label=bwlabel(im_BW);

    % search local maximun signal for particle position
    search_area=im_denoise(...
            position_Y(i)+((-search_distance):search_distance),...
            position_X(i)+((-search_distance):search_distance),...
            :);
    search_area(:,:,3) = search_area(:,:,3)+search_area(:,:,3).*(search_area(:,:,3)<0)*...
        (max([threashold_R threashold_G threashold_B_negative
threashold_B_positive])/threashold_B_negative-1);% intensify negative blue signal
    [~,temp]=max(...
        reshape(...
            sum( abs(search_area) , 3)...
            ,[(2*search_distance+1)^2 1] ...
        ));
    position_X(i)=position_X(i)+floor((temp-1)/(2*search_distance+1))-search_distance;
    position_Y(i)=position_Y(i)+mod(temp-1,2*search_distance+1)+1-search_distance;

    % calculate particle signal intensity and position
    if im_label(position_Y(i),position_X(i))==0 % lost particle
        % display tracking position
        im_display=im/1096;
        im_display(position_Y(i),:,1)=1;
        im_display(:,position_X(i),1)=1;
        im_display(position_Y(i),:,2)=0;
        im_display(:,position_X(i),2)=0;
        im_display(position_Y(i),:,3)=0;
```

```
        im_display(:,position_X(i),3)=0;
        imshow(imresize(im_display,display_magnification));
    else
        % calculate integral area
        integral_area=(im_label==im_label(position_Y(i),position_X(i)));

        % display integral area
        im_display=im/1096;
        integral_edge=edge(integral_area);
        im_display(:,:,1)=im_display(:,:,1)+integral_edge;
        im_display(:,:,2)=im_display(:,:,2)-integral_edge;
        im_display(:,:,3)=im_display(:,:,3)-integral_edge;
        imshow(imresize(im_display,display_magnification));

        % calculate signal intensity
        signal_R(i)=sum(sum(im_nobg(:,:,1).*integral_area));
        signal_G(i)=sum(sum(im_nobg(:,:,2).*integral_area));
        signal_B(i)=sum(sum(im_nobg(:,:,3).*integral_area));

        % calculate particle projected area
        projected_area(i)=-sum(sum(im_nobg(:,:,3)./im_background(:,:,3).*integral_area));

        % calculate accurate position in current frame

position_X(i)=round(sum(sum(integral_area.*repmat(1:imsize(2),imsize(1),1)))/sum(sum(integr
al_area)));

position_Y(i)=round(sum(sum(integral_area.*repmat((1:imsize(1))',1,imsize(2))))/sum(sum(inte
gral_area)));

    end

%   1. Creat a directory 'Graphout'
%   2. Select the type of picture to save
%   'im/1096': original picture
%   'im_nobg/1096': substracted background
%   'im_denoise/1096': denoised picture (no background)
%   'im_display': original picture with detected edge
%   for single color, use im(:,:,1) for red et al.
%   imwrite(im/1096,(strcat('.\Graphout\monitor',num2str(Num_start+i-1,'%08d'),'.tif')));

    % estimate particle position in next frame
    position_X(i+1)=position_X(i)+pixel_velovity;
    position_Y(i+1)=position_Y(i);
    i=i+1;
end
```

```
% reorganize results
num_of_frames=i-1;
position_X=position_X(1:num_of_frames,:);
position_Y=position_Y(1:num_of_frames,:);
signal_R=signal_R(1:num_of_frames,:);
signal_G=signal_G(1:num_of_frames,:);
signal_B=signal_B(1:num_of_frames,:);
projected_area=projected_area(1:num_of_frames,:);

% calculate average projected area of a particle
ignit_point=find(signal_R>0.15*max(signal_R),1,'first');
temp=projected_area(1:ignit_point);
temp=temp(temp~=0);
expfit=fittype(@(a,b,c,x) a-exp((x-b)/c));
exp_res=fit((1:numel(temp))',temp,expfit,'StartPoint',[0,numel(temp),5]);
if exp_res.b-3*exp_res.c<0
   disp('not enough effective data points for projected area calculation');
   projected_area_avg=0;
   projected_area_std=0;
else
   temp=temp(1:(fix(exp_res.b-3*exp_res.c)));
   projected_area_avg=mean(temp);
   projected_area_std=std(temp);
   while any(temp>=projected_area_avg+3*projected_area_std) ||
any(temp<=projected_area_avg-3*projected_area_std)
      temp=temp((temp>projected_area_avg-3*projected_area_std) &
(temp<projected_area_avg+3*projected_area_std));
      projected_area_avg=mean(temp);
      projected_area_std=std(temp);
   end
   plot(1:ignit_point,projected_area(1:ignit_point),...
      [1 exp_res.b-3*exp_res.c+sum(projected_area(1:fix(exp_res.b-3*exp_res.c))==0)],[1
1]*projected_area_avg,...
      [1 exp_res.b-3*exp_res.c+sum(projected_area(1:fix(exp_res.b-3*exp_res.c))==0)],[1
1]*(projected_area_avg+3*projected_area_std),...
      [1 exp_res.b-3*exp_res.c+sum(projected_area(1:fix(exp_res.b-3*exp_res.c))==0)],[1
1]*(projected_area_avg-3*projected_area_std));
end

%
Out2Excel=[...
   Num_start 0 0 0 0 0;...
   initial_position(1) 0 0 0 0 0;...
   initial_position(2) 0 0 0 0 0;...
   projected_area_avg 0 0 0 0 0;...
```

```
    projected_area_std 0 0 0 0 0;...
    position_X position_Y signal_R signal_G signal_B projected_area];
```

A.3 Group particle emission intensity extraction code

```
prefix='BackgroundFILENAME_';
Num_start=0;
Num_end=500;

im=double(imread(strcat(prefix,num2str(Num_start,'%08d'),'.tif')));
% Read the video files and convert each frame to tiff image files
for i=1:(Num_end-Num_start)
    % Sum of the images files after string concatenation to obtain average image data file
    im=im+double(imread(strcat(prefix,num2str(Num_start+i,'%08d'),'.tif')));
end
im=im/(Num_end-Num_start+1);
im_background=im;
save('background.mat','im_background');
histogram(im_background(:,:,3));
xlabel('Blue intensity (0-1096)');
ylabel('Number of pixels');
prefix='DataFILENAME_';
Num_start=0;
Num_end=6000;

% load the code below on a separate script

load('background.mat'); % Load the background for noise correction

im=double(imread(strcat(prefix,num2str(Num_start,'%08d'),'.tif')));
% Read the video files and convert each frame to tiff image files
for i=1:(Num_end-Num_start)
    % Sum of the images files after string concatenation to obtain average image data file
    im=im+double(imread(strcat(prefix,num2str(Num_start+i,'%08d'),'.tif')));
end
im=im/(Num_end-Num_start+1);
im_noBG=im-im_background;

signal_R=sum(im_noBG(:,:,1),1)'/size(im_noBG,2);
signal_G=sum(im_noBG(:,:,2),1)'/size(im_noBG,2);
signal_B=sum(im_noBG(:,:,3),1)'/size(im_noBG,2);
```

```
imshow(abs(im_noBG)/max(abs(im_noBG(:))));
pause;
plot(signal_R,'r');
hold on;
plot(signal_G,'g');
plot(signal_B,'b');
hold off;
xlabel('pixel');
ylabel('accumulated signal intensity');
legend('red','green','blue');
```

A.4 Single particle combustion modeling

A.4.1 Pre-ignition modeling

```
Clear
Clc
% time resolution
Delt=1E-4; % timestep size
T0=300;
timelength =0.06;

% atmospheres
% parameters for PRB coal
frac_moisture = 0.10;   % mass basis
frac_volatile = 0.39;   % volatile fraction, [1]
frac_ash=0.0813;        % ash fraction, [1]
frac_char=1-frac_moisture-frac_volatile-frac_ash;

% parameters for PRB coal particle
dp0= 150E-6;    % particle diameter, in m narrow class is (125-150)
density=1400;   % density, [kg/m^3]
m_p(1)=density*pi/6*dp0^3;  % mass of single particle, [kg]
m_ash=m_p(1)*frac_ash;      % mass of ash in single particle, [kg]
m_char=m_p(1)*frac_char;
m_moisture(1)=m_p(1)*frac_moisture;
m_u(1)=m_p(1)*frac_volatile;
f_moisture(1)=m_moisture(1)/m_p(1);
Cp=1680; % specific heat capacity of particle, [J/(kg*K)]
eps=0.8; % emissivity factor of particle [1]

% %% physical constants
sig=5.67E-8;    % boltzman constant, [W/(m^2*K^4)]
```

```
R=8.3145;       % ideal gas constant, [J/(mol*K)]

% %% kinetic parameters
A3=1.34e5; % [/s]
E3=74100; % [J/mol]
P_tot=101325;
MW_H2O=0.018;
MW_AIR=0.0284;
MW_CO2=0.044;
MW_N2=0.028;
MW_O2=0.032;

Tp(1)=300;
t(1)=0;
for i=2:1:timelength/Delt
t(i)=(i-1)*Delt;
%
% 1800 K gas flame, oxidizing atmosphere
%
T_case = 1800;                                                  % gas temperature in Kelvin
Tg(i-1)= (T_case+67.165)-(T_case-232.8578).*exp(-1.*t(i-1)/0.00582)-915.0673.*t(i-1);      %
1800 K gas enivronment
P_O2_c(i-1) = (19.90426-19.8641.*exp(-1.*t(i-1)/0.006386))./100.*101325;                  %
oxygen partial pressure in the reactor
X_O2_c(i-1)=P_O2_c(i-1)/P_tot;
P_H2O_0 = 0.2227*101325;
X_H2O_0=P_H2O_0/P_tot;
X_O2_0= 19.90426/100;
%
% 1300 K gas flame, oxidizing atmosphere
%
% T_case = 1300;                                                % gas temperature in Kelvin
% Tg(i-1)=(T_case-78.592)-(T_case-378.4971)*exp(-1.*t(i-1)/0.001);            % 1300 K gas
enivronment
% P_O2_c(i-1) = (20.49649-20.49649.*exp(-1.*t(i-1)/0.001001))./100.*101325;     % centerline
oxygen partial pressure
% X_O2_c(i-1)=P_O2_c(i-1)/P_tot;
% P_H2O_0 = 0.0654*101325;
% X_H2O_0=P_H2O_0/P_tot;
% X_O2_0= 20.49649/100;
%
% calculate near-particle atmosphere
X_CO2_0=X_H2O_0/2;
X_N2_0=1-X_H2O_0-X_O2_0-X_CO2_0;
X_H2O_c(i-1)=X_O2_c(i-1)/X_O2_0*X_H2O_0;
X_CO2_c(i-1)=X_O2_c(i-1)/X_O2_0*X_CO2_0;
```

```
X_N2_c(i-1)=1-X_O2_c(i-1)-X_CO2_c(i-1)-X_H2O_c(i-1);
MW_mix_c(i-1)=X_H2O_c(i-1)*MW_H2O+X_O2_c(i-1)*MW_O2+X_CO2_c(i-
1)*MW_CO2+X_N2_c(i-1)*MW_N2;
Y_H2O_c(i-1)=X_H2O_c(i-1)*MW_H2O/MW_mix_c(i-1);
rho_mix_c(i-1) = P_tot*MW_mix_c(i-1)/R/Tg(i-1);
%
% particle property
%
Dp(i-1)=dp0;                    % constant size assumption, [m].
rhop(i-1)=6*m_p(i-1)/pi/Dp(i-1)^3;  % constant size assumption holds during devolatilization
Ap(i-1)=pi*Dp(i-1)^2;            % surface area of particle, [m^2]

% transport and thermal parameters
kg(i-1)=5.2957E-5.*Tg(i-1)+1.4999E-2;   % thermal conductivity of gas [w/(m*K)], on
temperature [K]
D_O2(i-1)=1.5636E-9*Tg(i-1)^1.67003;    % binary diffusion rate of O2-N2, [m^2/s]
D_H2O(i-1)=0.282e-4*(0.5*(Tp(i-1)+Tg(i-1))/298)^1.5;
D_CH4(i-1)=0.217e-4*(0.5*(Tp(i-1)+Tg(i-1))/298)^1.5;
k_h2o(i-1)=2.0*D_H2O(i-1)/Dp(i-1);      % Sherwood number = 2.
k_vol(i-1)=2.0*D_CH4(i-1)/Dp(i-1);      % Sherwood number = 2.
%
% kinetic data for devolatilization
k3(i-1)=A3*exp(-E3/R/Tg(i-1)); % [/s]
k(i-1)=k3(i-1);
%
% coal particle mass and heat transfer-drying, boiling
% Calulate Bm
P_moisture_sat(i-1) = 101325*exp(-2.1286e5/Tp(i-1)/Tp(i-1)-3.8224e3/Tp(i-1)+11.77);     %Pa
L_h2o=2260000;   %j/kg
if Tp(i-1)<373.25
   X_H2O_s(i-1) = P_moisture_sat(i-1)/P_tot;
else
   X_H2O_s(i-1) = 1;
end
MW_mix_s(i-1)= X_H2O_s(i-1)*MW_H2O+(1-X_H2O_s(i-1))*MW_mix_c(i-1);
Y_H2O_s(i-1)= X_H2O_s(i-1)*MW_H2O/MW_mix_s(i-1);
Bm(i-1)= (Y_H2O_s(i-1)-Y_H2O_c(i-1))/(1-Y_H2O_s(i-1));
%
% drying
if (m_moisture(i-1)>0 && Tp(i-1)<373.25)
   h_v(i-1)=2*log(1+Bm(i-1))/Bm(i-1)*kg(i-1)/Dp(i-1);
   m_moisture(i)=m_moisture(i-1)-k_h2o(i-1)*Ap(i-1)*rho_mix_c(i-1)*log(1+Bm(i-1))*Delt;
   m_u(i)=m_u(i-1);
   m_p(i)=m_moisture(i)+m_u(i)+m_char+m_ash;
   Tp(i)=Tp(i-1)+((Ap(i-1)*(h_v(i-1)*(Tg(i-1)-Tp(i-1))+eps*sig*(T0^4-Tp(i-
1)^4)))*Delt/Cp+(m_p(i)-m_p(i-1))*L_h2o/Cp)/m_p(i-1)-(m_p(i)-m_p(i-1))*Tp(i-1)/m_p(i);
```

```
    X_vol_s(i-1)=0;

% boiling
elseif (m_moisture(i-1)>0 && Tp(i-1)>=373.25)
    h_v(i-1)=2*kg(i-1)/Dp(i-1);
    m_moisture(i)=m_moisture(i-1)-Ap(i-1)*(h_v(i-1)*(Tg(i-1)-Tp(i-1))+eps*sig*(T0^4-Tp(i-
1)^4))*Delt/L_h2o;
    m_u(i)=m_u(i-1);
    m_p(i)=m_moisture(i)+m_u(i)+m_char+m_ash;
    Tp(i)=373.25;
    X_vol_s(i-1)=0;

% devolatilization
elseif (m_moisture(i-1)<=0 && m_u(i-1)>0)
    h_v(i-1)=2*kg(i-1)/Dp(i-1);
    m_moisture(i)=0;
    m_u(i)=m_u(i-1)-m_u(i-1)*k(i-1)*Delt;
    m_p(i)=m_moisture(i)+m_u(i)+m_char+m_ash;
    Tp(i)=Tp(i-1)+(Ap(i-1)*(h_v(i-1)*(Tg(i-1)-Tp(i-1))+eps*sig*(T0^4-Tp(i-
1)^4))*Delt)/Cp/m_p(i-1)-(m_p(i)-m_p(i-1))*Tp(i-1)/m_p(i);
    X_vol_s(i-1)=m_u(i-1)*k(i-1)/k_vol(i-1)/Ap(i-1)*R*Tg(i-1)/P_tot;

% heating
else
    h_v(i-1)=2*kg(i-1)/Dp(i-1);
    m_moisture(i)= m_moisture(i-1);
    m_u(i)=m_u(i-1);
    m_p(i)=m_moisture(i)+m_u(i)+m_char+m_ash;
    Tp(i)=Tp(i-1)+(Ap(i-1)*(h_v(i-1)*(Tg(i-1)-Tp(i-1))+eps*sig*(T0^4-Tp(i-
1)^4))*Delt)/Cp/m_p(i-1);
    X_vol_s(i-1)=0;
end
% Tp(i)=Tp(i-1)+0.2;
f_moisture(i)=m_moisture(i)/m_p(i);
end

tt=t(1:timelength/Delt-1);
figure (1)
plot(t*1000, m_p*1e9);
xlabel('Res. time (ms)'), ylabel('particle mass (microgram)');
figure (2)
plot(tt*1000, X_vol_s);
xlabel('Res. time (ms)'), ylabel('Volatile mole fraction at particle surface');
figure (3)
plot(t*1000, m_u*1e9);
xlabel('Res. time (ms)'), ylabel('Volatile mass remaining in particle (microgram)');
```

```
figure (4)
plot(t*1000, Tp);
xlabel('Res. time, (ms)'), ylabel('Particle temperature');
figure (5)
plot(t*1000, m_moisture*1e9);
xlabel('Res. time, (ms)'), ylabel('Moisture mass remaining in particle (microgram)');

% Extract Data to file
Datalist=[t(1:0.06/Delt-1);m_moisture(1:0.06/Delt-1);m_u(1:0.06/Delt-
1);X_H2O_s;X_vol_s;Tp(1:0.06/Delt-1)].';
```

A.4.2 Combustion modeling

```
clear
clc
% time resolution
Delt=1E-4; % timestep size
T0=300;
timelength =0.1;
t(1)=0;

% physical constants
sig=5.67E-8; % boltzman constant, [W/(m^2*K^4)]
R=8.3145; % ideal gas constant, [J/(mol*K)]
MW_H2O=0.018;
MW_AIR=0.0284;
MW_CO2=0.044;
MW_N2=0.028;
MW_O2=0.032;
MW_vol=0.030;
MW_C=0.012;

% Coal property
% parameters for PRB coal
frac_moisture = 0.11;    % mass basis
frac_volatile = 0.39;    % volatile fraction, [1]
frac_ash=0.0813;         % ash fraction, [1]
frac_char=0.4287

hc= 3.2808E7;                % heat of char combustion C->CO2, [J/kg]
frac_of_heat_to_particle=0.3; % fraction of heat release returning for particle heating. Source:
ANSYS fluent literatures
```

```
% parameters for PRB coal particle
dp0= 64e-6;     %  particle diameter, in m narrow class is (125-150)
dp_radial=1000; % radial profile with j from 1 to 150 micron distance away from the particle
surface
density=1400;   % density, [kg/m^3]
m_p(1)=density*pi/6*dp0^3;  % mass of single particle, [kg]
m_ash=m_p(1)*frac_ash;      % mass of ash in single particle, [kg]
m_char(1)=m_p(1)*frac_char;
m_moisture(1)=m_p(1)*frac_moisture;
m_u(1)=m_p(1)*frac_volatile;
f_moisture(1)=m_moisture(1)/m_p(1);
Cp=1680; % specific heat capacity of particle, [J/(kg*K)]
eps=0.8; % emissivity factor of particle [1]

% pyrolysis kinetics
A3=1.34e5; % [/s] L. Cai et al. / Fuel 182 (2016) 958?66
% And R. Jovanovic et al./International Journal of Heat and Mass Transfer 54 (2011) 921?31
E3=74100; % [J/mol]

% Volatile reaction kinetics
hv_combustion= 2.77e7;
%[J/kg] HEATING VALUE OF VOLATILE COMBUSTION : Table 2 of Gururajan et al,
Mechanisms for the Ignition of Pulverized Coal Particles
hv=1000000;         % [J/kg] Heat of volatile decomposition/devolatilization
Avol_oxi=3.88e8;    % [m^3/mol/s]
Evol_oxi=1.591e5;   % J/mol % Mechanisms for the Ignition of Pulverized Coal Particles using
Vandenabeele et al kinetics in Table 1

% Char surface reaction kinetics
% Lei Chen Oxy-fuel combustion review paper of 2012 and
% Mechanisms for the Ignition of Pulverized Coal Particles,CNF 81: 119-132 (1990)
%0.000045; % [kg/m^2/s/Pa]

Ac_steam=0.00192; % [kg/m^2/s/Pa]
Ec_steam=147000;  % [J/mol] % Lei chen
Ac_co2=0.00635; % [kg/m^2/s/Pa]
Ec_co2=162000;  % [J/mol] % Lei chen

% Jovanovic et al./International Journal of Heat and Mass Transfer 54 (2011) 921?31
% Char surface oxidation reaction kinetics
Ac_oxi=0.0045;
Ec_oxi=69000; %
% Coal surface oxidation reaction kinetics
Acoal_oxi=0.016; % [kg/m^2/s/Pa]
Ecoal_oxi=1.49e5; % J/mol
```

```
% Operating Parameters/constants
P_tot=101325;
Tp(1)=300;
for i=2:1:timelength/Delt
 t(i)=(i-1)*Delt;
%
% 1800 K gas flame, oxidizing atmosphere
%
T_case = 1800;                                          % gas temperature in Kelvin
Tg(i-1)= (T_case+67.165)-(T_case-232.8578).*exp(-1.*t(i-1)/0.00582)-915.0673.*t(i-1);  %
1800 K gas enivronment
P_O2_c(i-1) = (19.90426-19.8641.*exp(-1.*t(i-1)/0.006386))./100.*101325;   % oxygen partial
pressure in the reactor
X_O2_c(i-1)=P_O2_c(i-1)/P_tot;
P_H2O_0 = 0.2227*101325;
X_H2O_0=P_H2O_0/P_tot;
X_O2_0= 19.90426/100;
Cpg= 1286; % for 1800 K, unit in J/kg-K Appendix Table C.1 of Stephen Turn's book on
combustion
%
% For 1800 K gas flame, reducing-to-oxidizing atmosphere, activate line 92 to 100 and
deactivate line 79-89
%
% T_case = 1800;                                          % gas temperature in Kelvin
% Tg(i-1)= (T_case+67.165)-(T_case-232.8578).*exp(-1.*t(i-1)/0.00582)-915.0673.*t(i-1);  %
1800 K gas enivronment
% P_O2_c(i-1) = (6295.2.*t(i-1).^3-2754.7.*t(i-1).^2+393.77.*t(i-1)-6.324)./100.*101325;
% X_O2_c(i-1)=P_O2_c(i-1)/P_tot;
% P_H2O_0 = 0.2227*101325;
% X_H2O_0=P_H2O_0/P_tot;
% X_O2_0= 2/100;
% Cpg= 1286;
%
% calculate near-particle atmosphere
X_CO2_0=X_H2O_0/2;
X_N2_0=1-X_H2O_0-X_O2_0-X_CO2_0;
X_H2O_c(i-1)=X_O2_c(i-1)/X_O2_0*X_H2O_0;
X_CO2_c(i-1)=X_O2_c(i-1)/X_O2_0*X_CO2_0;
X_N2_c(i-1)=1-X_O2_c(i-1)-X_CO2_c(i-1)-X_H2O_c(i-1);
MW_mix_c(i-1)=X_H2O_c(i-1)*MW_H2O+X_O2_c(i-1)*MW_O2+X_CO2_c(i-
1)*MW_CO2+X_N2_c(i-1)*MW_N2;
Y_H2O_c(i-1)=X_H2O_c(i-1)*MW_H2O/MW_mix_c(i-1);
rho_mix_c(i-1) = P_tot*MW_mix_c(i-1)/R/Tg(i-1);
%
% particle property
Dp(i-1)=dp0; % constant size assumption, [m]. MODIFIED_AG
```

```
rhop(i-1)=6*m_p(i-1)/pi/Dp(i-1)^3; %constant size assumption holds during devolatilization
Ap(i-1)=pi*Dp(i-1)^2; % surface area of particle, [m^2]
%
% transport and thermal parameters
kg(i-1)=5.2957E-5.*Tg(i-1)+1.4999E-2; % thermal conductivity of gas [w/(m*K)], on
temperature [K]
D_O2(i-1)=1.5636E-9*Tg(i-1)^1.67003; % binary diffusion rate of O2-N2, [m^2/s]
D_H2O(i-1)=0.282e-4*(0.5*(Tp(i-1)+Tg(i-1))/298)^1.5;
D_CH4(i-1)=0.217e-4*(0.5*(Tp(i-1)+Tg(i-1))/298)^1.5;
k_h2o(i-1)=2.0*D_H2O(i-1)/Dp(i-1);      % Sherwood number = 2. //MODIFIED_AG
k_vol(i-1)=2.0*D_CH4(i-1)/Dp(i-1);      % Sherwood number = 2. //MODIFIED_AG
%
% kinetic data for devolatilization
k3(i-1)=A3*exp(-E3/R/Tg(i-1)); % [/s]
k(i-1)=k3(i-1);

% coal particle mass and heat transfer-drying, boiling
% Calulate Bm
P_moisture_sat(i-1) = 101325*exp(-2.1286e5/Tp(i-1)/Tp(i-1)-3.8224e3/Tp(i-1)+11.77);     %Pa
L_h2o=2260000;   %j/kg
if Tp(i-1)<373.25
   X_H2O_s(i-1) = P_moisture_sat(i-1)/P_tot;
else
   X_H2O_s(i-1) = 1;
end
MW_mix_s(i-1)= X_H2O_s(i-1)*MW_H2O+(1-X_H2O_s(i-1))*MW_mix_c(i-1);
Y_H2O_s(i-1)= X_H2O_s(i-1)*MW_H2O/MW_mix_s(i-1);
Bm(i-1)= (Y_H2O_s(i-1)-Y_H2O_c(i-1))/(1-Y_H2O_s(i-1));

% drying
if (m_moisture(i-1)>0 && Tp(i-1)<373.25)
   h_v(i-1)=2*log(1+Bm(i-1))/Bm(i-1)*kg(i-1)/Dp(i-1);
   m_moisture(i)=m_moisture(i-1)-k_h2o(i-1)*Ap(i-1)*rho_mix_c(i-1)*log(1+Bm(i-1))*Delt;
   m_u(i)=m_u(i-1);
   m_char(i)=m_char(i-1);
   m_p(i)=m_moisture(i)+m_u(i)+m_char(i)+m_ash;
   Tp(i)=Tp(i-1)+((Ap(i-1)*(h_v(i-1)*(Tg(i-1)-Tp(i-1))+eps*sig*(T0^4-Tp(i-
1)^4)))*Delt/Cp+(m_p(i)-m_p(i-1))*L_h2o/Cp)/m_p(i-1);
   X_vol_s(i-1)=0;
   X_O2_s(i-1)=(1-X_H2O_s(i-1))*X_O2_c(i-1)/(X_O2_c(i-1)+X_CO2_c(i-1)+X_N2_c(i-1));
% boiling
elseif (m_moisture(i-1)>0 && Tp(i-1)>=373.25)
   h_v(i-1)=2*kg(i-1)/Dp(i-1);
   m_moisture(i)=m_moisture(i-1)-Ap(i-1)*(h_v(i-1)*(Tg(i-1)-Tp(i-1))+eps*sig*(T0^4-Tp(i-
1)^4))*Delt/L_h2o;
   m_u(i)=m_u(i-1);
```

```
    m_char(i)=m_char(i-1);
    m_p(i)=m_moisture(i)+m_u(i)+m_char(i)+m_ash;
    Tp(i)=373.25;
    X_vol_s(i-1)=0;
    X_O2_s(i-1)=(1-X_H2O_s(i-1))*X_O2_c(i-1)/(X_O2_c(i-1)+X_CO2_c(i-1)+X_N2_c(i-1));

% IGNITION AND COMBUSTION
elseif ((m_u(i-1)>m_u(1)*0.01 || m_char(i-1)>0) && Tp(i-1)>=573)
    h_v(i-1)=2*kg(i-1)/Dp(i-1);
    m_moisture(i)=0;
    X_vol_s(i-1)=m_u(i-1)*k(i-1)/k_vol(i-1)/Ap(i-1)*R*Tg(i-1)/P_tot;
    X_O2_s(i-1)=(1-X_vol_s(i-1))*X_O2_c(i-1)/(X_O2_c(i-1)+X_CO2_c(i-1)+X_N2_c(i-
1)+X_H2O_c(i-1));

% The Kinetic/Diffusion Surface Reaction Rate Model for char, coal
    R_diff(i-1)= 5.32E-12*((Tp(i-1)+Tg(i-1))/2)^0.75/Dp(i-1);       % Diffusion resistance of
oxygen to particle from Lei Chen data
    R_diff_steam(i-1)=5.77E-12*((Tp(i-1)+T_case)/2)^0.75/Dp(i-1);   % Diffusion resistance of
steam to particle from Lei Chen data and W. Prationo et al. / Fuel Processing Technology xxx
(2015) xxx–xxx
    R_diff_co2(i-1)=1.72E-12*((Tp(i-1)+T_case)/2)^0.75/Dp(i-1);     % Diffusion resistance of
steam to particle
    R_chem(i-1)= Ac_oxi*exp(-Ec_oxi/R/Tp(i-1));            % oxygen chemistry resistance at
particle surface [kg/m^2/s/Pa]
    R_chem_steam(i-1)= Ac_steam*exp(-Ec_steam/R/Tp(i-1));   % steam chemistry resistance at
particle surface [kg/m^2/s/Pa]
    R_chem_co2(i-1)= Ac_co2*exp(-Ec_co2/R/Tp(i-1));         % steam chemistry resistance at
particle surface [kg/m^2/s/Pa]
    R_chem_coal(i-1)= Acoal_oxi*exp(-Ecoal_oxi/R/Tp(i-1));  % oxygen chemistry resistance at
non-devolatilized coal surface [kg/m^2/s/Pa]

% Rate of devolatilization, volatile combustion, coal ignition and char ignition
    if (m_u(i-1)>m_u(1)*0.01)
        R_dev(i-1) = m_u(i-1)*k(i-1);
    else
        R_dev(i-1) = 0;
    end
    X_Vol_LFL=0.05;
    if (X_vol_s(i-1)<X_Vol_LFL || Tp(i-1)<573)
        R_vol(i-1)=0;
    else
        R_vol(i-1)= MW_vol*Avol_oxi*exp(-Evol_oxi/R/Tg(i-1))*(P_tot/R/Tg(i-1))^2*X_vol_s(i-
1)*X_O2_c(i-1); %R_homo is in kg/m3-s - Mechanisms for the Ignition of Pulverized Coal
Particles,CNF 81: 119-132 (1990)
    end
    if R_vol(i-1)>R_dev(i-1)
```

```
      R_vol(i-1)=R_dev(i-1);
    end
    R_coal(i-1) = Ap(i-1)*P_O2_c(i-1)/(1/R_diff(i-1)+1/R_chem_coal(i-1));
    R_char(i-1) = Ap(i-1)*P_O2_c(i-1)/(1/R_diff(i-1)+1/R_chem(i-1));

% HOMOGENEOUS IGNITION AND COMBUSTION
    if (R_dev(i-1)>R_coal(i-1) && R_vol(i-1)>R_char(i-1))
    % Devolatilization will occur and homogeneous reaction will occur
    m_u(i)=m_u(i-1)-m_u(i-1)*k(i-1)*Delt;
    % while char combustion reaction is stopped
    R_het_char(i-1)=0;
    end
% HETEROGENEOUS IGNITION AND COMBUSTION
if (R_dev(i-1)>R_coal(i-1) && R_vol(i-1)<R_char(i-1))
    % Devolatilization will occur and heterogeneous reaction will occur
    m_u(i)=m_u(i-1)-m_u(i-1)*k(i-1)*Delt;
    % while volatile combustion reaction is stopped
    % R_homo(i)=0;
    if (m_u(i-1)> m_u(1)*0.01)
     R_het_char(i-1)=0;
    else
    R_het_char(i-1)=Ap(i-1)*(P_O2_c(i-1)/(1/R_diff(i-1)+1/R_chem(i-1))+X_H2O_c(i-
1)*P_tot/(1/R_diff_steam(i-1)+1/R_chem_steam(i-1))+X_CO2_c(i-1)*P_tot/(1/R_diff_co2(i-
1)+1/R_chem_co2(i-1))); % kg/s char oxidation, gasification by steam and co2
    end
end
% HETERO-HOMOGENEOUS IGNITION AND COMBUSTION
   if (R_dev(i-1)<R_coal(i-1))
   % Devolatilization, homogeneous reaction and heterogeneous reaction will occur
        if (m_u(i-1)>m_u(1)*0.01)
            m_u(i)=m_u(i-1)-R_coal(i-1)*Delt;
            R_het_char(i-1)=0;
        else
            m_u(i)=m_u(i-1);
            R_het_char(i-1)=Ap(i-1)*(P_O2_c(i-1)/(1/R_diff(i-1)+1/R_chem(i-1))+X_H2O_c(i-
1)*P_tot/(1/R_diff_steam(i-1)+1/R_chem_steam(i-1))+X_CO2_c(i-1)*P_tot/(1/R_diff_co2(i-
1)+1/R_chem_co2(i-1))); % kg/s char oxidation, gasification by steam and co2
   end
   end
    m_char(i)=m_char(i-1)-R_het_char(i-1)*Delt; % heterogeneous combustion (mass of char left
in particle)
    m_p(i)=m_moisture(i)+m_u(i)+m_char(i)+m_ash;
    Tp(i)=Tp(i-1)+(Ap(i-1)*(h_v(i-1)*(Tg(i-1)-Tp(i-1))+eps*sig*(T0^4-Tp(i-
1)^4))*Delt)/Cp/m_p(i-1)-frac_of_heat_to_particle*(m_char(i)-m_char(i-1))*hc/Cp/m_p(i-1);
else
    h_v(i-1)=2*kg(i-1)/Dp(i-1);
```

```
    m_moisture(i)= m_moisture(i-1);
    m_u(i)=m_u(i-1);
    m_char(i)=m_char(i-1);
    m_p(i)=m_moisture(i)+m_u(i)+m_char(i)+m_ash;
    Tp(i)=Tp(i-1)+(Ap(i-1)*(h_v(i-1)*(Tg(i-1)-Tp(i-1))+eps*sig*(T0^4-Tp(i-
1)^4))*Delt)/Cp/m_p(i-1);%-(m_p(i)-m_p(i-1))*hc/Cp/m_p(i-1);
    X_vol_s(i-1)=0;
    X_O2_s(i-1)=P_O2_c(i-1)/P_tot;
    X_H2O_s(i-1)=X_H2O_c(i-1);
end
f_moisture(i)=m_moisture(i)/m_p(i);
end
%
tttt=timelength;
tt=t(1:tttt/Delt-1);
figure (1)
plot(tt*1000, X_vol_s);
xlabel('Res. time (ms)'), ylabel('Volatile mole fraction at particle surface');
figure (2)
plot(t*1000, m_u*1e9);
xlabel('Res. time (ms)'), ylabel('Volatile mass remaining in particle (microgram)');
figure (3)
plot(t*1000, m_char*1e9);
xlabel('Res. time (ms)'), ylabel('Char mass remaining in particle (microgram)');
figure (4)
plot(t*1000, Tp);
xlabel('Res. time, (ms)'), ylabel('Particle temperature');
% Extract Data to file
k=timelength;
Datalist=[t(1:k/Delt-1);m_moisture(1:k/Delt-1);m_u(1:k/Delt-1);m_char(1:k/Delt-
1);m_p(1:k/Delt-1);Tp(1:k/Delt-1);X_vol_s].';
```